

DISSERTATION

MONIQUE MEUSCHKE

VISUALIZATION, CLASSIFICATION, AND INTERACTION FOR  
RISK ANALYSIS AND TREATMENT PLANNING OF CEREBRAL  
ANEURYSMS









VISUALIZATION, CLASSIFICATION, AND INTERACTION FOR RISK  
ANALYSIS AND TREATMENT PLANNING OF CEREBRAL ANEURYSMS

DISSERTATION

zur Erlangung des akademischen Grades

**Doktoringenieurin (Dr.-Ing.)**

vorgelegt der Fakultät für Informatik  
Otto-von-Guericke Universität Magdeburg

von **M.Sc. MONIQUE MEUSCHKE**

geb. am 03.06.1988, in Wippra

Gutachter

Prof. Dr.-Ing. habil. Bernhard Preim  
Prof. Dr.-Ing. habil. Heidrun Schumann  
Prof. Dr.-Ing. Ingrid Hotz

Magdeburg, den 21. Januar 2019



Für meine lieben Eltern

– Christina & Jürgen –

und meinen lieben Bruder

– Norman –



## ABSTRACT

---

Cerebral aneurysms are weak vessel areas that can bulge out and balloon, caused by a pathologically altered structure of the vascular wall. They bear the risk of rupture, leading to internal bleeding causing high risks of mortality. Although most aneurysms will never rupture, the potential risk of bleeding makes the detection and risk-assessment of aneurysms a critical issue. Imaging methods are used for the detection and localization of aneurysms. The decision as to whether or not aneurysms should be treated must be carefully considered, as there is a risk of fatal outcome during surgery.

Their initiation and progression depend strongly on the interplay of vascular morphology and hemodynamics. Unfortunately, the processes causing aneurysm growth and rupture are not well understood. Blood flow simulations can obtain information about the patient-specific hemodynamics. It is also the basis for the development for new, low-risk treatment options since treatment success depends on blood flow characteristics.

In clinical routine, risk assessment and treatment planning are just based on morphological characteristics of an aneurysm and its surrounding vasculature. However, this information allows no reliable evaluation of the aneurysm state. To improve decision-making, medical and biomedical researchers analyze simulated flow data, which are multi-attribute data with high spatial and temporal complexity. The data exploration is performed quantitatively and qualitatively, where the former focuses on the evaluation of specific scalar values such as pressure or wall thickness and the latter focuses on the analysis of flow patterns such as vortices. Correlations between qualitative and quantitative characteristics can be revealed and formed into hypotheses that can lead to a better understanding of the internal aneurysm procedures. However, the visual exploration of flow data is a time-consuming process, which is affected by visual clutter and occlusions.

The goal of our work is to develop computer-aided methods that support the quantitative and qualitative visual exploration of morphological and hemodynamic characteristics in cerebral aneurysm data sets. Since this is an interdisciplinary process involving both physicians and fluid mechanics experts, redundancy-free management of aneurysm data sets is required to enable efficient analysis of the information. We developed a consistent structure to document aneurysm data sets, where users can search for specific cohorts, and individual cases can be analyzed more detailed to assess the aneurysm state as well as to weigh different treatment scenarios. The prerequisite for the visual exploration is the extraction of the ostium, which is a curved surface that separates the parent vessel from an aneurysm. We provide an automatic determination of the ostium. Based on this several other morphological descriptors are computed automatically. Besides an analysis of morphological aspects, the aneurysm data exploration comprises four more parts: a simultaneous evaluation of wall- and flow-related characteristics, a simultaneous analysis of multiple scalar information on the aneurysm wall, the analysis of mechanical wall processes as well as a qualitative characterization of the internal flow behavior. We provide methods for each of these parts: occlusion-free depictions of the vessel morphology and internal blood flow, interactive 2D and 3D visualizations to explore multi-attribute correlations, comparative glyph-based visualizations to explore mechanical wall forces and automatic classification of qualitative flow patterns. Our methods were designed and evaluated in collaboration with domain experts who confirmed their usefulness and clinical necessity.

## ZUSAMMENFASSUNG

---

Zerebrale Aneurysmen sind lokale Ausbeulungen der Gefäßwand, verursacht durch eine pathologisch veränderte Struktur dieser. Die Hauptgefahr für den Patienten besteht in einer Ruptur, was zu einer inneren Blutung führt und mit einer hohen Mortalität verbunden ist. Obwohl die meisten Aneurysmen nie rupturieren werden, macht das potenzielle Risiko einer Blutung die Erkennung und Risikobewertung von Aneurysmen zu einem wichtigen Thema. Bildgebende Verfahren werden zur Erkennung und Lokalisierung von Aneurysmen eingesetzt. Die Entscheidung, ob ein Aneurysma behandelt werden sollte oder nicht, muss sorgfältig abgewägt werden, da bei Eingriffen die Gefahr eines tödlichen Verlaufs besteht.

Ihre Entstehung und ihr Voranschreiten hängen stark vom Zusammenspiel der Gefäßmorphologie und Hämodynamik ab. Leider sind die Prozesse, die das Wachstum und die Ruptur des Aneurysmas verursachen, bisher nicht gut verstanden. Informationen über die patientenspezifische Hämodynamik können mit Hilfe von Blutflusssimulationen gewonnen werden. Diese sind auch die Grundlage für die Entwicklung neuer, risikoarmer Behandlungsmöglichkeiten, da der Behandlungserfolg von den Eigenschaften des Blutflusses abhängt.

In der klinischen Routine basieren die Risikobewertung und die Behandlungsplanung nur auf morphologischen Eigenschaften des Aneurysmas und seinem umgebenden Gefäßbaum. Diese Informationen erlauben jedoch keine zuverlässige Beurteilung des Aneurysmas. Um die Entscheidungsfindung zu verbessern, analysieren medizinische und biomedizinische Forscher simulierte Strömungsdaten. Dies sind Informationen mit hoher räumlicher und zeitlicher Komplexität, die eine Vielzahl an Attributen umfassen. Die Datenexploration wird quantitativ und qualitativ durchgeführt, wobei sich erstere auf die Bewertung spezifischer skalarer Werte wie Druck oder Wanddicke und letztere auf die Analyse von Flussmustern wie Wirbel konzentriert. Zusammenhänge zwischen qualitativen und quantitativen Merkmalen können aufgedeckt und zu Hypothesen geformt werden, die zu einem besseren Verständnis der Entwicklung und des Wachstums von Aneurysmen führen können. Die visuelle Exploration von Strömungsdaten ist jedoch ein zeitaufwendiger Prozess, der durch visuelle Verdeckung beeinflusst wird.

Ziel unserer Arbeit ist es, computergestützte Methoden zu entwickeln, die die quantitative und qualitative Exploration morphologischer und hämodynamischer Eigenschaften in zerebralen Aneurysmen unterstützen. Da es sich hierbei um einen interdisziplinären Prozess handelt, an dem sowohl Ärzte als auch Strömungsexperten beteiligt sind, ist eine redundanzfreie Verwaltung von Aneurysma-Datensätzen erforderlich, um eine effiziente Analyse der Informationen zu ermöglichen. Wir haben eine einheitliche Struktur zur Dokumentation von Aneurysma-Datensätzen entwickelt, in der Benutzer nach bestimmten Kohorten suchen können und einzelne Fälle detaillierter analysiert werden können, um den Zustand des Aneurysmas zu beurteilen und um verschiedene Behandlungsszenarien abzuwägen. Voraussetzung für die visuelle Exploration ist die Extraktion des Ostiums, das eine gebogene Fläche ist, die das Trägergefäß vom Aneurysma trennt. Wir haben eine automatische Extraktion des Ostiums entwickelt. Basierend darauf werden mehrere weitere morphologische Deskriptoren automatisch berechnet. Neben der Analyse morphologischer Aspekte umfasst die Datenexploration vier weitere Komponenten: eine gleichzeitige Analyse wand- und strömungsbezogener Merkmale, eine gleichzeitige Analyse mehrerer skalarer Informationen auf der Aneurysmawand, die Analyse mechanischer Wandprozesse sowie eine qualitative Charakterisierung des internen Strömungsverhaltens. Wir stellen Methoden für jede dieser Komponenten zur Verfügung: okklusionsfreie Darstellungen der Gefäßmorphologie und des inneren Blutflusses, interaktive 2D und 3D Visualisierungen zur Exploration von Korrelationen zwischen mehreren Attributen, vergleichende Glyphen-basierte Visualisierungen zur Exploration mechanischer Wandkräfte und eine automatische Klassifizierung qualitativer Strömungsmuster. Unsere Methoden wurden in Zusammenarbeit mit Experten entwickelt und bewertet, die ihren Nutzen und ihre klinische Notwendigkeit bestätigt haben.

## DANKSAGUNG

---

An dieser Stelle möchte ich meinen besonderen Dank den Personen entgegen bringen, ohne deren Mithilfe die Anfertigung dieser Arbeit niemals zustande gekommen wäre.

Mein Dank gilt zunächst meinem Doktorvater Prof. Bernhard Preim, der mich stets mit seiner Erfahrung und Vertrauen unterstützt hat. Egal in welcher Lebenslage, du hattest immer ein offenes Ohr und standst mir mit Rat und Tat zur Seite. In schwierigen Zeiten sagtest du zu mir: "‘Privat geht über Katastrophe'" und hattest stets Verständnis für alle Lebenslagen. Vielen Dank für deine Hilfe und ich hoffe, dass wir auch in Zukunft erfolgreich zusammenarbeiten werden.

Als nächstes möchte ich mich bei vielen Kollegen bedanken, die in den letzten Jahren auch zu Freunden geworden sind. Ganz besonders möchte ich an dieser Stelle Kai Lawonn danken. Die Zusammenarbeit mit dir ist etwas ganz besonders aus einem einfachen aber wichtigen Grund, nämlich, dass ich mich immer zu 100 % auf dich verlassen kann. Viele Stunden haben wir damit verbracht neue Ideen zu diskutieren und an deren Umsetzung zu tüfteln, was durch deine motivierende Art immer Spaß gemacht hat. In anstrengenden und nervenaufreibenden Zeiten vor einer Deadline, hast du mir die Zuversicht gegeben, dass wir als Team alles rechtzeitig fertig bekommen werden.

Daneben danke ich Benjamin Köhler, der mir während der Zeit meiner Masterarbeit als Betreuer zur Seite stand und mir mit seiner Erfahrung während dieser Zeit den Einstieg in die Promotionszeit sehr erleichtert hat. Als Ko-Autor hast du mir geholfen meine erste größere Publikation zu schreiben. Des Weiteren möchte ich Tobias Günther und Prof. Markus Gross danken, die es ermöglicht haben, dass ich einen dreimonatigen Forschungsaufenthalt an der ETH Zürich wahrnehmen durfte. Ich habe in dieser Zeit viele interessante Projekte kennen gelernt, wobei der Ausflug zu Disney Research ein besonderes Erlebnis war. Ebenso möchte ich Rocco Gasteiger danken, der mich während des Studiums als wissenschaftliche Hilfskraft betreut hat. Während dieser Zeit hatte ich die Möglichkeit mich mit den Grundlagen meines späteren Promotionsthemas vertraut zu machen und konnte dabei stets von der Erfahrung und besonnenen Art von Rocco profitieren.

Außerdem möchte ich mich bei meinen lieben Kollegen vom Lehrstuhl für Strömungsmechanik, Gábor Janiga, Philipp Berg und Samuel Voß bedanken, die mit ihrer Expertise im Bereich Blutflusssimulation den Ausgangspunkt für diese Arbeit geschaffen haben. Neben der ingenieurwissenschaftlichen Unterstützung, war die erfolgreiche Umsetzung dieser Arbeit auch stets auf medizinische Kooperationspartner angewiesen. Mein Dank gilt in diesem Zusammenhang Dr. Uta Preim, Dr. Oliver Beuing sowie Dr. Ralph Wickenhöfer für das Einbringen ihrer medizinischen Expertise und dem geduldgigen Evaluieren unserer entwickelten Methoden.

Darüber hinaus möchte ich mich bei meinen Kollegen Uli Niemann, Steffen Oeltze-Jafra, Benjamin Behrendt, Gabriel Mistelbauer, Nico Merten, Sebastian Wegener, Kai Nie, Sandy Engelhardt und Negar Chabi für die vielen lustigen Pausen in der Kaffeeküche bedanken. Neben kleinen Arbeitsstreichen standet ihr immer für fachliche Diskussionen oder motivierende Gespräche zur Verfügung. Ein ganz besonderer Dank gilt auch Steffi und den Petras aus dem Sekretariat sowie den Admins Thoro und Heiko. Danke für eure Hilfe in vielen organisatorischen und praktischen Dingen und vor allem Steffi für ihren Einsatz beim Korrekturlesen unserer Veröffentlichungen.

Tief verbunden und dankbar bin ich meiner Familie, Jürgen und Christina Meuschke, meinem Bruder Norman Meuschke sowie meinem lieben Opa Horst Maier und Dagmar Vinzenti für ihre nicht endende Unterstützung und ihr Verständnis bei der Anfertigung dieser Arbeit. Meine lieben Eltern haben mir meinen bisherigen Lebensweg ermöglicht und stets an mich geglaubt, auch wenn ich es manchmal nicht mehr getan habe. Ohne die Geduld und Motivation meines Bruders hätte ich das Studium wohl nie zu Ende gebracht. Ich danke dir dafür, dass du was in mir gesehen hast, was ich nie für möglich gehalten hätte. Die Lebensweisheiten und Naturverbundenheit meines Opas haben Besuche immer zu einem schönen Erlebnis gemacht und wesentlich dazu beigetragen sich von der ein oder anderen stressigen Phase zu erholen.





## CONTENTS

---

### I PRELIMINARIES

- 1 INTRODUCTION 5
  - 1.1 Motivation of this Thesis 6
  - 1.2 Structure and Contributions of this Thesis 6

### II BACKGROUND

- 2 MEDICAL BACKGROUND 13
  - 2.1 Aneurysm Epidemiology 13
  - 2.2 Aneurysm Pathogenesis 14
  - 2.3 Aneurysm Classification 15
    - 2.3.1 Etiology 15
    - 2.3.2 Localization 16
    - 2.3.3 Morphology 16
  - 2.4 Aneurysm Rupture 18
  - 2.5 Vascular Imaging for Intracranial Aneurysms 19
    - 2.5.1 Angiographic Imaging 19
    - 2.5.2 Intravascular Imaging 20
  - 2.6 Aneurysm Treatment Procedures 21
    - 2.6.1 Surgical Clipping 22
    - 2.6.2 Endovascular Embolization 22
  - 2.7 Summary and Conclusion 23
- 3 HEMODYNAMIC BACKGROUND 27
  - 3.1 Image Segmentation 27
  - 3.2 Surface Model Reconstruction and Enhancement 29
  - 3.3 Extraction of Geometric and Morphological Features 29
  - 3.4 Volume Mesh Generation 30
  - 3.5 Computational Fluid Dynamics Simulation 32
    - 3.5.1 Governing Equations 33
    - 3.5.2 Flow Properties 34
    - 3.5.3 Boundary Conditions 35
    - 3.5.4 Solution Methods 35
    - 3.5.5 Hemodynamic Characteristics 36
    - 3.5.6 Fluid Structure Interaction 37
    - 3.5.7 Virtual Aneurysm Treatment 38
  - 3.6 Validation of Blood Flow Simulations 40
  - 3.7 Summary and Conclusion 42
- 4 VISUAL EXPLORATION OF BLOOD FLOW DATA 45
  - 4.1 Task Taxonomy for the Visual Exploration of Blood Flow Data 46
  - 4.2 Techniques for Task-Based Visual Blood Flow Exploration 47
    - 4.2.1 Spatial Overview 47
    - 4.2.2 Interactive Probing 50
    - 4.2.3 Feature Filtering 52
    - 4.2.4 Temporal Analysis 56
    - 4.2.5 Comparison 58
    - 4.2.6 Context Visualization 58
    - 4.2.7 Uncertainty Analysis 62
  - 4.3 Conclusion 63

### III GUIDED EXPLORATION OF ANEURYSM DATA

5	ANEULYSIS - ANEURYSM ANALYSIS FRAMEWORK	69
5.1	Task-Based Requirements of Aneurysm Data Exploration	70
5.2	Data Acquisition and Pre-Processing	71
5.2.1	Simulated Flow Data	72
5.2.2	Measured Flow Data	73
5.3	General Structure	75
5.4	Workflow	76
5.4.1	Adding a Case	76
5.4.2	Editing a Case	77
5.4.3	Visualizing a Case	78
5.5	MorAVis - Morphological Aneurysm Visualization Module	79
5.5.1	Extraction of the Aneurysm Ostium	79
5.5.2	Calculation of Morphological Descriptors	82
5.6	Evaluation and Results	83
5.6.1	Comparison to Expert Results	83
5.6.2	Evaluation of the Ostium Extraction	84
5.6.3	Evaluation of the Data Administration	85
5.7	Discussion and Limitations	86
5.8	Conclusion and Future Work	87
6	SURFACE-BASED EXPLORATION OF ANEURYSM DATA	91
6.1	CoWaFloVis - Combined Wall and Flow Visualization Module	91
6.1.1	Requirement Analysis	91
6.1.2	General Structure	92
6.1.3	2.5D Aneurysm Overview	94
6.1.4	3D Aneurysm Visualization	95
6.1.5	Linking between 2.5D and 3D View	97
6.1.6	Collaboration Tools	97
6.1.7	Evaluation and Results	97
6.1.8	Discussion and Limitations	99
6.1.9	Conclusion and Future Work	100
6.2	MuScaVis - Multiple Scalar Field Visualization Module	101
6.2.1	Requirement Analysis	102
6.2.2	General Structure	102
6.2.3	Calculation of the 2D Aneurysm Map	103
6.2.4	Multi-Field Correlation Analysis using the Circle Plot	104
6.2.5	Multi-Field Correlation Analysis using Statistical Plots	106
6.2.6	Multi-Field Analysis on the Aneurysm Surface	107
6.2.7	Brushing and Linking	112
6.2.8	Evaluation and Results	113
6.2.9	Discussion and Limitations	118
6.2.10	Conclusion and Future Work	119
6.3	CoTenVis - Comparative Tensor Visualization Module	120
6.3.1	Requirement Analysis	120
6.3.2	Glyph-Based Tensor Visualization	121
6.3.3	Evaluation and Results	126
6.3.4	Discussion and Limitations	129
6.3.5	Conclusion and Future Work	130
6.4	Animations for Aneurysm Data	131
6.4.1	Interactive Planning of Animations	131
6.4.2	Automatic Calculation of Animations	133
6.4.3	Evaluation and Results	135
6.4.4	Conclusion and Future Work	136

7	VIFLEX - VISUAL FLOW EXPLORATION MODULE	139
7.1	Automatic Clustering of Flow Patterns	139
7.1.1	Requirement Analysis	140
7.1.2	Path Line Similarity	140
7.1.3	Path Line Clustering	144
7.1.4	Visualization of Blood Flow Clusters	144
7.1.5	Evaluation and Results	148
7.1.6	Discussion and Limitations	155
7.1.7	Conclusion and Future Work	157
7.2	Automatic Classification of Flow Patterns	158
7.2.1	Requirement Analysis	159
7.2.2	Flow Pattern Classification	160
7.2.3	Visualization of the Classification Results	164
7.2.4	Evaluation and Results	168
7.2.5	Discussion and Limitations	173
7.2.6	Conclusion and Future Work	175
IV	CONCLUSION	
8	CONCLUSION	181
8.1	Summary	181
8.2	Future Work	182
V	APPENDIX	
	BIBLIOGRAPHY	189
	LIST OF PUBLICATIONS	215
	ABBREVIATIONS	217
	DECLARATION	221
	CURRICULUM VITAE	223

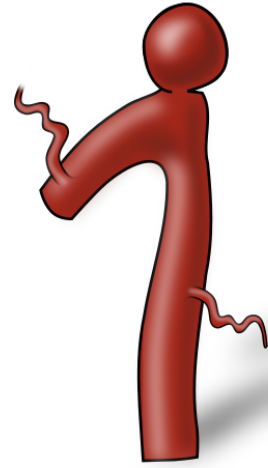


Part I

PRELIMINARIES



# Introduction







## INTRODUCTION

*Cardiovascular diseases* (CVDs) are a group of pathological changes that involve the heart and the vascular system. They include, for example, stroke, myocardial infarction, valvular heart disease, vascular constriction (stenosis), or vascular dilatation (an aneurysm), which can lead to fatal consequences for the patient such as cognitive and motor disabilities up to death. In recent years, the number of deaths from such a disease has risen continuously, from 12.3 million (25.8 %) in 1990 to 17.9 million deaths (32.1 %) in 2015. Thus, Cardiovascular diseases (CVDs) are currently the leading cause of death globally [248]. This percentage is expected to increase further in the coming years.

Aneurysms are among the most common CVDs, the two most important groups being cerebral aneurysms, occurring on the brain-supplying vessels, and aortic aneurysms. Their rupture leads to a *subarachnoid hemorrhage* (SAH), which is associated with a high mortality and morbidity rate [278]. Frequently, aneurysms are discovered by chance due to the increased use of imaging procedures for assessing the patient's state in case of widespread symptoms, e.g., persistent headaches. Most aneurysms are asymptomatic and will never rupture [403]. However, the detection of a cerebral aneurysm represents a severe dilemma - it has to be communicated to the patient and leads to anxiety. Treatment is often possible, but with a considerable risk of severe complications, which can exceed the danger of a natural rupture in everyday life [69]. A typical treatment is stenting, where a metal implant (stent) is inserted into the supporting vessel of an aneurysm. Especially cerebral aneurysms are difficult to treat, due to the long and convoluted way the doctor has to navigate the stent into the parent vessel. Thus, it is highly desirable to understand the individual risk better and to restrict treatment to high-risk patients.

Aneurysm initiation, evolution, and rupture are caused by several factors, such as genetics, vessel morphology, inflammation, hemodynamics and epidemiological factors such as gender and age. However, the interplay and correlations between these factors are not well understood. In clinical routine, aneurysm treatment is based on medical guidelines that consider only morphological features such as aneurysm location, size, and shape for risk assessment and treatment planning [35, 202, 352]. However, these attributes allow no reliable estimation of individual risk. Quantitative hemodynamic characteristics such as *wall shear stress* (WSS) or pressure as well as qualitative features, e.g., vortices seem to influence the aneurysm state including wall stability and thrombus formation [65, 69]. Therefore, information on patient-specific hemodynamics is used.

In larger arteries, e.g., the aorta, such data can be non-invasively acquired by *4D phase-contrast magnetic resonance imaging* (PC-MRI) [91]. In the smaller intracranial arteries, *computational fluid dynamics* (CFD) simulations and *fluid-structure interaction* (FSI) enable the investigation of the patient-specific internal wall mechanics and hemodynamics [164]. Both methods result in time-dependent flow data, representing one cardiac cycle. In recent years, the investigation of hemodynamic information has become increasingly important due to improved image modalities and higher computer performance, which results in more accurate modeling of blood flow behavior.

Based on this information, biomedical researchers can investigate how hemodynamic information influence the aneurysm initiation and progression as well as to evaluate different treatment options. They are interested in whether there are correlations between hemodynamic attributes that are associated with an increased risk of rupture and high-risk wall regions. Morphological and hemodynamic data are compared between ruptured and non-ruptured cases as well as between different stent configurations to assess the rupture risk and to find an optimal treatment. For treatment planning, CFD simulation tools enable the virtual use of certain stents in a patient-specific vessel geometry. Although the knowledge gained is not yet incorporated into the clinical routine, their integration into clinical research becomes relevant as measured and simulated flow data are increasingly available in clinical workstations. Therefore, in recent years physicians such as neuroradiologists have been increasingly involved in the investigation of hemodynamic data.

## 1.1 MOTIVATION OF THIS THESIS

Patient-specific data evaluation is needed to improve aneurysm risk evaluation and treatment planning. This includes a comparison to other ruptured and non-ruptured cases as well as an assessment of different treatment options. However, the visual exploration of aneurysm data is time-consuming and challenging due to several problems, which are rarely addressed by current visualization techniques.

Measured and simulated blood flow data are highly complex information comprising scalar, vectorial and tensor-based information whose visualization is often affected by visual clutter and occlusions. The vascular morphology is usually represented by a 3D surface mesh, where a series of manual rotations is necessary to gain a complete overview due to the complexity of the vasculature. On the surface, scalar quantities can be explored, where only one attribute can be displayed simultaneously using standard visualization techniques. During rotation and zooming, the experts switch scalar quantities such that different interesting regions are found. Thus, the experts have to memorize the areas and analyze them regarding other quantities, which makes the detection of critical attribute correlations very time-consuming. For more complex vascular branches, the number of *regions of interest* (ROIs) and occlusion problems increases such that a full analysis of various scalar values becomes quite challenging. The time-dependent behavior of the data additionally complicated the analysis, where animations are used to show changes in scalar attributes during the cardiac cycle. This procedure further enhances the manual exploration effort, because it is almost impossible to find critical regions during an animation since the rotation process itself needs a certain amount of time. The usage of side-by-side views only slightly improve data exploration, since they only allow to analyze few time steps and attributes and it is exhaustive to put these multiple images together mentally. Besides, the analysis of qualitative flow features is manually performed, which is a subjective and error-prone process with high inter-observer variability. Small structures can be easily overlooked, and the results are not reproducible, which impaired their interpretation. Finally, performing large medical studies with different domain experts is challenging, since different software solutions with inconsistent data formats are used. Thus, a collaborative analysis is challenging and time is wasted to augment acquired data with meta information manually.

## 1.2 STRUCTURE AND CONTRIBUTIONS OF THIS THESIS

The work presented in this thesis aims to support medical and CFD experts in evaluating the aneurysm rupture risk and treatment decision. The established methods were integrated into the developed software prototype named *Aneulysis*. Design decisions and developments are based on extensive discussions with domain experts comprising two neuroradiologists and two CFD engineers about their goals and tasks regarding aneurysm research as well as problems that arise with currently used visual exploration techniques. Accordingly, the solutions are tailored to the requirements and capabilities of the domain experts.

The background part of the thesis is structured as follows:

- Chapter 2 presents relevant medical background information about cerebral aneurysms including possible treatment options.
- Chapter 3 summarizes the flow data generation according to simulated data. It gives an overview of pertinent image and data processing steps as well as important hemodynamic attributes.
- Chapter 4 provides an overview of existing techniques to visualize blood flow data, where the approaches are classified according to a task taxonomy.

Based on the limitations of current visual exploration techniques for medical flow data, we made the following main contributions:

- **Consistent Data Management and Guided Exploration:** Until now, measured and simulated flow data are primarily used for research purpose. A significant reason is the lack of a consistent data management between domain experts with a different professional background as well

as standardized and easy-to-use exploration software with guided workflows and automatic techniques to classify interesting features.

The research prototype *Aneulysis* [431] was developed in collaboration with our domain experts. The general workflow, as well as the structure to manage the data, is presented in Chapter 5. Besides a general concept to administrate aneurysm data, *Aneulysis* provides five modules for visualizing the data. The first module focuses on an automatic extraction and visualization of morphological aneurysm descriptors, which is also introduced in Chapter 5. This includes the automatic detection of the ostium surface separating the aneurysm from the healthy parent vessel from which other essential descriptors are derived. Providing automatic measurement methods leads to reproducible and less error-prone results compared to manually performed measurements, where measurement deviations can significantly influence treatment decisions.

- **Surface-Based Data Exploration:** One interest of clinical and CFD experts is to find correlations between morphological and hemodynamic attributes that promote aneurysm growth and rupture. For this purpose, different wall- and flow-related scalar fields are mapped to the vertices of the triangular mesh representing the vessel wall. Wall-related attributes are, e.g., the thickness and deformation of the wall, whereas flow-related attributes comprise, e.g., pressure and WSS. The visual exploration of this time-dependent information using standard visualization techniques such as a 3D surface representation is quite challenging and time-consuming. Only, one attribute can be displayed simultaneously, where suspicious regions can be easily overlooked.

Several novel methods for a simultaneous exploration of wall-related and flow-related attributes during the cardiac cycle are presented in Chapter 6. The techniques are integrated into three further visualization modules. The first module focuses on a combined visual exploration of wall thickness and wall deformation together with the internal blood flow. The second module allows a simultaneous analysis of multiple scalar fields on the vessel surface, where both modules use a combination of several linked views showing the aneurysm data in different abstraction levels. Besides scalar and vectorial information, tensor-based data can be defined on the vessel wall describing mechanical shear forces. The third module focuses on the analysis of these stress tensors by providing different comparative glyph-based visualization techniques according to specific exploration tasks.

- **Flow-Based Data Exploration:** Besides quantitative flow attributes, qualitative flow features, e.g., specific flow patterns such as vortex flow seem to influence the aneurysm state as well as treatment success. Medical studies classify flow patterns according to their *complexity* and *temporal stability* to evaluate their influence, where differences were found between ruptured and non-ruptured as well as pre- and post-treated data sets. However, manual classifications based on standard flow visualization techniques are time-consuming, error-prone and not reproducible. Extensive and meaningful studies have to be carried out that generate reproducible results to integrate findings of flow patterns into clinical discussions.

Chapter 7 presents the fifth visualization module of *Aneulysis* that allows a detailed analysis of intra-aneurysmal flow patterns. It starts with an automatic clustering of integral lines to get groups of lines with similar flow behavior that represent the flow patterns. The grouping directly incorporates the temporal component of flow-representing path lines, leading to spatio-temporally compact clusters. Moreover, our clustering method can handle flow patterns that decay and reoccur during the cardiac cycle. The chapter proceeds with the automatic classification of the clustered flow patterns. Each cluster is assigned to one of six pre-defined flow types that can be easily extended to handle anatomical diversity. The classification provides reliable and reproducible results, where different visualization techniques support a detailed analysis of flow patterns and corresponding attributes such as their velocity and distance to the vessel wall.

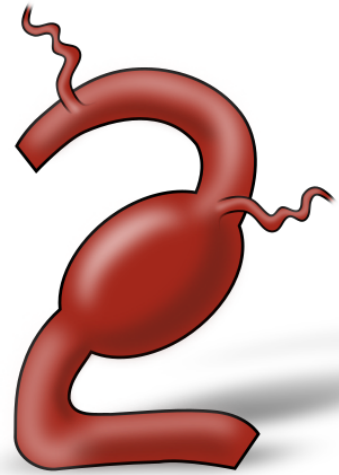


## Part II

### BACKGROUND



# Medical Background







## MEDICAL BACKGROUND

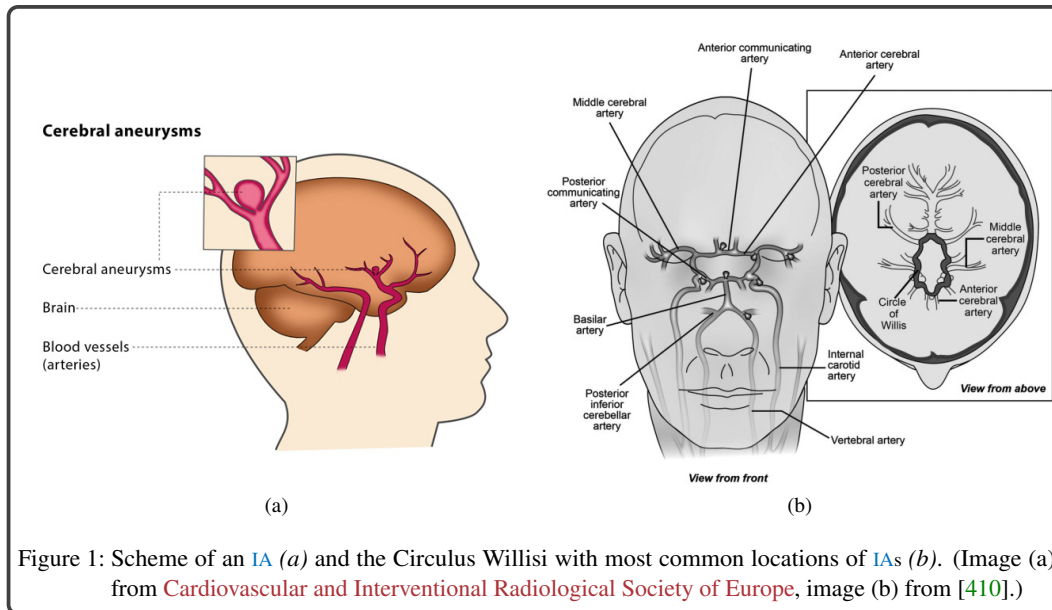
Stroke is the third most frequent cause of death, with about 270.000 people suffering from it every year in Germany and about 90.000 patients dying within one year. In 10-15 % a stroke is caused by a [SAH](#), which describes bleeding into the area between the brain and covering tissues, called subarachnoid space. Such bleeding is associated with severe consequences for the patient such as neurological deficits, depression or even death. Most [SAHs](#) are caused by rupture of *intracranial aneurysms* ([IAs](#)). At the moment, the pathophysiological mechanisms responsible for their formation and rupture are not sufficiently well understood. However, current imaging techniques allow clinicians to accurately characterize their morphology and relationship to the adjacent vascular system. Based on this, enormous progress has been made in the last decades in the field of minimally invasive endovascular surgery, whereby the respective interventions are aimed at separating the aneurysm from the healthy circulation with the aid of different medical implants. Clinical studies have shown that current methods often lead to successful treatment, as the inflow into an aneurysm is prevented. However, surgical interventions are associated with various risks for the patient. Aneurysms can rupture during surgery, or complete suppression of the inflow cannot be achieved. Besides, post-operative complications, such as slippage of the implants, can also occur after a long period, making it necessary to reattach the implants. Due to the possible treatment risks, the handling of accidentally discovered, asymptomatic aneurysms is discussed controversially, where a prophylactic treatment is not appropriate. Thus, there is an excellent interest in identifying factors that influence the growth and rupture of aneurysms and enable an assessment of the risk.

This chapter provides an overview of [IAs](#) from a medical point of view. It starts with a more detailed definition and classification of [IAs](#) based on the anatomy of healthy arteries, see Section 2.1 - Section 2.3. Moreover, a more detailed overview of rupture risk factors is given in Section 2.4. Then, medical imaging modalities for aneurysm diagnostic and treatment are presented in Section 2.5, followed by currently used treatment options, see Section 2.6.

### 2.1 ANEURYSM EPIDEMIOLOGY

[IAs](#) (also called cerebral or brain aneurysms) are abnormal local dilatations of intracranial arteries, resulting from a pathological weakness in the vessel wall, see Figure 1a. A generally accepted definition is a permanent dilatation of the vessel diameter above a factor of 1.5. Smaller dilatations are called ectasia.

The annual prevalence of [IAs](#) is around 5 % in the general population and affects about 1.5 and 6 million people respectively in Germany and the USA [197, 349]. But maybe higher for certain cohorts, such as patients older than 50 years, especially women, patients with kidney disease or aneurysm occurrence in family history [172, 390]. Multiple cerebral aneurysms develop in 15 % to 34 % of affected persons, which increases the likelihood of a possible rupture [308, 315]. The mean annual incidence of aneurysm rupture in Western Europe and the USA is 10 cases per 100.000 persons [160, 284]. In patients with [SAH](#), several aneurysms are diagnosed in up to 45 % of all cases [315]. The consequences of a ruptured aneurysm are devastating, with approximately 50 % of patients dying within 30 days [74, 410]. Furthermore, 25 % of the surviving patients have a severe disability, where the remaining patients have an increased risk of serious complications such as stroke or recurrent bleedings. However, 80 % to 85 % of all [IAs](#) will never rupture [349].



## 2.2 ANEURYSM PATHOGENESIS

Arteries are tubular tissue structures that transport the blood in the human or animal body. The wall of a healthy intracranial artery consists of three layers that enclose a cavity, the so-called lumen, see Figure 2. The innermost layer, the *tunica intima* consists of flat endothelial cells, which lie on an elastic inner connective tissue layer and form the contact with the blood. The middle layer, the *tunica media*, consists of ring-shaped muscle cells, which distribute the load evenly over the circumference of the vessel. Between the muscle cells, collagen fibers as well as the fiber protein elastin are arranged, which are essential for the wall stability. The outermost layer, the *tunica adventitia*, forms the transition to the surrounding tissue. The arrangement of its fibers counteracts the longitudinal expansion of the vessel [399]. In contrast to systemic arteries, intracranial arteries have significantly less elastin in the media, which is assumed to make them more susceptible to aneurysm formation.

There are two types of aneurysms, the *aneurysm verum* (a real aneurysm) and the *aneurysm spurium* (a false aneurysm). In a real aneurysm, all three vascular layers are affected by the expansion. The false aneurysm is not really an aneurysm. It is caused by an injury of the vessel wall, where the surrounding connective tissue retains the escaping blood. Thus, the aneurysm is not surrounded by a vascular wall but by a layer of connective tissue. All of the following concepts are based on real IAs.

The underlying assumption is that aneurysm formation is the result of vascular remodeling, whereby the body tries to restore homeostasis (stability) according to altered hemodynamic and biological conditions [145]. The endothelial cells of the tunica intima play an essential role here. These cells, which are slightly oriented in the direction of flow, react particularly to shear forces that occur on the vessel wall through the blood flow. One of the most crucial stress measures is the *WSS*, the frictional force induced by the tangential blood flow at the vessel wall [249]. This attribute is often related to aneurysm growth and rupture because of its effect on the endothelial cells. *WSS* is described as a mechanical trigger for the release of biological signal substances by endothelial cells, which regulate vascular remodeling with the aim of homeostasis. Accordingly, local *WSS* leads to activation of endothelial cells, which then change the arterial properties. Depending on the constellation, the wall is reinforced or weakened to adapt it to the hemodynamic conditions.

The *WSS* provoked a lot of controversial discussions. There are two theories regarding critical *WSS* values. The first one is that high *WSS* causes a faulty remodeling of endothelial cells, which leads to destructive processes such as the degradation of muscle cells in the media. This, in turn, favors growth and rupture probability since the structurally weakened wall can no longer sufficiently counteract blood pressure. The second one assumes that low *WSS* results from the stagnation of blood flow inside

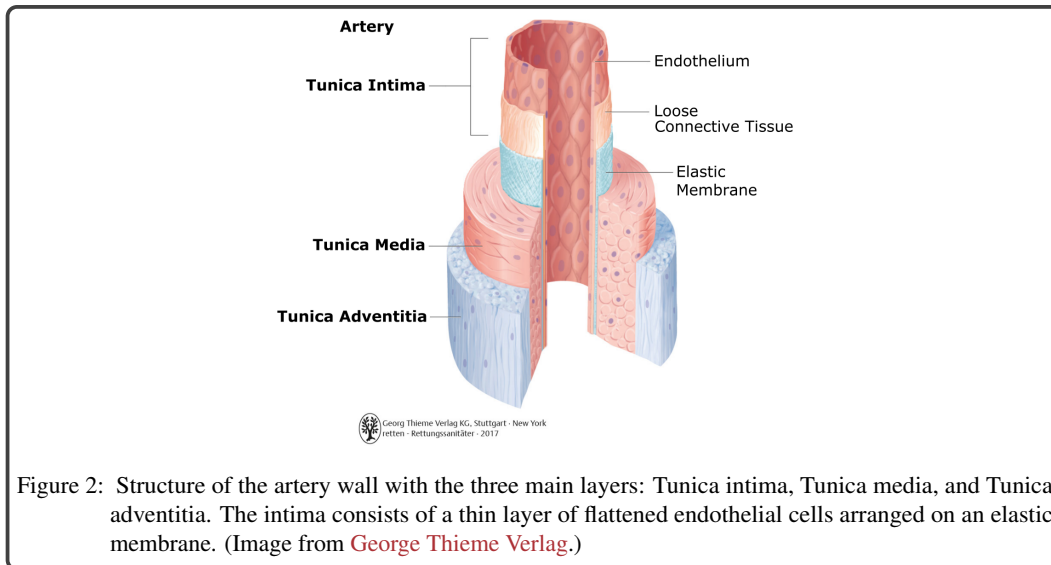


Figure 2: Structure of the artery wall with the three main layers: Tunica intima, Tunica media, and Tunica adventitia. The intima consists of a thin layer of flattened endothelial cells arranged on an elastic membrane. (Image from [George Thieme Verlag](#).)

an aneurysm. This causes inflammation in the wall, which promotes aneurysm formation and growth. Furthermore, specific anatomical configurations such as bifurcations with acute branching angles favor the occurrence of high and low [WSS](#). In this way, the inflow is focused on a locally limited area, which leads to destructive remodeling of the wall due to the increased physical stress.

Histological investigations of non-ruptured aneurysms have shown that they have no endothelial layer, a disturbed inner elastic lamina, a diluted media with degenerated muscle cells and inflammatory cells. During the formation and growth of an aneurysm, the wall may stabilize. However, a permanent effect of inflammatory processes and hemodynamic load can cause destabilization of the wall. If the intraluminal pressure exceeds the tensile strength of the aneurysm wall, rupture occurs.

## 2.3 ANEURYSM CLASSIFICATION

In clinical routine, [IAs](#) are classified according to their etiology, morphology, and location, where different morphological descriptors are distinguished. Based on this, clinicians assess the patient-specific rupture risk and have to decide if an aneurysm should be treated or not. In the case of treatment, an optimal treatment must be selected.

### 2.3.1 Etiology

The formation of an aneurysm can be caused by several factors [[186](#), [268](#)]. A distinction can be made between systemic and developmental causes. Systemic causes include external or internal stresses leading to a weakening of the vessel wall and aneurysm growth. Typical factors of this category are an unhealthy diet, high blood pressure, high cholesterol, excessive alcohol consumption, and tobacco consumption. These aspects probably promote the formation of inflammation and atherosclerotic deposits, which in turn can lead to destabilization of the wall and promote the formation of aneurysms. Furthermore, genetically induced vascular instabilities are among the systemic factors [[197](#), [334](#)]. Direct relatives of aneurysm patients have a higher risk of developing an aneurysm themselves. However, this can also be traced back to similarly unhealthy lifestyles within a family.

In contrast, developmental causes increase the likelihood of aneurysm formation with advancing age [[314](#)]. Due to structural changes in proteins, the elasticity of vessels decreases with age, which favors the development of aneurysms. The increased incidence of [IAs](#) in older women at a rate of 3:1 to men can be attributed to the loss of collagen as a result of postmenopausal estrogen deficiency [[228](#), [390](#)]. There are other rare causes of aneurysms. Infections of the arterial wall cause mycotic aneurysms. Moreover, tumors and trauma can also cause aneurysms to form.

### 2.3.2 Localization

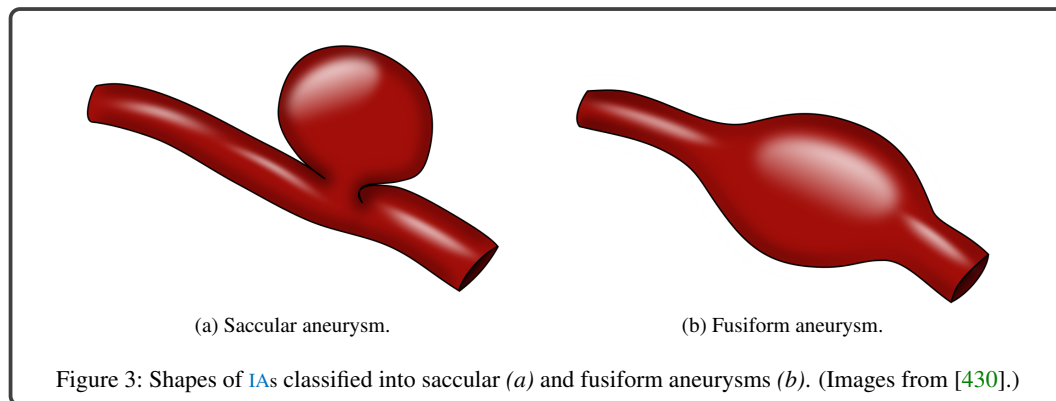
IAs often occur at arterial branches around the brain base. There they may be located directly on the *Circulus Willisi*, a localized arterial vascular ring, or adjacent branches and arteries, see Figure 1b. Aneurysms occurring at branchings comprising two arteries are called *bifurcation aneurysms*. In contrast, aneurysms that occur on the wall of one artery are called *side-wall aneurysms*. Medical studies [390, 402] have shown that aneurysms occur with different likelihood at certain sections of the *Circulus Willisi*, where different probabilities of occurrence could be derived. Aneurysms, therefore, occur most frequently in the anterior circulation at the *anterior communicating artery* (30 %), at the junction of the *internal carotid artery* and the *posterior communicating artery* (25 %), at the *middle cerebral artery bifurcation* (20 %) and the *carotid artery bifurcation* (7.5 %). In contrast, aneurysms in the posterior circulation occur at 7 % in the bifurcation of the *basilar artery* and 3 % in the origin of the *posterior inferior cerebellar artery* [47].

### 2.3.3 Morphology

In addition to the location of cerebral aneurysms, their morphology plays an essential role in the assessment of the aneurysm state. Basic morphological descriptors are the aneurysm shape and size. Besides, further landmarks and quantitative descriptors were defined that allow a classification of the aneurysm morphology.

#### Shape Classification

The shape of IAs is classified into two types: saccular and fusiform aneurysms [113], see Figure 3. In the majority of cases (80 - 90 %), an aneurysm has a saccular shape, which is characterized by a more or less spherical bulge on one side of the affected vessel. In contrast, fusiform aneurysms are an inhomogeneous dilatation over a certain length of the vessel. They very rarely emerge in cerebral arteries with an annual incidence of less than 0.1 % [14]. Either they occur acutely due to damage of the internal elastic lamina, which leads to intramural bleeding, or as chronic fusiform aneurysms, which presumably arise from atherosclerotic degeneration of the aneurysm wall [266].



Saccular aneurysms are additionally divided into two anatomical areas: the aneurysm neck and aneurysm body (also called sac), see Figure 4. The neck describes the area where an aneurysm exits the parent vessel. In contrast, the aneurysm body represents the actual bulge in the vessel with a rounded *dome*. Due to the widening of the vessel wall, the sac may have thinner wall areas than the parent vessel, at which an increased rupture risk is assumed. Besides, further small bulges, called *blebs* or satellites, can form on the body. Such structures indicate remodeling due to inflammatory processes within the vessel wall probably leading to lower stability and increased rupture risk. The area at the transition between the parent vessel and the aneurysm neck is called *ostium*. It can be seen as an imaginary surface, where the border is called *ostium contour*.

The extraction of *morphological features* is expressed as a surface decomposition task [275]. The primary decomposition into an aneurysm (diseased) and parent vessel (healthy) can be further refined by differentiating between affected (near) and non-affected (far) sections of the parent vessel, see Figure 4. Given such a decomposition, clinically relevant morphological descriptors describing aneurysm size, shape, and spatial relations to the parent vessel can be derived.

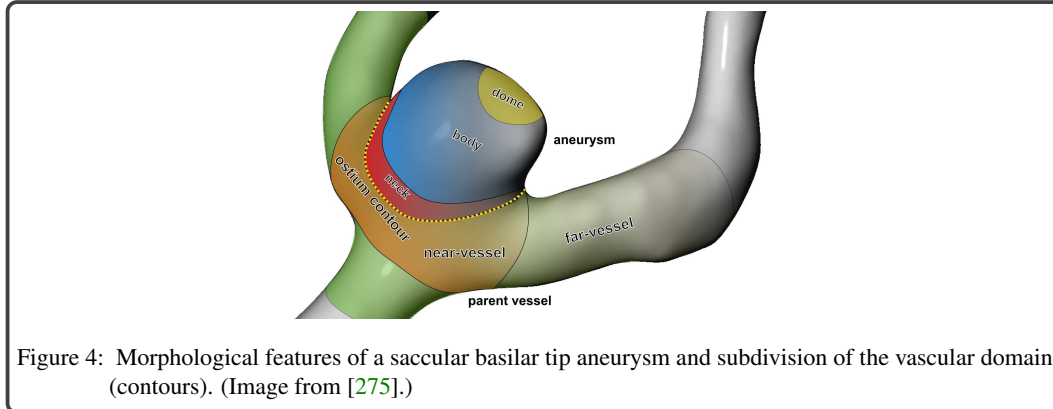


Figure 4: Morphological features of a saccular basilar tip aneurysm and subdivision of the vascular domain (contours). (Image from [275].)

### Morphological Descriptors

Based on the ostium and dome area, medical studies derive several morphological descriptors, which allow a more differentiated classification of the aneurysm morphology concerning risk evaluation and decision-making [68, 84, 159, 231, 310, 401]. Here, a distinction between 1D and 2D descriptors is made, where some groups use in-house tools to compute the descriptors semi-automatically [84, 211]. The most frequently used 1D descriptors are:

- **Aneurysm height:** From the center of the ostium surface, the point on the aneurysm with the maximum Euclidean distance to the center is determined, where the distance between these two points defines the height (aneurysm size), and the point on the aneurysm is called *dome point*. A distinction is made between small (< 15 mm), large (15 - 25 mm), giant (25 - 50 mm) and super giant aneurysms (> 50 mm).
- **Aneurysm width:** Along the height vector, the largest extent of the aneurysm body perpendicular to the height vector is defined as width.
- **Maximum diameter:** The maximum diameter is measured as the maximum width of the aneurysm body.
- **Neck diameter:** The diameter of the neck is measured as the greatest extent of the ostium contour. Here, aneurysms with a narrow and wide neck are distinguished. Wide-neck aneurysms exhibit a neck diameter of at least 4 mm, or at least half as wide as high [397].
- **Bulge height:** The bulge height represents the part of the aneurysm height, where the maximum width along the height occurs.
- **Aneurysm volume:** The aneurysm volume is measured as the volume of a whole aneurysm consisting of neck and body area, which is very difficult to determine manually.
- **Aneurysm angle:** The aneurysm angle reflects the inclination of an aneurysm to the ostium. It is measured as the angle between the ostium plane and the line representing the aneurysm height. A rupture was observed more frequently in strongly inclined aneurysms. Due to the inclination of an aneurysm, the blood probably hits the aneurysm wall at a higher speed, which leads to increased stress on the aneurysm wall [84].

- **Vessel angle:** This descriptor is measured as the angle between the centerline of the parent artery and the ostium plane. The aneurysm- and vessel angle are dependent on the view direction. Thus, for measuring both angles, it has to be ensured that the ostium plane is perpendicular to the viewing plane [84].
- **Parent artery diameter:** This diameter is measured as the maximum extent of the parent artery, from which an aneurysm has evolved.

Based on this, several 2D descriptors are derived, which indicate whether an aneurysm is more spherical or ellipsoidal:

- **Aspect ratio:** The aspect ratio describes the relationship between the aneurysm height and neck width. Aneurysms with a large aspect ratio are considered as more likely to rupture [401].
- **Height-width ratio:** This factor describes the ratio between the aneurysm height and width. An increased risk was found for aneurysms higher than wide and vice versa [159].
- **Bottleneck factor:** The bottleneck factor describes the ratio between aneurysm width and neck width. Similar to the height-width ratio, this descriptor was also significantly associated with rupture [159].
- **Bulge location:** The bulge location is the ratio between the aneurysm height and bulge height.
- **Aneurysm/parent artery ratio:** This descriptor integrates information about the parent vessel by measuring the ratio between the aneurysm size and diameter of the parent artery.
- **Undulation index:** This index describes the smoothness of the aneurysm wall concerning blebs. The ratio is formed from the volume of an aneurysm and the volume of the convex envelope of an aneurysm. It is assumed that very irregular shaped aneurysm have an increased risk of rupture [68].
- **Ellipticity index:** This index characterizes how elongated an aneurysm is by using the ratio between the volume of the convex aneurysm hull and the surface area of the convex hull.
- **Non-sphericity index:** This index is quite similar to the ellipticity index by using the ratio between the aneurysm volume and the surface area of an aneurysm. However, possible surface undulations would artificially increase the surface area leading to erroneous values and interpretations of the aneurysm shape. For the calculation of all three indices, computer assistance is needed.

Besides these descriptors, some other morphological features were used to investigate aneurysm rupture. This includes, e.g., different definitions for the width and height of an aneurysm [159]. However, these descriptors seem to have a similar influence on aneurysm rupture risk as the given definitions of height and width of an aneurysm.

## 2.4 ANEURYSM RUPTURE

The aneurysm growth and rupture relies on the biomechanical behavior of the aneurysm wall, which in turn depends on the cellular organization and strength of the wall layers. Since the pathophysiological processes have not yet been sufficiently understood, in clinical routine, aneurysms are classified according to more objectively determinable factors to assess the risk of rupture and the associated need for treatment. These factors essentially include the aneurysm location and morphology, recall Section 2.3.2 and Section 2.3.3.

According to this, higher rupture rates were observed for certain vascular segments. Ruptures were observed more frequently for aneurysms of the *basilar artery* and *middle cerebral artery* [402]. Besides the localization, the aneurysm size is the most critical clinical descriptor for the assessment of the rupture risk. Based on clinical studies [182, 284, 407], asymptomatic aneurysms smaller than



7 mm are assumed to have a low risk of rupture. Therefore, IAs with a size of more than 7 mm are usually treated. However, often small, inconspicuous aneurysms are affected by rupture [84], known as the aneurysm size paradox [247]. Yasui et al. [416] investigated clinical features of 25 ruptured aneurysms. In 16 cases (64 %), the aneurysm was smaller than 5 mm. Similar observations were made by Juvela et al. [173], who investigated 142 patients with 181 aneurysms for a mean period of 13.9 years with an aneurysmal size of less than 4 mm. A rupture occurred in 27 patients, resulting in a rupture rate of 19 %.

As 1D descriptors allow no reliable risk estimation, clinical studies evaluated 2D descriptors for rupture risk assessment [68, 84, 159, 231, 310, 401]. Statistically significant differences between ruptured and non-ruptured aneurysms were detected according to the aspect ratio, undulation index, non-sphericity index, and aneurysm/parent artery ratio. However, until now there are no 2D descriptors that combine patient-specific meta information such as age, gender and aneurysm location. Moreover, existing 2D descriptors allow also no reliable risk estimation of asymptomatic aneurysms. Niemann et al. [277] extracted 22 1D and 2D morphological descriptors based on 100 IAs to investigate the potential of these measures for status classification of the rupture risk. Based on multiple commonly used learning algorithms, several prediction models were trained, where the best classifier only achieves an accuracy of ~69 %. This suggests that other factors may also influence the aneurysm state.

For aneurysms with additional blebs, an increased risk of rupture is assumed [70, 143]. Blood flow simulations have shown that increased and irregular stress values occur in bleb regions. It is likely that these regions undergo an active transformation process, whereby the mechanical functionality decreases and ultimately the wall can no longer withstand the physiological loads [235, 310]. Furthermore, the experience of neurosurgeons suggests that there is probably a correlation between wall thickness and rupture risk. However, this relationship is currently challenging to analyze because there is no in vivo technique available in clinical routine to measure aneurysm wall thickness. There are some studies [112, 174] that investigated wall thickness conditions of treated aneurysms. Histological examinations and evaluation of intra-operative images showed that the wall thickness of an aneurysm is very variable (with a thickness of 16 to 400  $\mu\text{m}$ ) containing areas of thick, intermediate and super-thin translucent tissue [174]. An increased rupture rate was observed for super-thin and heterogeneous aneurysm walls [112].

## 2.5 VASCULAR IMAGING FOR INTRACRANIAL ANEURYSMS

In clinical practice, imaging systems play a central role in the diagnosis and therapy of IAs. Angiographic modalities enable the extraction of vascular morphology, which is essential as input for CFD simulations and computer-aided analysis. In contrast, intravascular modalities provide more detailed information about the internal structure of the wall.

### 2.5.1 Angiographic Imaging

Medical imaging procedures to identify an aneurysm or to provide information about a possible SAH and its severity include *magnetic resonance imaging (MRI)*, *computed tomography (CT)*, *2D digital subtraction angiography (DSA)*, and *3D rotational angiography (RA)* [47, 196]. During CT and MRI, contrast agents are injected intravenously to enhance vessels in the image data yielding *computed tomography angiography (CTA)* and *magnetic resonance angiography (MRA)*. *Time-of-flight (ToF) magnetic resonance (MR)* sequences use the different magnetization of the blood flow in contrast to the stationary surrounding tissue to create high vessel-to-tissue contrast. Thus, no contrast agents are needed. However, MR signals can be extracted, especially in large aneurysms, resulting in reduced vascular imaging. Current clinical images have a size of  $512 \times 512 \times 256$  voxels in the x-, y-, and z-direction with a spatial resolution of  $0.35 \times 0.35 \times 0.5 \text{ mm}^3$  for CTA and  $0.7 \times 0.5 \times 0.9 \text{ mm}^3$  for MRA using a field strength of 1.5 or 3 T. For research purposes, MRI scanner of up to 7 T with a spatial resolution of  $0.11 \times 0.11 \times 0.11 \text{ mm}^3$  are utilized, where local thickenings of larger intracranial arteries become visible [375]. The sensitivity and the specificity of CTA for the diagnosis of the aneurysms depend on the aneurysm size, location and the experience of the performing radiologist.



The sensitivity of **CTA** in the detection of aneurysms smaller than 4 mm is 92.3 %, whereas for greater aneurysms it is close to 100 % [244]. Similar sensitivity values can be reached by using **MRA** images [265]. However, **CTA** is not suitable for allergy sufferers or patients with impaired renal functions due to the large bolus of contrast agent, whereas **MR** acquisition takes considerably longer which is problematic in critically ill patients [47]. Thus, **MR** is mostly used for follow-up examinations of patients after endovascular treatment and in the case of pregnant patients.

A contrast agent is injected through a hollow plastic tube (catheter) into the intracranial arteries to acquire **DSA** and **3D RA** data. They are therefore more invasive than either **CT** or **MRI**, but can be combined with subsequent endovascular treatment. The acquisition of **DSA** data is based on moveable C-Arm (the X-ray source and detector) that rotates around the patient resulting in one or more **2D** X-ray projections. Here, a pre-contrast image (the so-called mask) and a contrast-enhanced image are acquired. Subtracting the mask from the contrast-enhanced image results in a **DSA** image, where only the vessels are visible. In the last years, **DSA** was considered as the gold standard in cerebral aneurysm imaging since it can be performed in real time by exhibiting a high spatial and temporal resolution [196]. However, different image artifacts can occur due to the **2D** projection of **3D** vessel structures, which could lead to wrong diagnosis [138]. **3D RA** imaging overcomes these limitations by generating rotational projections using the C-Arm. From these multiple **DSA** images, a **3D** volume is reconstructed, see Figure 9. Typically,  $512 \times 512 \times 256$  voxels in the x-, y-, and z-direction are generated with a size of  $0.5 \times 0.5 \times 0.5 \text{ mm}^3$ . However, imaging artifacts may arise due to incomplete flushing of contrast agents, which reduces the quantitative analysis of morphological descriptors such as aneurysm size [335]. Thus, **DSA** continues to play an essential role in determining the optimal management strategy [368]. However, in a computer-aided analysis including hemodynamic simulations, a **3D** data set is mandatory for the extraction of an aneurysm surface model. A comparison of **DSA** and **3D RA** identifies **3D RA** as more suitable for the detection of small ( $\leq 3 \text{ mm}$ ) aneurysms [382].

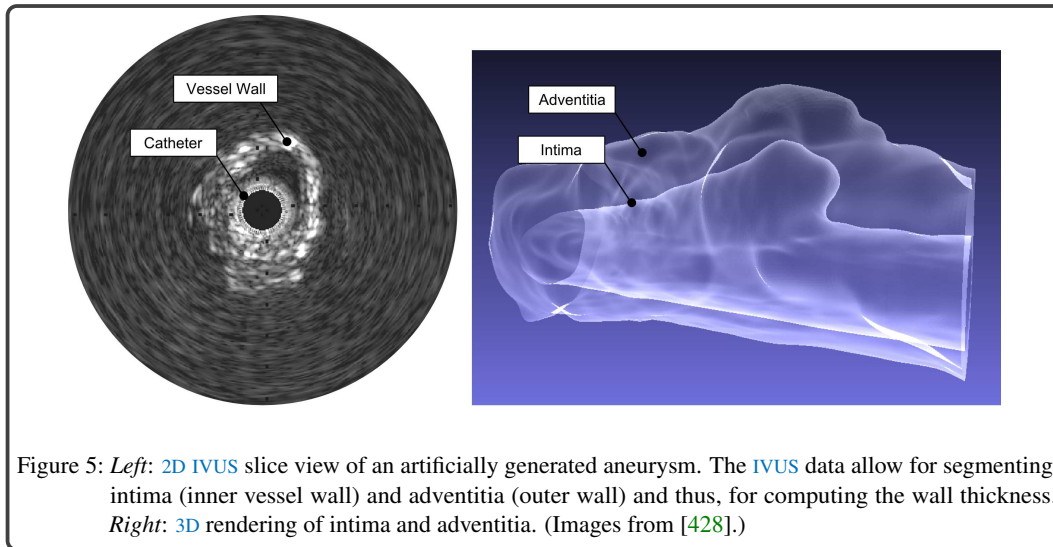
### 2.5.2 Intravascular Imaging

Angiographic methods usually provide limited information about the development of vascular pathologies, as it is not possible to assess the layers of the vascular walls. However, this is of great interest to improve prevention and therapy of such diseases. *Catheter-assisted intravascular ultrasound* (**IVUS**) and *optical coherence tomography* (**OCT**) are currently the only methods for assessing the condition of walls. They allow measuring the wall thickness, which is an essential factor for rupture risk analysis and treatment planning.

**IVUS** is a minimally invasive procedure, where a catheter with a miniaturized ultrasound probe is inserted into the artery. The probe transmits high-frequency waves at 20-40 MHz, which are reflected by the surrounding tissue. A transducer receives a part of the reflected sound waves and transforms it into electrical pulses. Each pulse is converted to a gray value depending on its transit time, depth and strength. These gray values form a **2D** slice image with white as strong and black as zero pulses. Due to fast data processing, real-time observation is possible, and the movement can also be detected using the Doppler effect. In general, **IVUS** transducers exhibit an axial resolution of 70 to 200  $\mu\text{m}$  with a penetration depth of 4 to 8 mm [263, 313]. More recently, higher-frequency **IVUS** catheters have been developed using frequencies up to 60 MHz and achieving axial resolution of 40  $\mu\text{m}$  [45]. Therefore, with **IVUS** the dimensions of the lumen, the size of sediments on the wall, called plaque, and the extent of positive remodeling can be measured.

**OCT** is also a minimally invasive image modality, which works similar to **IVUS**. Instead of ultrasound waves, it uses light waves in the near-infrared or infrared range. It is suitable also for the examination of the lumen dimensions. But it also has a better spatial resolution of less than 15  $\mu\text{m}$  with a limited penetration depth of around 2 mm and less noise than imaging by **IVUS** [313]. Moreover, image acquisition can be performed around three times fast than with **IVUS**. However, an additional contrast agent is used to image the vessel wall, which cannot be used for all patients. Currently, **OCT** is not used in clinical routine to examine cerebral arteries since the size and flexibility of the catheter does not allow safe application in these relatively small vessels.

However, medical studies comprising animal studies and ex vivo studies have successfully used OCT for the investigation of the larger carotid arteries [243, 417]. Moreover, Glaßer et al. [130, 131, 132] performed ex vivo experiments. IVUS and OCT were applied for imaging the cerebral aneurysm wall, see Figure 5. Recently, OCT was successfully applied to silicone phantoms of cerebral side-wall aneurysms [158], where structural information such as differences in wall thickness or plaque could be identified. Problems occurred for larger aneurysms ( $> 4$  mm) or aneurysms with a steep rising wall, which leads to signal losses and incorrect imaging of the aneurysm geometry. Moreover, in vivo conditions such as the presence of blood in aneurysms were neglected within this study, but would probably further complicate the application of OCT. However, due to its ability to characterize pathological vascular wall changes and its high spatial resolution, OCT imaging of the cerebral arteries is expected to be used and approved for clinical use soon.



## 2.6 ANEURYSM TREATMENT PROCEDURES

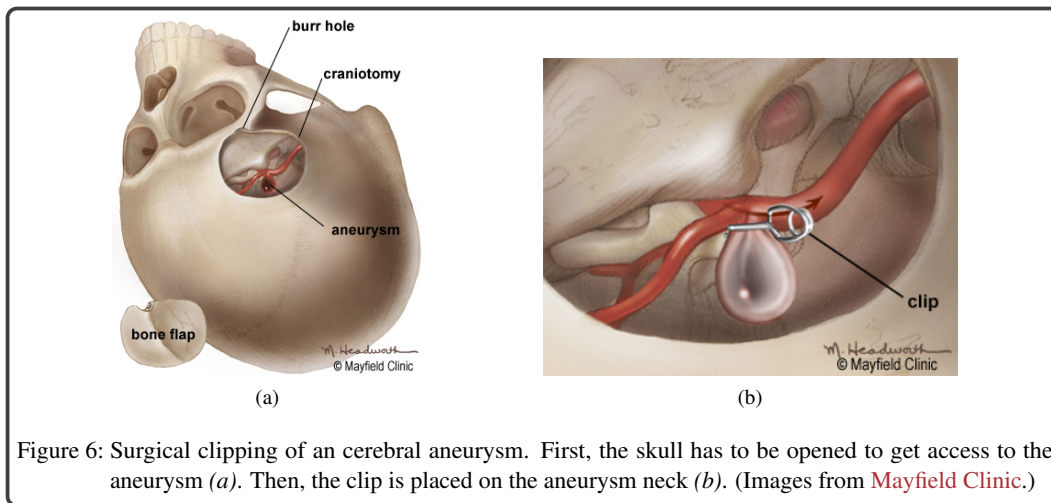
IAs can be detected by chance or by suspected SAH, which is usually characterized by symptoms such as severe headaches, limitation of vision or loss of consciousness. Currently, there are two ways to treat an IA: *surgical clipping* and *endovascular embolization* [412]. Both methods aim to reconstruct the primary bloodstream by separating the aneurysm from the vascular system. This prevents the inflow into aneurysm sac and leads to the formation of a thrombus (so-called embolization). However, both methods are associated with a considerable risk of severe complications. Therefore, rupture and treatment risk must be carefully weighed against each other [389]. This is further complicated in the case of multiple aneurysms, where the physician has to decide which of them should be treated first. In clinical routine, decision-making depends on the following factors [279]:

- aneurysm size and shape,
- aneurysm location and its anatomical reachability,
- ruptured versus non-ruptured,
- the general condition of the patient (age and vital functions), and
- medical history of the patient.

In the following, the basic principle of both treatment techniques is explained.

### 2.6.1 Surgical Clipping

Surgical clipping has been the standard treatment for cerebral aneurysms for many decades. This is an invasive procedure, where the surgeon needs free access to an aneurysm, which requires an opening in the patient's skull (called craniotomy), see Figure 6a. Then, a metal clip (e.g., made of titanium) is placed on the neck of an aneurysm using microsurgical techniques to separate it from the vascular system, see Figure 6b. In addition to the open surgical area, there is a risk to clamp off smaller vessels close to the aneurysm neck and thus preventing blood flow into healthy brain regions. This would lead to ischemia (loss of blood circulation) and damaging of the affected areas. Besides, clipping cannot be performed in the case of wide-neck aneurysms or the aneurysm location cannot be reached surgically [89]. Besides this, surgical clipping is very stressful for the patient and involves longer operating times, lying times and recovery times.



### 2.6.2 Endovascular Embolization

Endovascular embolization is a minimally invasive alternative to clipping. The surgeon navigates a catheter through the body to the aneurysm location. For this purpose, just a small opening in the femoral artery has to be made. Then, *detachable coils* (spirals of platinum wire), a stent (metal implant), or small *latex balloons* can be used to separate an aneurysm from the supplying vessel, which are transported through the catheter. Navigating the catheter into an aneurysm and subsequent insertion of devices is done under angiography control to monitor the catheter position continually.

Figure 7a shows the deposition of coils via a microcatheter into an aneurysm. The coils fill the lumen of an aneurysm and thus stagnate the blood flow in an aneurysm, forming a thrombus. The amount of coils used depends on the size of an aneurysm, where enough coils have to be used to avoid the reflow of the aneurysm lumen. For wide-neck aneurysms, there is a risk of coils from an aneurysm entering the supplying vessel, which could lead to a vascular occlusion. Therefore, an additional stent can be inserted into the vessel to stabilize the coils [298], see Figure 7b. Besides a stent, a latex balloon can be used to support coiling, which is placed under an aneurysm via a microcatheter. Then, the balloon is pumped up to achieve a better compression of the coils and to increase the stagnation of blood. Since the balloon closes the parent vessel, it has to be removed after a short time. In many cases, coiling in combination with a stent or balloon leads to successful treatment, which involves fewer risks for the patient compared to surgical clipping. However, quite large aneurysms often cannot be filled with coils. Therefore, new stent devices were developed such as *flow-diverter* [11], which are close-meshed stents that reduce the blood flow into an aneurysm and lead to a thrombus formation without bringing additional material into an aneurysm. Furthermore, the treatment of wide-neck bifurcation aneurysms is difficult based on stent-assisted or balloon-assisted

coiling. For a few years, *Woven EndoBridge* (WEB) devices are used to treat such aneurysms, see Figure 7d. WEB devices are particular stents, which are placed inside the aneurysm sac to interrupt the intra-aneurysmal flow and, subsequently, to create a thrombosis [297]. The size of the device depends on the diameter of an aneurysm, where too small devices lead to incomplete flow disruption.

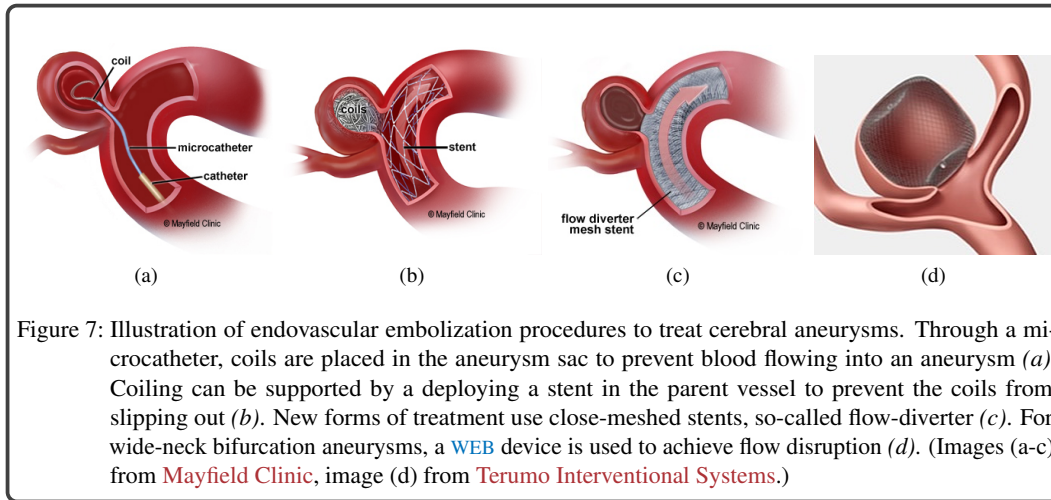


Figure 7: Illustration of endovascular embolization procedures to treat cerebral aneurysms. Through a microcatheter, coils are placed in the aneurysm sac to prevent blood flowing into an aneurysm (a). Coiling can be supported by a deploying a stent in the parent vessel to prevent the coils from slipping out (b). New forms of treatment use close-meshed stents, so-called flow-diverter (c). For wide-neck bifurcation aneurysms, a WEB device is used to achieve flow disruption (d). (Images (a-c) from Mayfield Clinic, image (d) from Terumo Interventional Systems.)

Endovascular methods have become increasingly established in recent years and often enable successful treatment of cerebral aneurysms. Compared to surgical clipping, they exhibit a lower risk of an unfavorable therapeutic outcome [256]. However, surgical therapy cannot yet be replaced entirely, as specific morphological configurations, such as aneurysms of highly branched vessels, prevent the use of endovascular techniques [377]. Furthermore, navigating the catheter and inserting coils and stents is a difficult task, and the success of treatment depends strongly on the skills and experience of the performing physician. Thus, overfilling the aneurysm with coils can lead to injury of the vessel wall, which can trigger a rupture [224]. Moreover, the insertion of a stent could probably lead to an increased rupture risk due to increased pressure values [58]. Besides, medical studies showed post-operative complications of stenting, such as late rupture or in-stent-stenosis [58, 336].

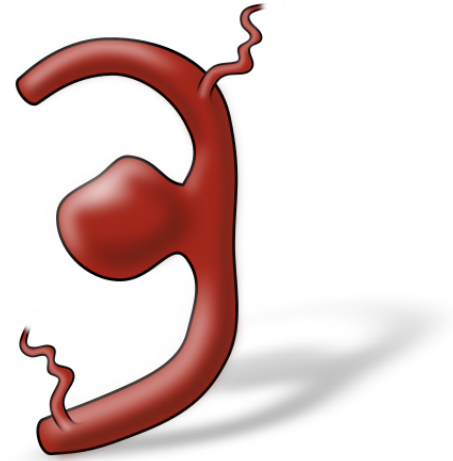
## 2.7 SUMMARY AND CONCLUSION

IAs are pathological dilatations of cerebral arteries. Their rupture leads to a SAH and is associated with a high mortality and morbidity rate. IAs are increasingly being discovered by chance, where most of them are asymptomatic and do not lead to complications (mean annual rupture rate of non-ruptured aneurysms  $\leq 0.05\%$ ). In case of a rupture, therapy is essential. In asymptomatic cases, treatment options have to be evaluated compared to the rupture risk because treatment may also cause a rupture.

According to the management of non-ruptured aneurysms, medical guidelines recommend several factors as an indication of a necessary treatment namely, large aneurysmal size (larger than 7 mm), symptomatic lesions, evidence of growth, multiple lesions, posterior circulation location, and history of SAH [349, 352]. However, all of these factors were mainly observed in the case of poor surgical outcome [182, 350, 411]. In contrast, small asymptomatic aneurysms located in the anterior circulation are traditionally thought to be less rupture-prone [182, 284, 407]. However, even such small, inconspicuous aneurysms can rupture. Besides, treatment of these aneurysms showed the most excellent chance of a positive outcome. These contradictions show that the rupture risk of an individual aneurysm cannot be described sufficiently based on currently used descriptors, and no information about future changes of the aneurysm morphology or the rupture risk can be derived [65, 135]. One reason for this is probably the strong correlation between the shape of an aneurysm and the internal dynamic flow processes. The aneurysm shape is influenced by the flow behavior and vice versa. Thus, also hemodynamic aspects should be considered for the evaluation of the aneurysm state to understand the individual risk of an aneurysm better and to restrict treatment to high-risk patients.



# Hemo- dynamic Background



This chapter is partly based on:

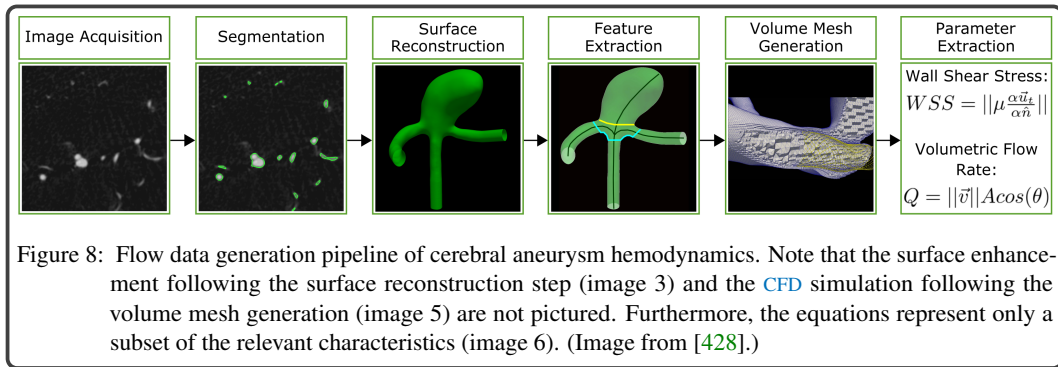
Steffen Oeltze-Jafra, Monique Meuschke, Matthias Neugebauer, Sylvia Saalfeld, Kai Lawonn, Gabor Jániga, Hans-Christian Hege, Stefan Zachow and Bernhard Preim, Generation and Visual Exploration of Medical Flow Data: Survey, Research Trends and Future Challenges; Computer Graphics Forum, 2018.





Several works indicate that the interplay of intra-aneurysmal hemodynamics and degenerative changes of the arterial wall plays a significant role in the development, growth, and rupture of aneurysms. Due to the small diameter and wall thickness of cerebral arteries together with the limited resolution of today's scanning devices, neither the hemodynamics nor the wall can directly be measured at a sufficiently high resolution. **CFD** simulations combined with **FSI** is a promising method to investigate intra-aneurysmal flow and internal wall mechanics based on the patient-specific vascular geometry extracted from medical images. From the simulation results, hemodynamic characteristics can be derived that are related to aneurysm rupture. Moreover, **CFD** simulations facilitate therapeutic decision-making. In virtual stenting/coiling, a geometric model of the coils/stent is integrated into the simulation, and hemodynamic characteristics are compared before and after treatment.

**CFD** simulations form the data basis for the classification and visualization techniques developed within the scope of this thesis. This chapter explains the pipeline to model intra-aneurysmal hemodynamics, which is illustrated in Figure 8. Based on medical image data, the aneurysm and parent vessel part are segmented, where a surface is reconstructed from the segmentation mask. Then, a surface enhancement step (not shown here) is included to correct possible segmentation errors. Next, geometric features such as the vessel centerline are extracted that support the quantitative and qualitative exploration of aneurysm data. Afterward, the enhanced surface mesh is transformed into a volume mesh as input for the **CFD** simulation. Specific steps (not shown here) are necessary for virtual stenting/coiling for integrating stent/coil geometry into the mesh. Based on particular boundary conditions and an approximated fluid model, **CFD** simulations are subsequently performed. Finally, hemodynamic and wall-related attributes can be derived. In the remainder of this chapter, each step of the pipeline is described in more detail. Efficient implementations of hemodynamic data generation pipelines are presented for the reliable, reproducible, and robust generation of **CFD** models in the context of cerebral aneurysm hemodynamics. A more compact overview of the flow data generation pipeline is given by Urick et al. [370].



### 3.1 IMAGE SEGMENTATION

The patient-specific simulation of cerebral aneurysm hemodynamics requires a high-resolution anatomy acquisition. In general, it is sufficient to simulate blood flow only in a local environment around an aneurysm. The aim of segmentation is therefore not to detect the entire intracranial vascular tree, but to enable a detailed representation of the lumen in the area of an aneurysm. Angiography is a suitable method to image the lumen of blood vessels and aneurysms, recall Section 2.5. Note that clinical image modalities captures only the lumen not the wall and provide merely a snapshot of the



current condition. Wall properties must be determined separately, and pulsatile vessel motion must be subsequently modeled as part of the *FSI* simulation since the pulsation of intracranial arteries is too small to be represented by current image modalities.

A variety of segmentation techniques have been proposed for segmenting the vessel lumen [222]. Intensity-based approaches such as thresholding and region growing are frequently used to segment the lumen of cerebral aneurysms and surrounding vasculature due to the high vessel-to-tissue contrast. They are fast and easy to implement, see Figure 9. The result is a binary voxel mask, where a following surface reconstruction method such as *Marching Cubes* [229] has to be applied to get a vessel surface mesh. However, there are two fundamental problems with intensity-based procedures. First, the results are strongly dependent on the choice of the threshold. Consequently, an unfavorably selected threshold leads to an over- or under segmentation. Second, these methods are highly sensitive to image artifacts, such as an inhomogeneous contrast or blending of an aneurysm and near-by vessels due to the partial volume effect. Alternatively, *Marching Cubes* [229] has been used to directly reconstruct the aneurysm surface based on intensity values and an isovalue [59, 128]. However, the challenge remains to set an appropriate threshold, and non-contrasting areas cannot be segmented.

Deformable model approaches such as active contours or level set segmentation can be used to handle areas with insufficient contrast enhancements. They integrate model assumptions about the shape of an aneurysm to compensate for missing image information. The basic principle is to deform an initial 2D contour or 3D surface concerning external forces derived from the image data, e.g., gradient information, and internal forces controlling the degree of deformation, e.g., curvature. Here, results of intensity-based segmentations can be used for initialization [62]. Deformable models are less sensitive to image artifacts such as blending and inhomogeneous signal intensity distributions within the lumen. Moreover, they avoid the step of surface reconstruction and create a segmentation at the sub-voxel level. However, they are computationally more expensive, and their parametrization is challenging. Alternatively, interactive segmentation approaches [17, 386] can be applied to segment cerebral aneurysms [169]. Here, the user is asked to place seed-points to start and connect contours from there [17] or to mark for-and background parts in the image data [386]. Furthermore, the segmentation step can be combined with an automatic aneurysm detection, e.g., based on the analysis of the cerebral vessels medial axes [212], a rule-based system comprising several low-level and high-level features [154], or dedicated blobness and vesselness filters [169].

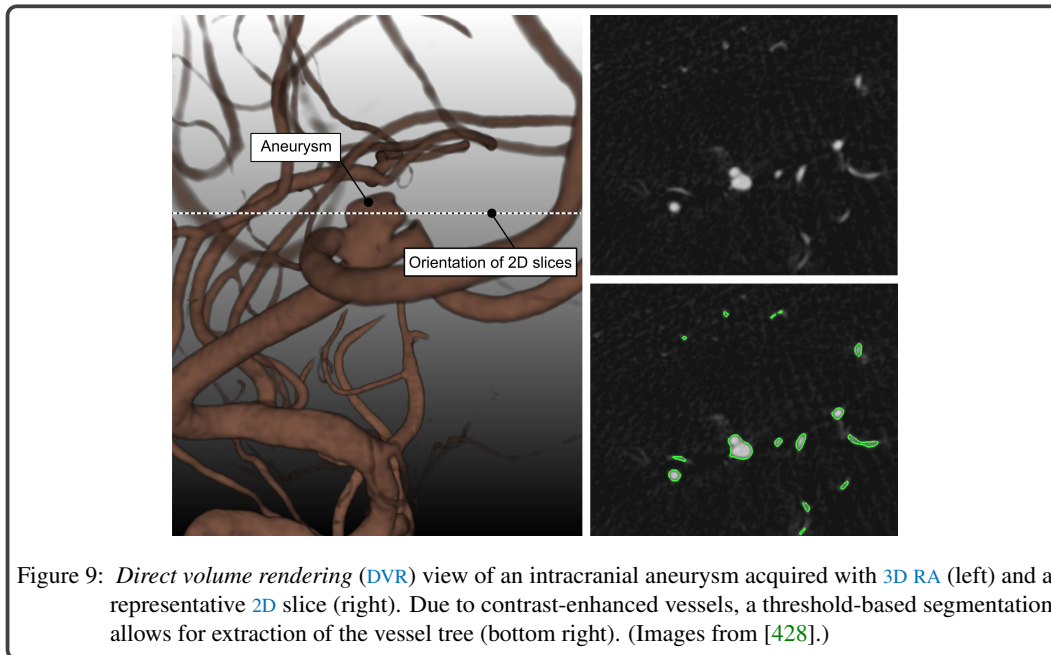


Figure 9: *Direct volume rendering (DVR)* view of an intracranial aneurysm acquired with 3D RA (left) and a representative 2D slice (right). Due to contrast-enhanced vessels, a threshold-based segmentation allows for extraction of the vessel tree (bottom right). (Images from [428].)

### 3.2 SURFACE MODEL RECONSTRUCTION AND ENHANCEMENT

Based on the segmentation result, the surface model can be reconstructed. The reconstruction either aims explicitly at generating a smooth surface or is followed by a mesh smoothing step. The CFD simulation of hemodynamics demands a very high volume mesh quality, which again is dependent on the quality of the surface mesh. Hence, surface enhancement methods are employed to improve the triangle aspect ratio and achieve the lowest possible amount of triangles.

Due to the substantial local variations of cerebral vasculature and pathological aneurysms, as well as artifacts caused by contrast agent administration, e.g., blending artifacts or pseudo-stenoses, the reconstructed surface meshes are often locally corrected [128, 169, 388].

Concerning simulating hemodynamics, the mesh quality must be improved. Local methods swap and remove triangle edges if the resulting triangles are more equilateral [63]. However, due to the local nature, this cannot ensure minimum quality for the overall mesh, which is crucial for simulation convergence. Global remeshing methods involve additional geometric descriptors to optimize the mesh for specific fields of application [9]. Aneurysms can be seen as strong local curvature deviations. To reflect those while still gaining mostly equilateral triangles, areas of high curvature should be represented by smaller triangles with a smooth transition of size. This can be achieved by *advancing fronts* methods that start from pre-defined feature edges and generate triangles along a shifting front concerning the underlying curvature [337], see Figure 10. Further information about the optimization of vascular surface models for CFD simulation can be found in the overview by Mönch et al. [257].

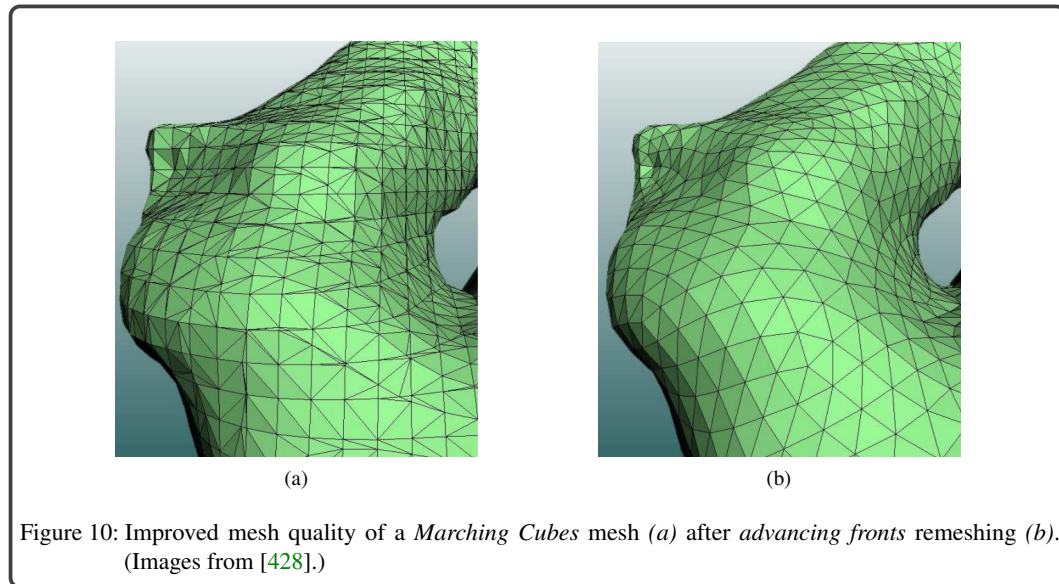


Figure 10: Improved mesh quality of a *Marching Cubes* mesh (a) after *advancing fronts* remeshing (b). (Images from [428].)

### 3.3 EXTRACTION OF GEOMETRIC AND MORPHOLOGICAL FEATURES

Geometric and morphological features are extracted mainly to assist in focusing the flow exploration on certain parts of the anatomy. A typical feature of the former class is the vessel centerline, while the aneurysm sac is comprising a balloon-like *body*, a narrow opening *neck*, and a rounded *dome*, see Figure 4, are typical morphological features. They are used directly as seeding geometry for integral curves or for generating cut/slicing planes perpendicular to the flow direction. In the following, approaches to extract morphological aneurysm descriptors such as the centerline or ostium are described. Computing the centerline also plays an essential role in the investigation of aortic hemodynamics. There, the centerline is the only frequently extracted feature despite work on, e.g., aortic aneurysm segmentation [242] and coarctation detection [272].

To obtain the *centerline* of blood vessels thinning methods, distance transformations or Voronoi diagrams can be used [391]. A general approach is a method by Antiga et al. [16]. First, a Voronoi diagram of the vessel structure is built. Afterward, the Eikonal equation is solved over the whole diagram, and the maximum descent of the solution provides the centerline. Tagliasacchi et al. [359] give an overview of general centerline extraction methods.

The *ostium* surface is handy for analyzing and visualizing the blood exchange between vessel and aneurysm, e.g., as seeding geometry for streamlines [122]. Karmonik et al. [178] presented an image-based approach that extracts the ostium through fitting circles into the vessel's cross-section and analyzing the lumen diameter along the circle. Wong et al. [414] used cylindrical surface models to reconstruct the normal vasculature starting from the centerline branches. Ford et al. [107] digitally restored the former healthy vessel surface and defined the ostium as the difference between restored and given vessel geometry. These vessel-side approaches assume regular, circular vessel cross-sections.

Aneurysm-side approaches extract the ostium plane starting from an aneurysm and require an initial identification of the aneurysm body. Piccinelli et al. [296] applied the method of Ford et al. to identify the aneurysm body and computed the medial aneurysm axis through the 3D Voronoi diagram. A planar ostium plane is aligned and positioned concerning this axis. Cardenes et al. [56] computed a distance field on the aneurysm body surface, concerning the splitting point of the parent vessel centerline below an aneurysm. The ostium contour is represented by the shortest closed path on this distance field. In contrast to the approach of Piccinelli et al., this leads to a curved ostium contour that reflects the underlying anatomy more precisely. Other works [146, 210, 255] used deformable contour models to extract the ostium.

Neugebauer et al. [269] employed a surface distance field concerning the parent vessel centerline to identify the aneurysm dome point. From there, control points are shifted towards the vessel, whereas the distance change rate is used to determine the transition from an aneurysm to vessel. The curved ostium contour is defined by four control points within the transition zone. Using a bilinear interpolation scheme, a smooth triangular ostium surface is created from the contour [276]. Jerman et al. [169] introduced a ray-casting approach, where rays are emitted from the aneurysm center towards the vessel wall. Based on the intersection distance, ostium points are detected. Finally, a closed-curve is fitted to these points to obtain the neck curve. These methods fail for aneurysms with small arteries around the ostium or for wide-neck aneurysms, as the cross-section of the ostium exceeds the aneurysm width [55]. Recently, Saalfeld et al. [325] presented a semi-automatic ostium extraction that is based on the method by Neugebauer et al. [269] and slightly improves this approach. They also employed the vessel centerline to detect four landmarks on the 3D aneurysm surface that are used to define the ostium contour. However, their method depends strongly on the quality of an initial point on the aneurysm specified by the user from which the dome point is determined. Moreover, multiple parameters determine the output of their extraction, which can be controlled by the user. If a setting is changed, usually large parts of the reconstruction have to be recalculated, which prevents an interactive correction of the result.

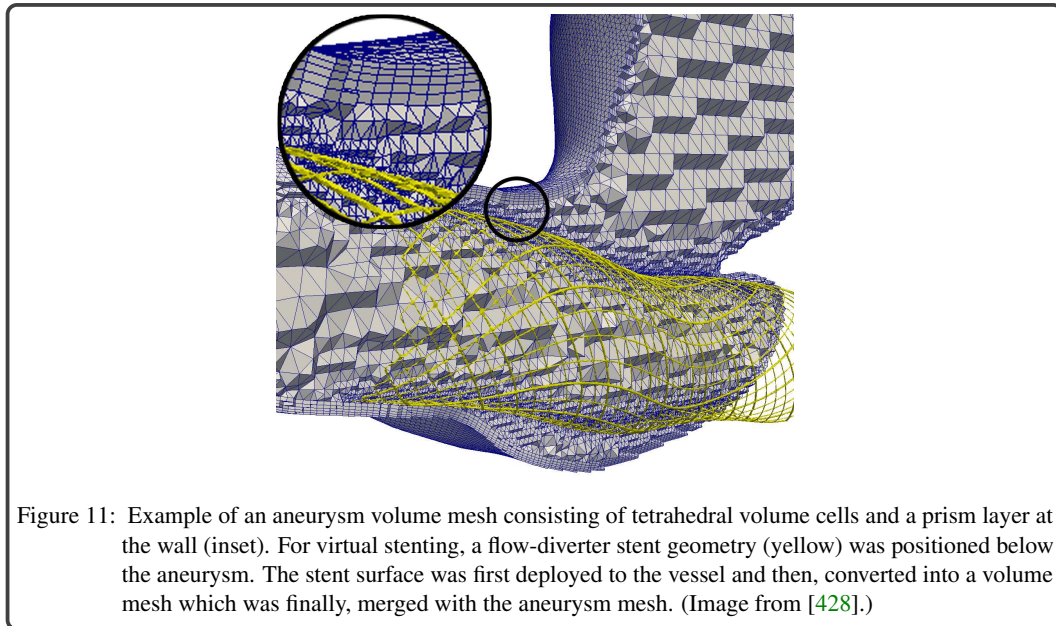
To support a differentiated flow analysis in the parent vessel, Cebal et al. [66] introduced the separation into near- and far-vessel segments. They defined the near-vessel part to be within a certain distance to the ostium ( $< 1$  cm). Neugebauer et al. [275] applied a more general, geometric definition: far-vessel segments exhibit ellipsoid cross-sections with small changes in diameter, whereas the near-vessel section strongly deviates concerning cross-sectional shape and diameter.

### 3.4 VOLUME MESH GENERATION

For numerical simulations like CFD, the whole computational domain has to be discretized, i.e., a volumetric mesh has to be built based on the optimized surface mesh (recall Section 3.2). The generation of volumetric meshes is a very extensive research area. In the following, fundamental aspects of this process which are essential for the understanding of this work are explained, whereby more technical explanations are given for example in the following references [1, 92, 225].

While the volumetric mesh might in principle be of any type (structured/unstructured/mixed, regular/irregular/hybrid), depending on the situation, typically several of the following requirements have to be met:

1. the type of the mesh should fit the numerical procedure applied (finite difference methods require structured meshes, while finite volume and finite element methods allow irregular meshes) and the simulation software used,
2. faces in the volume mesh should accurately represent complex geometric shapes of individual anatomical structures and internal interfaces,
3. if *computer-aided design* (CAD) models, like, e.g., stents, need to be integrated, it should be possible to include geometries defined by parametrized curves and surfaces,
4. if fine geometric details have to be modeled, locally varying element sizes should be possible,
5. if the solution of the *partial differential equation* (PDE) to be solved exhibits isotropies, the mesh should well capture these,
6. if adaptive numerical methods are to be applied, local mesh refinement/coarsening should be possible (without changing the type of the mesh),
7. if hierarchical numerical methods are to be applied requiring geometric levels of detail, hierarchical meshes should be used, and
8. if parallel simulation methods are to be implemented, a block decomposed mesh might be necessary.



Many of these requirements can be met by using unstructured tetrahedral meshes, see Figure 11. They are particularly suitable for complex geometries and can be generated efficiently and robustly. Moreover, they can be adaptively refined, using a user- or algorithmically defined sizing field [203]. *ANSYS IcemCFD* [15] is a commercial tool to robustly generate unstructured meshes composed of tetrahedral cells using the Octree method. It can be considered as a top-down approach. Because of its robustness, it is also used to create a closed surface mesh. Further methods, such as *Delaunay* [123, 227, 289, 312] or *Advancing Layers* [327] algorithms, require a sealed surface for the representation



of the individual anatomical objects to create a volume mesh. These bottom-up methods produce smoother transitions between regions of different volume element sizes.

In the case of flow simulations, requirement (5) becomes particularly important. To match the anisotropy of the flow, often stretched elements are used. It turns out that in near-wall regions and in boundary layers, where large gradients in the velocity field appear, extended hexahedrons typically perform better than stretched tetrahedra. Recent methods use quaternionic mesh representations [116] or multi-block grid-based approaches [37] to create mixed meshes composed of tetrahedral and hexagonal elements. Prismatic cells are also often used to resolve areas of the volume grid more finely, see Figure 11. For near-wall regions of an aneurysm, one to three prism layers are typically used. Thus a resolution of approximately  $20\text{ }\mu\text{m}$  can be achieved in the direction of the surface normal. Recently, Botella et al. [43] introduce an indirect algorithm to create mixed meshes of tetrahedral, prismatic and hexagonal cells by first generating a tetrahedral mesh whose tetrahedra are then merged into other primitives (hexahedrons, prisms, and pyramids).

Various criteria guide the selection of the applied mesh resolution. A compromise is usually needed between the computational effort and the accuracy of a given computation. The size of the smallest mesh elements is determined by the smallest considered features of the given geometry and the minor features of the solution of the PDE, e.g., the smallest eddies in the flow. The discretization error – one possible source of error during simulation – is caused by the finite mesh resolution. To reduce the effect of the discretization, typically several simulations with different resolutions are considered to know when a so-called *mesh-independent solution* has been achieved.

Besides, intravascular implants can also be included in the simulation. For this purpose, unstructured grids are required for the integration of a flow-diverter stent geometry into the volume mesh in the course of *virtual stenting* [163, 165] and also for integrating meshes of coils in *virtual coiling* [259]. The finest geometry detail often determines the mesh resolution. For instance, as a wire of a flow-diverter stent is typically around  $30\text{ }\mu\text{m}$ , the direct resolution requires a much finer mesh as an untreated case. For the numerical simulations of intracranial aneurysms, usually, a few million cells are applied for a finite volume computation. However, virtually treated cases with flow-diverter or coils can only be discretized with a finer mesh using up to around 5-10 million cells [163].

### 3.5 COMPUTATIONAL FLUID DYNAMICS SIMULATION

The final step of the data acquisition pipeline is the simulation of the intra-aneurysmal blood flow. CFD is an established numerical method to approximate hemodynamics in IAs. Unlike experimental blood flow measurements, no elaborate test set-ups are necessary and 3D aneurysm representations from clinical imaging procedures can be used as input data. Furthermore, flow and wall attributes can be derived directly from the simulation results, as they do not contain any signal noise. Another advantage is the ability to vary the aneurysm geometry and flow parameters to model possible future changes in blood flow, allowing a possible future rupture to be estimated. To obtain meaningful results, it must be ensured that the simulation model reproduces reality sufficiently accurately by defining boundary conditions. However, the more physical effects are integrated, the more the complexity of the model increases, which can lead to calculation times of up to several days.

The following sections provide an overview of CFD-based blood flow simulations, which comprise the following steps:

- writing the mathematical equations governing the motion of a fluid (set of PDEs),
- discretization of these PDEs,
- division of the domain into small grids or elements and
- solving the discretized PDEs by using specific boundary conditions.

Besides, the integration of wall mechanics based on FSI simulations and the simulation of treatment scenarios such as stenting will be discussed. Like mesh generation, CFD is a broad field in its own. This is true even for the subfield dealing with biofluid dynamics, where more detailed information on these topics are given in the textbooks [137, 187, 423].

### 3.5.1 Governing Equations

CFD simulations enable a computer-aided mapping of the dynamic behavior of fluids. For this purpose, the properties of the liquid must be described by a mathematical model. The motion of fluid within some spatial volume is defined by the following conservation laws [19, 316]:

- conservation of mass (continuity equation),
- conservation of momentum (*Navier-Stokes equations* (NSE)), and
- conservation of energy (energy equation).

The first law states that mass cannot be produced or destroyed. The starting point for the conservation of momentum is *Newton's Second Law*. Thus, the rate of change of momentum corresponds to the sum of the forces acting on a fluid particle. The third law represents the first law of thermodynamics, which states that the energy of a closed system is constant. Thus, the rate of change of energy is equal to the rate of change of heat input and work on a fluid particle. The motion of a fluid is considered as a continuum if macroscopic aspects only influence it and molecular effects can be ignored. A fluid element thus represents the physical behavior of a sufficiently large number of molecules at a point in the domain at a certain point in time. At the level of the continuum, the fluid element is the unit to which the conservation of mass, momentum, and energy refers [205].

Some simplifications are assumed for the CFD simulation to reduce the calculation effort. First, blood is expected to be an incompressible, isothermal fluid. These are valid assumptions for liquids under normal pressure and with low-temperature fluctuations, including blood. Conservation of mass for an incompressible fluid is defined as zero divergence of the flow velocity vector  $\mathbf{v}$ :

$$\nabla \cdot \mathbf{v} = 0. \quad (1)$$

This implies that an equal amount of mass that enters the system also has to leave it.

Although blood is a non-Newtonian fluid, is assumed to be a Newtonian fluid, i.e., a fluid with constant density and viscosity. Then, for a fluid element, the rate of change of momentum can be expressed by:

$$\rho \left( \frac{\partial \mathbf{v}}{\partial t} + \mathbf{v} \cdot \nabla \mathbf{v} \right), \quad (2)$$

where  $\rho$  is the density of the fluid and  $t$  the time. The rate of change of momentum compensates the forces acting on a fluid element. These forces can be divided into body and surface forces. Body surfaces are, e.g., gravity, centrifugal and Coriolis and electromagnetic forces, which are included through a source term  $S$ . Surface forces include pressure and viscous forces, which are expressed by a stress tensor  $\sigma$ . For a Newtonian fluid that exhibits a constant viscosity, the stress tensor is described as the sum of pressure and viscous forces:

$$\sigma = -\nabla p + \mu \nabla^2 \mathbf{v}, \quad (3)$$

where  $p$  is the pressure and  $\mu$  the viscosity of the fluid. Based on the body and surface forces, which balances the rate of change of momentum [19], the NSE is defined by:

$$\rho \left( \frac{\partial \mathbf{v}}{\partial t} + \mathbf{v} \cdot \nabla \mathbf{v} \right) = -\nabla p + \mu \nabla^2 \mathbf{v} + S. \quad (4)$$

The left-hand side of Equation 4 represents the inertia per fluid element composed by the unsteady and convective acceleration  $\frac{\partial \mathbf{v}}{\partial t}$  and  $\mathbf{v} \cdot \nabla \mathbf{v}$ , respectively. The convective acceleration describes the change in velocity over the position, e.g., by a constriction in a pipe, rather than over time  $t$ . The right-hand side of Equation 4 defines a pressure gradient, a viscosity term, and a source term uniting the body forces. Together with Equation 1, and appropriate initial and boundary conditions, the NSE allow adequate description of a fluid's velocity  $\mathbf{v}(x, t)$  and pressure field  $p(x, t)$ .

Non-Newtonian components of blood such as solids and liquids can lead to a change in viscosity. In most cases, non-Newtonian effects seem to be negligible, at least in arteries with a diameter larger than 1 mm and shear rates above  $100 \text{ s}^{-1}$ . In these cases, a density of  $1055 \text{ kg/m}^3$  and a viscosity of  $0.004 \text{ Pa} \cdot \text{s}$  [332] is defined. But, for pathological changes, such as aneurysms, it may be relevant to include non-Newtonian properties due to low local shear rates [342]. Conventional approaches to model the non-linear relationship between viscosity and shear rates that characterize a non-Newtonian fluid are the Power-law, Casson, and the Carreau-Yashuda model [125].

### 3.5.2 Flow Properties

Flows can be classified according to their temporal and spatial behavior. Regarding time, *steady* and *unsteady* flow is distinguished. Steady flow represents a flow description independent from time. In contrast, unsteady flow is known as time-dependent flow, where flow properties can change over time. In most cases, first, steady simulations are performed, because such simulations are useful for spatial convergence tests and significant aspects of aneurysmal hemodynamics can be inferred from a steady flow. Moreover, steady simulations are more straightforward to compute, and their exploration is easier. Mantha et al. [237] showed that significant flow patterns, especially for smaller aneurysms, are very similar to those found under pulsatile conditions. However, to analyze time-dependent flow patterns resulting from the pumping motion of the heart, unsteady simulations are needed.

Within the second category, laminar and turbulent flow is distinguished. An important parameter to estimate whether turbulence occurs is the so-called *Reynolds number*, which represents the ratio of inertial and viscous forces:  $\text{Re} = \frac{\rho U L}{\mu}$ , where  $U$  is the mean velocity and  $L$  the length of the blood vessel. If the Reynolds number is low, the resulting flow is laminar. If the Reynolds number is high, the flow becomes turbulent, i.e., inherently time-dependent and chaotic, and the computing time explodes. Since in case of turbulence, not all details of the flow are interesting, but only the influence of turbulence on the averaged flow, the *NSE* is replaced by the:

- *Reynolds-averaged Navier-Stokes (RaNS)* equations and the
- turbulence equations.

The equations can be written in a generalized form (Equation 5) applicable for each mass-related and transported quantity  $\Phi$  (e.g., velocity  $v$ , enthalpy  $h$ , turbulent kinetic energy  $k$ , the rate of turbulent dissipation/vorticity  $\epsilon/\omega$ ), where  $S_\Phi$  is a production term, and  $\Gamma_\Phi$  describes the diffusion coefficient of the respective quantity that is to be considered:

$$\frac{\partial}{\partial t}(\rho\Phi) + v_j \frac{\partial}{\partial x_j}(\rho\Phi) = \Gamma_\Phi \frac{\partial^2 \Phi}{\partial x_j^2} + S_\Phi. \quad (5)$$

The *shear-stress-transport (SST)* turbulence model [140] can be used, considering both, the transport of turbulent kinetic energy  $k$  as well as the rate of turbulent dissipation  $\epsilon$ , respectively, vorticity  $\omega$ . The *SST* turbulence model combines the  $k/\epsilon$  and the  $k/\omega$  turbulence models [409] via a blending function, which is 1 near the boundaries (activating the  $k/\epsilon$  model) and 0 for free shear flows (choosing the  $k/\omega$  model). Thus, the near-wall performance of the  $k/\omega$  model can be utilized without the flaws potentially arising from its free stream sensitivity. The *SST* turbulence model also yields a modification of the definition of the eddy viscosity [250], which is required to capture the onset of separation under pressure gradients accurately.

Empirical studies have determined a threshold of 2300 for the Reynolds number as a transition between laminar and turbulent flow [301]. Commonly, the flow in intracranial arteries is assumed to be laminar with Reynolds numbers well below this threshold. But there are also isolated studies showing that turbulence is possible and could play an essential role in the assessment of *IA* [371, 372]. In the context of *IAs*, a mixture of laminar and turbulent flow was observed, called *transitional flow*, where turbulence occurred more in the center of the aneurysm sac, and laminar flow near vessel wall. However, turbulence probably plays only a role in large aneurysms, where high speeds occur (inlet boundary condition) and a sharp segmentation kernel was used.

### 3.5.3 Boundary Conditions

To be able to solve the [NSE](#) for a specific problem, boundary conditions have to be specified for the domain boundaries, which are usually represented by inlets, outlets, and walls. The difficulty lies in choosing the right number of conditions since the boundary conditions influence convergence and physical plausibility of the solution.

On the orthogonal inlets, often a time-dependent mass flow rate or velocity profile is defined. For a patient-specific flow simulation, measured velocity profiles should be used that can be acquired by Doppler ultrasound or [PC-MRI](#) measurements [31]. On the outlets, a general boundary condition is to apply pressure. Since the [NSE](#) describes only the gradient of the pressure, the absolute pressure value within the model has to be defined. For this purpose, usually, a zero pressure condition is applied, which creates a relative dependence of the pressure within the model from the pressure on the outlets.

A commonly used boundary condition for vessel walls is the *no-slip boundary*, i.e., zero velocity at the wall. The vessel wall can be considered to be rigid, have a pre-defined motion, or deform as a consequence of the fluid pressure [205]. Moreover, conditions regarding smoothness or roughness can be applied to the walls to model irregularities of the wall. Besides, the wall can be assumed to be permeable to study mass transfer from the blood flow into the wall layers. In this way, Lantz et al. [206] showed a correlation of flow features and the accumulation of lipoproteins in the aneurysm wall that promotes the development of atherosclerosis and a destabilization of the wall.

### 3.5.4 Solution Methods

The [NSE](#) bring the velocity, pressure, density and dynamic viscosity of the fluid into relation, or – regarding forces – the inertial, pressure, viscous, and the external forces. Based on the defined boundary conditions, a solution for this set of coupled nonlinear [PDEs](#) can be determined and, the time-dependent fluid velocity and pressure can be predicted. An analytical solution of the governing equations can only be found for very simple configurations neglecting various effects. However, to solve them for particular aneurysm configurations, numerical approximation methods are used. For this purpose, the partial derivatives of the [NSE](#) are formulated and solved as finite differential equations for discrete sections of the flow field.

There are various approaches of discretization: *Lattice Boltzmann method* ([LBM](#)) [355] and *finite differences method* ([FDM](#)), *finite volumes method* ([FVM](#)) or *finite elements method* ([FEM](#)) [73]. [FDM](#) and [FEM](#) are typically applied on body-fitted or unstructured volume meshes. [LBM](#) and [FDM](#) are often considered meshless approaches. Although a no body-fitted mesh is required for their application, a regular Cartesian grid is applied in the background. Therefore, a direct use is not straightforward for complex geometries in medicine, such as patient-specific aneurysms. The combination with, e.g., an *immersed boundary method* ([IBM](#)) can alleviate this problem without the necessity of volume mesh generation [2]. [LBM](#) has gained popularity since it offers good parallel scalability due to its local nature and thus, can be efficiently computed on the [GPU](#). Finally, the discretized equations can be written in a linear algebraic matrix equation either for a steady state or for pulsatile inflow conditions, except [LBM](#) which is an unsteady approach. The process is iterative and delivers the requested variables, such as the flow velocity or pressure for each cell. For this purpose, the solutions are determined for all cells until the result difference between two iterations is below a predetermined value, the so-called residue. If this is the case, the simulation is converged. In unsteady simulations, each subsequent time step is initialized with the flow field of the previous time step, in addition to the correspondingly adapted boundary conditions. The [CFD](#) simulation of a cardiac cycle is typically conducted with a temporal resolution in the range of 0.0025-0.005 s yielding a 3D velocity vector field at each of the 200-400 time steps [118]. A computational rupture challenge for intracranial aneurysms is documented in [31], summarizing almost 30 computational groups worldwide with their [CFD](#) methods and setup.



### 3.5.5 Hemodynamic Characteristics

Several hemodynamic characteristics can be derived from the CFD simulation results. They can be classified into *local attributes* and *non-local characteristics*. While the former are computed per vertex, volume element, voxel or region of the domain, the latter represent structures and properties of the blood flow patterns and are often derived in a visual inspection using general flow visualizations techniques such as integral curves, colored cut planes, and *line integral convolution (LIC)* [53]. Alternatively, they are explicitly extracted as geometries, using feature extraction techniques [302]. The exact meaning and relevance of the different attributes and characteristics are subjects of ongoing research. In the following, the most commonly used features are explained. A more in-depth discussion of all characteristics according to cerebral aneurysm hemodynamics is given in [65, 66].

#### Local Attributes

The most important local attributes are:

- **Velocity** encodes flow direction and speed per grid point and time step by a vector  $\mathbf{v}$ . All other local characteristics are derived from  $\mathbf{v}$ . SI unit: cm/s or m/s.
- **Fluid pressure**  $p$  constitutes the scalar kinetic energy per unit volume of a fluid particle. It is computed per grid point and time step. SI unit: Pascal (Pa).
- **Wall shear stress** encodes the force tangential to the vessel wall exerted by the blood flowing past. It is computed for each time step at grid points along the wall as the scalar magnitude of the corresponding **WSS** vector  $\vec{\tau}_{WSS}$ . SI unit: Pascal (Pa).
- **Volumetric flow rate**  $Q$  represents the scalar amount of blood volume passing through a pre-defined surface region per unit time. SI unit: cm<sup>3</sup>/s or m<sup>3</sup>/s.
- **Oscillatory shear index (OSI)** indicates flow disruption by the time average strength of temporal deflection of  $\vec{\tau}_{WSS}$  from the time-averaged **WSS** vector. Dimensionless scalar per grid point along the wall.
- **Turnover time (ToT)** encodes the average elapsed time of a blood flow particle from entering to leaving a particular vessel region. SI unit: s.

An imbalance of pressure and **WSS** is among the factors may have an impact on aneurysm growth and rupture [66]. Both, abnormally high and low shear stresses of the cerebral aneurysm wall have been related to an increased risk of rupture [249]. The volumetric flow rate of the ostium surface is determined before and after virtual stenting to predict the therapy success [166]. High values of **OSI** seem to promote aneurysm initiation [21].

#### Non-Local Characteristics

Essential non-local characteristics are:

- **Vortices** represent regions of flow swirling around a straight or curved axis line which is also referred to as *vortex core line*. The visual inspection of vortices is often supported by emphasizing flow with high *vorticity*, i.e., a high magnitude of the vorticity vector describing the curl of the flow velocity:  $\vec{\omega} = \nabla \times \vec{v}$ .
- **Recirculating zones** occur when a forward stream of blood reverses and flows back into an area, where the flow was divided into different directions (separation zone).
- **Flow complexity and stability** are related to the number of vortices and recirculating zones in the flow and their persistence over the cardiac cycle. A flow is supposed to be *simple* if only one vortex or recirculating zone exists. It is said to be *stable* if this vortex or recirculating zone neither moves nor collapses and reappears over time.

- **Flow type** can be *laminar* or *turbulent*. In laminar flow, particles run mostly parallel or in a swirling motion along a common axis (vortices) while in turbulent flow, chaotic property changes are observed. The *Reynolds number* indicates the flow type with very high numbers (> 2300) correspond to turbulent flow.
- **Inflow jet and impingement zone** refer to the structure of rapid, parallel inflow into an aneurysm and the associated wall region of the first impact.

Vortices have received considerable attention in IAs. They were related to cerebral aneurysm rupture. A simple and stable flow was more frequently seen in non-ruptured aneurysms while complex and unstable flow was mostly observed in ruptured aneurysms [52, 65]. Recirculating zones have been investigated in the context of cerebral aneurysm growth and rupture [346, 361]. Blood flow in the cerebral arteries exhibits rather small Reynolds numbers (200-700) and is commonly assumed to be laminar [118]. In a large-scale study, ruptured aneurysms showed a more compact inflow jet and a rather small impingement zone as compared to non-ruptured aneurysms [65].

### 3.5.6 Fluid Structure Interaction

Due to the complexity of the patient-specific blood flow behavior, where specific individual properties are unknown, e.g., cerebral flow rates and vital parameters under activity, several simplifications of the simulation model are made to apply CFD. The most common simplification is the assumption of a rigid, inflexible wall with infinite resistance since the segmentation results based on contrast-enhanced image data that contain no information about the wall structure. However, a study by Frosen et al. [112] demonstrated the heterogeneity of cerebral vessels, especially when diseases occur. Since the surrounding arteries and the aneurysm itself deform under blood pressure and shear forces, the vessel wall behavior is strongly correlated to rupture, assuming that rupture is caused by wall tension that exceeds wall strength. Kadasi et al. [174] reported on a relation of wall thickness and aneurysm rupture risk. Cebal et al. [61] demonstrated that wall thickness could be measured ex vivo and related to simulated hemodynamics based on 3D printouts of a patient-specific aneurysm model and a resected aneurysm sac overlayed on the 3D model. Recently, Voß et al. [393, 394] compared hemodynamic and wall stress attributes based on multiple FSI simulations. They defined different wall thickness models generated from OCT data comprising minimum, mean, maximum, and diameter-dependent thicknesses. A strong variability of the analyzed characteristics was reported depending on the wall thickness models, which highlights the importance of integrating patient-specific wall thickness distributions. So far, no non-invasive in vivo imaging technique is available in the clinical routine that adequately visualizes the aneurysm wall. Therefore, to consider mechanical exchanges between blood flow and the surrounding vessel tissue, FSI simulations are carried out.

Addressing the FSI simulation, the whole simulation domain  $\Omega$  is divided into two subdomains: the fluid  $\Omega_F$  domain with the boundary  $\Gamma_F$  and the solid domain  $\Omega_S$  with the boundary  $\Gamma_S$ . The intersecting surface of the fluid and the solid domain is called interface  $\Gamma_{FS}$ . The way in which both domains interact with each other depends on the coupling at the interface. There are two types of linkage: a strong and weak coupling. In a strong coupling, both the fluid and solid equations are solved in a single matrix. Although this approach offers advantages according to stability and convergence, it is difficult to implement and to validate. In a weak coupling, both domains are solved separately, where forces and displacements are iteratively passed between two solvers through the interface. The information from the other subdomain is used as updated boundary conditions in the next calculation step. The exchange of information can be one-way or two-way, where the former means that data is transferred just in one direction from one solver to the other, while in the latter data is transferred in both directions between the solvers in a loop. An example of a one-way exchange is the transfer of fluid forces to the solid domain to calculate strain and stresses, but the resultant deformation is not transferred back to the fluid domain as it is assumed that the deformation is too small to influence fluid forces significantly. In a two-way exchange, the resultant deformation would be transferred back to the fluid domain, where the fluid domain would be deformed, and the resulting forces would again be transferred to the solid domain.

Inside the fluid domain, CFD is used to calculate the hemodynamics. For the solid domain, the governing equation can be described by the equation of motion:

$$\rho_S \frac{\partial^2 \mathbf{d}_S}{\partial t^2} = \nabla \cdot \boldsymbol{\sigma}_S + \mathbf{f}_S, \quad (6)$$

where  $\rho_S$  is the wall density,  $\mathbf{d}_S$  is the displacement vector,  $\boldsymbol{\sigma}_S$  is the *Cauchy stress tensor*, and  $\mathbf{f}_S$  represents an external body force vector. The wall thickness is artificially generated by extruding the wall along the normal vector about 0.2 to 0.6 mm [77, 374]. Moreover, boundary conditions have to be defined at the interface to realize the interaction of both domains, which can be formulated as:

$$\mathbf{v}_S = \mathbf{v}_F, \quad (7)$$

$$\boldsymbol{\sigma}_S \cdot \mathbf{n}_S = \boldsymbol{\sigma}_F \cdot \mathbf{n}_F, \quad (8)$$

where  $\mathbf{v}$  are velocities,  $\boldsymbol{\sigma}$  are stress tensors, and  $\mathbf{n}$  are surface normals. The first condition states that the velocities of the fluid and solid must be compatible along the interface, where the second condition states that the traction is balanced along the interface. Together with a specification that relates the mechanical stress to the mechanical strain, the equation system can be solved locally for each finite element, based on the conservation of momentum. The most simple relationship between strain and stress is defined by the *Hooke's Law* that relates the stress to the strain times a material constant, called the *Young's Modulus*. In summary, the following wall properties can be determined:

- **Wall thickness** encodes the thickness of the vessel wall per vertex by a scalar. SI unit: mm.
- **Deformation** is represented by a vector per vertex, which yields the direction and the length of the deformation. SI unit: mm.
- **Stress tensor  $\mathbf{S}$**  describes the stress state of a tiny element, which is represented by a symmetric  $3 \times 3$  matrix per vertex resulting in six independent components. SI unit: Pa =  $\text{Nm}^{-2}$ .

Rotating  $\mathbf{S}$  leads to zero shear stress and maximum normal stress components, which are obtained by the eigenvectors. Regarding aneurysms, stress inside the wall is caused by the hemodynamic pressure and leads mainly to tension in the circumferential direction. Accordingly, the first two eigenvectors are expected to be tangential and the third to be normal to the wall, respectively. Due to the loading condition and the thin aneurysm wall, some studies, e.g., [332] calculated the wall stress based on shells instead of solid elements. As a consequence, some effects in the normal direction of the wall which are less dominant are neglected.

### 3.5.7 Virtual Aneurysm Treatment

In the last decades, numerous advances have been made in the treatment of cerebral aneurysms. Minimally invasive techniques such as coiling and stenting show promising results and have several advantages over a surgical clipping, e.g., a decreased treatment risk and shorter hospital stay, recall Section 2.6. However, there are several intra- and post-operative complications [58, 224, 336], where the outcome of the procedures regarding aneurysm embolization and altered hemodynamics is less predictable. Several approaches were developed dealing with pre-treatment simulations of coiling and stenting [30, 81] to support patient-specific decision-making.

#### Virtual Coiling

During a coiling intervention, the radiologist has to decide how many coils of what size have to be inserted into an aneurysm to trigger thrombus formation by altering intra-aneurysmal hemodynamics. This can be a challenging task, where 15 % - 25 % of coiled aneurysms show a reflow of blood into the aneurysm sac. This can be caused by either coil compaction or aneurysm regrowth due to hemodynamic forces. In these cases, a re-intervention is necessary. Medical studies propose some

quantitative parameters to predict coiling success. One of these parameters is the packing density, the percentage of aneurysm volume occupied by coils, where a high density should be aimed for. Another clinical parameter is the aneurysm occlusion rate, which indicates the strength of the aneurysm obliteration due to the coils. However, none of these parameters allows reliable predictions about the success of coiling, or consider the post-operative hemodynamics. One main reason for this is probably that the result depends strongly on the experience and ability of the performing physician.

Geometric models of different coils can be placed in patient-specific vascular representations using virtual coiling, which can help to understand their intra-aneurysmal behavior. Several computational techniques were developed to simulate endovascular coiling and its effect on local hemodynamics, which can be distinguished into explicit and implicit methods [259]. The first group explicitly model the coils by using a geometric representation of individual coils. Then, CFD is employed to calculate the flow behavior after coiling. An important fact for the simulation of coil deployment is the accurate modeling of contacts that occur between the coils themselves and between the coils and the aneurysm wall [81, 254]. Implicit methods adapt the governing equations of the fluid domain in the coiled region using a porous medium to model the influence of the coils. Compared to explicit methods, implicit approaches are faster to compute, but the definition of necessary assumptions according to the homogeneity or permeability of the medium complicates the simulation.

Current explicit methods enable interactive virtual coiling, where high packing densities are reached for multiple aneurysm shapes [81]. Virtually coiled aneurysms show a similar distribution of coils compared to real coiled aneurysms [400]. Moreover, hemodynamic changes could be identified. The virtual coils lead to decreased WSS and velocity values within aneurysms, which was also observed in coiled aneurysm phantoms.

#### *Virtual Stenting*

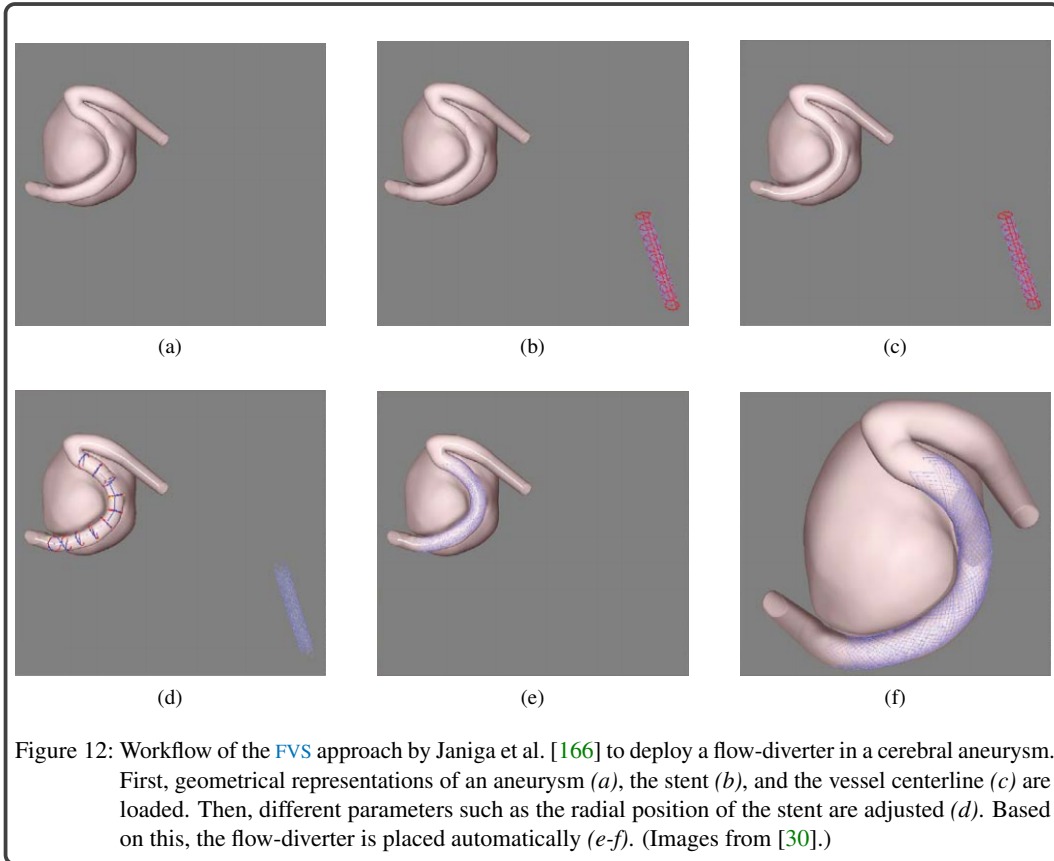
At the moment, several stent designs exist, which differ in length, diameter, and porosity. Furthermore, aneurysms have a high anatomical diversity, which differs in location, shape, orientation and parent artery morphology. Thus, selecting a stent configuration comprising the number of used stents, the stent designs and their positions that lead to the desired embolization by re-establishing the physiological blood flow can be a challenging task. A geometric representation of different stents can be placed in patient-specific vascular configurations using virtual stenting to analyze which option is most appropriate. An endovascular device must be modeled very precisely to simulate its deployment as realistically as possible. This includes the resolving of individual stent cells and the interaction between the stent and the vessel wall.

Virtual stenting approaches can be divided into explicit and implicit methods. The first group is based on a direct description of the stent properties such as the size of the stent cells, whereas implicit methods do not directly model the stent properties. Here, the stent is approximated by a cylinder made of porous material. The main disadvantage of implicit methods is that specific values such as the permeability and inertial resistance have to be approximated, which can be challenging.

Explicit methods can be divided into two groups: *finite element analysis* (FEA) and *fast virtual stenting* (FVS) techniques [30]. FEA approaches, such as the method by Ma et al. [232], allow a very detailed modeling and simulation of the mechanical stent deployment including stent crimping, fitting into a microcatheter, delivery, and expansion. Compared to other virtual stenting techniques, FEA approaches lead to the highest accuracy. However, several simplifications have to be made to simulate these complex models. According to this, a rigid wall is assumed, vessel straightening due to the stent deployment is not considered, and pulsatile blood flow effects are neglected.

Furthermore, FEA approaches exhibit long computational times of up to 100 h per virtual stent deployment, which reduces the usability concerning the testing of many stent configurations. FVS methods were developed that focus on the most relevant stent properties such as the length, angle, and pattern of the struts as well as the radius of the deployed stent to reduce the computational effort [209]. The stent geometry can be mapped to a cylinder, which is then deformed according to the surrounding vessel geometry [64, 166]. To avoid non-linear distortions of individual stent cells, deformable simplex models can be used [209, 290]. FVS methods enable a realistic stent deployment within seconds on a standard personal computer. Figure 12 shows the deployment of a flow-diverter

according to the method by Janiga et al. [166]. Based on imported geometrical representations of the vessel and stent geometry as well as several defined parameters, the flow-diverter is automatically placed. Compared to real stents released in silicone phantoms **FVS** approaches lead to impressive qualitative and quantitative results according to hemodynamic conditions [209]. Quantitative studies have shown that the performance of flow-diverter strongly depends on the size and shape of the stent struts [58, 184, 264, 364]. Even at a relatively high porosity of about 80 %, the intra-aneurysmal flow and **WSS** at the wall are significantly reduced, where the **WSS** on the stent is increased. However, flow-diverter can also cause a rupture due to increased pressure values within an aneurysm [58], where the precise effects are still not well understood.



### 3.6 VALIDATION OF BLOOD FLOW SIMULATIONS

**CFD** simulations offer the possibility to model the patient-specific blood flow behavior. This raises an important question, namely to what extent the simulation reflects reality. Verification and validation methods have to be used to prove the reliability of **CFD** simulations. Until now, **CFD** models have rarely been verified, e.g., by comparing numerical and analytical solutions [365]. Most of the work concentrates on validating **CFD** results by comparing them with in vitro and in vivo measurements to check the correctness of certain model assumptions. However, this area has also not yet been sufficiently discussed and analyzed. The main problem is the lack of ground truth about real intra-vascular flow conditions, as the currently available flow measurement modalities are not able to capture them. Nevertheless, it is assumed that the flow measurements represent the real conditions with sufficient accuracy [365]. For this purpose, mostly in vitro experiments in the form of flow measurements from aneurysm phantoms are carried out. In vivo validation is difficult since it shows a lower spatio-temporal resolution and poorer signal quality or is even not possible at all.



*Particle image velocimetry (PIV)* is a imaging method for the in vitro investigation of flow fields [309]. The basic idea is to observe the behavior of illuminated markers within a flow by recording the scattered light with suitable cameras. With the help of double pulse lasers, two consecutive images are taken with a short time interval to each other. From these images, velocities of particle ensembles can be derived by applying correlation techniques. Roloff et al. [319, 320] demonstrated that PIV is feasible to record flow information of complex geometries and flow conditions, e.g., in IAs.

Ford et al. [109] generated virtual angiographic images based on a CFD model of a giant aneurysm located at the internal carotid-posterior communicating artery. They compared these images to clinical 3D RA images, where the images show an excellent agreement. Besides, they constructed silicone models of carotid and cerebral aneurysms and compared velocity profiles of CFD simulations and PIV measurements [108]. Apart from some local discrepancies, a good match of the velocity vector fields between the two data sources was observed. Also, a large vortex could be identified in the measured and simulated flow data. Similar results were obtained by Raschi et al. [311], where a consistent representation of the main intra-aneurysmal flow structures was observed in CFD and PIV vector fields. Differences were found mainly in the near wall region. Gasteiger et al. [119] investigated the agreement between CFD simulation and in vitro 4D PC-MRI measuring (7 T) of flow in a cerebral aneurysm model. They performed a qualitative analysis concerning flow patterns and quantitative analysis concerning the average volumetric flow rate and flow speed. There were moderate to strong correlations regarding the pulsative development of flow quantities between the measured and simulated blood flow data. However, the further away from the inflow area and the narrower the vessel sections, the higher the deviation between the 4D PC-MRI data and the CFD data regarding local flow characteristics and flow quantities.

Besides these in vitro investigations, some in vivo validations are performed by comparing CFD and PC-MRI data. Boussel et al. [46] reported a strong agreement on flow patterns in measured 4D PC-MRI (1.5 T) and CFD results in IAs. For quantitative values such as the absolute values of WSS and flow velocity larger discrepancies were observed, e.g., significantly larger WSS in the measured data, but locations of high and low values were similar. Isoda et al. [162] and Cebal et al. [57, 67] came to similar conclusions by comparing CFD, 4D PC-MRI, and DSA data, respectively. The location of the inflow jet and the main vortex structures showed good agreement. In general, with decreasing diameter of the vessel, the deviations between CFD and PC-MRI measurements increase. This is probably due to the limited resolution of PC-MRI sequences, in which smaller vessels are not well represented due to the small number of voxels and the *partial volume effect*, leading to error-prone results. This problem can be reduced by using an MR scanner with higher field strengths. Berg et al. [33] compared CFD simulations and 4D PC-MRI (7 T) data of a healthy Circle of Willis and of two IAs. Non-local flow characteristics showed an excellent agreement and also local features such as the flow velocity exhibit significantly smaller discrepancies compared to MR-based measurements with lower field strengths. However, using higher field strengths extends the scanning time and the size of the measurable volume is reduced.

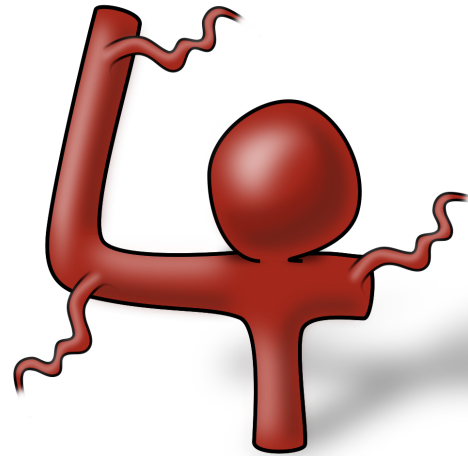
According to the validation of virtual treatment techniques, two phases can be distinguished. First, the geometrical properties of a deployed device, i.e., of a stent [166, 233] or coils [22, 82], can be compared with in vivo or in vitro deployments. For both treatment methods, good qualitative agreements could be observed. The position and overall geometry of the virtually deployed devices largely coincide with in vivo or in vitro data. However, there are some problems with the validation of virtual treatments. Due to their small size, a high-resolution CT scanner is needed to acquire data from cerebral devices in vivo. Furthermore, in most cases, an additional registration has to be applied since the virtual treatment is modeled in a different coordinate system. Besides, a quantitative comparison is quite challenging due to the limited resolution, measuring artifacts and the complex structure of deployed devices [30]. The second phase of validation analyzes the effects on blood flow from the deployment of a device. Similar to the validation of non-treated cases, PIV or PC-MRI can be used to measure flow velocities in stented [64] or coiled [3] phantoms. Here, problems may arise due to the reduced optical accessibility of devices. Moreover, devices can lead to image artifacts in MRI-based velocity measurements. Nevertheless, in vivo or in vitro experiments can be used to investigate the influence of endovascular treatment options and to find an optimal treatment [30, 64].

### 3.7 SUMMARY AND CONCLUSION

CFD simulations can generate patient-specific flow data on discretized volume grids, where NSE describes hemodynamics inside the lumen. By integrating FSI simulations also the mechanical wall behavior can be modeled. For solving the resulting system of PDEs numerically, different methods were developed in the past. To ensure that the simulation converges and the simulation results achieve a sufficient accuracy, the volume mesh must be of high quality. Typically, a combination of tetrahedral and prismatic elements is used to generate the volume mesh. For the simulation itself, different boundary conditions and flow specifications have to be defined making the simulation model arbitrarily complex. This can be further extended by modeling specific treatment options, e.g., by integrating a flow-diverter or coils. To increase the accuracy of simulation results by using more complex assumptions, these must be parametrized correctly. However, it is not always possible to obtain the necessary information from underlying clinical and biomedical data.

The accuracy of the results concerning real patient-specific flow conditions can only be evaluated to a limited extent. Established validation methods perform optical flow measurements in aneurysm phantom models. By comparing the measurements with the results of the CFD simulation, the correctness of certain model assumptions can be verified. Even if this provides indications for the general applicability of the simulation, it is not sure that the flow conditions in the aneurysm phantom correspond to those in the patient. This can be improved by comparing simulation results with results from in vivo measurement, e.g., via PC-MRI. However, to measure blood flow in the small cerebral arteries high field strengths of the MR modality are necessary, where the current resolution and signal quality reduce the meaningfulness of the data. Nevertheless, the coupling of measured and simulated flow data represents a trend-setting possibility to gain additional boundary conditions for a more precise simulation and to compare these results to in vivo conditions to a certain extent.

# Visual Exploration of Blood Flow Data



This chapter is partly based on:

Steffen Oeltze-Jafra, Monique Meuschke, Matthias Neugebauer, Sylvia Saalfeld, Kai Lawonn, Gabor Jániga, Hans-Christian Hege, Stefan Zachow and Bernhard Preim, Generation and Visual Exploration of Medical Flow Data: Survey, Research Trends and Future Challenges; Computer Graphics Forum, 2018.

Julian Kreiser, Monique Meuschke, Gabriel Mistelbauer, Bernhard Preim, and Timo Ropinski, A Survey of Flattening-Based Medical Visualization Techniques; Computer Graphics Forum, 37(3), pp. 597-624, 2018.





In recent years, the measurement and simulation of blood flow inside the human circulatory system play an increasingly important role in personalized medicine for the prevention, diagnosis, and treatment of CVDs. The motivation behind this is the increasing evidence that quantitative and qualitative changes of the blood flow behavior influence the pathogenesis of several CVDs. An investigation of the complex and often dynamic simulation and measurement data requires the coupling of sophisticated visualization, interaction, and data analysis techniques.

Flow information is complex, with multivariate data usually available for each point in the simulation grid. This includes scalar fields such as pressure, vector information such as velocity and tensor-based information such as stress tensors. In the case of unsteady flow data, this information also changes over time. Based on this, flow information can describe complex flow patterns (e.g., vortices) with variable orientation, characteristics and behavior over time. The distribution and characteristics of areas of similar flow behavior can also be relevant.

Due to the spatial and temporal complexity of the flow fields, it is not possible to display all characteristics with a single visualization method. A multitude of visualization techniques was developed, which mostly focus on the representation of a particular aspect of the flow data. Existing techniques can be divided into four categories, distinguished by the degree of abstraction in the representation of the flow field: *direct*, *texture-based*, *geometric* and *feature-based methods* [148]. Direct methods represent the flow data on a low abstraction level. The representation of the information takes place without a complex conversion of the data or complex calculation of specific characteristics. This allows an immediate investigation of the flow data. Texture-based methods distort a random texture according to the underlying vector field [207]. This allows the flow direction to be displayed locally, for example, to display structures such as to detect turbulence. Geometry-based methods use integral lines to reflect characteristic flows of a vector field, which are calculated from defined seed points [246]. This enables qualitative analysis of flow information. Feature-based methods aim at the extraction and visualization of specific structures such as critical points, shock waves or vortices within a vector field [208, 302]. Thus, the information content of the visualization can be increased, and the viewer can focus more on interesting structures. For feature extraction, either the topology of the underlying vector field is used, or methods are applied to simplify the vector field by combining areas of similar flow.

In addition to this abstraction-based classification of flow visualization techniques, existing methods can also be classified according to specific exploration and analysis tasks that they support. This is particularly true for the visualization of blood flow data, where specific tasks of medical or engineering experts need to be encouraged to improve risk assessment and treatment planning. Therefore, Oeltze-Jafra et al. [428] proposed a task taxonomy and categorized relevant works in the field of medical flow visualization that contribute significantly to the solution of at least one of the tasks. They focused on three application areas: CFD simulations of blood flow in cerebral aneurysms, CFD simulations of nasal airflow and 4D PC-MRI of aortic hemodynamics. The categorization further considers the spatial scope of the visual exploration, i.e., whether the investigation is restricted to the vessel lumen/cavity or the vessel/mucous wall or whether it addresses both.

In the following, the task taxonomy and corresponding visualization techniques are summarized, where the author of the thesis was involved in defining the tasks and writing the corresponding sections of the state-of-the-art report. Within the next sections, the main focus is on techniques to visualize intra-aneurysmal hemodynamics, which are most relevant for this thesis. Furthermore, some suitable methods for visualizing aortic hemodynamics are explained.

## 4.1 TASK TAXONOMY FOR THE VISUAL EXPLORATION OF BLOOD FLOW DATA

Oeltze-Jafra et al. [428] extended the surveys by Vilanova et al. [387] and Köhler et al. [188] by an updated, more fine-granular task taxonomy for the visual exploration of medical flow data. Depending on the targeted application, related literature is categorized according to supported visual exploration task(s) and addressed the spatial scope of exploration. Instead of mapping the literature to an existing low-level [10, 345], or high-level [149] task taxonomy, the tasks are directly derived from the papers as well as from literature focusing on medicine, CFD, and flow imaging. This procedure provides an overview of the assistance required for the examination of medical flow data as well as which tasks are lacking support and where further development would be useful. According to blood flow data, the surveyed literature addresses the following spatial scopes of visual exploration:

- Vessel lumen,
- Vessel wall,
- Vessel lumen+vessel wall.

Note that the first two scopes require entirely different visualization approaches since the former is defined by a volume grid and the latter by a surface mesh. Even more complex methods are required for their joint exploration.

The following visual exploration tasks in investigating blood flow data were derived from the literature:

- Spatial overview,
- Interactive probing,
- Feature filtering,
- Temporal analysis,
- Comparison,
- Context visualization,
- Uncertainty analysis.

Another task is the validation of simulated and measured flow data. This topic was already described in Section 3.6, where currently more general flow visualization methods (e.g., color-coded scalar fields depicted in side-by-side views) are used.

**Spatial overview.** The examination of a medical flow data set often begins with an overview of the hemodynamics and the wall properties over the entire domain. This is crucial for the assessment of the overall flow structure, the spatial distribution of wall property values and the correlation between several flow attributes and wall properties. The main challenges for visual exploration approaches are an uncluttered depiction of several data attributes and the reduction of occlusion problems in 3D.

**Interactive probing.** Once an overview has been obtained, the investigation often focuses on some spatial areas such as the neck of a cerebral aneurysm. The flow in these regions can be more relevant for answering a specific research question than flow in the aneurysm sac. Therefore, visual exploration approaches must include an interactive way of probing the flow at the desired locations.

**Feature filtering.** Besides the targeted exploration of specific regions, the extraction of physically meaningful patterns is a frequently used method of flow analysis, whereby the visualization is limited to these so-called *features*. Features can be extracted either by explicitly describing them or by filtering uninteresting flow parts until only the features are preserved. The filtering depending on specific features supports, e.g., the investigation of the flow complexity and stability, which are characterized in particular by features such as vortices and the detection of suspicious vessel wall regions with high WSS and low thickness. Visual exploration approaches must include filtering and/or feature extraction techniques and their coupling with a visualization of physical space.

**Temporal analysis.** To assess the complexity and stability of the flow, flow properties must be investigated over the entire cardiac cycle. There are indications that unstable flow, i.e., collapse and the recurrence of flow characteristics, especially of vortices, predicts a worse outcome for the patient. Approaches to visually explore blood flow data should present interesting features and their temporal development to enable a detailed investigation of these features.

**Comparison.** The comparison of several instances of medical flow data is essential, e.g., to assess the effects of virtual treatment procedures such as stenting or coiling and different treatment scenarios, to investigate the variability between patients or to validate CFD simulations by measurements. Visual exploration approaches must provide an integrated representation of multiple data instances to allow comparison by highlighting differences between instances and providing interaction capabilities to examine these differences at different levels of detail.

**Contextualization.** The vascular anatomy provides relevant contextual information for the visual flow exploration. The representation of the vessel supports spatial orientation and facilitates the correlation of flow and morphology, which contributes to understanding the development and progression of pathology. Through the depiction of the anatomical context, visual exploration approaches should help to relate the local flow with the morphology and vice versa. Thus, flow in the vicinity of aneurysm blebs, could be investigated.

**Uncertainty analysis.** Through the flow data generation pipeline, there are several sources of uncertainty, e.g., image modalities, yielding data that suffers from noise, calibration errors, non-linearities, and partial volume effects, as well as manual parameter adjustments through the grid generation. Simplifying assumptions of the simulation model and numerical inaccuracies contribute to the aggregated uncertainty during simulation. It is essential to investigate the influence of these sources on the interpretation of flow data to integrate them into clinical discussions. Visual exploration approaches should assist the user to understand the potential variability of flow characteristics and wall properties based on multiple data sets generated with different parameter settings.

## 4.2 TECHNIQUES FOR TASK-BASED VISUAL BLOOD FLOW EXPLORATION

Several tasks have been identified for the exploration of blood flow data which are essential for the understanding of morphological and hemodynamic relationships. In the following sections, related publications dealing with blood flow visualization are presented depending on the supporting tasks. The focus is on papers, where the introduced method offers support beyond that of general flow visualization methods. Excellent overviews of general flow visualization methods such as straightforward side-by-side views to compare data sets or path lines, particles as well as animating 3D feature extraction over time with the emphasis on application to blood flow data are provided in the doctoral theses of Gasteiger [118] and Neugebauer [268].

### 4.2.1 Spatial Overview

Biomedically oriented literature comprising CFD or flow imaging methods aims to gain an overview of the vector flow field through its dense visual sampling using integral curves [69, 360], arrow glyphs [50] or particles [415]. The resulting depictions are affected by occlusion and visual clutter. Visual clutter is often reduced by using a lower sampling density or by filtering the primitives. 3D surface representations of the vessel anatomy are commonly used to depict wall-related attributes such as WSS, which are color-coded on the surface, and only the currently visible surface parts can be explored [18, 69, 88]. An occlusion-free overview even of a single scalar attribute over the lumen and a simultaneous display of multiple attributes (and the vector flow field) are not supported.

In the following, advanced visualization approaches for obtaining a spatial overview are explained. Due to the complexity of medical flow data, it is impossible to provide an overview of the entire simulation domain [345]. However, advanced approaches produce a less cluttered overview of the vector field, an occlusion-free projection view of wall-related attributes and near-wall flow or an integrated visualization of several aspects for the current view of the scene.

### *Vessel Lumen*

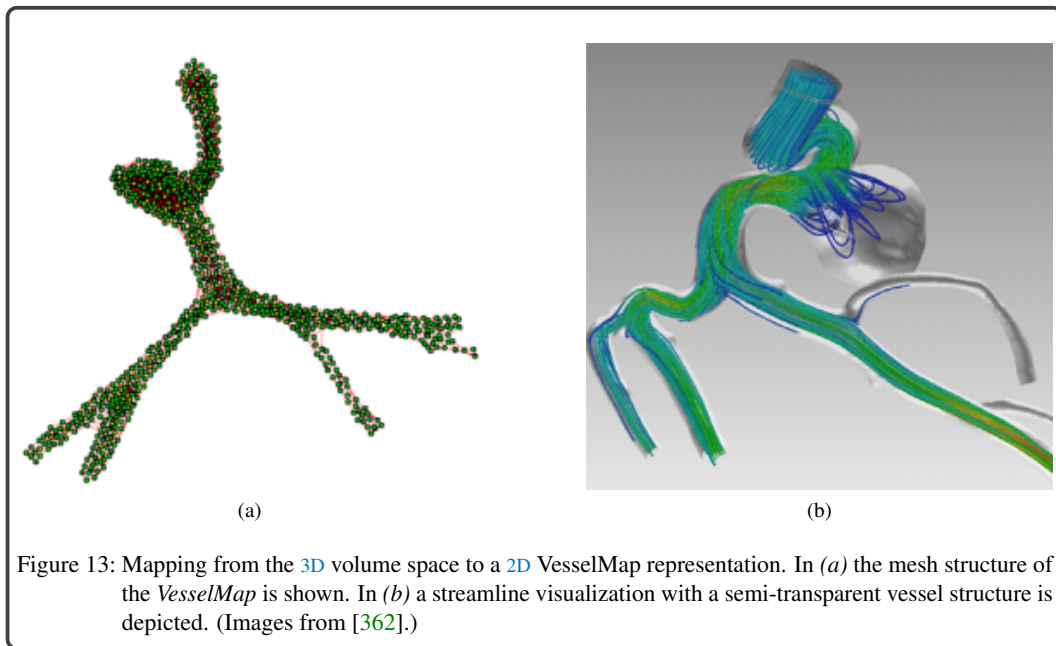
Flow partitioning techniques can be applied to get an overview of the flow within the vessel lumen. With this, the flow is decomposed into regions of common structure [330]. Graphical representatives of the flow regions can be computed and aggregated in a visual summary giving an overview of the flow. This has been exploited for the investigation of cerebral aneurysms and aortic hemodynamics in multiple ways. Van Pelt et al. [380] proposed a spatio-temporal hierarchical clustering of the vector field applied to 4D PC-MRI data of the aorta. For each cluster, a representative path arrow is computed that can be animated over time. Their coarse hierarchical approach strongly reduces the computational complexity based on merging multiple clusters instead of a single pair per iteration. The final flow decomposition for a selected hierarchy level is visualized using a representative path arrow per cluster. Most approaches decompose the flow field based on integral curves since, in contrast to local vectorial information, they represent continuous flow patterns traced over the domain. Kuhn et al. [199] hierarchically partitioned a vector field according to curvature-based characteristics. At first, a scalar field is calculated, which reflects the curvature behavior of streamlines. Afterward, an implicit clustering is performed on the scalar field that is caused by semantic dependencies. Thus, an initialization of the clustering as it is necessary with many explicit methods, e.g., by specifying the number of centroids, which strongly influences the result of the clustering, is avoided. For the implicit grouping, a density function is defined whose minima separate the individual clusters. For the visualization, an enveloping semi-transparent surface per cluster is calculated. This is colored depending on the cluster's flow behavior, whereby clusters with laminar, swirling and turbulent flow are distinguished. Oeltze et al. [282] compared three state-of-the-art approaches to cluster a dense set of streamlines in the context of aneurysm hemodynamics. Streamline similarities were computed based on line geometry [76] or flow field attributes. They conducted a quantitative evaluation of *k-means*, an *agglomerative hierarchical clustering (AHC)* with four linking criteria, and *spectral clustering (SC)*. Based on cluster validity measures, spectral clustering and AHC with average link and Ward's method performed best. A visual summary of the flow is generated, containing one representative streamline per cluster visualized as stream tube to reduce visual clutter. The user can select individual representatives triggering a display of the corresponding streamline set.

Visual overview representations can also be generated by using 2D depictions. Angelelli et al. [13] presented a standardized method to straighten surface representations of the aorta and inner flow. This illustration facilitates the analysis of any abnormalities in vessel diameter or blood flow. Besides, side-by-side views are used to compare a large number of representations. Orientation cues along the straightened structure facilitate the mental integration of corresponding aortic regions. An overview of aortic flow could be given, e.g., by juxtaposing a straightened visual flow summary [282], flow feature extraction result [189], and volume renderings of multiple hemodynamic attributes. Saalfeld et al. [323] provided a simplified occlusion-free 2D view of the anatomy, the approximated flow, the pathology, and the stent or coils to support patient education before an endovascular intervention.

### *Vessel Wall*

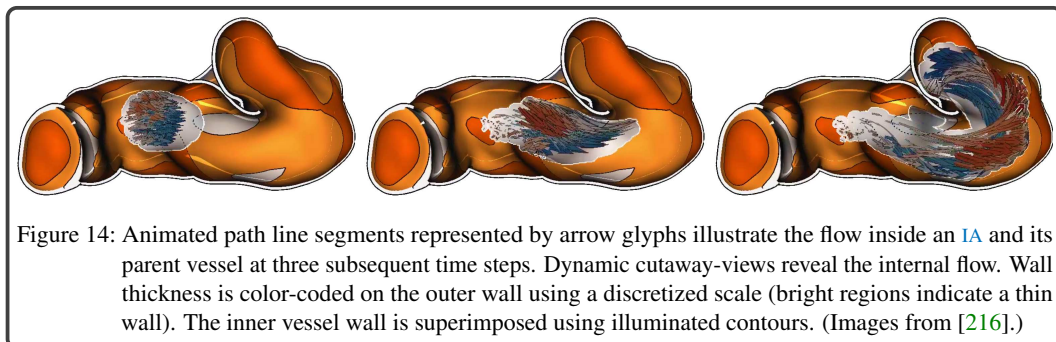
Several works parametrize the vessel wall to generate more abstract representations. Neugebauer et al. [270] employed a multi-perspective 2D projection map for a combined exploration of the aneurysm morphology and hemodynamic data. A scalar field can be color-coded to decode the information on the surface and the 2D map. Moreover, the map is linked to a 3D view of the aneurysm to establish a spatial relation between both views. Goubergrits et al. [135] transformed the aneurysm surface to a uniform spherical shape to analyze statistical WSS distributions. The vertices of the aneurysm surface are transformed towards its center of mass, where they ensured that the distance to the center is equal for all vertices. The sphere is then mapped to a disc using an azimuthal equidistant projection. Tao et al. [362] presented the *VesselMap*, a 2D visualization of a 1A and parent vasculature, see Figure 13. The view-dependent mapping is formulated as a 2D graph layout optimization problem. Small spatial partitions of the vasculature in 3D are considered as nodes that must not overlap in 2D while at the same time spatial relations must be preserved. The result exhibits rather strong local distortions, but the overall vascular topology is maintained.

Concerning the wall thickness as an important rupture risk factor of aneurysms, Glaßer et al. [132] presented a framework for the visual exploration of vessels with wall thickness. They visualized the wall thickness combined with *WSS* by using an overview depiction for their joint analysis for the current viewing direction. A semi-transparent surface rendering of the outer wall is augmented by surface ribbons whose color encodes the distance to the embedded inner surface. The latter can be colored concerning *WSS* of the inner wall, wall thickness or a combined risk score. It is visually subdivided into homogeneous regions based on the same attribute and a *region merging* approach to support an assessment of the attribute value distribution further. More recently, Rocha et al. [317] used *decal-maps* to visualize multivariate data. Decals are a set of images directly mapped to 3D surfaces that allow the depiction of different attributes. They transformed the flower glyphs, introduced by van Pelt et al. [439] to a decal representation to give an overview of pressure distributions on the aneurysm surface.



#### Lumen+Wall

Less work is currently being done on an integrated visualization of the vessel lumen and wall. Lawonn et al. [216] aimed at an integrated, occlusion-free visualization of wall thickness and near-wall flow, see Figure 14. Wall thickness is color-coded on the outer wall surface, the inner wall surface is superimposed using illuminated contours, and the near-wall flow is displayed over time by arrowhead glyphs in dynamic cutaway views.





### 4.2.2 Interactive Probing

Standard probing techniques to explore blood flow data in biomedical research comprise cut planes to color-code an attribute [26], isosurfaces of an attribute [66], and integral curves seeded at a subdomain of the volume mesh or a cut plane [408]. Interactive analysis is not intended or at least not discussed.

Advanced probing approaches support interactive exploration of vectorial flow information, of hemodynamic attributes, or wall properties at interesting locations in space. For a joint investigation of flow and wall, it is necessary to support the interactive probing of the flow of interesting wall regions or the probing of the wall in the vicinity of interesting flow structures. The provision of a flexible probing geometry that can be drawn through the spatial domain allows a detailed analysis of conspicuous regions. Additional views are often used to display details of the probing results.

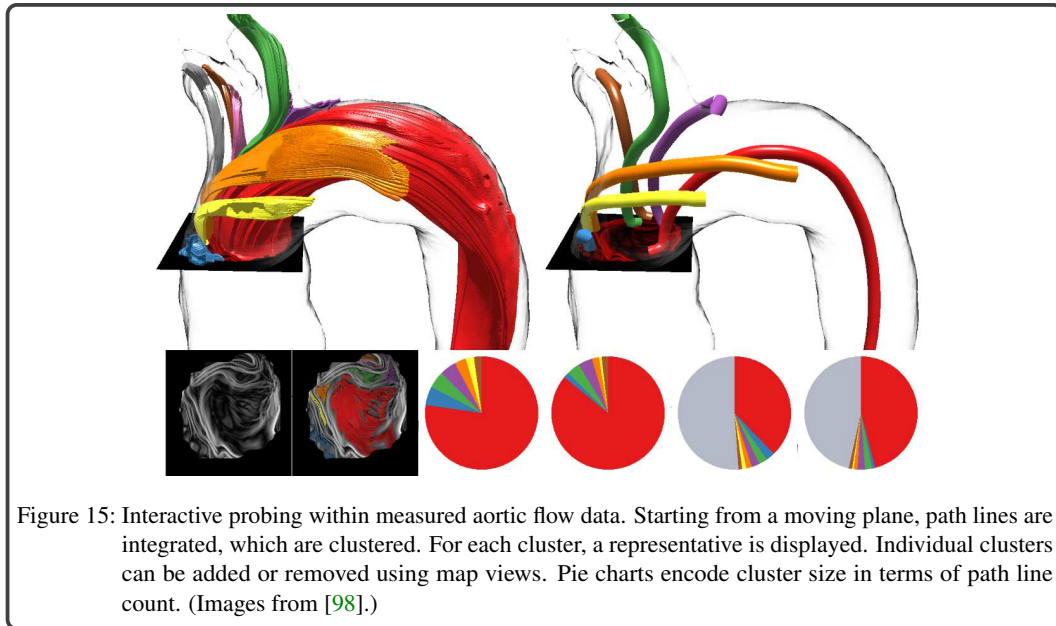
#### *Vessel Lumen*

To investigate intra-aneurysmal flow, Neugebauer et al. [273] employed the ostium surface illustrated in Figure 4 as probing geometry. Moreover, different interactive widgets are provided to explore the parent vessel and the aneurysm. Within the vessel, a cut plane can be dragged along the vessel centerline, which fulfills several functions. It can be used as a seeding geometry for streamlines or to color-code a hemodynamic attribute. Furthermore, an additional height field shows the local velocity profile and a LIC [53] visualization reveals flow features. Within an aneurysm, multiple cut planes can be defined orthogonal to each other and jointly dragged and rotated along the central aneurysm axis. Arrow glyphs encode flow close to the planes.

Arranging cross-sectional cut planes within the aorta is much easier due to its simple shape and can be realized by a one-click interaction. Hennemuth et al. [151] and Köhler et al. [193] require segmentation of the aorta and its centerline for this purpose. Both construct cross-sections perpendicular to the centerline, but Köhler et al. refine the orientation for more accurate quantifications of heart function parameters. Van Pelt et al. [378, 379] and Krishnan et al. [198] introduced probing approaches to facilitate a visual data exploration on the spot, where no vessel segmentation is needed. Van Pelt et al. [379] enable an interactive translation of 2D vessel cross-sections determined by a sequence of image processing steps. This is later extended by an interactive virtual probing using a 3D virtual truncated cone, which is oriented along the underlying flow field [378]. The cone can be dragged along this orientation, and the base and top radius can be adjusted. It serves as a seeding geometry, and the flow behavior is depicted using illustrative techniques like speed lines and particle animations based on elliptical glyphs. For the probing by Krishnan et al. [198], the user is asked to place a seeding geometry in the form of a planar circular inside the vessel. Based on this, stream- or path lines are integrated, where the integration is automatically restricted to the vessel lumen using the *finite-time Lyapunov exponent* (FTLE) measuring the separation of flow.

The probing can be further supported by combining 3D and 2D representations of the probed region. This facilitates the interpretation of the obliquely oriented probe, and additional information can be displayed. Van Pelt et al. [379] integrated an exploded view of cut planes at cross-section positions into the 3D vessel visualization. Hennemuth et al. [151] provided multiple views to show the original image data aligned with and perpendicular to the cut plane based on *multiplanar reformations* (MPRs), where flow information can be superimposed. Diagrams are displayed for quantitative analysis of flow velocity and through-flow of the plane. Angelleli et al. [13] augmented their straightened aortic depictions with histograms and line graphs of flow magnitude for user-defined cut planes. Englund et al. [98] presented an interactive probing to explore flow patterns of measured aortic data, see Figure 15. Starting from a moving plane, path lines are integrated, which are clustered and for each cluster, a representative is displayed. Pie charts and map views provide additional information.

In contrast to the methods presented so far, the probing approach by Saalfeld et al. [323, 324] does not employ a probing geometry. They developed a prototype for the patient and medical education, where the user can sketch vascular pathologies. Based on this, a strongly simplified model is used to approximate the blood flow, where the user can inject a virtual dye or blood cell shaped particles.



### *Vessel Wall*

For the investigation of wall thickness, Glaßer et al. [132] provided a slice widget that can be dragged through the vessel and is oriented perpendicular to the vessel centerline. To facilitate the inspection of local wall thickness variations, an additional 2D view is presented showing the contour of the inner and the outer wall within the cross-section.

### *Lumen+Wall*

For the simultaneous analysis of the lumen and vessel wall, Gasteiger et al. [121] introduced the *FlowLens* – an interactive focus-and-context approach for the simultaneous exploration of anatomical and hemodynamic information. With the help of a flexible lens that can be dragged across the scene in image space, correlations between a focus attribute (outside lens) and a context attribute (inside the lens) can be analyzed. For instance, pressure can be related to the underlying flow based on an opaque vessel surface rendering outside the lens and a transparent rendering inside the lens. Outside, the pressure is mapped to color while inside, streamlines are shown to reveal the underlying flow field. Inside the lens, further probing employing cut planes is supported. Lawonn et al. [216] integrated the slice-based wall thickness probing method of Glaßer et al. [132]. Combined with their additional visualization of the underlying flow field it allows for correlating wall thickness and near wall-flow at the probe location. Markl et al. [240] proposed cross-sectional cut planes at pre-defined positions within the aorta to explore *WSS* and *OSI* in correlation with aortic plaques. They used plot-based depictions linked to the cross sections, where each plot is divided into 12 segments representing the aortic circumference. Each segment is color-coded to the averaged *WSS* and *OSI*, and numerical plaque thickness values. Recently, Rocha et al. [318] presented *decal-lenses* - an interaction technique that extends the concept of magic lenses, which was also used for the *FlowLens* concept by Gasteiger et al. [121]. Similar to the decal-maps [317], the decal-lenses are directly mapped on the surface representation following its geometry, which avoids problems of existing lens approaches related to placement and orientation [121]. Within the lens, the user can easily switch between different attributes allowing, for example, an exploration of curvature and pressure on the aneurysm surface as well as the flow velocity.



### 4.2.3 Feature Filtering

In the medical or flow-related literature, filtering is rarely explicitly addressed. Often manually pre-filtered flow visualizations are shown to illustrate the characteristics, e.g., a subset of traced integral curves [68] or a colored area representation limited to a specific value range [117]. Sometimes characteristics are derived from a precise visual inspection of full-fledged integral curve representations [241]. In CFD literature, isosurfaces of a vortex criterion or a vortex core line extraction algorithm are often used, followed by manual fine-tuning of an integral curve tracing seeded at the core line to achieve a less cluttered visualization of vortex flow [51, 52].

In the following, advanced approaches for focusing the visualization of medical flow data on features of the flow field, the wall or both are examined. Exemplary features are user-defined regions with specific attribute values, near-wall flow in areas with high surface curvature, vortices and critical points. The presented approaches limit the visualization to features or emphasize them in a focus-and-context style. They offer interactive filtering mechanisms such as dynamic queries or linking and brushing for feature definition or integrate state-of-the-art feature extraction algorithms. Some filter mechanisms take into account the current viewing direction and zoom level, e.g., when filtering out attribute values that are connected to currently invisible wall parts.

#### *Vessel Lumen*

**Manual filtering.** Neugebauer et al. [273] presented a qualitative visual analysis of flow features in cerebral aneurysms. They provided streamline filtering to separate aneurysm inflow and outflow as well as slow and fast flow based on a transfer function that considers the dynamic flow direction and velocity. These flow properties can be investigated separately to gain a better understanding of the overall aneurysm flow. Köhler et al. [425] have coupled their 2D plot visualization of vortical flow with slider-based filtering of the underlying  $\lambda_2$ -vortex criterion.

**View-dependent filtering.** To reduce visual clutter of streamline-based flow representations, Günther et al. [141] presented a global line selection approach that reveals user-defined features, e.g., vortices. Based on the curvature of streamlines, an importance measure is calculated, which is used as input for a view-dependent opacity-modulation to filter out less essential streamlines. While they maintain as much context information as possible, Lawonn et al. [217] introduced a streamline selection method, that reduces distracting context to improve understanding of critical areas. For this purpose, they proposed a view-dependent attenuation of streamlines using a suggestive contour measure [80]. The opacity of streamlines is controlled by user-defined thresholds, where the vortical flow is emphasized. The major disadvantage of such global opacity optimization techniques is the high memory consumption in the case of large and dense sets of lines. To improve this, Kanzler et al. [175] combined several local approaches that reveal user-defined features, e.g., vortices. Based on an importance measure using streamline curvature and balanced line hierarchies to adapt line density depending on the view direction, less important streamlines are filtered out.

**Line predicates.** Salzbrunn et al. [329, 331] introduced *line predicates* for stream- and path lines, which are Boolean functions that decide if integral curves fulfill properties of interest. They can be used to extract specific flow features such as vortices. For this purpose, several scalar criteria are computed for each point of an integral line that are used as filtering criteria. Born et al. [42] utilized line predicates to identify relevant flow features such as jets, vortices, and blood with high residence times in cardiac 4D PC-MRI data sets. Later they proposed the low-cluttered, illustrative visualization of the extracted line bundles, based on ribbon-shaped representatives derived for each bundle from its skeleton [41]. They also defined a predicate for filtering vortices and used tubular structures with a hatched texture for the representation. Köhler et al. [189] presented a semi-automatic approach to filter vortex-representing path lines. They compared different local vortex criteria used as line predicates, where the  $\lambda_2$ -criterion was determined as most suitable. Recently, Köhler et al. [191] improved their vortex extraction by using an intravascular, relative pressure calculation. In contrast to the  $\lambda_2$ -criterion, the results suffer significantly less from noise. Jankowai et al. [167] used path line predicates to filter the flow in 4D PC-MRI data of the whole heart. In addition to some basic predicates

such as length and velocity, they used a region of interest predicate to query path lines that run through a particular area, e.g., the pulmonary artery or the right ventricle. These queries are based on an image mask that contains unique identifiers for the various heart vessels/ventricles.

**Space partitioning.** Furthermore, space partitioning methods are used to extract and clearly illustrate flow features. Krishnan et al. [198] coupled their interactive probing approach with a feature-based seeding of integral surfaces. First, a *flow map* [351] is computed for the probing plane. Depending on the seed points of the particles it encodes their destination after advection. Afterward, the flow map is segmented, and from the outline of each segment, an integral surface is propagated. Englund et al. [98] employed a partitioning approach for the exploration of aortic hemodynamics. They used **FTLE** to measure the separation of path lines and derived coherent areas, see Figure 15. Thus, flow patterns are extracted, which allows more detailed exploration of these features and their influence on specific diseases, e.g., aneurysms. Oeltze-Jafra et al. [283] proposed an automatic extraction of *embedded vortices*, i.e., a small vortex enveloped by a larger one swirling in the opposite direction, forming around a saddle-node bifurcation, see Figure 16. Their method comprises a vortex core line extraction, a saddle-node detection, a streamline seeding along the core line, and a tailor-made streamline clustering approach. A smart-visibility approach supports the visual exploration of flow exhibiting multiple vortices. To facilitate a detailed exploration of a single vortex, vortices not considered by the user are attenuated. While the user zooms in on a vortex, more information such as associated critical points are displayed.

Köhler et al. [192] presented a time-dependent extraction of flow jets within cardiac flow data. For this purpose, equidistant measurement planes are automatically placed orthogonally along the vessel's centerline. Then, for each plane over time, the position of the flow jet and the region with the highest velocities are extracted automatically. The main flow jet is visualized as an animated tube, where a net around it represents high-velocity areas. Moreover, a plot-based depiction is provided for a selected plane that visually summarizes qualitative and quantitative flow jet characteristics. Recently, Kanzler et al. [176] presented an interactive approach to exploring flow features of time-independent vector fields and applied their method to cerebral aneurysm data. They employed a clustering of flow-representing streamlines, where for each cluster a consistency measure and a hull geometry was calculated. In the case of multiple depicted hull geometries, the user can brush on the geometries, where the consistency measure of the clusters is used to control their shown line density. With this, only the most interesting parts of the depicted clusters are shown, which reduces occlusion problems.

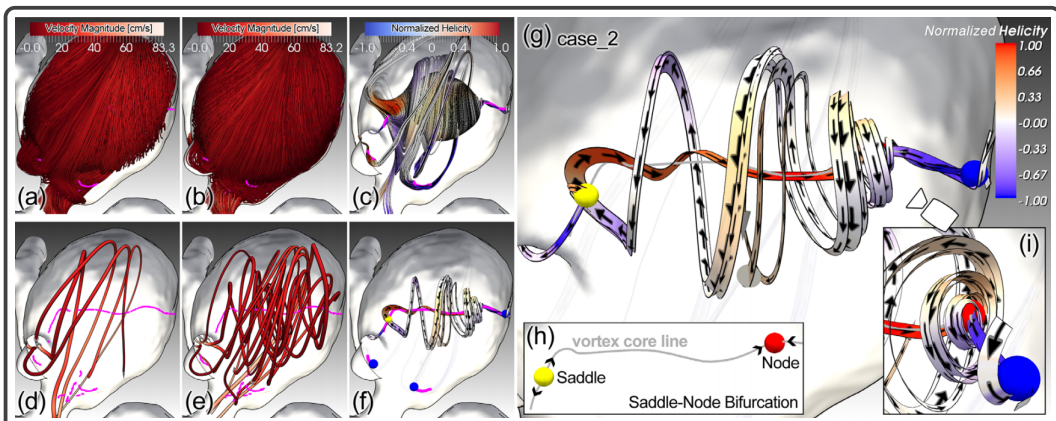


Figure 16: Aneurysm flow with a major center swirl. Vortex core lines are rendered magenta in (a-f). Neither streamlines seeded at the aneurysm inlet (a) or inside (b) nor the cluster representatives (d-e) clearly convey the swirl. Grouping streamlines seeded at vortex core lines (c) and display of custom representatives (f) reveal an embedded vortex (g), i.e., a small vortex enveloped by a larger one swirling in the opposite direction, forming around a saddle-node bifurcation (h). In (g-i) arrows indicate local flow direction, and the core line of the major swirl is rendered gray. (Images from [283].)

**Vortex classification.** Besides an extraction of vortical flow, medical studies manually classify vortices according to specific properties such as their orientation or shape. This requires a precise definition of spatio-temporal vortex entities, which is also performed manually. This task is time-consuming for more extensive studies and error-prone due to inter-observer variability. Van Pelt et al. [293] introduced an automatic vortex classification based on pattern matching. They proposed a set of helical and vortical patterns that can be parametrized by a single variable. The classification results are visualized using color-coded path lines, where the color scheme indicates the vortex shape and orientation. A significant disadvantage of this method is that the number of distinguishable patterns depends on the number of used template flow patterns. Therefore, we provided a semi-automatic vortex classification that calculates the vortex characteristics based on geometrical properties and relations of vortex-representing path lines and the vessel surface [432]. This vortex classification requires a precise definition of spatio-temporal vortex entities. For this purpose, our previous work on vortex clustering [433] is used, where an efficient calculation of a dissimilarity measure was introduced that groups spatio-temporally adjacent vortices and combined it with widespread clustering techniques. Finally, the classification results are presented by a 2D and 3D visualization technique, see Figure 17. The 2D depiction in the form of a circular plot shows the spatio-temporal vortex behavior, where the 3D representation displays the size as well as the orientation by using a color-coding and arrow glyphs.

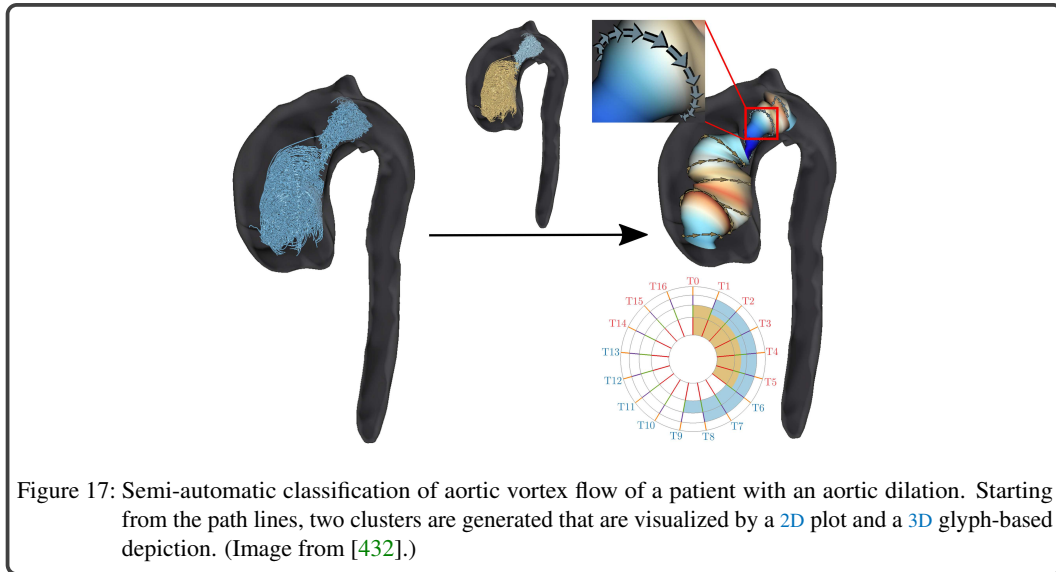
**Miscellaneous.** Broos et al. [49] extracted specific flow characteristics such as high-speed vortices based on a feature-based seeding. They used an interactive generation of transfer functions to define ranges of values that are used to seed path lines in interesting areas. Köhler et al. [190] adapted the *ambient occlusion* (AO) technique for lines (*LineAO*), which was introduced by Eichelbaum et al. [94], to animations of path lines extracted from measured cardiac blood flow data. They presented a line alignment factor to reduce the AO-induced darkening if closely spaced lines exhibit a similar flow direction. The perception of homogeneous flow is further enhanced by using depth-dependent halos. While the full flow context is preserved, their method facilitates the user to identify prominent flow structures while showing the full flow context. Kwon et al. [200] presented adapted the opacity of streamlines representing aortic flow according to their similarity to the centerline. Lines that are similar to the centerline are rendered transparently, while the different ones are shown more opaquely. Thus, abnormal flow patterns such as vortices were highlighted. Recently, Engelke et al. [97] presented a flexible particle system, where the density of the particles is automatically adapted based on local importance measures to emphasize interesting flow features such as vortices. These measures include geometric features such as particle distances, flow-related attributes, e.g.,  $\lambda_2$ -criterion, and aspects of the particle history, e.g., local curvature along the particle's path. The user can interactively combine these measures as well as adjust the system's sensitivity to them. Using this, a probability is calculated that controls the multiplication or death of particles. Moreover, Engelke and Hotz [96] introduced an evolutionary algorithm to highlight the most interesting flow features without an initial sampling of the whole domain. In an iterative process, appropriate streamlines are selected based on a user-defined fitness function. They applied their method to a time-independent aneurysm data set, where complex flow patterns in the aneurysm sac could be detected.

#### *Vessel Wall*

Glaßer et al. [132] generated a global scatter diagram of WSS and wall thickness, where brushed areas in the scatter plot are emphasized on the aneurysm wall. This is extended by a "local" scatter plot that shows only attribute values of currently visible wall parts. Goubergrits et al. [135] calculated averaged WSS vector fields for different groups of patients. Then, streamlines are integrated within each field to extract critical points that together characterize the group.

#### *Lumen+Wall*

To improve the understanding of human physiology in healthy and diseased vessels, a combined analysis of wall characteristics and hemodynamic features inside the lumen is essential. The *FlowLens* by Gasteiger et al. [119] is coupled with a filtering mechanism. The hemodynamic attribute displayed



within the lens area (focus) can be filtered interactively, e.g., the isovalue range of pressure surfaces or surface contour lines for **WSS** depiction. Lawonn et al. [216] provided filtering techniques to explore the internal flow behavior at suspicious surface regions. Based on the wall thickness color-coded on the aneurysm surface, the user can adjust the opacity at thin wall regions to uncover the internal blood flow. Besides, the expert can set two thresholds that control the visualization of near- and far-wall flow via color-coded path line glyphs. Van Pelt et al. [439] used glyph depictions for view-dependent filtering of lumen and wall features. Zooming closer to the wall initiates a shifting of the scope of interest from the lumen to the wall. On zoom levels more distant to the wall, glyphs encoding the internal flow are visualized, which are attenuated by zooming in while at the same time, the visibility and detail of surface glyphs encoding wall-related hemodynamic attributes are increased.

Gambaruto et al. [115] introduced a qualitative and quantitative analysis of flow features that are potentially related to cerebral aneurysm rupture. They extracted **WSS** critical points, vortices and surface shear lines, which are visualized using standard techniques such as spherical glyphs, vortex-isosurfaces, colored inner wall surface, and surface lines with arrowheads. Moreover, other qualitative information such as the *inflow jet*, the size of the *impingement zone* and near-wall flow patterns play a significant role in the investigation of the risk of rupture and the resulting treatment options. Gasteiger et al. [120] presented an automatic detection and visualization of the *inflow jet* and its *impingement zone*. First, an inflow jet seeding curve is extracted by utilizing local streamline properties. Based on this, a boundary contour of the inflow jet is integrated, which is used to identify its impingement zone on the aneurysm wall. Finally, the inflow jet is visualized using a boundary surface or an arrow glyph, whereas an isocontour depicts the impingement zone. Neugebauer et al. [274] developed a qualitative exploration of near-wall hemodynamics in cerebral aneurysms. Several 2D widgets are used to simplify the flow representing streamlines at different positions on the surface. They were particularly interested in near-wall flow at regions of high surface curvature potentially representing prospective rupture sites. Each widget shows the near-wall flow using unrolled and hence, occlusion-free streamlines. Behrendt et al. [27] used information visualization techniques to filter flow patterns. Scatter plots and parallel coordinates are equipped with brushing facilities and linked to a 3D view showing the path line selection in a focus-and-context style. Furthermore, regions on the surface, where a scalar attribute is color-coded can be selected. Based on this, only flow close to the selection is shown. Petz et al. [294] and Pöthkow et al. [303] presented the extraction of vortex cores and critical points from uncertain time-varying flow fields and **WSS** vector fields. They applied their approach to an ensemble simulation of a cerebral aneurysm data set. The spatio-temporal development and stability of critical points probabilities provide information that domain experts considered as essential to assess the rupture risk.

#### 4.2.4 Temporal Analysis

More general works dealing with the visualization of time-dependent data [5, 7, 262] categorized existing visualization techniques according to the characteristics:

- of the time axis,
- of the data itself,
- and their representation.

For the former, *time points* and *time intervals*, as well as *linear*, *cyclic* and *branching* time axis, are distinguished. Regarding the data itself, *abstract* and *spatial* data, as well as the number of variables (*univariate* vs. *multivariate*), are distinguished. Here, also the *level of abstraction*, e.g., by calculating aggregated data is considered. For the latter, *static* and *dynamic representations*, as well as their dimension (*2D* vs. *3D*), are distinguished.

Related to this taxonomy, blood flow data are spatial multivariate data with a cyclic behavior, simulated at a specific point in time, where usually multiple cycles are simulated, but only the last one will be post-processed. For their representation, both, static and dynamic, as well as *2D* and *3D* depictions, are used, where also more abstract visualizations such as plot-based techniques are used. In medically, *CFD*, or flow imaging focused literature; side-by-side views are commonly used to support a temporal analysis mostly by visualizing consecutive time steps of the cardiac cycle [102, 413]. Mentally combining these multiple images is a tedious and time-consuming task, which complicates the interpretation. Advanced approaches use animations, where important spatio-temporal features are highlighted over time or generate an integrated static visualization of multiple time steps showing the evolution, e.g., of flow features, in particular, vortices.

##### *Vessel Lumen*

Van Pelt et al. [379] introduced a framework for the interactive exploration of *4D PC-MRI* data. Instead of path line animations, they used specular highlights on path lines and illustrative renderings like arrow-trails to illustrate time-dependent blood flow dynamics. This avoids a shortening of the path lines due to a decrease in the blood flow velocity over time, which could be wrongly interpreted as a reversal of the flow direction. Moreover, van Pelt et al. [378] used elliptical glyphs for particle animation, see Figure 18. A high speed leads to elongated ellipsoids. Furthermore, speed lines indicate the particle trajectory for a limited time, whereby the velocity is mapped to the line width. Visually aligned speed lines indicate that the particle is entirely within the flow field; otherwise, the particle remains near the tissue boundary. Angelelli et al. [13] demonstrated the usefulness of their straightened representation of the aorta using temporal flow analysis. They juxtaposed up to 13 streamline visualizations showing consecutive time steps of the cardiac cycle to illustrate the temporal evolution of the flow pattern. Lawonn et al. [215] presented a visualization of animated path lines within cerebral and cardiac vessels, where a shading technique was employed that highlights near-by surface regions. A graphical user interface is available for the visual exploration of path lines, which contains standard media player functions for controlling the animation. Besides, the user can jump to a specific keyframe, which allows an intuitive and fast exploration of the animation. Coppin et al. [75] applied different illustrative rendering styles to simulated blood flow data of cerebral aneurysms for highlighting the most interesting flow features. Side-by-side views are used to show the spatio-temporal evolution of these features.

Köhler et al. [425] projected vortex-representing path lines to a *2D* circular plot that shows the spatio-temporal behavior of present vortex flow in the aorta at one glance. The temporal component of each path line point is mapped to the plot's angle. For this purpose, the plot area is divided into  $T$  equally large sectors, where  $T$  is the number of time steps. Thus, a clock metaphor is used, where the first time step is located at 12 o'clock; the direction is clockwise. The plot's radius encodes the spatial aortic position of the occurring vortex flow. Thus, the plot center corresponds to the approximate aortic valve location, and an increasing radius encodes positions in the aortic arch and



descending aorta. For each plot segment, the mean  $\lambda_2$ -value according to the corresponding path lines is calculated, which is color-coded within each segment. We extended this plot to depict the spatio-temporal behavior of path line clusters representing vortices [432]. For this purpose, also the plot's radius is discretized representing four anatomical aortic regions. Afterward, for each cluster, the corresponding segments are determined and dyed according to the cluster color, see Figure 17. Köhler et al. [194] introduced a feature-driven approach to generate videos, that slows down the animation time if interesting features such as vortical flow are visible. In contrast, the animation time for frames that represent an uninteresting flow is accelerated. For this purpose, a feature visibility function is evaluated for each frame, and the result is used to adapt the animation speed.

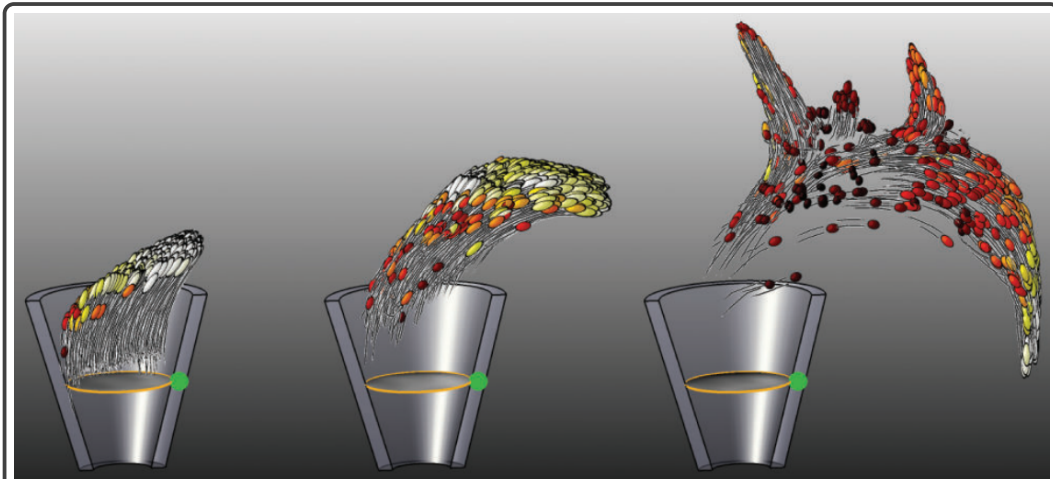


Figure 18: Illustrative particle visualization using elliptical glyphs seeded from a virtual probe. Speed lines indicate the particle trajectory for a limited time. (Images from [378].)

#### *Vessel Wall*

Concerning the vessel wall, Van Pelt et al. [439] designed surface glyphs, called *flower glyphs*, showing the temporal development of *WSS* for different stent configurations over the cardiac cycle in a static view. For each stent, circles for a user-defined sub-sampling of the time domain are drawn, whose areas are scaled concerning a regional *WSS* mean. Furthermore, the circles are connected with time variation strips to encode the entire domain. Glaßer et al. [129] compared three visualization techniques to depict *WSS* in cerebral aneurysms over the cardiac cycle. They used statistical visualizations of time-varying *WSS* values as well as animated and static color-coded depictions at peak-systole. They recommended employing statistical or animated visualizations for the detection of elevated time-dependent *WSS*.

#### *Lumen+Wall*

Simultaneous analysis of interesting wall and flow features during the cardiac cycle is a challenging task due to the visual complexity and occlusion problems. Lawonn et al. [216] presented a framework for an occlusion-free blood flow visualization combined with wall thickness information. For this purpose, they introduced dynamic cutaway-views, where animated path lines of near-wall flow become visible over time, and wall thickness in relation to near-wall flow can be investigated. Another possibility to support the analysis of time-dependent data is a capable camera control including an adequate viewpoint selection. Neugebauer et al. [274] augmented their 2D display of suspicious near-wall flow by standard media player features to iterate over time. Besides, they integrated an automatic animation consisting of appropriate viewpoints in 3D+t to accelerate the inspection of suspicious regions and their flow patterns.

#### 4.2.5 Comparison

Literature, focusing more on medicine, CFD, or flow imaging, supports the comparison task solely by arranging two visualizations in a side-by-side view [12, 117, 209]. Its interpretation is tedious and time-consuming. Advanced visualization approaches are based on an integrated comparative visualization or use more abstract representations of the spatial domain. They aim at comparing medical flow data before and after a virtual treatment procedure, among different treatment scenarios, across patients, and originating from CFD simulation and medical imaging.

##### *Vessel Lumen*

Oeltze et al. [282] proposed linked side-by-side views of flow field partitioning results generated before and after the virtual stenting of a cerebral aneurysm and for different stent locations. Linking is achieved by coupling the camera parameters of the different views. Goubergrits et al. [136] analyzed the effect of coiling in an aneurysm model. An integrated bicolored streamline visualization of the flow before and after coiling was generated as well as of different coil packing densities. De Hoon et al. [79] proposed glyph-based depictions to visually compare measured and simulated aortic flow. Measured vectors are represented by gray vector glyphs, while the simulated vectors are colored according to the vector difference concerning the orientation angle. Moreover, path lines extracted from the measured data are depicted in gray while those traced in the simulated data are color-coded according to the Hausdorff distance between the path line sets. Saalfeld et al. [323, 324] used an approximate blood flow model for their sketching approach of vascular pathologies and treatment options. Their method supports the comparison, e.g., of different stent lengths or coil packaging densities since the simplified model allows to update blood flow with interactive frame rates if the sketch was modified. Angelelli et al. [13] generated a standardized straightened representation of the aorta which would simplify the comparison of flow across multiple patients in a cohort study.

The comparison task can be simplified by using abstract 2D representations of the interesting spatial domain, which are created by employing a standardized anatomy-driven subdivision scheme. Köhler et al. [425] designed an abstract 2D plot of the spatial aortic domain. They employed it to compare the temporal development as well as vortex strength across patients using side-by-side views of multiple plots. Since the criterion has no fixed minimum, the user has to define a minimum  $\lambda_2$ -value. Based on this, the  $\lambda_2$ -value is scaled and clamped to [0,1], which is color-coded in the 2D plot. The closer the selected minimum is to 0, the more sensitive the visualization is towards vortex flow.

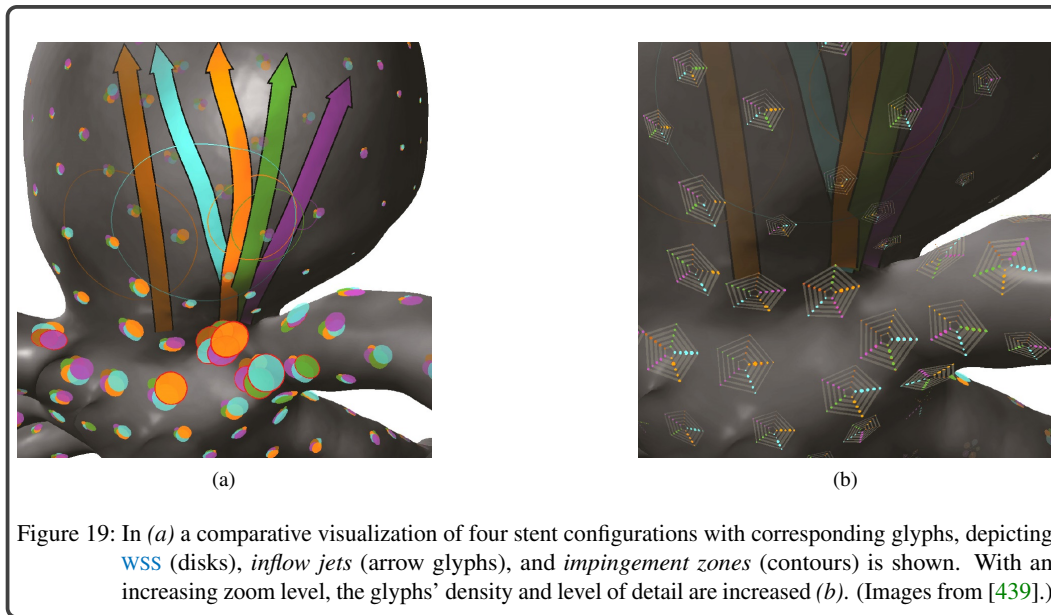
##### *Vessel Wall or Lumen+Wall*

Goubergrits et al. [135] compared cohorts with ruptured and non-ruptured aneurysms based on a flattening of the wall and group-specific characteristics derived from WSS vector fields.

To support the analysis of wall and flow data, van Pelt et al. [439] developed a comparative visualization of *inflow jet*, *impingement zone*, and WSS for the simultaneous investigation of an untreated aneurysm and up to four virtual stenting scenarios, see Figure 19. For the extraction of *inflow jets* and the *impingement zones*, the automatic approach by Gasteiger et al. [120] is used. They are visualized by arrow glyphs and surface contours, respectively and their color encodes the configuration ID. Flower glyphs are employed to jointly encode the WSS of the untreated case and the stenting configurations. The flower glyphs are drawn at evenly distributed locations on the vessel surface. Depending on the zoom level, the glyph density, as well as their level of detail, are adapted.

#### 4.2.6 Context Visualization

In the scope of medical flow visualization, the depiction of the surrounding vascular system equals an embedded surface visualization problem. As internal flow is strongly influenced by enclosing structures (e.g., vessel or an aneurysm) it is often necessary to represent both simultaneously to support the spatial orientation and to facilitate the correlation of flow and morphology, which contributes to understanding the initiation and progression of pathology. To avoid visual clutter and occlusion,



the enclosing structure needs to be visually de-emphasized. This is often made possible by the use of transparency. In psychology, the perception of transparency has been studied for decades. Metelli et al. [251] presented one of the first physical models to describe the visual perception of transparency, which is similar to the "blending" function used in computer graphics. Thus, literature focused on medical, CFD or flow imaging shows mainly an embedding of the flow in a semitransparent surface visualization of the vascular system [12, 115], see Figure 20a. The semitransparent depiction, however, hinders the interpretation of shape, the perception of depth, and suffers from visual clutter through various anatomical parts whose projections overlap in the image. Fleming and Bühlhoff [105] identified several factors like shadow, lighting, contrast, and color as critical visual cues to reveal transparency. Gerbino et al. [124] showed that luminance is an essential channel in conveying transparency information. Singh and Anderson [348] extended this theory by integrating contrast to evaluate the transparency of layers in images. To enhance transparency, visual hints are frequently used that emphasize the luminance profile of the image. For example, the combination of lighting and color [395] can be used to achieve clear luminance and contrast with transparent structures.

Based on these more general findings of transparency perception, three classes of advanced approaches dealing with the problem of embedded surface visualization have emerged:

- front face removal,
- adapted/augmented transparency, and
- contour rendering.

Flow in the vicinity and inside a cerebral aneurysm is commonly integrated into a representation of the near-vessel wall. This visualization can, in turn, be embedded in a contextual representation of the entire cerebral tree (near- and far-context). A depiction of aortic hemodynamics is embedded in a contextual representation of the aorta and references to the outgoing arteries (near-context) or the ventricles and coronaries (near- and far-context).

#### *Near-Context*

Gasteiger et al. [122] combined several rendering styles to show the influence of the surrounding vascular and aneurysm shape on the internal blood flow. Depending on the view-angle, the transparency of the front faces is adapted to provide an occlusion-free depiction of internal blood flow-representing streamlines, where visual shape hints about the enclosing surface are maintained. To facilitate depth



perception, local shadows and atmospheric attenuation are applied to the visual representations of the vasculature and internal flow. Van Pelt et al. [380] coupled these techniques with a comic style rendering of the back faces [379] for an investigation of the flow in the great heart vessels. Saalfeld et al. [324] combined a physically-based shading based on the idea of energy conservation with a view-dependent transparency adaption of the vasculature to increase visual realism and subsequently support depth perception. Inspired by the suggestive contour measure [80], Lawonn et al. [215] presented an illustrative surface visualization, see Figure 20b. Based on the local curvature of the surface, the transparency is adapted, which visually emphasizes convex and concave regions. Furthermore, they used shadows and blurring effects to improve the perception of depth and spatial relations to distant branches. Similar to the suggestive contour measure [80], Jankowai et al. [167] employed illustrative techniques to improve the spatial perception of the heart anatomy by visually emphasizing silhouettes and contours of the heart vessels and chambers.

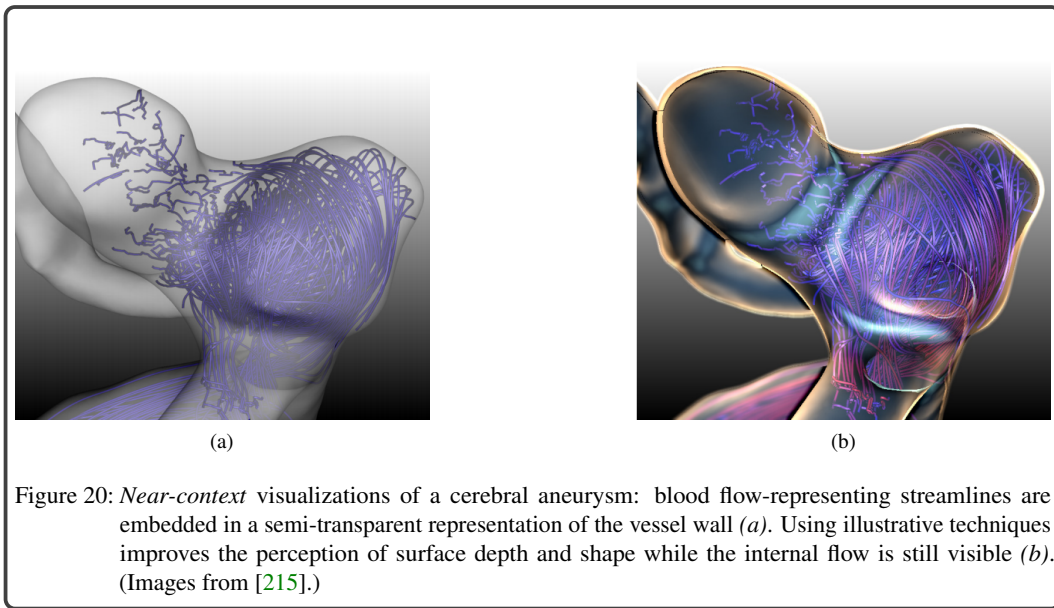


Figure 20: *Near-context* visualizations of a cerebral aneurysm: blood flow-representing streamlines are embedded in a semi-transparent representation of the vessel wall (a). Using illustrative techniques improves the perception of surface depth and shape while the internal flow is still visible (b). (Images from [215].)

If the goal is to show specific flow structures, the embedding problem can be solved by removing the front faces of the enclosing vascular system. De Hoon et al. [79] applied a *toon shading* to aortic surface representations, where the front-faces culling was applied to make the internal flow visible. Köhler et al. [425] linked their 2D plot-based visualization of vortical flow to a path line rendering of the corresponding vortex embedded in a 3D surface depiction of the aorta with culled front faces. Behrendt et al. [29] transferred the effect of front face culling to direct volume visualization of vascular structures. While for indirect volume visualizations, the relation between the normal of the polygonal surfaces and the view direction is employed to remove front faces, whole parts of the vessel volume must be removed to achieve a similar effect for direct volume visualizations. For this purpose, they proposed an automated ray-sampling algorithm, where the points of entering and leaving the vessel are tracked along each casted ray.

Instead of using line renderings, surface representations or direct volume renderings of the internal flow can be used to depict flow-specific properties. Since this visualization style fills the entire vessel lumen, the shape of the vessel is already implicitly depicted. Thus, an additional highlighting of the silhouettes is sufficient to represent the anatomical context. Kuhn et al. [199] clustered 3D steady flow fields into areas of similar behavior. For each cluster an enclosing surface is constructed, where these surfaces fill great portions of the lumen, depending on the applied similarity measure. Thus, a simple rendering of the outer vessel contour is used to convey the course of the vessel where no clusters are drawn. Schumann et al. [339] employed an adapted *maximum intensity projection (MIP)* approach to depicting pressure fields within the cerebral and cardiac arteries with the aim of visually perceive areas of low and high pressure. Similar to Kuhn et al. [199], only outer-contours are emphasized to

depict the vessel shape, as the entire vessel lumen is visually filled. Lawonn et al. [214] extended the outer-contour rendering by a curvature-based streamline depiction to improve the shape perception of the vascular context. Moreover, streamlines are seeded on the vessel surface, where a maximum or a minimum of a calculated curvature field occur to generate local hatching. More recently, Behrendt et al. [28] combined the commonly used *Pseudo Chromadepth* rendering with a discretized color scale to visualize a hemodynamic attribute such as *WSS* on the aneurysm surface. It is based on a *Fresnel*-inspired blending mask, where depth hints given by the *Pseudo Chromadepth* are maintained.

#### *Near- and Far-Context*

Near-context visualizations focus on representing functional relationships between focus and context objects. In contrast, the addition of a distant context is intended to indicate how the structure of interest is positioned in the body or linked to surrounding systems. Thus, the depiction of the far-context concentrates on the representation of the overall shape and orientation instead of local surface features. Since adding more context also reinforces the embedded visualization problem, cutting, filtering, visual and dimensional reduction are typical approaches to avoid visual clutter and occlusion.

Hastreiter et al. [147] presented a *DVR* approach of cerebral aneurysms together with the cerebral arterial system for a fast localization and classification of an aneurysm, which supports diagnosis and intervention planning. Volumetric rendering of the skull provides further hints about location and orientation, where axis-aligned clipping planes avoid occlusions of an aneurysm. Van Pelt et al. [378] used a temporal *MIP* as input for a volume rendering of the morphology of cardiovascular tissue. This provides a clean, filtered representation of the vessel context and reduces visual distraction. Within the vessel lumen, a virtual probe is placed to track the internal blood flow. To avoid occlusions from the vascular context, it is clipped along the parallel plane of the probe.

Another possibility to avoid visual clutter and occlusion within volume renderings of the vascular far-context is filtering. The filtering should be mostly automatic to ensure an efficient generation of far-context visualizations. Neugebauer et al. [271] filtered larger cerebral arteries automatically based on common assumptions about their location within the skull to generate volumetric far-context visualizations for cerebral aneurysms. Besides, distance-based filtering is applied to depict smaller structures in the vicinity of an aneurysm. Kersten-Oertel et al. [181] evaluated different methods to improve the depth perception of filtered volumetric vessel data, where the most promising results were delivered by fog, local shadows, and color-coding the distance to the viewer. For a better perception of small vessels, vesselness filters can be applied. Joshi et al. [170] presented an adapted filter that exhibits an improved detection of small vessels compared to a Hessian vesselness filter. As their approach deviates from a pure detection of cylindrical structures, also the branching regions of small vessels are depicted.

During the volume rendering also transfer functions can be applied to filter the data, instead of direct filtering. Standard transfer functions are not able to visually differentiate between the vessel and bone tissue since contrast-enhanced vessel regions exhibit similar intensity values than bones. Thus, far-context regions of a cerebral aneurysm are occluded by using intensity-based transfer functions. To overcome this limitation, Higuera et al. [155] designed a *2D* transfer function that includes gradient magnitudes, which allows a depiction of an aneurysm far-context regions if an aneurysm is located close to the skull base. But the definition of such a *2D* transfer function also adds complexity by introducing another *degree of freedom (DOF)* when generating the far-context visualization. Thus, in [156] an automatic approach for designing *2D* transfer functions is presented. They mapped manually defined transfer functions to the intensity/gradient profiles of new data sets employing elastic deformation.

Besides *DVR*, surface visualizations are commonly used to depict far-context. Due to the explicit description of local surface properties, e.g., direction and curvature, a wide range of rendering styles can be used. A typical approach is to reduce saturation and transparency to avoid visual distraction from the focus visualization. Hennemuth et al. [151] combined a transparent, shaded surface with contour rendering to depict vessels close to the aortic arch. To avoid occlusions of the internal path lines, the arch itself is rendered with low contrast. Van Pelt et al. [379] used *toon shading* together with different illustrative techniques to render contours, which allows a visual differentiation between

vessels and occluded vessel regions. Born et al. [41, 42] augmented a half-toning shading with silhouette-rendering to communicate shape of cardiac far-context vessels. Moreover, shaded, gray backfaces are added to emphasize the near-context and provide a sufficiently contrasting background for the bright-colored streamlines.

Another way to display far-context efficiently is dimension reduction, where 2D slices of the 3D morphology are shown to provide context information. Broos et al [49] aligned a 2D slice concerning the long axis of the heart ventricle, which supports the detection of the left ventricle. For applications that do not focus on a single structure of interest, the slice placement can be interactive. In the work by Hennemuth et al.[151] up to three slices can be added. Their location and orientation are linked with three 2D viewers (axial, sagittal, coronal) that are part of the visualization system. Venkataraman et al. [385] also used three slice renderings concerning the main axes of the original data set. To avoid visual overlap with the central visualization of aortic flow, the slices are arranged in the background, using a cube layout.

#### 4.2.7 Uncertainty Analysis

The visualization of uncertainties in the context of vector/flow data is an active field of research [38, 48]. However, quantification and presentation of the uncertainty of medical flow data have been widely neglected so far. This section describes approaches to visualize and analyze the uncertainty introduced by the generation and processing of medical flow data. The methods either take into account the flow field and use ensembles of simulations or focus on the wall and compare segmentation results based on different imaging modalities or an adjustment of the image parameters, or integrate flow and wall.

##### *Vessel Lumen*

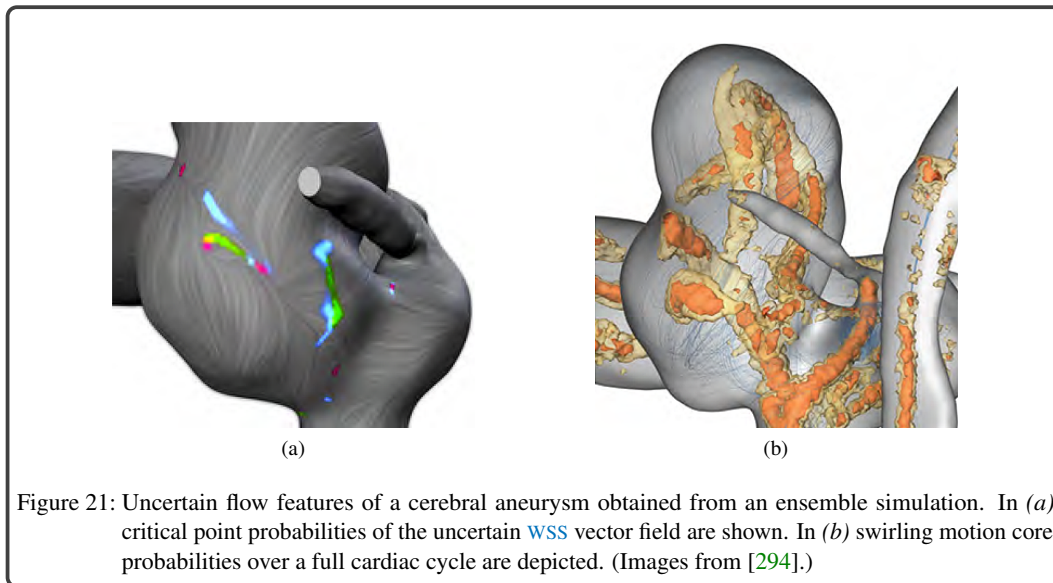
Due to the susceptibility of measured flow data against image artifacts, integral lines may represent wrong paths. Friman et al. [111] introduced an uncertainty quantification of the integration in 4D PC-MRI data. Streamlines and path lines are generated using a probabilistic approach that employs a sequential *Monte Carlo* sampling. The resulting trajectories are visualized with standard techniques such as color-coded integral lines and flow maps. Schwenke et al. [340] computed blood flow trajectories as minimal paths in PC-MRI images based on an anisotropic *Fast Marching* method. Uncertainty in the estimated blood flow vectors is modeled as a tensor, which is used as metric for the Fast Marching. Besides the Fast Marching, a distribution of the flow connectivity is calculated, which is used to identify the most likely flow trajectories. Similar to Friman et al. [111], conventional visualization techniques are employed to depict the resulting uncertainty. Köhler et al. [193] evaluated uncertainties in the context of quantifying the *net flow volume* (NFV) that describes the volume of pumped blood per heartbeat. Medical experts determine the NFV by measuring the flow that passes through a manually placed plane above the aortic or pulmonary valve. However, the calculations are highly sensitive towards the plane's angulation since the orthogonally passing flow is considered. Köhler et al. [193] determined vortex flow as a main cause for quantification uncertainties. They suggested a systematic evaluation of measuring planes with slightly different angulations. This yields a distribution of NFVs, which are illustrated using a box plot-based graph.

##### *Vessel Wall*

Glaßer et al. [127] quantified the influence of different reconstruction kernels in RA on generating 3D geometric aneurysm models for CFD simulations. They compared sharp, normal and smooth reconstructions, where substantial differences occurred regarding branching vessels and vessel diameters. Moreover, the size of the ostium area varied between the reconstructions and shrinking as well as the expansion of small vessels could be observed. To visualize detected differences, standard techniques are used such as semi-transparent surface meshes and statistical depictions that represent calculated error measures.

*Lumen+Wall*

According to the combined analysis of the vessel wall and lumen, Petz et al. [294] presented a feature-based visualization of uncertain time-varying vector fields. The fields are modeled as Gaussian fields, and probabilities for the presence of local features are computed by Monte Carlo integration. This enables a calculation of the spatial distributions of local features, which can be used to display essential structures of the data. Pöthkow et al. [303] extended the approach by Petz et al. [294] from Gaussian fields to more flexible non-parametric models. Both works use nested semi-transparent isosurfaces and surface LIC for generating a quasi-temporal visualization of flow feature probabilities, see Figure 21. In this example, they applied their approach to a cerebral aneurysm data set. Uncertain flow features are depicted over a full heart cycle, where critical point probabilities are depicted in the left image and probabilities for swirling motion cores in the right image.



## 4.3 CONCLUSION

This section concludes with an interpretation of the task taxonomy concerning how well visualization techniques in the spatial scopes support a task. In the cerebral domain, all spatial ranges are addressed while the approaches in the cardiac domain are restricted to the vessel lumen. An apparent reason is that *WSS* can easily be derived from *CFD* while flow imaging in the cardiac domain cannot resolve *WSS* at a high enough spatial resolution. Moreover, aneurysm wall properties were recently determined using experimental intravascular imaging and *FSI* simulations. Regarding the tasks, the best-supported task is the *feature filtering*. A likely reason is that medical and *CFD* research results are linking features such as vortices to the initiation, progression, and severity of pathology. The second best-supported task is the *contextualization* task. This underpins the importance of relating hemodynamics to morphology. About half of the approaches also provide a rendering of the far-context indicating that an additional spatial reference is often useful. The *interactive probing* and *temporal analysis* task are equally often supported. The *spatial overview* and *comparison* task have received a little less overall attention. The *spatial overview* task was more often addressed in the context of cerebral aneurysm hemodynamics. Most of the corresponding approaches incorporate wall-related properties, both of which being harder or impossible to derive from measured *4D PC-MRI* data. In the cerebral domain, the *comparison* task is mostly accomplished to determine the optimal outcome of a virtual intervention while in the cardiac domain, measured and experimental simulated data, patients or time steps are compared. The *uncertainty analysis* task is the least supported. To quantify uncertainty, ensemble simulations must be carried out, or image data must be acquired and pre-processed.

Despite promising works in the field of aneurysm blood flow visualization, more carefully designed focus-and-context views are needed since people tend to perceive local details and global context. Current approaches [121, 318] limit the data exploration to a small area on the surface defined by a lens, where a lot of interaction is needed to get a complete overview of the data. Moreover, qualitative and quantitative exploration needs to be supported. When CFD engineers and physicians gain more experience with the analysis of flow data, quantitative information and related statistics, e.g., flow volumes, flow rates, and turnover times in an aneurysm, get more important. To investigate the local distribution of such numbers along with depicting the corresponding regions of the flow may support decisions more directly. Besides, flow features, e.g., vortices, recirculation zones, and inflow jets, seem to be related to the emergence and progression of pathology. In the context of cerebral aneurysms, such features are often manually extracted or the extraction depends on manually defined inputs such as the aneurysm ostium. To avoid errors resulting from these dependencies, their (semi)-automatic identification and quantification should be more supported. Moreover, methods are needed that focus on their monitoring over the cardiac cycle to support the assessment of flow complexity and stability. Flow visualizations should be coupled with feature extraction, flow filtering, and flow partitioning methods to reduce their visual complexity. Showing only specific features or representatives of homogeneous regions helps in comprehending the flow structure. Furthermore, approaches are needed that generate more abstract 2D representations of the 3D anatomy and combine them with a depiction of wall- and flow-related attributes. Thus, a quick occlusion-free overview of flow attributes and their correlations would be given. Moreover, they can simplify the comparison of groups of subjects and facilitate a cohort analysis. In the following chapters, we address the limitations of current visualization and exploration techniques for cerebral aneurysms and suggest multiple solutions to improve aneurysm rupture risk assessment and treatment planning.

### Part III

## GUIDED EXPLORATION OF ANEURYSM DATA



# Aneulysis - Aneurysm Analysis Framework



This chapter is partly based on:

Monique Meuschke, Tobias Günther, Ralph Wickenhöfer, Markus Gross,  
Bernhard Preim and Kai Lawonn,  
Management of Cerebral Aneurysm Descriptors based on an Automatic  
Ostium Extraction;  
IEEE Computer Graphics and Application, 38(3), pp. 58-72, 2018.





Decision-making to treat a non-ruptured aneurysm can be a challenging task that involves a patient-specific risk analysis. A lot of different aspects seem to influence the aneurysm initiation and progression comprising patient-specific meta information, morphological descriptors, and intra-aneurysmal flow information, recall Section 2.3 and Section 3.5.5. Biomedical researchers try to identify risky configurations of this information to enable more reliable decision-making. However, there are two principal problems of analyzing aneurysm data:

1. Essential features such as morphological descriptors or flow patterns are manually extracted from clinical images and simulation results, which is an error-prone process.
2. Performing large medical studies with different domain experts is challenging since different tools with inconsistent data formats are used.

Thus, time is wasted to augment acquired data with meta information manually. This highlights the need for standardized and guided techniques to analyze these highly complex data. Equally important are software solutions that integrate such methods into easy-to-use workflows.

To address the **first problem**, methods for the computer-aided extraction of morphological descriptors of aneurysms were developed, recall Section 3.3. However, these methods fail for more complex aneurysm shapes such as wide-neck aneurysms. Besides, some research groups use in-house tools to compute the aneurysm size or diameter automatically [84, 211]. However, these tools need manually extracted input data, e.g., the centerline.

To address the **second problem**, some method focus on structured documentation systems of clinical data. In clinical practice, reports describe the patient's state, diagnosis, and treatment recommendations, and serve for communication between referring clinicians. Due to their free-text form, they generally lack structure and readability, which complicates the data analysis and interpretation. To improve this, *structured reports* were developed. The basic idea of such systems is to provide pre-defined data entries. Karim et al. [177] offered clinical information using a web-based application to generate structured reports for aortic aneurysms. For this purpose, different graphical widgets, e.g., drop-down menus, diagrams or pre-defined images are used. Wibmer et al. [406] presented a standardized diagnostic certainty lexicon for reporting the likelihood of prostate cancer, which prevents miscommunication and supports clinical decision-making. With this, the number of expressions used by radiologists to indicate their levels of diagnostic certainty was reduced. Pankau et al. [291] developed a 3D documentation system that allows a standardized reporting for head and neck cancer including the tumor staging. The role of visual elements, e.g., standardized and individualized screenshots, was emphasized by the physicians.

More advanced methods support the collaborative analysis of medical data sets by using visual analytics techniques. To manage large volume segmentations in neuroscience, Ai-Awami et al. [4] presented a web-based system in which users have different permissions to edit and verify results. Bannach et al. [24] combined medical image analysis and *radiomics* with visual analytics to build, filter, analyze, and evaluate patient cohorts. With radiomics, quantitative image features are determined, which are complemented with additional metadata like the patient's age and gender. For several years there is a growing interest in radiomics. Radiologists try to define image markers in a similar way like genomics and proteomics add to diagnosis and disease understanding. Filter masks are provided to determine cohorts that should be statistically analyzed. The main disadvantage of existing systems is that they are concentrated on the analysis and structured management of clinical image data. However, to investigate cerebral aneurysms, simulated data or geometry data has to be included.

Therefore, the software *Aneulysis* was developed. It was designed to improve the aneurysm risk assessment and treatment planning. For this purpose, we discussed the current research workflow to analyze aneurysm data with neuroradiologists and CFD experts. Based on the summarized limitations

of existing visualization techniques, recall Section 4.3 and occurring difficulties during the analysis, requirements are derived that should be fulfilled to improve aneurysm data evaluation, see Section 5.1. Before the general structure of *Aneulysis* is introduced in Section 5.3, Section 5.2 describes the necessary pre-processing steps according to the simulation and measurement of flow data, which are not part of *Aneulysis*. Besides, an overview of used data sets within this thesis is given. Section 5.4 describes the workflow of *Aneulysis*, which comprises creating, editing and searching of cases, as well as more advanced analysis and visualization techniques such as automatic extraction of morphological descriptors (Section 5.5). To assess the general suitability of *Aneulysis*, we performed different evaluations, where the results are presented in Section 5.6. Finally, current limitations and future improvements are discussed in Section 5.7 and Section 5.8.

## 5.1 TASK-BASED REQUIREMENTS OF ANEURYSM DATA EXPLORATION

We closely cooperated with two neuroradiologists (16 and 25 years of work experience), who regularly treat cerebral aneurysms, and two engineers working on CFD simulations for cerebral aneurysms (five and eight years of work experience). The goal of the neuroradiologists is to assess the rupture risk, which requires a better understanding of risk factors. This also includes a comparison of ruptured and non-ruptured cases. In contrast, for the CFD engineers, it is important to validate the physical plausibility of the simulation results. For this purpose, they analyze fluid-wall interactions by exploring scalar quantities on the vessel wall and try to find spots of interesting combinations. This verification process also includes a determination of the most dominant flow patterns based on different boundary conditions for simulation. Furthermore, we asked them about the importance of analyzing flow patterns over the cardiac cycle. The CFD experts stated that in most cases, first, steady simulations are performed, because such simulations are useful for spatial convergence tests and significant aspects of aneurysmal hemodynamics can be inferred from a steady flow. Unsteady data can provide additional information, which is likely to be more important in larger aneurysms where optimal treatment needs to be found. However, the experts stated that it is not clearly known at which point in the cardiac cycle the rupture risk is maximum and thus, exploring only a single time step is not sufficient.

Both types of experts use similar concepts and techniques to manage and analyze aneurysm data. For each aneurysm data set, different kind of information for different points in time, i.e., pre- and post-operative data, are available. The data is stored on a *File Transfer Protocol (FTP)*-server, where quantitative information such as morphological descriptors are stored in Microsoft Excel tables. Morphological descriptors are determined manually from 2D image slices using clinical software, or from 3D surfaces using the open-source software *ParaView*. Both procedures are described as time-consuming by the experts. *Paraview* is also used to manually extract the aneurysm ostium, which requires a tedious placement of cut planes and to analyze simulation results. Scalar measurements, e.g., WSS or pressure, are color-coded on the 3D vessel surface to examine the aneurysm state. Additional blebs are of particular interest, recall Section 2.3.3. However, the experts consider the sole presentation of a 3D model as not sufficient since important information can be occluded. Due to the complexity of the surface, a series of manual rotations is necessary to gain a complete overview. The time-dependent behavior of the data further enhances the manual exploration effort, because it is almost impossible to find critical regions during animation since the rotation process itself needs a certain amount of time. Besides scalar quantities mapped to the vessel wall, the blood flow is depicted either by streamlines or by path lines as an animation over the cardiac cycle. Based on such standard flow visualizations, experts manually classify flow patterns according to pre-defined types such as in the study by Cebal et al. [60], which allows for a more detailed analysis of the flow behavior. However, this is a time-consuming process with high inter-observer variability. Visual clutter makes the classification error-prone. Since the surface morphology and flow behavior influence each other, the experts stated that an integrated view of both characteristics is needed. At the moment, the aneurysm surface is depicted semi-transparently and animated path lines represent the internal blood flow. However, this makes it challenging to identify relationships between surface characteristics and internal flow patterns.

Besides the individual exploration of aneurysm data by one expert, our domain experts stated that a collaborative analysis is essential to improve the exchange of information. However, to analyze the data collaboratively is challenging, because no consistent storage structure exists. Moreover, searching for specific cohorts is cumbersome, e.g., female patients with a ruptured aneurysm larger than 7 mm. However, this is relevant for medical studies to investigate risk factors.

In Section 4.2 a comprehensive overview of current visualization techniques according to seven pre-defined tasks is given. Besides, Section 4.3 summarizes the limitations of existing methods concerning supporting these tasks. Regarding the visualization of aneurysm data, the spatial overview, the feature filtering, the temporal analysis, the comparison, and the contextualization task should be stronger supported. Based on this and the discussions with our domain experts, we summarize significant requirements as follows:

**Req. 1 A CONSISTENT AND EFFICIENT DATA MANAGEMENT.** A consistent structure for data management is needed that allows fast integration of new data sets, including different meta information and data files. It should be flexible to incorporate new data types if necessary. Moreover, information about existing data sets should be easily editable, and filter techniques are needed to select cohorts according to specific criteria.

**Req. 2 AUTOMATIC FEATURE EXTRACTION.** The *feature filtering task* should be supported by automatic methods to compute morphological descriptors as well as to extract and classify qualitative flow features, which ensures comparability and reproducibility of the results.

**Req. 3 A COMPARISON OF DATA SETS.** The *comparison task* must be supported more strongly by enabling comparison of ruptured and non-ruptured data sets as well as pre- and post-treated data including different stent scenarios to improve risk assessment and decision-making.

**Req. 4 SIMPLIFIED VISUALIZATIONS.** To better support the *spatial overview task*, simplified depictions of the aneurysm morphology, and internal flow information are needed that reduce the complexity of 3D time-dependent aneurysm data.

**Req. 5 INTEGRATED FLOW VISUALIZATIONS.** Aneurysm flow data comprise scalar, vectorial and tensor information. To better support the *contextualization task*, this information should be visualized in an integrated manner to allow a detailed analysis of possible rupture-prone configurations.

**Req. 6 ANIMATIONS FOR DATA EXPLORATION.** To improve the *temporal analysis*, the exploration of the time-dependent aneurysm data should be supported by animations. An automatic camera movement passing interesting vessel regions should be provided.

**Req. 7 COLLABORATION TOOLS.** For collaboration purposes, it should be possible to set landmarks in different animation steps. An external researcher should be able to analyze the regions around the landmarks and discuss them with other colleagues.

## 5.2 DATA ACQUISITION AND PRE-PROCESSING

In this thesis, 26 aneurysm data sets were used. In the Chapters 5 - 7 describing the visualization concepts of *Aneulysis*, a subset of these data sets is used since not all data sets were available from the beginning of the development. The respective data sets are referenced in every chapter based on Figure 22. A total of 24 cerebral aneurysm data sets (C3 - C26) were available, where one aneurysm has a fusiform shape, and the remaining aneurysms have a saccular shape. Moreover, two cases with a fusiform aortic aneurysm (C1 - C2) are considered in Chapter 6 to show the applicability of a novel parametrization approach. Table 1 summarizes relevant information about the aneurysm data sets such as their location, shape, rupture status, type of flow data and if virtual stenting was performed.

In the following, the data acquisition and pre-processing steps to simulate the flow within cerebral aneurysms are described. Moreover, the measuring of cardiac flow data is shortly recapped due to the used fusiform aortic aneurysms. However, we just used the surface mesh since fusiform aneurysms are usually treated surgically due to occurring symptoms. So, in the past, the assessment and analysis of blood flow data played a minor role.

### 5.2.1 Simulated Flow Data

The principle pipeline to simulate cerebral blood flow was described in Chapter 3 comprising the image acquisition, the surface reconstruction, the calculation of flow data and the virtual stenting. For all cerebral data sets, CFD simulations are performed. Besides, for some non-stented data sets, we performed FSI simulations. In the following paragraphs, details about the used methods for each of these steps are given.

**Image acquisition.** First, clinical image data comprising CTA, MRA, and DSA of the aneurysm morphology are acquired. The clinical images have a size of  $512 \times 512 \times 256$  voxels in the x-, y-, and z-direction with a spatial resolution of  $0.35 \times 0.35 \times 0.9 \text{ mm}^3$ .

**Surface reconstruction.** Based on the image data, the vessel surface is reconstructed using the pipeline by Mönch et al. [257]. Due to the used contrast agents or special sequences, the images exhibit high vessel-to-tissue contrast. This facilitates the usage of a threshold-based segmentation followed by a connected component analysis to separate an aneurysm and its parent vessel from the surrounding tissue. The 3D vessel surface is extracted via *Marching Cubes* [229], applied to the segmented image data. To prepare a geometric model as input for the flow simulation, it is necessary to manually correct artifacts (details can be found in [257]). For our cerebral data sets, the resulting mesh resolution for the entire vessel surface varies between 19.261 and 45.827 triangles, and the resolution of the aneurysm surface part varies between 2.096 and 8.582 triangles. Moreover, the mesh quality was optimized by a combination of metric and topological changes such as edge collapses and edge flips [337]. The results are evaluated by one of the neuroradiologists to ensure anatomical plausibility. Based on the optimized mesh, a hybrid volume mesh was generated as input for the simulation.

**Virtual stenting.** To simulate different treatment scenarios, a fast virtual stent deployment approach was chosen [30]. This explicit methodology allows for the consideration of each stent strut and is superior compared to other approaches, e.g., based on a porous medium that represents the stent. Due to the usage of geometric deformation, this method can be applied within seconds without being computationally expensive. Due to the absence of simulation results after neurosurgical clipping, the integrated visualization methods of *Aneulysis* aim at supporting endovascular treatments.

**CFD simulation.** The pre- and post-treated mesh configurations were spatially discretized using a combination of tetrahedral and prismatic cells as input for the CFD simulation. An appropriate grid size was chosen to obtain simulation results that would not be significantly changed by an improvement in resolution (mesh-independent results) [163]. The number of cells of the volume meshes ranged from 1.11 - 2.01 million and 5.2 - 8.3 million for the pre- and post-stented cases, respectively. Based on the FVM, the conservation of mass and momentum is solved locally within each time step. For this purpose, blood is assumed as an incompressible Newtonian fluid with a density of  $1055 \text{ kg/m}^3$  and a dynamic viscosity of  $0.004 \text{ Pa} \cdot \text{s}$  [332]. Flow measurements of a healthy volunteer are used as inlet boundary conditions [33] due to the absence of patient-specific data. Zero pressure boundary conditions were applied at each outlet cross-section. Moreover, a rigid wall is assumed for the vessel and the stent. In every case, three cardiac cycles with a time step size of  $\Delta t = 0.001 \text{ s}$  are calculated. To avoid inaccuracies from initialization, only the last cycle was used for analysis. Hemodynamic simulations were carried out using the solver *STAR-CCM+ 11*. All calculations are performed on a standard workstation (using four Intel Xeon E3 cores with 3.3 GHz and 32 GB *random-access memory* (RAM)) and lasted between 2 and 8 h, depending on their complexity.

**FSI simulation.** Addressing the FSI simulation, every aneurysm is divided into two subdomains: the fluid and solid domain. Hemodynamic aspects inside the fluid domain are numerically solved

using [CFD](#). Furthermore, structural simulations are performed to include the vessel wall behavior. For this purpose, the deformable wall is considered as homogeneous, isotropic and linear elastic. The Young's modulus (1 m Pa) and Poisson's ratio (0.45) are taken from [\[374\]](#). Wall thickness is set in the range of 0.2 to 0.6 mm obtained by normal extrusion of the wall [\[374\]](#), because such data cannot be extracted yet from radiologic image data. To prevent rigid body motion, the vessel in- and outlet cross-sectional planes are fixed. Other domain parts have no movement restrictions. Using the [FEM](#), the relation of deformation, mechanical strain, and mechanical stress is solved locally for each finite element, based on the conservation of momentum. The deformation of the solid domain reacts on the fluid domain and therefore on the flow characteristics, inducing a complex coupling of both domains. This coupling is located at the interface, the intersecting surface of fluid and solid. Thus, [FSI](#) is implemented as data transfer at the interface, exchanging fluid pressure as well as [WSS](#) and wall displacement, respectively as updated boundary conditions at defined time steps.

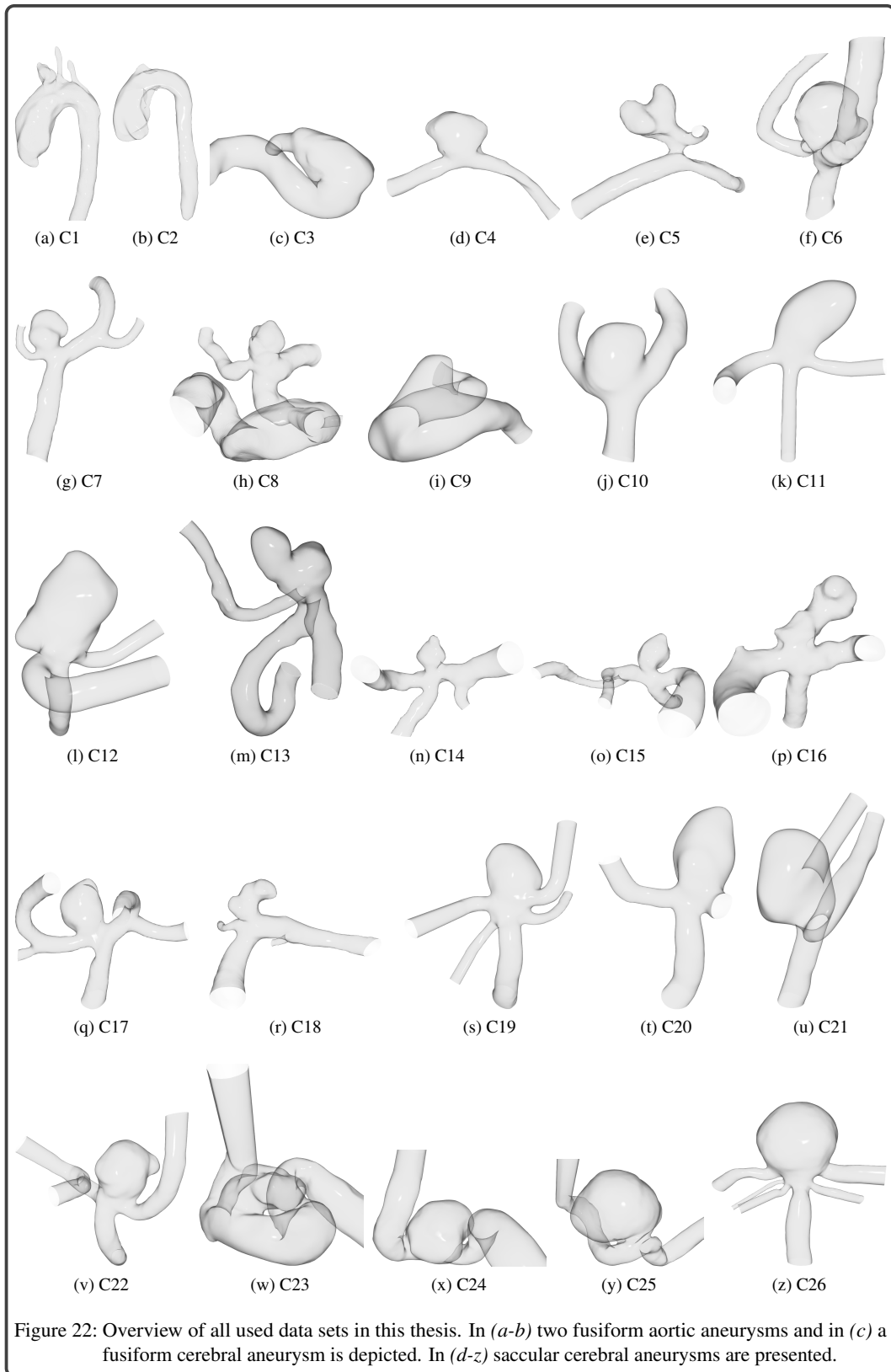
**Post-processing.** This includes the mapping of cell-based variables to the vertices of the surface mesh. Moreover, path lines are integrated with an adaptive fifth order Runge-Kutta method on the ostium to assess the aneurysm inflow. The integration is performed every 0.01 s. This is necessary since a path line usually does not exist during the whole cardiac cycle due to the high velocities (up to 1.51 m/s) and the small spatial domain size (5 - 15 mm in the x, y, z-direction). For seeding, the centers of the ostium triangles are used resulting in a homogeneously distributed number of vertices [\[273\]](#). The integration terminates if the current line leaves the spatio-temporal domain. Finally, the ostium surface is used to remove path line parts outside an aneurysm that are not relevant for the upcoming classification and visualization methods.

### 5.2.2 Measured Flow Data

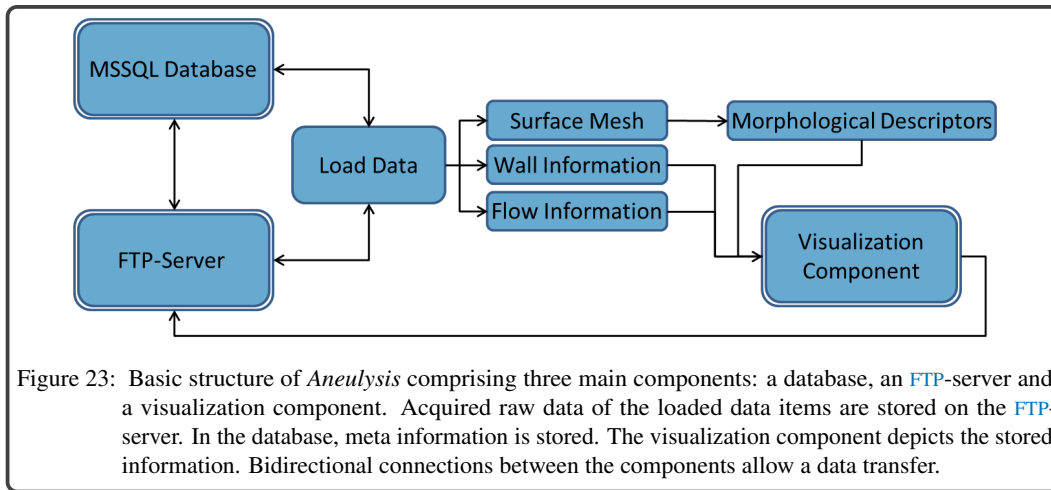
Blood flow data of the aorta are acquired by performing [4D PC-MRI](#) using a 3 T Siemens Magnetom Verio [MR](#) scanner with a maximum expected velocity of 1.5 m/s per dimension. For each direction (x, y, and z), time-resolved flow and magnitude images are determined to describe the direction and strength of the flow, respectively. For the spatial domain, 15 to 23 slices are acquired with a grid size of  $132 \times 192$  voxels covering  $1.77 \times 1.77 \times 3.5$  mm<sup>3</sup>. Between two of the 14 to 21 time steps, a distance of 50 ms exists. Artifacts in the flow images, considering *Phase wraps* [\[85\]](#) and *velocity offsets* [\[204\]](#) are corrected using the magnitude images. Then, a *temporal maximum intensity projection* ([tMIP](#)) is calculated as the basis for a binary segmentation. For each voxel, the flow velocity is considered, and the maximum is taken from all time steps. This leads to a good contrast everywhere where fast flow over time occurs. This reduces the [4D](#) image to a high-contrast [3D](#) image. From this [3D](#) image, the vessel surface is extracted via *Marching Cubes* [\[229\]](#). For our aortic data sets, the resulting mesh resolution for the entire vessel surface varies between 11.350 and 13.592 triangles, and the resolution of the aneurysm surface part varies between 5.102 and 6.571 triangles. For a more specific and in-depth introduction to the data generation pipeline, data quality insurance, and quantitative analysis methods of measured cardiac flow data, we refer to the survey of Köhler et al. [\[188\]](#).

Table 1: Summarizing information about the used data sets.

Case (C)	Location	Shape	Ruptured	Flow Data	Virtually Stented
1-2	aortic	fusiform	non-ruptured	measured	non-stented
3	cerebral	fusiform	non-ruptured	-	-
4-13	cerebral	saccular	non-ruptured	simulated	non-stented
14-22	cerebral	saccular	ruptured	simulated	non-stented
23-25	cerebral	saccular	non-ruptured	simulated	stented
26	cerebral	saccular	ruptured	simulated	stented







### 5.3 GENERAL STRUCTURE

*Aneulysis* is a *Windows Forms application*, which is a toolkit of the *Microsoft .NET Framework* to design *graphical user interfaces (GUIs)* and written in C#. Basically, it consists of three components: a database, an **FTP-server** and a visualization component, see Figure 23. For the database, a *Microsoft SQL Server* is used, where the *Microsoft .NET Framework* provides extensive functionality to built up a connection between the **FTP-server**, the database and **GUI** of *Aneulysis*. For rendering, the *open toolkit library (OpenTK)* is used, a C# graphics library that provides access to graphics tools contained in the *open graphics library (OpenGL)*. Moreover, *OpenTK* provides multiple helpful data types such as **3D** vectors, **4D** vectors, and matrices with specialized functionality for specific dimensions, such as cross-product for **3D**.

The acquired raw data and data representations derived from it are stored on the **FTP-server** using a consistent structure that avoids redundancy shown in Figure 24. For each patient, a new case is created on the server, with pre- and post-treated data that is organized in studies. Each study comprises four information elements: scanner data comprises different image modalities such as **CTA** and **MRA** data. Geometric information is stored in reconstruction data, e.g., the ostium and centerline. Moreover, flow simulations are stored, for either single (steady) or multiple (unsteady) time steps. Different formats such as *Ensign* or *OpenFoam* are distinguished. Here, also integration results in the form of stream or path lines are stored. Media data contains characteristic images or videos, e.g., showing wall regions with higher risk.

Furthermore, metadata is stored for the cases, studies and corresponding data items in the database. This includes, e.g., the study type (patient or proband), gender and age. Besides, more detailed information about the pathology, e.g., the location of an aneurysm, the number of existing aneurysms or information about rupture and treatment are collected in the database.

There are three types of data for a selected data set: a surface representation showing the vessel morphology, wall-related information comprising scalar, vectorial and tensor data defined on the vessel surface and flow-related information specified within the vessel lumen describing the internal blood flow. These three types of data are used as input for the visualization component, where from the surface representation morphological descriptors can be derived. The visualization component consists of different visualization modules, which allow a detailed visual analysis of the three types of data. Moreover, each visualization module communicates with the database and the **FTP-server** to store results such as images or landmarks from the interactive exploration.



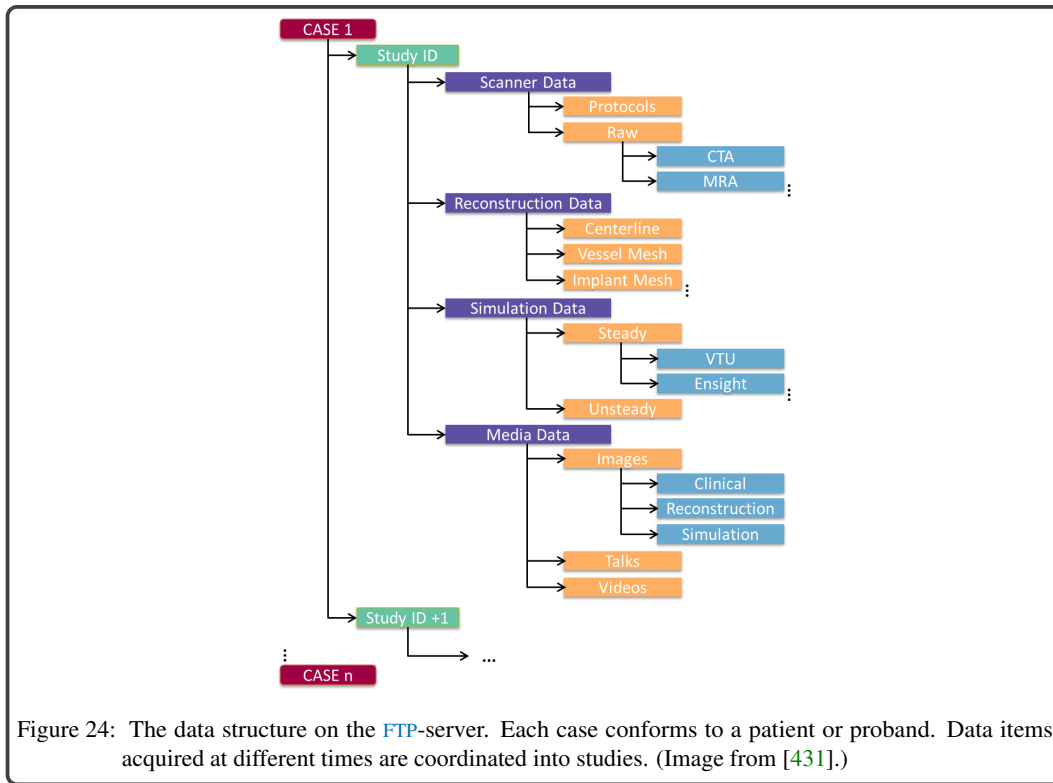


Figure 24: The data structure on the [FTP-server](#). Each case conforms to a patient or proband. Data items acquired at different times are coordinated into studies. (Image from [431].)

## 5.4 WORKFLOW

This section summarizes the principle workflow of *Aneulysis*. A primary concern during its development was to provide a *guided workflow*, where domain experts with different professional background are able to analyze data sets collaboratively. The guidance aspect was realized on the main screen, where different processing screens are successively enabled depending on the previous action of the expert. The collaboration aspect was realized by the redundancy-free management of data sets, and previously detected findings can be displayed during data exploration using the visualization modules.

If *Aneulysis* is started, the user has to enter login information comprising a username and password. When a new user needs access, first an account has to be created containing a name and email address as well as entering a master password to protect the system from unauthorized access. Afterward, the user gets access to the main screen, see Figure 25. Here, an overview of existing cases using a tabular representation is given. Besides basic information, a preview picture on the aneurysm is shown, generated with our method to calculate appropriate viewpoints (see Section 6.4.2). At this point of the analysis workflow, the user has three options to proceed. Firstly, a new case or study can be added by clicking the *Add* button in the bottom left corner of the main screen. Secondly, the user can select a specific instance from the tabular overview, which activates the *Edit* button in the bottom left corner. Thirdly, we provide configurable filtering masks to search for particular cohorts. Figure 25 shows two masks, where users can select study information (top, left) and aneurysm descriptors (bottom, left). Data sets that do not satisfy the selected criteria are removed from the tabular overview. Based on the filtering result, an entry from the summary can be selected for further editing.

### 5.4.1 Adding a Case

Pressing the *Add* button activates a new widget to include new cases and studies, see Figure 26. For a new instance, the hospital of data acquisition has to be selected, and optional tags can be added. Besides, a new study can be added for an existing case, e.g., to manage pre- and post-treated data of a patient. For this purpose, various meta information such as the study type as well as age and gender

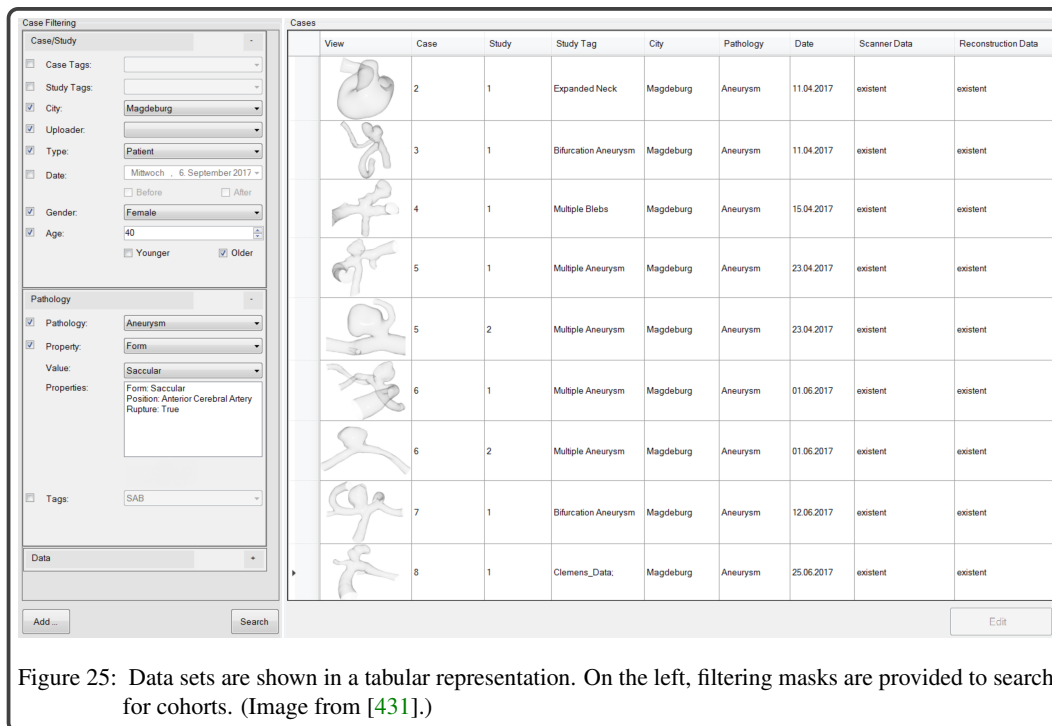


Figure 25: Data sets are shown in a tabular representation. On the left, filtering masks are provided to search for cohorts. (Image from [43].)

of a person have to be provided. After adding a new study, the lower part of the widget becomes active, see Figure 26b. Here, the user can add specific information about existing pathologies. In this example, the female patient has two aneurysms. For each aneurysm, different data can be defined such as location, height and rupture status. To enter the characteristics of pathology for the current study the left part of the lower pathology widget is used. Already defined pathologies for the present study are summarized in the right part of the widget. Pressing the *Upload pathologies* button (bottom, right) sends all information to the database, where it is stored.

#### 5.4.2 Editing a Case

Besides adding new cases and studies, selected cases from the overview can be edited. Pressing the *Edit* button, see Figure 25 (bottom, right), displays a summary of meta information and existing pathologies, see Figure 27a. Moreover, four tables summarize existing data on the FTP-server depending on the data category. Metadata can be edited, or new information can be added, i.e., further aneurysm descriptors. For this purpose, the user has to select the type of information and the data files as well as additional attributes depending on the chosen type. Within the edit widget, the user has three options for further action:

1. Existing data files can be downloaded from the FTP-server to a local storage medium by pressing the *Download* button. Here, either the checkboxes next to the tables can be selected to download all existing data files within the corresponding data category or single entries of a table can be chosen to download a specific subset of data files.
2. New data files can be uploaded to the FTP-server by pressing the *Upload* button, which opens an upload widget, see Figure 27b. Here, the data type of the new files has to be defined as well as some further meta information and the data themselves have to be selected. After closing this widget, the summarizing tables in the first edit widget are updated to show the previously uploaded data items.
3. Users can activate the visualization component, which is described in more detail in the following section.

(a)

(b)

Figure 26: Widget to add new cases and studies as well as the corresponding meta information (a). For a study, pathology-specific meta information can be added (b).

(a)

(b)

Figure 27: The user interface to manage and explore aneurysm data. Existing data is summarized, can be edited (a) and uploaded on the [FTP-server](#) (b). (Images from [431].)

### 5.4.3 Visualizing a Case

Pressing the *Visualize* button activates the visualization component. *Aneulysis* provides five visualization modules. Per default, the *morphological aneurysm visualization* (*MorAVis*) module is enabled, which represents the current clinical workflow to evaluate aneurysm treatment necessity. It allows an interactive exploration of the vessel morphology including automatically calculated morphological descriptors, see Section 5.5. Besides this, three visualization modules are provided that support the visual analysis of wall- and flow-related information based on a surface representation of the vasculature, see Chapter 6. For the visual exploration of intra-aneurysmal flow patterns, the *visual flow exploration* (*ViFIEx*) module was developed, see Chapter 7. For this purpose, the internal blood

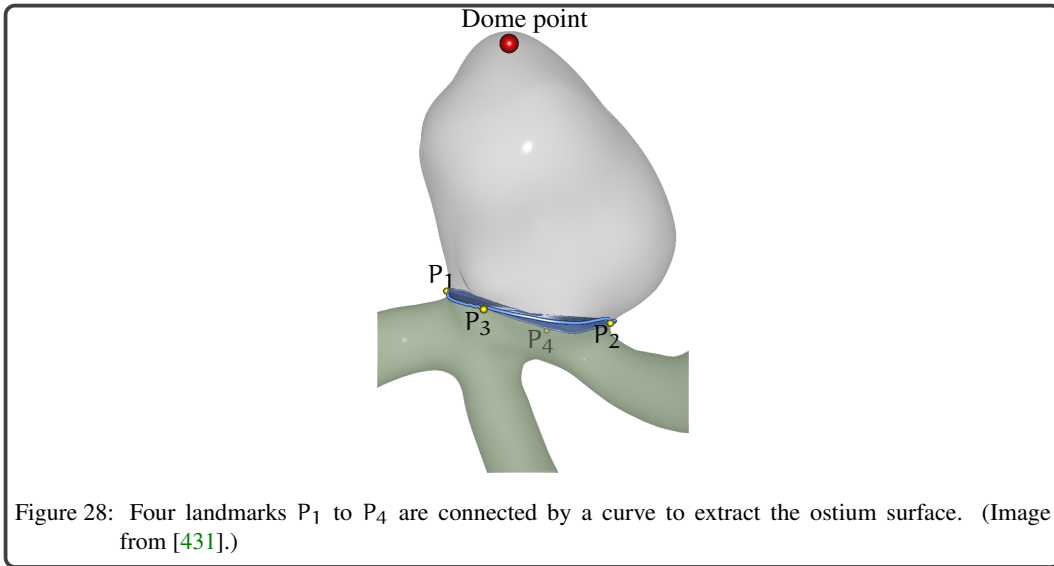
flow is represented by integral lines. These lines must be clustered to get groups of lines with similar flow behavior that represent flow patterns, see Section 7.1. Afterward, the flow patterns are classified according to pre-defined types, see Section 7.2. Besides, multiple techniques are provided to visualize the detected flow patterns as well as their interplay with the vessel wall.

## 5.5 MORAVIS - MORPHOLOGICAL ANEURYSM VISUALIZATION MODULE

This section describes the *MorAVis* module, which allows an automatic extraction and interactive exploration of morphological descriptors, including the ostium based on a 3D surface representation of the vasculature. An automatic calculation of these features based on 2D clinical image data would require automatic detection of aneurysms. However, recent approaches [72, 152, 153] have still problems with false detections as well as missed detections, and a reliable 2D ostium extraction is also challenging [178].

### 5.5.1 Extraction of the Aneurysm Ostium

To identify correlations between morphological descriptors and rupture, many data sets have to be analyzed, which requires a fast descriptor extraction. An important descriptor is the aneurysm ostium. Due to the lack of a unified definition, the ostium extraction is challenging. The ostium can be seen as an imaginary surface that separates the aneurysm sac from the non-pathological parent vessel. Thus, the vessel structure without an aneurysm needs to be predicted. Most detection algorithms require a priori knowledge, e.g., the centerline of the parent vessel or user interaction [269, 325], such as selecting the dome point, see Figure 28. To avoid such dependencies on precomputed data, we developed an efficient extraction algorithm. Our method automatically calculates an initial surface representing the ostium. This can be interactively corrected if necessary since manually defined ostium contours by medical experts exhibit a certain degree of variation among themselves since they interpret the ostium differently depending on personal experience [325].



For extraction, a more geometric definition of the ostium is needed. We used the description of Neugebauer et al. [269], who defined the ostium as a contour comprising four landmarks,  $P_1$  to  $P_4$ , see Figure 28. The first two points,  $P_1$  and  $P_2$  are located on the transition between an aneurysm and the parent vessel. The other two landmarks control the bending of the ostium around the parent vessel. The goal is to identify these four points. Our algorithm consists of six steps, as described in the following.

**1. Skeleton extraction:** Before we can compute the precise positions of  $P_1$  to  $P_4$ , we have to estimate which vessel part represents an aneurysm. For this purpose, we used the skeleton of an aneurysm and parent vessel geometry, which is determined using the method by Au et al. [20]. This method performs automatically and thus; no a priori knowledge is needed as input data. Iterative implicit Laplacian smoothing is applied to generate a zero-volume skeletal shape, see Figure 29. Global positional constraints are defined to preserve the connectivity, which yields in curves that represent the vessel skeleton. Afterward, each skeleton vertex corresponds to faces (and vertices) of the surface.

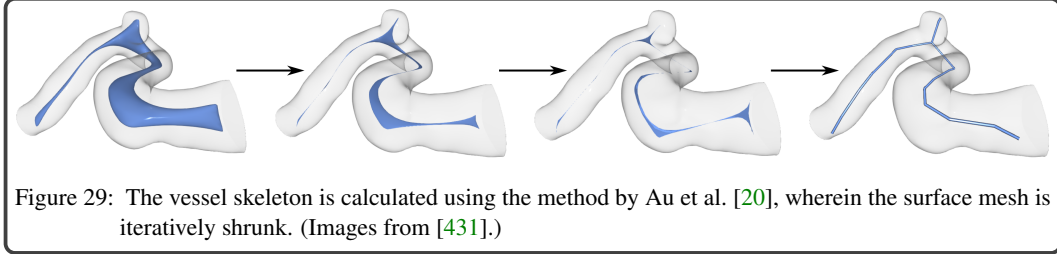


Figure 29: The vessel skeleton is calculated using the method by Au et al. [20], wherein the surface mesh is iteratively shrunk. (Images from [431].)

**2. Aneurysm identification:** In the second step, we use the skeleton to identify the aneurysm vessel part. The nodes of the vessel skeleton can be characterized according to their number of outgoing edges: end nodes (one edge), intermediate nodes or non-junction nodes (two edges) and junction nodes (more than two edges). Junction nodes occur at bifurcations of the original surface. We determine all end nodes, and for each, the nearest junction node is searched by traversing the skeleton, see Figure 30. We have to decide if the path from the end node to the junction node (over intermediate nodes) represents a section of the parent vessel or an aneurysm. These paths inherit a corresponding amount of vertices on the original surface. For these vertices, we compute the shape index  $S_i = \frac{1}{2} - \frac{1}{\pi} \arctan\left(\frac{\kappa_1 + \kappa_2}{\kappa_1 - \kappa_2}\right)$  and average them, with  $\kappa_1 \geq \kappa_2$  being the principal curvatures. Since aneurysms are usually spherical structures, skeleton sections representing the aneurysm exhibit a higher  $S_i$  than segments representing the elongated parent vessel. Based on this, we determine the junction  $P_{AJ}$  (green) and end node  $P_{AE}$  (red), representing the aneurysm, see Figure 30b. With this, inaccuracies due to small arteries around the ostium are avoided. In case the highest  $S_i$  does not represent an aneurysm (did not occur in our cases), the user can correct the detection by selecting the correct end node  $P_{AE}$ .

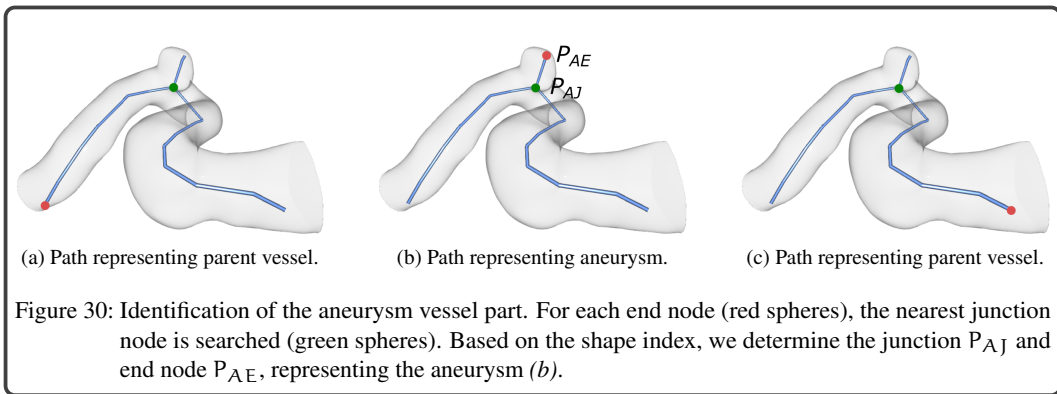


Figure 30: Identification of the aneurysm vessel part. For each end node (red spheres), the nearest junction node is searched (green spheres). Based on the shape index, we determine the junction  $P_{AJ}$  and end node  $P_{AE}$ , representing the aneurysm (b).

**3. Extraction of  $P_1$  and  $P_2$  :** Based on the detected aneurysm vessel part, we identify the first two landmarks  $P_1$  and  $P_2$  by generating a curve on the vessel over an aneurysm, see Figure 31a. Inspired by Neugebauer et al. [269], who project the centerline on the surface along the vector pointing from the centerline to the aneurysm's dome, we determine another curve on the surface that gives us  $P_1, P_2$ . This is achieved by first determining the path from the junction node to the remaining end nodes

(except the end node, corresponding to an aneurysm). If more than two paths exist, we determine the first tangent vector of each path by subtracting the coordinates of the first neighbor node of the junction node and the junction node itself. For each of these vectors, we calculate the enclosing angle with  $P_{AE} - P_{AJ}$ . The two paths, which are closest to  $90^\circ$  are used for further consideration as these paths represent the parent vessel and paths representing further in- or outgoing vessels are excluded in additional computations. Then, the Euclidean distances between the surface points, belonging to the current node of the skeleton path and the point  $P_{AE}$  are determined. This is performed for all skeleton nodes, where the vertices representing the minimal distance are connected using the Dijkstra algorithm concerning neighbored nodes of the skeleton. This yields a path  $f$  on the aneurysm surface, see Figure 31a. Afterward,  $f$  is split into two paths  $f_1$  and  $f_2$  at the global minima, which represents the aneurysm's dome position. For  $f_1$  and  $f_2$ , we determine the positions where the distance to the junction node is minimal, which yields the landmarks  $P_1$  and  $P_2$ . For aneurysms with more than two outgoing vessels, more ostium points are detected, where we take the two with the maximum occurring distance for  $P_1$  and  $P_2$ .

**4. Extraction of  $P_3$  and  $P_4$  :** To define a contour that represents the correct bending of an aneurysm, two more landmarks  $P_3$  and  $P_4$  are needed, where all landmarks should be evenly distributed throughout the ostium contour. For this,  $P_1$  and  $P_2$  are connected using the Dijkstra algorithm, where the cost function of this algorithm considers the edge length of the triangle edges and tries to minimize their sum. On this path,  $P_3$  is determined so that it has the same distance to  $P_1$  and  $P_2$ . These three points define a plane  $E$ . Then, we calculate two geodesic distance fields  $d_1$  and  $d_2$  [78]. The first distance field starts at  $P_1$  and the second begins at  $P_2$ . Based on  $d_1$  and  $d_2$ , we compute a third distance field  $d_3 = d_1 - d_2$ , which is color-coded on the surface in Figure 31b. To get  $P_4$ , we determine the isoline  $I$  representing  $d_3 = 0$  that lies between  $P_1$  and  $P_2$ , and compute the intersection points between  $I$  and  $E$ . From these points, we take the intersection point  $S_3$  that has the larger distance to  $P_3$  to fulfill the condition of evenly distributed landmarks. From  $S_3$ , we go along  $I$  in the direction of the smaller distance from  $P_{AJ}$ . This minimum represents  $P_4$ , see Figure 31b.

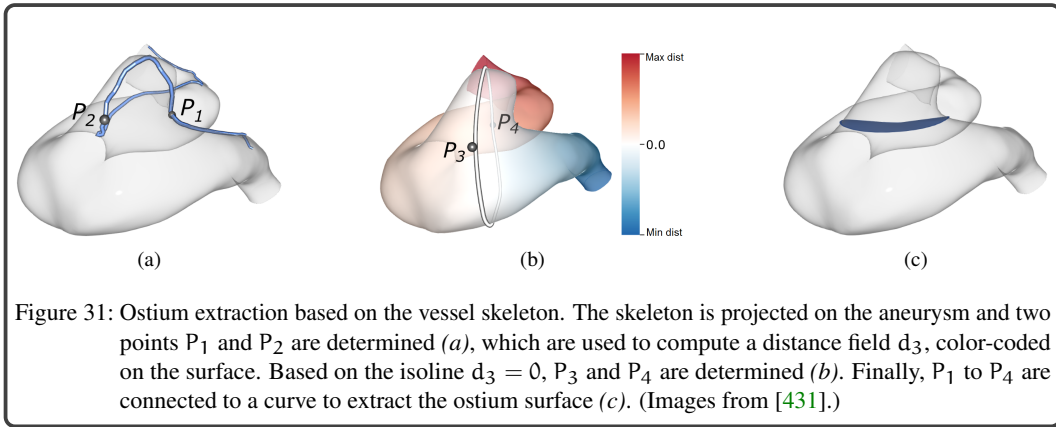
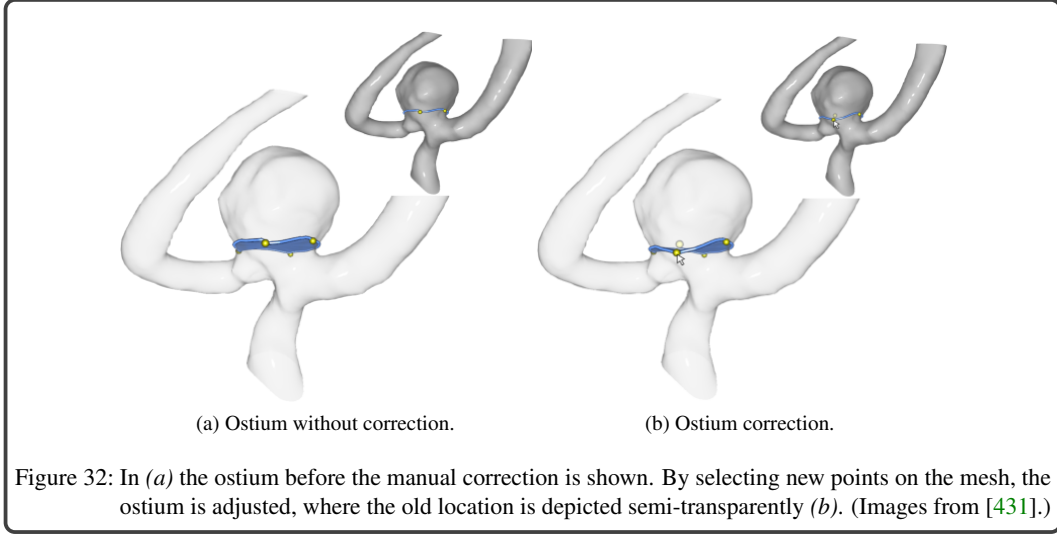


Figure 31: Ostium extraction based on the vessel skeleton. The skeleton is projected on the aneurysm and two points  $P_1$  and  $P_2$  are determined (a), which are used to compute a distance field  $d_3$ , color-coded on the surface. Based on the isoline  $d_3 = 0$ ,  $P_3$  and  $P_4$  are determined (b). Finally,  $P_1$  to  $P_4$  are connected to a curve to extract the ostium surface (c). (Images from [43].)

**5. Ostium extraction:** Then,  $P_1$  to  $P_4$  are connected to a curve  $C_{ostium}$  using the method by Surazhsky [358], determining the shortest geodesic path between points on a triangular mesh. Finally, the enclosing area, representing the ostium surface is triangulated by determining the mean point  $\bar{p}$ , where adjacent points on  $C_{ostium}$  form a triangle with  $\bar{p}$ , see Figure 31c.

**6. Ostium correction:** Due to the anatomical diversity,  $P_1$  to  $P_4$  are not always optimal. Therefore, the user can select other positions on the mesh to correct  $C_{ostium}$ . Figure 32a shows the automatically calculated ostium surface, where  $P_1$  to  $P_4$  are rendered as yellow spheres. For selecting a new point  $P_{new}$ , we determine which of  $P_1$  to  $P_4$  has the smallest geodesic distance to  $P_{new}$ . Then,  $P_{new}$  replaces this ostium point, the corresponding contour parts are recalculated, and a new triangulation of the ostium surface is generated, while the old ostium point is depicted semi-transparently, see Figure 32b. The recalculation takes less than 1 s.



### 5.5.2 Calculation of Morphological Descriptors

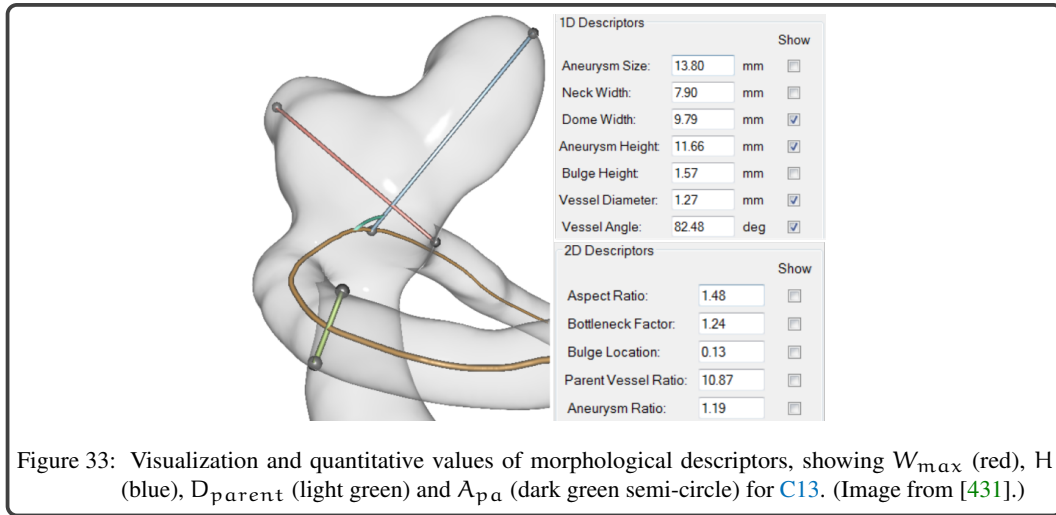
Inspired by the study of Hoh et al. [159], we compute seven 1D and five 2D descriptors based on the extracted ostium and the dome point. These can be used for a more in-depth assessment of the aneurysm state. The 1D criteria are aneurysm height ( $H$ ), maximum width ( $W_{\max}$ ), diameter ( $D_{\max}$ ), neck width ( $W_{\text{neck}}$ ), bulge height ( $H_{\text{bulge}}$ ), parent artery diameter ( $D_{\text{parent}}$ ), and the angle between parent artery and aneurysm apex ( $A_{\text{pa}}$ ), recall Section 2.3.3. The 2D criteria are aspect ratio, height-width ratio, bottleneck factor, bulge location, and aneurysm/parent artery ratio.

The length of vector  $\mathbf{v}_h = \mathbf{p}_d - \mathbf{p}_o$  with dome point  $\mathbf{p}_d$  and ostium center  $\mathbf{p}_o$  represents  $H = \|\mathbf{v}_h\|$ . To calculate  $W_{\max}$  for each aneurysm vertex  $\mathbf{v}_i$ , we determine the corresponding point  $\mathbf{p}_i$  on  $\mathbf{v}_h$ :  $\mathbf{p}_i = \mathbf{p}_o + \frac{(\mathbf{v}_h)^T(\mathbf{v}_i - \mathbf{p}_o)}{(\mathbf{v}_h)^T(\mathbf{v}_h)} \cdot (\mathbf{v}_h)$ . Using  $\mathbf{p}_i$ , a ray  $r$  is defined:  $r = \mathbf{p}_i + t(\mathbf{p}_i - \mathbf{v}_i)$ . Based on  $r$ , all intersection points with the aneurysm surface are calculated and the intersection  $\mathbf{v}_j$  with the greatest Euclidean distance to  $\mathbf{p}_i$  is used to calculate  $W_{\max} = \|\mathbf{v}_j - \mathbf{p}_i\|$ . The diameter is given by the two aneurysm points  $\mathbf{v}_i$  and  $\mathbf{v}_j$  with the greatest Euclidean distance. Similarly,  $W_{\text{neck}}$  is defined as the maximum Euclidean distance between two points belonging to the ostium contour. To calculate the bulge height, we use:  $H_{\text{bulge}} = \|\mathbf{p}_i - \mathbf{p}_o\|$ . From the skeletonization, the vessel diameter is known at each node by considering the minimum diameter of the corresponding vessel cross section. We assign the median radius to  $D_{\text{parent}}$ . To compute  $A_{\text{pa}}$ ,  $\mathbf{v}_h$  and the nearest skeleton node to the ostium center  $\mathbf{cp}_i$  as well as the tangent  $\mathbf{t}$  at this point are used. The angle between  $\mathbf{v}_h$  and  $\mathbf{t}$  is  $A_{\text{pa}}$ . When manually correcting the ostium, the descriptors are recalculated and stored in the database.

#### Visualization of Morphological Descriptors

The descriptors are depicted within the 3D vessel surface, which is depicted semi-transparently, and Phong shaded to support shape perception. For the 1D descriptors, the defining endpoints are rendered as spheres. Their connecting line is shaded as tube [353] to improve its perception, see Figure 33. For this purpose, we constructed view-aligned quads on the GPU [216]. The consecutive start- and end points  $\mathbf{p}_i$  and  $\mathbf{p}_{i+1}$  are used to determine the normalized tangent vector:  $\mathbf{t} = \mathbf{p}_{i+1} - \mathbf{p}_i$ . With the given view direction  $\mathbf{v}$ , we calculate the extent of the quad by using the normalized cross-product  $\mathbf{e} = \mathbf{v} \times \mathbf{t}$ . For every generated quad, we assign a parameter  $y \in [-1, 1]$  to define its color:  $\text{color} = c_{\text{col}} \cdot \cos(0.5y \cdot \pi)$ , where  $c_{\text{col}}$  is set to a specific RGB color for each criterion, which results in a shaded cylinder. For the choice of colors, we used the ColorBrewer website [239]. We selected seven colors, which differ perceptually well since seven 1D descriptors are distinguished. For the 2D descriptors, the corresponding 1D structures are depicted. The user can activate individual descriptors for her exploration. Moreover, the corresponding quantitative values are listed.





## 5.6 EVALUATION AND RESULTS

To show the improved accuracy of automatically calculated descriptors, we compared the automatic results with manually measured descriptors provided by the two neuroradiologists, recall Section 5.1. Moreover, we compared our ostium extraction with manual expert results and with the results of an existing approach. Finally, informal interviews with the two CFD engineers and the two neuroradiologists were performed to evaluate the general workflow of *Aneulysis*.

### 5.6.1 Comparison to Expert Results

The experts manually determined the 1D descriptors based on CTA slice images for 10 data sets (C4 - C8, C14 - C18 in Figure 22). Moreover, the manual measurements were performed on the 3D surface mesh. For this purpose, they selected points on the surface that define the endpoints of the descriptors. The angle  $A_{\text{pa}}$  could not be measured in 2D, because it is challenging to find an appropriate slice. We compared the manual 2D (2DM) and manual 3D (3DM) measurements to our 3D automatic computations (3DA), see Table 2. In medical guidelines, an increased rupture risk is assumed for aneurysms larger than 7 mm and therefore, they are usually treated. Moreover, the experts stated that measurement deviations of more than 0.5 mm would be critical since this could influence the treatment decision. Besides the aneurysm size, the accessibility of an aneurysm within the vascular tree plays a vital role in routine clinical treatment. Although medical studies [83, 186] argue against the influence of size on rupture risk, we take size into account as it significantly controls clinical decisions.

Measurement deviations differed for the individual descriptors. For height, the maximum difference between 2DM and 3DM was 1.3 mm and between 2DM and 3DA 1.5 mm. However, between 3DM and 3DA the deviation was reduced to 0.4 mm. Similar differences occurred for the bulge height that had a maximum difference of 1.1 mm, 1.3 mm and 1.3 mm for 2DM/3DM, 3DM/3DA and 2DM/3DA. The aneurysm width and diameter showed larger deviations between 2DM/3DA with 2.2 mm and 2.3 mm, which are highly critical deviations according to the treatment decision. Also, the median differences were increased with 1 mm for width and 1.2 mm for diameter. For 3DM/3DA, a maximum difference of 0.8 mm occurred for both. The neck width showed a maximum difference of 0.8 mm between 2DM/3DM and 3DM/3DA, but between 2DM/3DA a maximum deviation of 1.4 mm occurred. The measurements for  $A_{\text{pa}}$  exhibited a maximum difference of  $15.7^\circ$  between 3DM/3DA. For the parent artery diameter, the lowest maximum differences occurred with 0.1 mm, 0.2 mm and 0.1 mm for 2DM/3DM, 3DM/3DA and 2DM/3DA.



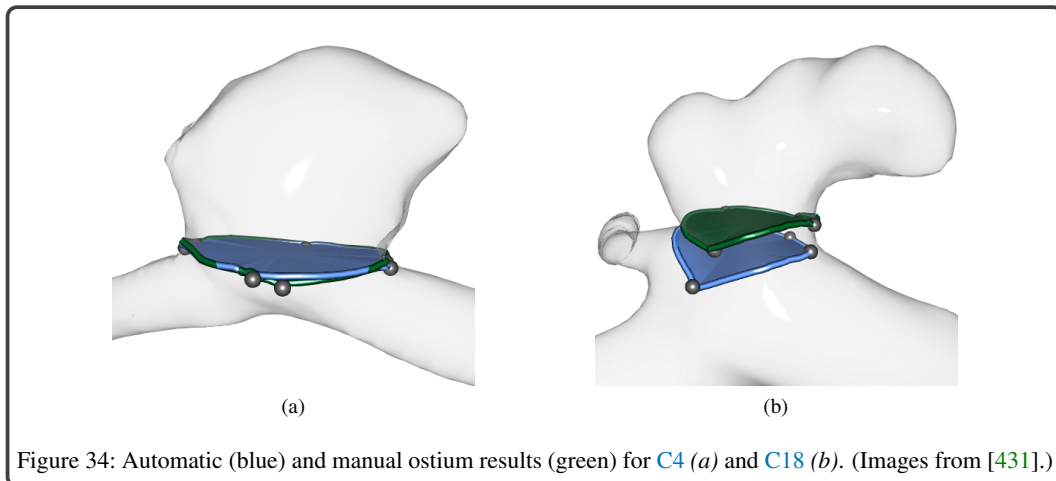
Table 2: Comparison of our automatically calculated (3DA) descriptors to manually measurements based on 2D image slices (2DM) and the 3D aneurysm surface (3DM). Maximum occurred deviations are emphasized.

Criteria	Measure	C4	C5	C6	C7	C8	C14	C15	C16	C17	C18
Height (mm)	2DM	4.5	6.0	5.0	4.1	4.7	3.8	4.6	7.8	<b>4.6</b>	5.3
	3DM	4.4	5.3	5.7	4.5	4.6	3.7	4.1	8.4	<b>5.9</b>	5.1
	3DA	4.8	5.5	5.7	4.6	4.9	4.1	4.4	8.5	<b>6.1</b>	5.4
Width (mm)	2DM	4.5	5.3	5.4	3.8	4.2	3.4	4.8	4.2	<b>4.5</b>	3.0
	3DM	5.3	4.8	6.7	4.7	5.1	3.2	4.7	5.7	6.5	<b>4.3</b>
	3DA	5.5	4.9	7.0	4.8	5.2	3.6	5.0	5.8	<b>6.7</b>	<b>5.1</b>
Diameter (mm)	2DM	<b>4.5</b>	6.2	5.5	4.4	5.7	4.4	5.0	9.1	5.5	6.1
	3DM	6.5	6.3	7.6	5.0	6.5	4.9	4.8	<b>9.9</b>	6.7	6.3
	3DA	<b>6.8</b>	6.4	7.7	5.6	6.9	5.3	5.2	<b>10.7</b>	7.4	7.0
Neck Width (mm)	2DM	4.6	1.4	3.4	2.3	3.3	2.1	2.4	3.6	<b>2.7</b>	2.5
	3DM	4.5	2.0	<b>3.6</b>	3.0	4.1	2.3	2.8	<b>3.6</b>	3.5	3.2
	3DA	4.9	2.5	<b>4.4</b>	3.0	4.3	2.7	2.8	<b>4.4</b>	<b>4.1</b>	3.4
Bulge Height (mm)	2DM	2.2	3.0	<b>2.9</b>	1.4	1.0	1.5	<b>0.9</b>	7.0	3.0	0.8
	3DM	<b>2.6</b>	2.8	<b>4.0</b>	1.6	0.9	1.4	1.3	6.7	2.9	0.8
	3DA	<b>1.3</b>	2.9	3.1	1.7	1.1	1.4	<b>2.2</b>	6.4	3.3	1.0
Artery Diameter (mm)	2DM	0.8	0.6	0.7	1.1	<b>0.9</b>	1.0	0.9	<b>1.0</b>	0.9	1.2
	3DM	0.9	0.6	0.7	1.0	1.1	1.0	0.7	<b>1.0</b>	0.8	1.2
	3DA	0.9	0.7	0.8	1.0	<b>1.1</b>	1.0	0.8	<b>1.2</b>	0.8	1.3
Apex Angle (°)	2DM	x	x	x	x	x	x	x	x	x	x
	3DM	49.9	55.2	51.4	<b>60.3</b>	77.3	60.7	75.5	50.6	80.6	48.3
	3DA	38.1	41.8	59.8	<b>44.6</b>	83.4	54.7	80.1	45.8	89.5	54.4

### 5.6.2 Evaluation of the Ostium Extraction

To assess the quality of our ostium extraction, we compared the results using the Hausdorff distance  $H_d$  to manually defined ostium curves by the neuroradiologists, see Table 3 (first row). The experts selected points on the 3D surface that were connected by the method of Surazhsky [358].

Our automatic approach and the manual approach lead to similar results. The maximum occurring  $H_d$  is 0.75 mm (C18), whereas the best result has a  $H_d$  of 0.19 mm (C4), both depicted in Figure 34. The aneurysm of C18 is parallel to the vessel, which leads to a similar distance to the skeleton. Thus, the applied distance metric returns no optimal positions for  $P_1$  and  $P_2$ . However, the experts stated that the correction of the ostium is easy to use and allows for a fast adaption.



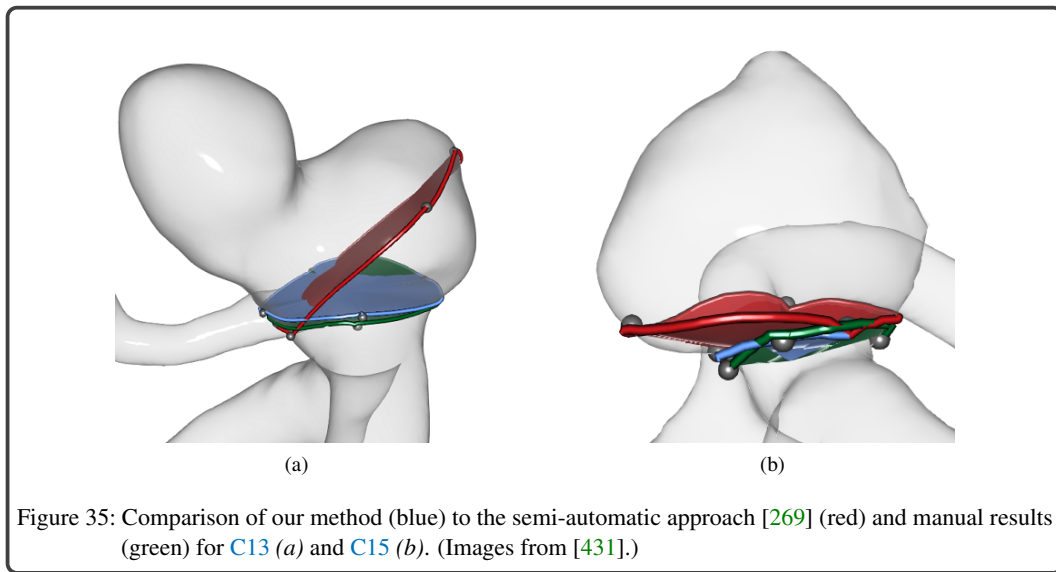
We also investigated the influence of deviations between the manually and automatically extracted ostium on morphological descriptors, see Table 3. For C18, the maximum difference is 0.63 mm for the bulge height and for C14, the diameter deviates by 0.54 mm. The experts recommend a manual

correction for a deviation of more than 0.5 mm. As for the angle differences, they were unsure about an acceptable variance, because there are no studies that show a significant influence of the angle on the rupture risk. However, for the distance-based criteria, the comparison indicates that our ostium extraction leads to appropriate results for the majority of the tested data sets.

Table 3: Hausdorff distance between the automatically and manually generated ostium as well as deviations for the morphological descriptors calculated based on both ostium surfaces.

Criteria	C4	C5	C6	C7	C8	C14	C15	C16	C17	C18
Hausdorff (mm)	0.19	0.31	0.31	0.25	0.39	0.61	0.40	0.35	0.38	<b>0.75</b>
Height (mm)	0.01	0.05	0.35	0.01	0.1	0.23	0.01	0.07	0.12	0.33
Width (mm)	0.02	0.09	0.03	0	0.1	0.23	0.01	0	0.01	<b>0.61</b>
Diameter (mm)	0.23	0.14	0	0	0.03	<b>0.54</b>	0	0	0.22	0.27
Neck Diameter (mm)	0.07	0.08	0.05	0.04	0.05	0.43	0.21	0.14	0.23	0.28
Bulge Height (mm)	0.16	0.24	0.17	0.01	0.01	0.28	0.05	0.07	0.06	<b>0.63</b>
Apex Angle (°)	0.88	0.49	0.46	0.11	0.73	1.01	0.58	0.58	0.19	1.87

We compared our method with the semi-automatic ostium extraction of Neugebauer et al. [269], which inspired our approach. Figure 35 shows two results of our approach (blue), of the semi-automatic method (red) and manually generated (green) for wide-neck aneurysms. The semi-automatic method leads to very different results compared to manual surfaces due to a wrong determination of  $P_4$ . Our method is much closer to the manual results, which is reflected in the Hausdorff distances with 5.14 mm (a) and 1.67 mm (b) for the semi-automatic approach and 0.30 mm (a) and 0.40 mm (b) for our technique.



### 5.6.3 Evaluation of the Data Administration

Informal interviews were conducted with the four domain experts to evaluate the general workflow of *Aneulysis* regarding data administration. During the evaluation the following tasks were performed:

1. Adding a new case.
2. Adding a new study to an existing case, including information about the pathology.
3. Editing a study by uploading additional files and changing morphological descriptors.
4. Searching for a cohort that fulfills specific descriptors with a specified variance.

First, we described the functionality of *Aneulysis*. Then, the experts performed the defined tasks, while we noted their spoken comments.

The adding of new cases and studies was described as simple by all experts (**Req. 1**). For this purpose, the adding wizard has to be activated, see Figure 25 (bottom, left). The pre-defined drop-down menus enable a fast selection of meta information. Short text-based descriptions can be added to cases and studies, for which experts wished for suggestions of already used descriptions. Besides, they emphasized the possibility to upload files for selected pathology information, i.e., images of aneurysm location or reports about rupture. Furthermore, the experts wished for an option to add new studies to the chosen case in the main view. This would avoid the selection of the corresponding case from a drop-down list in the adding wizard.

For editing, the experts selected a case from the tabular overview. They were able to edit meta information and to upload different types of data using the pre-defined structure, see Figure 24. They liked the overview of already uploaded data which avoids redundancy. Besides, they used the *MorAVis* module to explore and edit morphological descriptors. The automatic calculation was considered very helpful, as it saves time and avoids measurement errors (**Req. 2**). They wished for a *visual summary* for clinical documentation and treatment planning.

Finally, the experts searched for specific cohorts. The pre-defined property lists enable a fast definition of individual filtering masks. The possibility to define a permitted variance for each property was emphasized, as it allows a detailed analysis of ruptured and non-ruptured cases. The experts would like to have a statistical analysis of morphological descriptors within a filtered cohort.

## 5.7 DISCUSSION AND LIMITATIONS

The calculated descriptors were compared to manually measured values. Since anatomical accuracy is ensured during the vessel reconstruction, recall Section 5.2.1, occurring deviations between manual and calculated descriptors were interpreted as descriptor-dependent measurement errors. The aneurysm diameter and width show strong variations since the maximum extent is difficult to find manually in 3D. Considerable slicing and rotation efforts are needed, respectively, in 2D and 3D, where the maximum extent can be missed. Measuring aneurysm angles is almost impossible in 2D. In contrast, measurements of the parent artery diameter, which is independent of aneurysm shape, show the lowest deviations. Thus, manual measurements are error-prone and time-consuming. Processing a data set took between 8-10 min, whereas our method needs 1.0-1.9 min. In clinical routine, such measurements are currently the basis for decision-making. Thus, aneurysms are treated, that could initially be observed based on automatic objective measurements. This is important since treatment also carries a considerable risk of severe complications. Moreover, medical studies assign greater importance to curvature-based measures such as the non-sphericity index concerning rupture estimation [83, 186]. However, these parameters cannot be determined manually, but *MorAVis* could be easily extended to calculate such parameters. This aside, manual measurements are not reproducible. To better understand the rupture risk and to evaluate the aneurysm state over time as well as to find an optimal treatment, reproducible measurements are needed, as provided by the *MorAVis* module.

Besides, we compared our automatic ostium extraction with manually generated ostium contours and with the method by Neugebauer et al. [269]. Our results are very similar to manual expert results, even in cases with multiple in- and outgoing vessels. Furthermore, our results exhibit significantly lower Hausdorff distances than the results by Neugebauer et al [269]. Moreover, our method is independent of pre-defined input data and overcomes limitations of existing approaches handling wide-neck aneurysms and small arteries around the ostium.

However, our approach is limited to cases with one aneurysm. For multiple aneurysms (about 20 % of all cases), ostium surfaces have to be computed separately. Moreover, problems occur if an aneurysm runs parallel to the parent artery, which is uncommon according to the medical experts. For these cases, we allow for a manual ostium correction. The medical literature provides no unique ostium definition leading to slightly different ostium contours by different domain experts. Thus, we calculated the variances of morphological descriptors between our automatic and the manually defined

ostium. Except for two data sets, no significant changes occurred and thus our ostium calculations are appropriate to analyze the aneurysm morphology.

The informal study showed that all experts were able to use *Aneulysis* without major problems efficiently and they stated that they would employ it for exploration and management of aneurysm data. To the best of our knowledge, no comparable concept focuses on the management of aneurysm data, comprising images, flows as well as morphological descriptors and patient-specific meta information. *Aneulysis* allows for efficient filtering of data sets, which supports the collaboration of different research groups. In contrast, at the moment, a lot of time is wasted to find and explore data sets, where each group uses various tools and data structures. Furthermore, the descriptors are visualized qualitatively and quantitatively, which could also be used for documentation and patient education in clinical routine. The analysis of cohorts has to be further supported by statistical methods combined with visual analytics to provide a more detailed investigation of descriptors. This would also require techniques that allow for a visual comparison of multiple data sets.

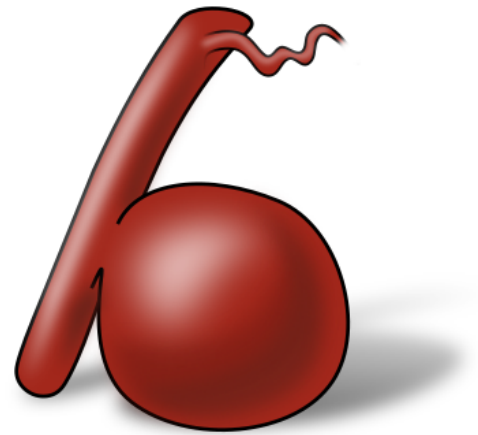
## 5.8 CONCLUSION AND FUTURE WORK

*Aneulysis* allows a powerful management of aneurysm data. Different visualization modules support the visual exploration of the complex morphological and flow information. Per default, the *MorAVis* module is activated, which allows an objective analysis of morphological descriptors that are associated to rupture. Based on an automatic ostium extraction, these descriptors are automatically calculated, which is less time-consuming and error-prone than manual measurements. A consistent data structure was defined to ensure redundancy-free storage of aneurysm data. Filtering of cohorts supports domain experts to understand individual risk factors better. Details about the remaining visualization modules and the corresponding evaluations are given in Chapter 6 and Chapter 7.

In the future, we intend to apply our ostium extraction to a larger amount of data sets to further evaluate its robustness and to extend it to multiple aneurysms. Therefore, further manual ostium extractions are required by domain experts. Besides, we want to compute the morphological descriptors for time-dependent simulation data that consider the vessel deformation during the cardiac cycle. For this, visualization techniques would be needed that show the behavior of the descriptors over time. Until now, *Aneulysis* is a research prototype. A distribution in free or commercial form is planned for the future. For use in a clinical environment, a connection to the *picture archiving and communication system* (PACS) would be required.



# Surface-Based Exploration of Aneurysm Data



This chapter is partly based on:

Monique Meuschke, Samuel Voß, Oliver Beuing, Bernhard Preim and Kai Lawonn,  
Combined Visualization of Vessel Deformation and Hemodynamics  
in Cerebral Aneurysms;  
IEEE Transactions on Visualization and Computer Graphics, 23(1), pp. 761-770, 2017.

Monique Meuschke, Tobias Günther, Philipp Berg, Ralph Wickenhöfer, Bernhard Preim  
and Kai Lawonn,  
Visual Analysis of Aneurysm Data using Statistical Graphics;  
IEEE Transactions on Visualization and Computer Graphics, 25(1), pp. 997-1007, 2018.

Monique Meuschke, Samuel Voß, Oliver Beuing, Bernhard Preim and Kai Lawonn,  
Glyph-Based Comparative Stress Tensor Visualization in Cerebral Aneurysms;  
Computer Graphics Forum, 36(3), pp. 99-108, 2017.

Monique Meuschke, Wito Engelke, Oliver Beuing, Bernhard Preim and Kai Lawonn,  
Automatic Viewpoint Selection for Exploration of Time-Dependent Cerebral  
Aneurysm Data;  
In Proc. of Bildverarbeitung für die Medizin, pp. 352-357, 2017.



To improve rupture risk assessment and decision-making, we developed three further visualization modules. Depending on the underlying data type, i.e., scalar, vectorial or tensor data, the modules allow interactive exploration of this information by overcoming limitations of currently existing visualization approaches. The *combined wall and flow visualization* (CoWaFloVis) module allows an extended visualization of the vessel morphology by showing the wall thickness and wall deformation together with a hemodynamic scalar field and a context visualization of the internal blood flow, see Section 6.1. The *multiple scalar field visualization* (MuScaVis) module focuses on a simultaneous exploration of multiple scalar fields on the vessel wall during the cardiac cycle, see Section 6.2. The *comparative tensor visualization* (CoTenVis) module enables a comparative depiction of tensor data between the inner and outer vessel wall, see Section 6.3. For the development of each module, we derived specific requirements from discussions with medical doctors. Based on these requirements, user studies and informal interviews are performed to evaluate the suitability of the modules to improve aneurysm data exploration. Besides an adequate visualization, a capable camera control including an adequate viewpoint selection is crucial for an efficient analysis of the complex data. To support the time-dependent data analysis, we introduce techniques to calculate appropriate camera paths automatically, see Section 6.4. We developed an interactive planning of animations as well as an automatic calculation on appropriate viewpoints. Both methods can be activated within the visualization modules, where the results are stored in the database of *Aneulysis*.

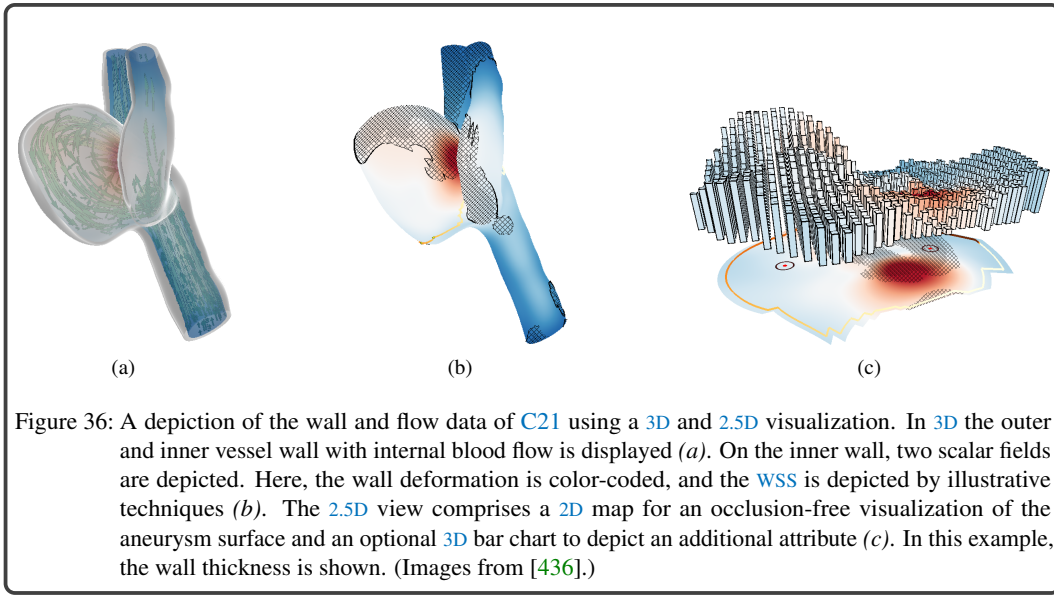
## 6.1 COWAFLOVIS - COMBINED WALL AND FLOW VISUALIZATION MODULE

Experts are interested in whether there are correlations between hemodynamic attributes that are associated with an increased risk of rupture and high-risk wall regions. However, the simultaneous visual examination of several characteristics on the vessel wall is currently only supported to a limited extent, recall Section 4.2.3. Some solutions illustrate two hemodynamic attributes with the surrounding vessel [121, 317] or depict the wall thickness with one hemodynamic factor [132, 216], but a combined visualization was not possible so far. The *decal-lenses* by Rocha et al [318] allow a visual analysis of more than two attributes, but the exploration over time remains challenging since a high manual effort is needed to investigate the data on the 3D aneurysm surface. Moreover, existing approaches rigidly present the aneurysm wall. However, the vessel deformation is an essential factor to estimate the rupture risk and should, therefore, be visualized [288]. We developed the CoWaFloVis module, which provides an integrated visualization of the vessel morphology considering thickness and deformation of the wall as well as hemodynamic attributes and the internal blood flow. It comprises a 2.5D view linked to a 3D depiction of the aneurysm walls such that two attributes can be analyzed simultaneously, see Figure 36. The 2.5D view combines existing techniques that build up a novel, occlusion-free overview visualization of the aneurysm data. The 3D visualization represents the focus upon which the exploration of the scalar data and blood flow data over time takes place.

### 6.1.1 Requirement Analysis

The exploration of scalar quantities mapped to the aneurysm wall plays a central role in the research of rupture risk. Our domain experts stated that they try to identify attribute characteristics and correlations that might have caused the rupture. Using standard visualization techniques, e.g., integrated into *Paraview*, only one attribute can be displayed simultaneously. During rotation and zooming, the experts switch scalar quantities such that different interesting regions are found. Thus, the experts have to memorize the areas and analyze them regarding other quantities as well, which makes the detection of critical attribute correlations very time-consuming. For more complex vascular branches,





the number of ROIs and occlusion problems increases such that a full analysis of various scalar values becomes quite challenging. Besides, the experts stated that they want to know the distance of the flow near the wall, because it may lead to further pathological vessel dilation. For this purpose, they try to visually approximate the distance of the path lines to the vessel wall. However, this is a very demanding and error-prone task, because considerable rotation effort is needed. They wished a visualization that enables fast and straightforward evaluation of morphological and mechanical wall properties as well as hemodynamic attributes and their correlations. In addition to the seven more general requirements in Section 5.1, we summarize further requirements for a simultaneous exploration of wall-related and flow-related characteristics:

**Req. 8** SIMULTANEOUS EXPLORATION OF ATTRIBUTES. The experts want to evaluate whether local changes of hemodynamic attributes occur on morphologically abnormal wall sections or not. For this purpose, a visualization is needed that enables the simultaneous analysis of at least two attributes to identify correlations between them.

**Req. 9** DEPICTION OF BLOOD FLOW. The blood flow needs to be visible during the whole animation. Moreover, the experts are interested in the distance of the flow to the vessel wall.

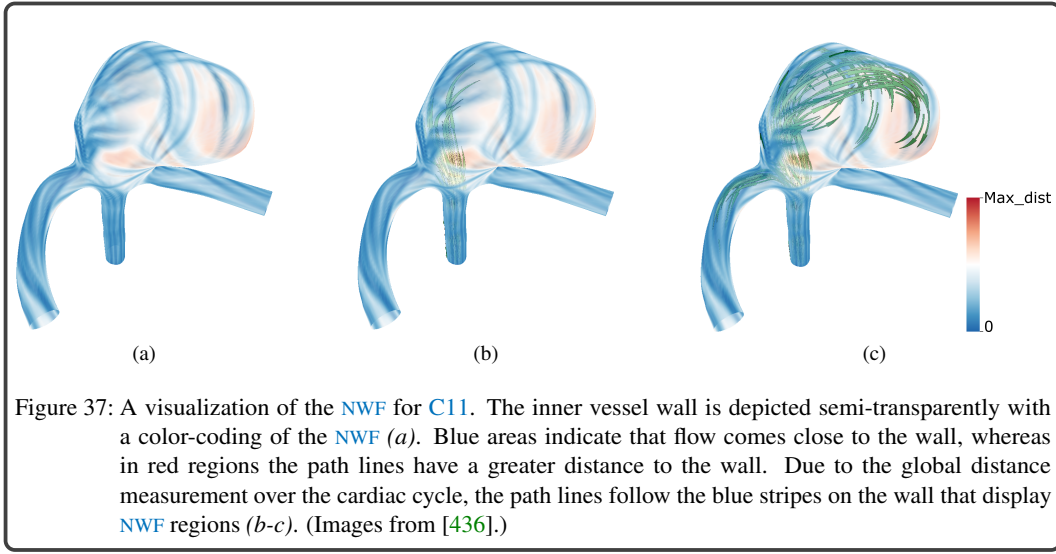
**Req. 10** VESSEL VIEW WITH WALL DEFORMATION AND THICKNESS. Since wall deformation and thickness are essential characteristics to assess rupture risk, visualization techniques are needed that highlight strong local changes of these attributes during the cardiac cycle.

### 6.1.2 General Structure

The CoWaFloVis module consists of two equally-sized linked views. The first view comprises a novel 2.5D aneurysm depiction, whereas the second view shows a 3D aneurysm visualization, see Section 6.1.3 and Section 6.1.4. There exists a bidirectional linking between both views to enable a visual correspondence, discussed in Section 6.1.5. Moreover, collaborative data exploration is supported, see Section 6.1.6.

The CoWaFloVis module allows a simultaneous exploration of up to three scalar attributes. In consultations with our domain experts, we distinguish nine hemodynamic and morphological attributes that can potentially be extended. The attributes can be explored on the aneurysm surface to detect rupture-prone regions and to uncover high-risk attribute correlations.

**Hemodynamics.** Concerning the patient-specific hemodynamics, *WSS*, *OSI*, and pressure are three of the most important quantities to describe the flow field. Furthermore, the tension inside the wall can be explored describing the load induced by the hemodynamics. For this, the local stress tensor is converted to a scalar value using the common stress theory of von Mises (like in [374]). This value describes the norm of the pairwise differences of principal stresses, represented by the eigenvalues of the tensor, scaled with 0.5. Moreover, the *near-wall flow* (*NWF*) can be explored (Req. 9). Therefore, we determine for each vertex of the surface mesh the nearest path line point using the Euclidean distance. Finally, we took for each vertex the minimum overall path line points independent of the time steps to represent the global near-wall flow. This enables a visualization that depicts the trace of the path lines over time. Figure 37 shows the *NWF* using a color-coding. Blue regions indicate flow that comes close to the wall, whereas in the red regions the flow has a greater distance to the wall, based on the path lines. Regions, where the flow is more distant to the wall, indicate that there are thickenings of the inner wall due to the formation of a thrombus or inflammation processes stated by our neuroradiological experts.



**Morphology.** The morphological attributes comprise the wall thickness and wall deformation. Moreover, we identify interesting regions such as blebs based on the curvature measures, similar to Neugebauer et al. [274]. For this, we employed the *shape index* as well as the *curvedness scalar*. The curvature is calculated with the algorithm of Rusinkiewicz [322]. For every triangle, the shape operator is estimated by defining the deviation of the normal along every edge. This provides an equation system which can be numerically solved by the method of least squares. Afterward, the shape operator is accumulated for every vertex by taking the operator of the incident triangles into account. The eigenvalues of the shape operator yield the principal curvature values  $\kappa_1, \kappa_2$  of every point. Given the curvature measures, the shape index is computed as:

$$s = \frac{1}{2} - \frac{1}{\pi} \arctan \frac{\kappa_1 + \kappa_2}{\kappa_1 - \kappa_2}, \quad (9)$$

with  $\kappa_1 \geq \kappa_2$ . The shape index ranges from 0 to 1, where 0 stands for a cup-shaped and 1 for a cap-shaped form. The curvedness is given by:

$$c = \sqrt{\frac{\kappa_1^2 + \kappa_2^2}{2}} \quad (10)$$

and starts with values of 0 for flat regions.

### 6.1.3 2.5D Aneurysm Overview

IA could have irregularly deformed shapes, which complicates the simultaneous exploration of scalar quantities in 3D. This could slightly be improved by side-by-side views, as they only allow to analyze few time steps and attributes and it is exhaustive to put these multiple images together mentally.

To improve this, we provide a novel 2.5D visualization as a combination of existing visualization methods that ensures a fast overview such that the distribution of a chosen scalar quantity can be explored without any occlusions. Similar to Neugebauer et al. [270], we use a map to display the information, which is inspired by other medical overview techniques, such as colon [25] and brain flattening [396] as well as the more abstract *bull's eye plot* (BEP) [285] used in cardiology. In contrary, we did not visualize the map in combination with the 3D render context, but in an additional render context to avoid visual clutter.

The map generation is based on the 3D aneurysm surface, separated from the parent vessel. To separate saccular-shaped aneurysms, we employ our automatic ostium detection, recall Section 5.5.1. The aneurysm surface part is yielded by cutting the 3D surface along the detected ostium, see Figure 38.

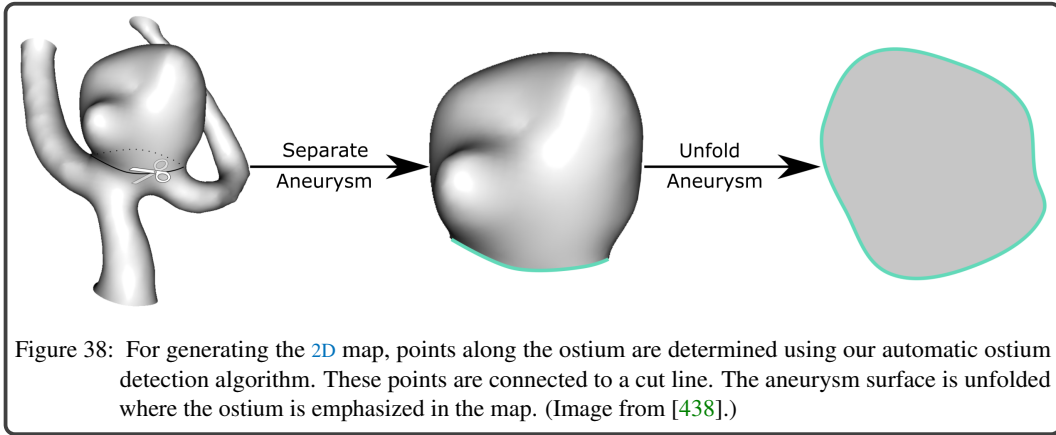
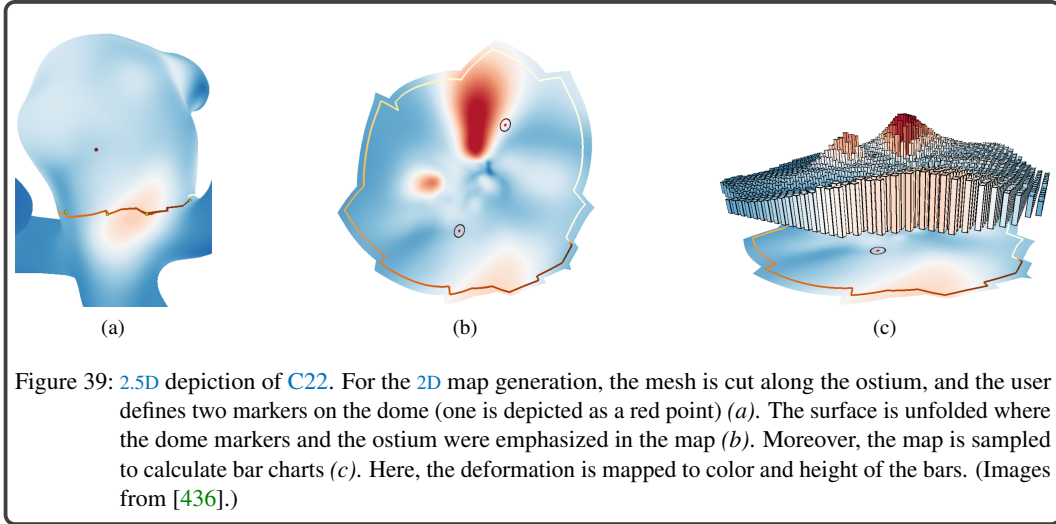


Figure 38: For generating the 2D map, points along the ostium are determined using our automatic ostium detection algorithm. These points are connected to a cut line. The aneurysm surface is unfolded where the ostium is emphasized in the map. (Image from [438].)

Afterward, the aneurysm surface is parametrized to the 2D domain, where the ostium is color-coded on the 3D mesh and the map to establish a spatial correlation between both views, see Figure 39. The map is determined with a parametrization algorithm that maps every point  $\mathbf{p}_i \in \mathbb{R}^3$  on the surface mesh to a point  $\mathbf{p}'_i \in \mathbb{R}^2$  in the plane. We employed the *least squares conformal maps* (LSCM) [223] approach because it is boundary-free and only two points need to be set as constraints for the parametrization. LSCM employs the conformality condition, which states that the gradients of the 2D coordinates are perpendicular  $\nabla \mathbf{v} = (\nabla \mathbf{u})^\perp$ , where  $\perp$  denotes the counterclockwise rotation of  $90^\circ$  around the normal  $\mathbf{n}$ . It is necessary to fix the coordinates of at least two points to have a well-defined optimization problem. In the CoWaFloVis module, we implemented an interaction scheme to add the constraint points, where the user is asked to place two landmarks on the mesh that are mapped to (0,0) and (0,1), see Figure 39. However, different placements would lead to different results. For a more detailed explanation and an overview of other parametrization techniques, we refer to the surveys of Floater and Hormann [106] and Sheffer et al. [343].

**Bar charts.** Based on the discussions with our domain experts, it is helpful to explore the wall thickness or deformation in combination with two other scalar fields to better understand the role of wall morphology in the rupture risk assessment. To display a third scalar field, we included a 3D bar chart besides visualizing scalar quantities on the 2D map. By default, the height of the bars represents the wall thickness, see Figure 39c. However, other attributes can be set as well. To obtain an appropriate distribution of the bar charts, we sampled the 2D map regularly. Afterward, we take only grid points into account which lie inside the 2D map. We ensure this by checking if the grid points lie inside a triangle. Afterward, we calculate the barycentric coordinates of the grid points with the corresponding triangle and use these coordinates to interpolate the chosen scalar field to the grid



point. To generate the bars, we employ triangle strips on the GPU and construct a cuboid. Adding an outline for the edges emphasizes the bars and avoids visual clutter. The bar charts immediately show whether there are local maxima or minima of the chosen scalar field, which could be possible rupture areas, e.g., thin wall regions. The user can then explore these regions in the 3D view.

#### 6.1.4 3D Aneurysm Visualization

The 3D aneurysm view enables a detailed attribute exploration. Besides a depiction of the wall thickness, different scalar attributes, and inner blood flow, we incorporate the dynamic vessel motion during the cardiac cycle (Req. 10). Based on FSI simulations, for each vertex of the surface mesh a deformation vector is known. This information at each time step is used to displace the vertices during the animation.

**Vessel visualization.** The visualization of the vessel wall is divided into the depiction of the outer and the inner vessel wall. For the display of the outer vessel wall, we apply the technique presented by Glaßer et al. [132], which was inspired by the ghosted view approach by Gasteiger et al. [122]. For this, the transparency depends on the shading term  $\alpha = 1 - \langle \mathbf{n}, \mathbf{v} \rangle$ , where  $\mathbf{n}$  denotes the normal and  $\mathbf{v}$  the view direction of the camera, see Figure 36a. In case the camera faces towards the surface, e.g.,  $\mathbf{n}$  and  $\mathbf{v}$  align, the surface is transparent. If  $\mathbf{v}$  is perpendicular to  $\mathbf{n}$ , the mesh appears more opaque. This technique enhances the spatial impression of the surface (see the evaluation by Baer et al. [23]). On the inner vessel wall, the exploration of scalar attributes takes place. To enable a depiction of the internal blood flow, the inner wall is visualized semi-transparently. However, the user can adjust the transparency to his/her needs. In the following section, we describe the depiction of the scalar data.

**Scalar field visualization.** According to Req. 8, a visualization is needed that enables the simultaneous exploration of two scalar fields. We decided to map the first attribute to a discretized cool-to-warm color scale. Lower values are mapped to a bluish color and higher values to a reddish color. Five colors are used to represent the chosen attribute. However, the user can adapt the number of discretized colors to his/her own needs or select a linear color-coding. An isoline representation visualizes the second attribute. For this, the user selects the second scalar field, and a parameter needs to be set. This parameter serves as a threshold, such that depending on the type of the scalar field, either lower or higher values are emphasized. For example, if the domain experts select the wall thickness, they are interested in values that fall below the threshold, whereas in case of pressure they are interested in regions that are greater than the threshold. The depiction of the region is done by an image-based hatching scheme introduced by Lawonn et al. [216]. In contrast, higher (lower) values are emphasized with a greater number of lines and cross-hatches.

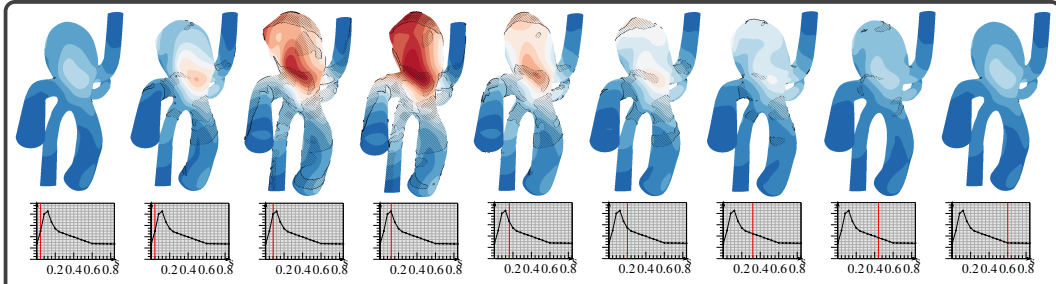


Figure 40: The wall deformation is color-coded on the aneurysm surface (C19) during the cardiac cycle. Furthermore, the **WSS** is depicted by isolines and hatching, where a threshold of 22.3 Pa was selected. Until the peak of the systole (until 0.2 s) the deformation and **WSS** increase continuously, while during the systolic end and diastole both attributes decrease. (Image from [436].)

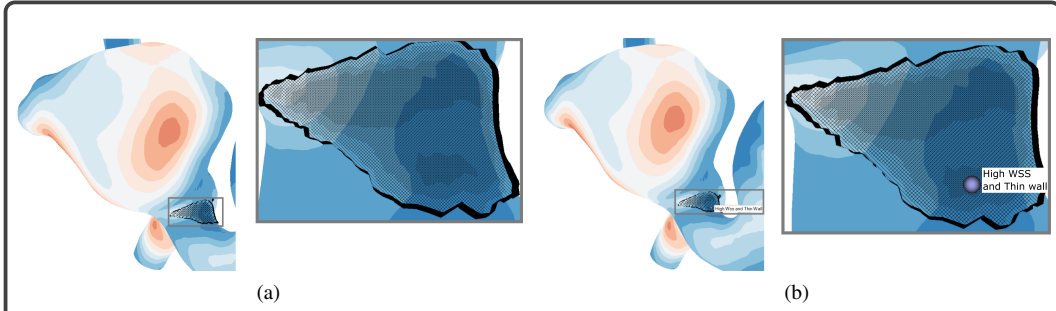


Figure 41: A domain expert detected a suspicious surface region for C22, where the wall thickness is very thin and a high **WSS** exists (a). He created a landmark at this region and assigned an individual label, represented as purple sphere (b). (Images from [436].)

Thus, the experts can set two attributes, e.g., wall deformation and **WSS**, to display **ROIs** with a high deformation and high **WSS** values, see Figure 40. Here, the deformation is color-coded for different time steps, where the diagram below shows the mean deformation changing during the cardiac cycle and the red bar indicates the current time step. Moreover, the **WSS** is depicted by an isoline and hatching. Until the systolic peak (until 0.2 s) the deformation increases, indicated by the red regions, and also an increased **WSS** exists. Afterward, both attributes decrease and are always low during diastole (0.27 - 0.81 s). Figure 41 shows another example of data exploration. Here, the wall thickness is color-coded, and an isoline represents the **WSS**. The user depicted a **ROI** with low wall thickness and high **WSS** values. The blue region indicates a thin wall, where high **WSS** values exist, which is a high-risk rupture area. Moreover, the scalar data is also visualized in the 2.5D depiction using color-coding and illustrative techniques, see Figure 36c.

**Path line visualization.** The path lines are visualized by using an arrow glyph and by color. Inspired by Everts et al. [101], we constructed a view-aligned quad on the GPU to depict the path lines. The successive path line points  $\mathbf{p}_i$  and  $\mathbf{p}_{i+1}$  are used to determine the normalized tangent vector:  $\mathbf{t} = \mathbf{p}_{i+1} - \mathbf{p}_i$ . With the given view direction  $\mathbf{v}$  (of the camera), we calculate the extent of the path lines by using the normalized cross-product  $\mathbf{e} = \mathbf{v} \times \mathbf{t}$ . Then, we parametrize the path lines with two parameters. The first parameter is the current animation time of the cardiac cycle and, thus, similar to the approach by Lawonn et al. [216]. The second parameter is set for the extent and is in the range of  $[-1, 1]$ . Using the parametrization allows to draw arrow glyphs on the path lines. An offset for the current time is set and gives the range of the current path line part. The start and end points are used to construct the arrow, see [101, 216]. This approach allows an easy interpretation of the speed. If the animation pauses, the length of the depicted path line part corresponds to the speed. Furthermore, another value, e.g., the pressure can be visualized by a color scheme. For this, we used a dark green to light yellow color map, see Figure 37.



### 6.1.5 Linking between 2.5D and 3D View

To facilitate the correlation between the 2.5D and 3D view, we provide a linking between them. Concerning the direction from 2D to 3D, the user can pick a specific point in the 2D map, and the camera rotates automatically to the corresponding 3D position in a smooth way. In 3D, this point is presented as a green sphere at the corresponding position. Thus, interesting regions were presented to the user without a manual search. Furthermore, we integrate a brushing for the 2D map. Instead of picking specific points, the user can brush in the map, and the corresponding 3D regions are emphasized by hatching. The brush radius can be controlled with the mouse wheel. Moreover, regions on the 3D surface can be highlighted in the 2D map depending on the zoom level. The closer the user zooms into the 3D scene, the more opaque the corresponding 2D region is depicted. This supports the perceived spatial correspondence between a 3D region and its related 2D area.

### 6.1.6 Collaboration Tools

To support the collaboration between domain experts, we allow the user to place landmarks on the vessel surface (Req. 7). Each landmark gets an individual color, and an individual label can be set, see Figure 41b. Therefore, a textual description of each landmark is available, e.g., for documentation. After the placement, a screenshot is taken, and all selected parameters, as well as the camera settings, are stored. Another expert can see the landmarks on the surface, and they are listed together with their labels as a preview in the top right corner. Selecting a landmark in the preview loads the corresponding scene. Landmarks can also be placed, if the automatic animation is active. During placing and labeling a mark, the animation stops and continues after pressing the enter button.

### 6.1.7 Evaluation and Results

For the evaluation of the CoWaFloVis module, we conducted a user study with five unpaid participants (1 female, 4 male; 28-48 years old; median 35 years). Among them were: two physicians (14 and 16 years of experience in radiology) and two CFD engineers involved in the hemodynamic analysis (five and eight years of professional experience). Furthermore, we added one expert for medical visualization (six years of work experience). At the beginning of the study, we described the functionality to the experts and afterward the participants were encouraged to explore the visualization techniques on their own. During exploration, we noted the experts' spoken comments and their interaction with the system. They had to try both views and the bidirectional connection between them to find suspicious regions. Finally, we asked them to answer a questionnaire.

#### Questionnaire

The questionnaire comprises mainly aspects of our visualization concept and its medical relevance. Besides open-ended comments, we asked questions that had to be answered using a five-point Likert scale (—, —, ○, +, ++). The questionnaire comprises the following aspects.

**Medical relevance.** The first aspect considers the subject's opinion about the general importance of wall thickness, wall deformation, and blood flow as well as their combined analysis for the investigation of cerebral aneurysms. Moreover, we asked about the importance of data exploration during the entire cardiac cycle.

**3D visualization.** We asked whether the combination of color and illustrative techniques is appropriate to explore two attributes simultaneously. Then, we inquired if the color-coding of the vessel surface is useful to highlight the near-wall flow. Next, we asked if the transparency of the vessel wall enables the visual tracking of the inner blood flow.

**2.5D visualization.** Here, we asked whether the 2D map provides a fast overview of the time-dependent data. Then, the participants were questioned if the selection of single map points together with a camera changing in 3D supports the data exploration in the 3D view. Finally, we asked whether the color-coding of the ostium contour in 2D assists the orientation in 3D.

**Wall thickness visualization.** Due to the importance of the wall thickness investigation, we asked the participants to assess our different wall thickness depictions. First, the participants were asked if the wall thickness can be estimated using the semi-transparent 3D visualization. Next, we inquired the suitability of color-coding or illustrative techniques as well as using the bar charts to represent the wall thickness.

**Collaboration aspects.** Here, we asked the subjects to comment if the save and load, as well as the individual labeling of the landmarks, supports the collaboration with other domain experts.

### Results

The user study was performed on a standard desktop computer with an Intel Core i5 with 2.8 GHz, 16 GB RAM, and an NVidia GeForce GTX 1080 Ti. For all presented models we achieve a real-time performance of approximately 40 *frames per second* (FPS), except for the initial calculation of the 2D map with a computation time per case between 9 and 14 s, depending on the number of triangles, recall Section 5.2. This performance test was conducted with a resolution of  $1920 \times 1080$ , and both views (3D and 2.5D view) covered approximately half of this resolution. For the interpretation of our pre-defined Likert score categories, we provide the number  $S(\cdot)$  of experts who chose the individual classes. The overall result of the empirical evaluation is shown in Figure 42.

**Medical relevance.** All domain experts confirmed the high importance of analyzing the wall thickness ( $S(++) = 4$ ;  $S(+) = 1$ ) and wall deformation ( $S(++) = 4$ ;  $S(+) = 1$ ) for the rupture risk assessment in cerebral aneurysms. They also stated that the combined evaluation of wall thickness and deformation together with different hemodynamic attributes is important to identify rupture risk-related correlations ( $S(++) = 3$ ;  $S(+) = 2$ ). Moreover, they emphasized the importance of the data exploration during the whole cardiac cycle instead of just the systolic part, because it is unknown if the aneurysm rupture risk is higher at the systole or diastole.

**3D visualization.** All participants confirmed that the combination of color-coding and illustrative techniques enables the simultaneous exploration of two scalar attributes on the aneurysm surface ( $S(++) = 3$ ;  $S(+) = 2$ ). Two participants wished to have an additional path line filtering, e.g., vortex-representing path lines or path lines with high velocity. This would enable exploration of specific flow patterns, which are reported to be indicators of high rupture risk. The usefulness of the color-coding on the surface to highlight the NWF was rated with  $S(++) = 3$  and  $S(+) = 2$ . Moreover, they stated that the surface transparency reveals the qualitative flow behavior ( $S(++) = 4$  and  $S(+) = 1$ ).

**2.5D visualization.** All participants found that the 2.5D depiction provides a fast overview about the data ( $S(++) = 3$ ;  $S(+) = 2$ ). Moreover, all experts commented that the shape of the map together with the color-coding of the ostium establishes a visual correspondence between both views ( $S(++) = 4$ ;  $S(+) = 1$ ). Furthermore, the selection of individual points on the map, followed by changing the camera in 3D, was described as helpful ( $S(++) = 2$ ;  $S(+) = 3$ ).

**Wall thickness visualization.** The semi-transparent representation of the outer wall was rated as least suitable by most participants for the assessment of the wall thickness ( $S(+) = 2$ ;  $S(\circ) = 2$ ;  $S(-) = 1$ ). The perceived thickness depends strongly on the perspective to the surface and requires a lot of manual rotation effort. In contrast, both the color-coding as well as the illustrative rendering were valued with  $S(++) = 3$  and  $S(+) = 2$ . The bar charts were also perceived as very appropriate to assess the local wall thickness ( $S(++) = 2$ ;  $S(+) = 3$ ). Two participants indicated that the bar charts immediately communicate whether there are local minima or maxima, but the indication of the corresponding 3D position should be improved, e.g., by using brushing on the bar charts.

**Collaboration aspects.** All experts appreciated the placement and loading of landmarks ( $S(++) = 3$ ;  $S(+) = 2$ ). Moreover, the possibility to annotate the landmarks was emphasized of being helpful for the collaboration with other experts ( $S(++) = 3$ ;  $S(+) = 2$ ). One participant wished to have a temporal summary image of all placed landmarks.

	--	-	o	+	++
	Clinicians		CFD Experts		Visualization Expert
	P1	P2	P3	P4	P5
<b>Medical Relevance</b>					
The wall thickness is important to assess the rupture risk.	++	++	+	++	++
The wall deformation is important to assess the rupture risk.	++	++	++	+	++
The combination of wall thickness and deformation is important to assess the rupture risk.	++	++	+	+	++
The combined analysis of wall- and blood flow data over the cardiac cycle is important to assess the rupture risk.	++	+	+	++	++
<b>Wall thickness (can be estimated by: )</b>					
Semi-transparent depiction in 3D.	o	o	+	+	-
Color or illustrative visualization respectively.	+	++	++	++	+
Bar Charts.	+	+	+	++	++
<b>3D Visualization</b>					
The combination of color and illustrative techniques is suited to explore two attributes simultaneously.	++	++	+	++	+
The color-coding of the surface is suited to emphasize near-wall flow.	++	++	+	+	++
The surface transparency reveals the qualitative flow behavior.	+	++	++	++	++
<b>2.5D Map depiction</b>					
The 2D map provides a fast overview about the data.	++	+	+	++	++
The shape of the map together with the color-coding of the ostium establishes a visual correspondence between both views.	++	++	++	+	++
The selection of individual points on the map, followed by changing the camera in 3D supports the data exploration.	++	+	+	+	++
<b>Collaboration</b>					
The saving and loading of landmarks supports the data analysis and collaboration with other experts.	+	++	++	+	++
The possibility to annotate landmarks supports the data analysis and collaboration with other experts.	+	++	++	+	++

Figure 42: The evaluation results of the CoWaFloVis module with color-encoded Likert scores. Each box represents the answer of one expert: the two left-most boxes depict the physicians, the middle two boxes show the CFD experts, and the right-most box represents the medical visualization expert. (Image from [436].)

### 6.1.8 Discussion and Limitations

All experts stated that they were able to use our techniques without significant problems and that they would employ them for simultaneous evaluation of morphological and hemodynamic aneurysm attributes. After a short explanation of the exploration and navigation features, the participants were able to find suspicious regions on the surface. Similar to the current exploration process, we provide a 3D depiction of the aneurysm surface, because the experts are familiar with such visualizations. Moreover, we choose a 2D mapping of the 3D aneurysm surface to provide an occlusion-free overview depiction of the data. We restricted the mapping to an aneurysm and neglected outgoing vessels since the experts are focused on the aneurysm. Therefore, we needed a parametrization of the mapping that preserves the round shape of an aneurysm. For this, the selected algorithm was suitable. However, there are distortions of the 2D flattening according to the parametrization, which is angle-preserving but not area-preserving. During the evaluation, we advised the experts of possible distortions. Due to the color-coding of the ostium in both views and the fact, that the 2D map serves as an overview depiction, the experts did not perceive possible distortions as cumbersome to get a first impression of the data. Using the combination of color-coding and cross-hatching our experts were able to detect suspicious surface regions. Also, other techniques such as a 2D color scale could be used to decode two attributes simultaneously. However, previous discussions with domain experts, described by Preim and Botha [306], showed that they preferred a combination of color and isolines. The 3D bar chart should provide an overview depiction of a third attribute. To handle possible occlusions by the bar chart, the user can optionally turn it off to see just the 2D map or rotate the 2.5D view. Alternative depictions such as two juxtaposed 2D maps would not lead to occlusions, but then the user would have to combine three views, which is probably quite challenging mentally. Another possibility would be



the direct visualization of a third attribute in the 2D map using another color scale or iso-heightlines, but the visual perception of three attributes in one depiction is also complicated.

**Improvements.** The experts wished to have more interaction in the 3D view. An interactive path line seeding, e.g., at morphologically conspicuous surface regions, would improve the analysis of near-wall flow patterns. Moreover, if the user selects a point on the vessel surface, the current active attribute values should additionally be listed. For the 3D bar charts, quantification of their height using, for example, labels when the mouse hovers a bar would facilitate the exploration of the presented scalar field.

**Domain applications.** Besides the rupture risk and treatment assessment, there are other possible application scenarios of the CoWaFloVis module. Thus, our module may also be helpful to explore the predicted blood flow after different treatment options, such as coiling and stenting. Another important application field is research and education of patients and students. Moreover, CFD and FSI play an essential role also in other vascular structures, such as the aorta, to better understand cardiovascular diseases. A common disease of the aorta is an abdominal aortic aneurysm. The amount of vessel wall deformation is even larger there and the solution presented here would probably be useful in these applications as well. Unfortunately, we currently do not have similar data for aortic cases with multiple scalar fields mapped to the vessel wall.

#### 6.1.9 Conclusion and Future Work

We presented techniques for the analysis and exploration of cerebral aneurysms to improve the rupture risk evaluation. By providing a linked 2.5D and 3D aneurysm depiction, a simultaneous analysis of the aneurysm morphology such as wall thickness and deformation, hemodynamic and internal blood flow becomes possible for the first time. The combination of a 2D and 3D aneurysm visualization provides, on the one hand, a fast overview of the complex data and on the other hand a detailed exploration and assessment of rupture-prone attributes. The usage of modern visualization methods such as image-based hatching and brushing facilities enable the detection of suspicious surface regions without a time-consuming manual search. All these methods put together, we present essential morphological and hemodynamic elements for the aneurysm rupture risk assessment in an integrated visualization. Thanks to our GPU implementation we achieve real-time rendering speeds even on mid-class computers. To evaluate our methods, we conducted a qualitative expert evaluation. This evaluation indicates that our overall approach is valid and applicable in medical research and other domains.

Although we got positive feedback from the domain experts, some issues still need to be improved. First, the depiction of the tension inside the vessel should be improved to enable a more detailed exploration of the simulation results. At the moment, the stress tensor is reduced to a scalar field. However, a visualization would be necessary that depicts if the maximum tension occurs on the inner or outer wall. Furthermore, a depiction of the whole tensor using tensor glyphs would also be a helpful extension. Moreover, we should compare other mapping strategies that better preserve the aneurysm shape including adjacent vessels. This would be important for the analysis of different stent configurations and their influence on the blood flow in adjacent vessels. Besides, scenario-based evaluations should be performed, where domain experts comment on the whole exploration process using our visualization methods. This would make it possible to gain a deeper understanding of the suitability of the provided techniques. Finally, we want to improve the FSI simulation by integrating real measured wall thickness values that are expected soon, as the vessel wall imaging is an active research area.

## 6.2 MUSCAVIS - MULTIPLE SCALAR FIELD VISUALIZATION MODULE

The **CoWaFloVis** module, described in the previous section focuses on a simultaneous exploration of up to three scalar attributes in the context of morphology and flow visualization. In principle, however, correlations between more than three attributes can influence the risk. But visualizing more than three attributes together with the internal flow would lead to highly complex and overloaded depictions. Thus, we provide the **MuScaVis** module that focuses on a simultaneous exploration of multiple scalar fields on the vessel wall. Here, also the homogeneity of attributes is investigated. Experts assume that the thinner the wall and the more inhomogeneous attributes such as **WSS** or pressure are, the higher the risk of rupture. Vectorial flow information is not shown to reduce the visual complexity.

Previous attempts used information visualization techniques to uncover correlations between multiple attributes. An early example is the WEAVE system [139], where cardiac simulation data is mapped to the heart anatomy and to scatterplots and histograms that are integrated into multiple coordinated views. Thus, brushing allows to specify features in the attribute space and to link highlights corresponding locations on the heart surface. A prominent example for this line of research is the SimVis system [86, 87] that provides linked scatterplots, scatterplot matrices, and parallel coordinate views to extract features of time-dependent simulations of vehicle dynamics. Moreover, a feature-based analysis in time-dependent data involves *feature tracking* over time [180]. This means that, e.g., regions that fulfill specific conditions are detected over time and visualizations are provided to explore their temporal behavior, e.g., diagrams showing statistical properties of features over time.

Glyphs are another way to visualize multiple scalar fields. Borgo et al. [40] presented general guidelines for glyph design and summarized major merits and possible problems of glyph visualizations. In contrast to typical information visualizations such as parallel coordinates, glyphs are more suitable to convey spatial relationships encoded in the data. They can be used independently of the domain density, but an unsuitable sampling can lead to occlusions. Moreover, their design should be memorable and should allow a rapid semantic interpretation. This can be a challenging task depending on the complexity of the underlying data. Ropinski et al. [321] presented a taxonomy and guidelines for glyph-based medical visualizations. Existing glyph-based visualizations are classified to this taxonomy. Thereby, two applications were selected: glyphs for *diffusion tensor imaging* (DTI) and cardiac data to depict functional and structural parameters of the heart. Oeltze et al. [281] introduced a 3D ring-shaped glyph to represent scalar attributes of cardiac perfusion data in conjunction with their ventricular anatomical context. Meyer-Spradow et al. [253] presented an interactive placement of 3D glyphs to visualize parameters of myocardial perfusion data. Rocha et al. [317] applied *decal-maps* to the aneurysm surface representing different attributes. However, the temporal behavior of scalar data cannot be depicted. Therefore, van Pelt et al. [439] used tailor-made glyphs to show the influence of various stent scenarios on scalar attributes over time. The main drawbacks are the limited number of depicted time steps and the lack of presenting quantitative information. Tominski et al. [367] visualized spatio-temporal data on maps by using the sides of pencil and helix icons. However, this requires manual rotations to perceive correlations between scalar attributes visually.

To overcome limitations of existing methods, the **MuScaVis** module combines information and scientific visualization techniques organized in multiple coordinated views. Brushing and linking techniques aid the user to study risky correlations. We use a GPU-based implementation of statistical plots to show the temporal behavior of scalar data with interactive frame rates between different data sets. Thus, a comparison of data sets is enabled. Moreover, the generation of the 2D aneurysm map is extended to fusiform aneurysms. Besides, we present a novel 2D plot providing a temporal overview about correlations between multiple scalar attributes instead of depicting just a single quantity [425, 432]. For a more detailed analysis of attribute correlations on a specific surface region, we introduce a checkerboard visualization and provide novel glyphs to show the temporal behavior of scalar data. The checkerboard approach overcomes the reduced ability of a quantitative analysis using image-based hatching [436]. Compared to the glyphs by Tominski et al. [367], we combine cylindrical glyphs with disk-shaped glyphs that do not require manual rotations. Moreover, we extend the clustering by Glaßer et al. [132] to multiple time-dependent attributes to identify heterogeneous and homogeneous surface regions.

### 6.2.1 Requirement Analysis

A relevant aspect of the estimation of the rupture risk is to compare ruptured and non-ruptured cases according to morphological and hemodynamic characteristics. Based on this, optimal treatment advice has to be made. Since, it is still unclear, which attributes and correlations between them promote rupture, the physicians investigate color-coded attributes, e.g., [WSS](#) and pressure, on the aneurysm surface. Of particular interest are blebs. Besides, the homogeneity of attributes within regions is explored, since strongly varying quantities may indicate endangered regions. To analyze the data over time, animations are utilized, whereby only one attribute is encoded at a time. Exploring a single time step is not sufficient because it is not known at which point in the cardiac cycle the rupture risk is maximum. However, the time-dependent behavior of the data further enhances the manual exploration effort.

The goal is to tailor a visualization module such that experts can efficiently analyze scalar attributes over the cardiac cycle. The physicians stated that an overview of existing attributes and their possible correlations would facilitate in-depth research of specific surface regions. Furthermore, they wished to have the possibility to explore selected surface regions. With this, vessel wall changes such as blebs could be investigated in detail to assess the rupture probability in these regions.

Besides this, aneurysm stenting leads to different scalar quantities on the wall. Furthermore, different stent locations are possible, where the physicians have to decide on the best choice. For this purpose, techniques are needed that visualize differences of scalar quantities before and after stenting as well as a comparison of different stent scenarios. Related to this is the visualization of differences between ruptured and non-ruptured data sets. This is important to identify rupture-prone attribute thresholds, which might lead to a more reliable risk assessment. In addition to the seven more general requirements in Section 5.1 and others in Section 6.1.1, we summarize further requirements for a simultaneous exploration of multiple scalar fields on the aneurysm surface:

**Req. 11** A VISUAL OVERVIEW SHOWING ATTRIBUTE CORRELATIONS OVER TIME. A simplified representation of existing scalar fields is needed that enables fast analysis of possible attribute correlations over the cardiac cycle.

**Req. 12** A CLUSTERING SHOWING HOW HOMOGENEOUS REGIONS ARE. A time-dependent clustering of scalar attributes should be provided to be able to analyze the homogeneity of attributes within specific surface regions.

**Req. 13** VISUALIZING THE CHANGE OF ATTRIBUTES OVER THE CARDIAC CYCLE. Quantitative and qualitative visualizations are needed that show the temporal behavior of selected attributes.

### 6.2.2 General Structure

The [MuScaVis](#) module consists of four equally-sized linked views. The first view comprises a novel [2D](#) plot that shows existing attributes and their correlations over the cardiac cycle (see Section 6.2.4). In the remaining views, the aneurysm data is presented animatedly, representing the cardiac cycle, where the animation time is consistent between the views. The second view shows the scatterplots and histograms of scalar attributes (see Section 6.2.5). The third view presents a [3D](#) aneurysm visualization, whereas a [2D](#) aneurysm map is displayed in the fourth view (see Section 6.2.6). On the map, glyphs can be activated showing the temporal behavior of selected scalar attributes. Separating the visualizations into different views avoids occlusion problems. Since the simultaneous observation of three animated views is cognitively demanding, we propose two workflows, one for risk assessment and one for treatment planning, see Section 6.2.8. These each contain a default order in which the views should be used. In the following, the individual views and their interactive connection is described in more detail. First, the calculation of the [2D](#) aneurysm map is explained, since some of our visualization techniques are based on this representation.

### 6.2.3 Calculation of the 2D Aneurysm Map

The previously used [LSCM](#) approach [223] to generate the aneurysm map suffers from distortions, and manual user inputs are needed to define constraints. Therefore, we improve the map generation for saccular aneurysms in the [MuScaVis](#). Besides, existing approaches can only handle saccular aneurysms, which occur more frequently in cerebral arteries. In contrast, we integrated a mapping, which can also handle fusiform aneurysms, which occur more frequently in cardiac arteries. Similar to our previous approach, the map generation is based on the 3D aneurysm surface part, separated from the parent vessel. In the following, we describe the mapping for both aneurysm shapes.

#### *Saccular Aneurysm Mapping*

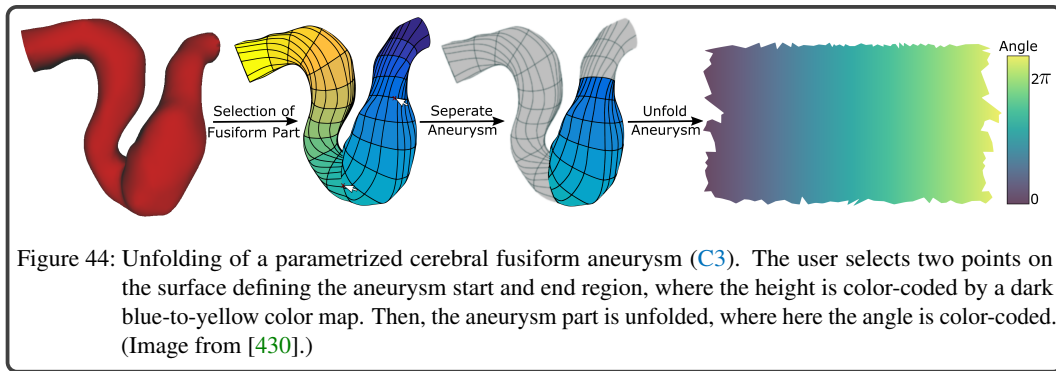
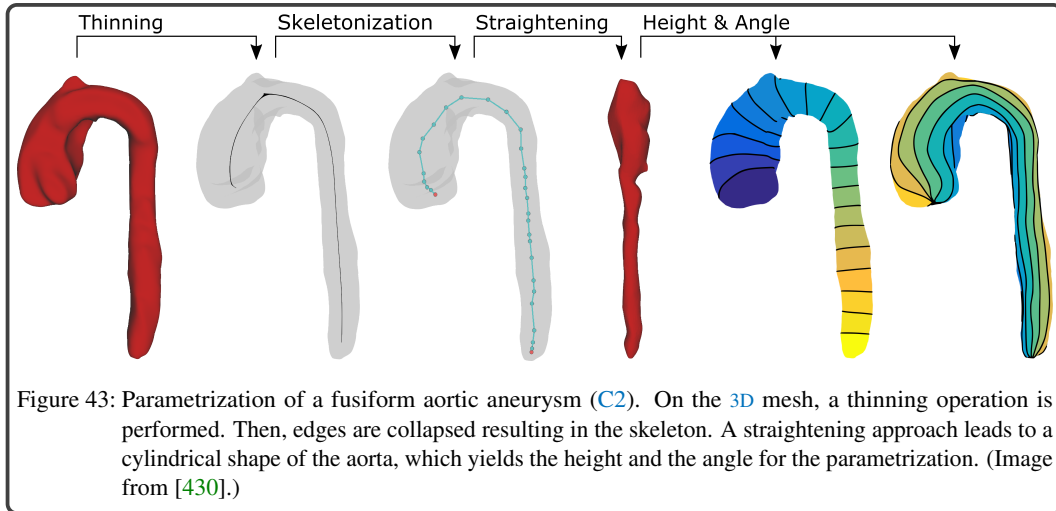
First, the aneurysm is isolated from the parent vessel geometry by using our automatic ostium detection method, recall Section 5.5.1. Instead of using the [LSCM](#) approach [223], we employ the *spectral conformal parametrization* (SCP) [261], another frequently used angle-preserving parametrization technique. Similar to [LSCM](#) every point  $\mathbf{p}_i \in \mathbb{R}^3$  on the aneurysm surface part is mapped to a point  $\mathbf{u}_i \in \mathbb{R}^2$  in the plane. We need an angle-preserving map, as we want to display a checkerboard texture on the 2D map to explore two attributes simultaneously and then project this onto the 3D surface. Using an area-preserving map would result in less length distortion, but the  $90^\circ$  condition at the corners would not be held.

In contrast to the [LSCM](#), [SCP](#) parametrizes the mesh without constraints. It tries to optimize the boundary of the mesh such that the mapping leads to appropriate results. Unfortunately, length distortions are inevitable. To reduce distortions, we further process the vertices on the 2D domain according to Zayer et al. [420]. They are iteratively moved such that the length distortion is reduced by holding the conformal condition. The one-time necessary computation of the map takes between 1.1 and 6.8 s on a standard desktop computer, depending on the number of triangles, recall Section 5.2.

#### *Fusiform Aneurysm Mapping*

The principle idea of the fusiform mapping is to determine cylindrical coordinates that represent the cylindrical aneurysm shape. Our parametrization was inspired by a geodesic parametrization approach [295] and the straightening approach developed by Angelelli and Hauser [13]. According to parametrization approaches in the field of colonoscopy [426], two works are related to the flattening of fusiform aneurysms [142, 144]. These are the only ones that just need the mesh as input. Nevertheless, for the flattening of the surface mesh the end regions need to be cut open to generate a genus 1 mesh.

In contrast, our algorithm works semi-automatically without additional user-input. Angelelli and Hauser [13] employed the vessel centerline and created consecutive planes along the centerline. Vertices on the vessel mesh between these planes need to be identified and the space defined by these planes is transformed such that the vertices are stacked. Contrarily, we generate the vessel skeleton with the method by Au et al. [20], where every point on the skeleton corresponds to vertices on the original mesh. With this, we can easily straighten the skeleton and apply the same transformation to the corresponding vertices on the mesh, see Figure 43. For this, we define a direction, e.g.,  $(1, 0, 0)$  as height direction. Afterward, we start with an endpoint of the skeleton and determine the consecutive tangent vectors along the skeleton. For every point on the skeleton, we use the previously defined tangent vector and rotate it such that it coincides with the direction vector. The same transformation is applied to the corresponding mesh vertices, which results in a straightened vessel. For every vertex on the straightened vessel, we determine the height and angle, resulting in cylindrical coordinates. Afterward, the user needs to define the beginning and end of an aneurysm by clicking on the surface. The part between the selected vertices is extracted by considering only this part, whose height is between them. Afterward, we roll the part out, see Figure 44. The generation of the fusiform maps takes between 4.3 and 9.6 s due to the thinning operation. Note that we encountered only fusiform aneurysms without furcations, which results in just two endpoints. In case of furcations, we could ask the user first to select the beginning and the ending of an aneurysm to detect the correct part on the skeleton, which can then be used for the straightening.

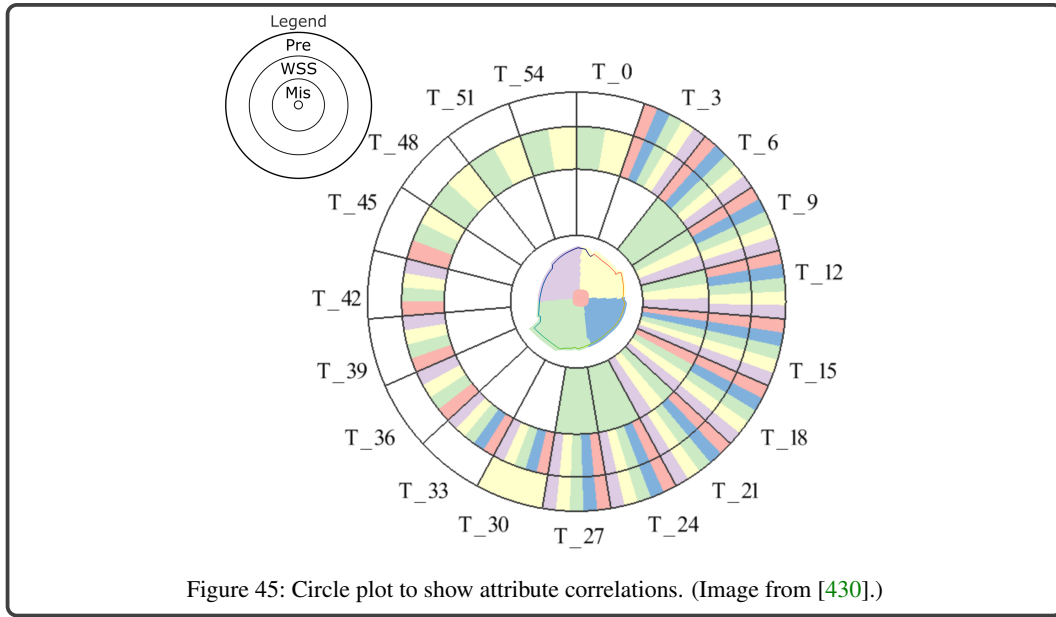


#### 6.2.4 Multi-Field Correlation Analysis using the Circle Plot

In clinical routine, the **BEP** [285], is a commonly used 2D plot to visualize quantitative perfusion data of the left ventricle at a glance. Since clinicians are used to the representation by round plots, we developed a 2D circle plot presenting possible correlations between scalar attributes over the cardiac cycle, see Figure 45. The plot presents an analogy to a clock, which is reasonable to depict periodic time-dependent data. With this, interesting surface regions and time steps according to occurring scalar values can be detected without an exhausting exploration in 3D using animations.

For this purpose, the plot area is decomposed into  $T$  equal parts, where  $T$  is the number of acquired time steps. Based on the design of a clock, the first time step starts at 12 o'clock; the direction is clockwise. Due to a large number of time steps (up to 93 in simulated data), the user can reduce the number of presented time steps. In Figure 45, every third time step is used. This is a reasonable simplification since the scalar changes between two time steps are quite low for such a high temporal resolution. It would also be possible to use the median or average of three time steps, but such metrics led only to minor changes in our data sets. Then, each of these sectors is subdivided into  $S$  equally large segments along the radius  $r$ , where  $S$  is the number of scalar fields in a data set. A legend in the top left corner shows the order of the scalar fields along the radius, where each quantity is represented by the first three initial letters.

In the center of the plot, a 2D map is shown, which is subdivided into five colored regions. Each aneurysm vertex is assigned to one of these regions. Moreover, the expert can manually define a threshold for each scalar field. If there is an aneurysm vertex, where the current scalar value is greater than or equal to the threshold, the corresponding temporal plot region is colored to the vertex's region color. For example, at  $T_{24}$ , within the red region, there is lower stress according to Mises than the



defined threshold (no red area on the inner segment), but the **wss** and pressure exceed the selected thresholds. In case that more than one map region fulfills the threshold conditions, the corresponding plot segments are further subdivided.

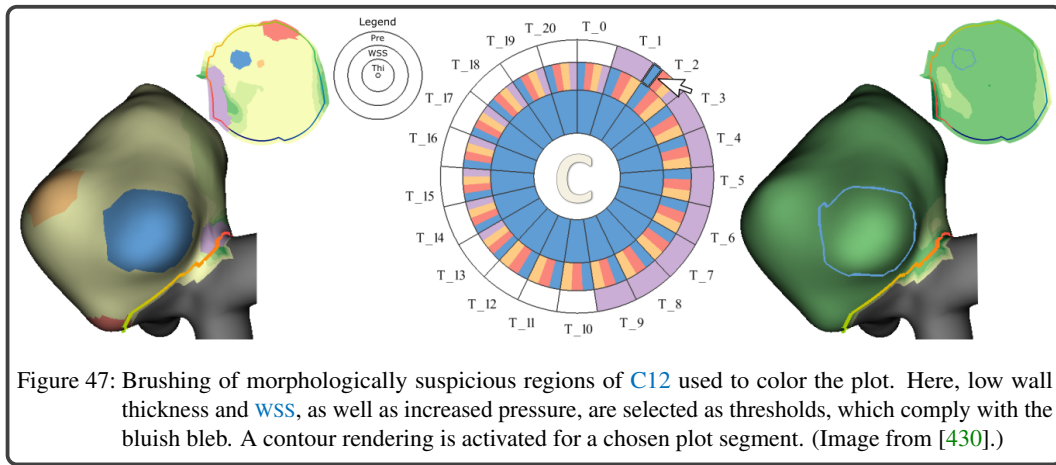
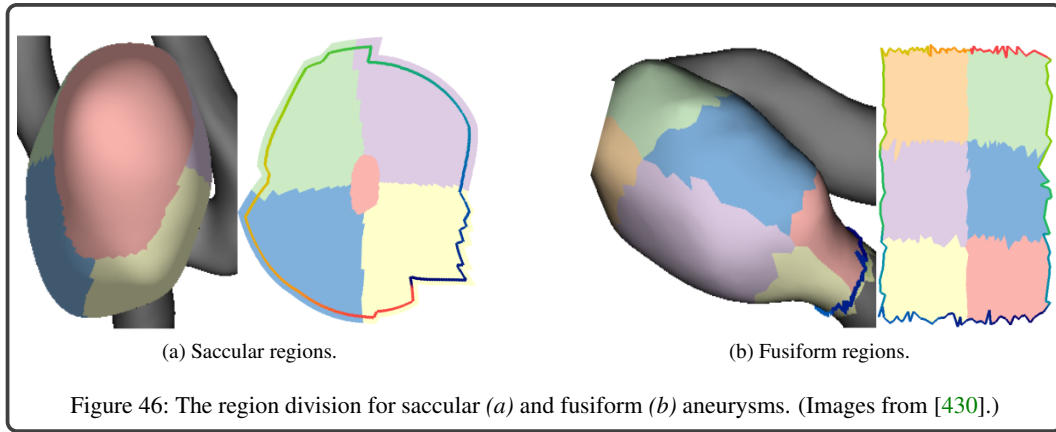
#### Region Division

As an entry point for exploration, we define an initial region division. For saccular aneurysms, we divide the map into five regions with a similar surface area, see Figure 46a. One region should represent the aneurysm dome (red area) since this is a rupture-prone area. Around the dome, we generate four more regions. First, we need a target area for each region given by  $\frac{1}{5}A_{\text{aneu}}$ , where  $A_{\text{aneu}}$  is the total aneurysm area. Second, we extract the vertex with the largest geodesic distance from the boundary, i.e., the dome point, using the heat method [78]. From the dome point, we look for a geodesic distance such that the inscribed area approximates the target area. The geodesic distance can be determined with the golden-section search [183]. The engraved area yields the first region  $R_1$ . Then, we use a sweep line from left to right, concerning the coordinates of the 2D map. Again, the golden-section search yields a position such that the remaining area is divided in half. For each half, we search for the horizontal line such that both areas approximate the target area. This yields region  $R_2, R_3$  for the left part and  $R_4, R_5$  for the right part. For fusiform aneurysms, six regions are generated based on the rectangular shape of the 2D map, see Figure 46b. Based on the cylindrical coordinates, two regions are placed along the angle, and three regions are defined along the height.

#### Plot Interaction

There are different options to interact with the circle plot. Initially, the thresholds for each scalar field are set to one-third of the corresponding range. If a threshold is changed, the coloring of the plot segments is updated in real time. This immediately shows if there is a wall region that fulfills the selected threshold conditions. Moreover, the user can brush individual regions on the 2D map or the 3D surface, where a 'C' is rendered in the plot center to indicate the 'Custom' region brushing. The aneurysm in Figure 47 exhibits multiple blebs that are brushed. Here, low wall thickness and **wss**, as well as increased pressure, are selected as thresholds. Only the blueish region fulfills all conditions, which indicates a possible rupture-prone area. To explore this region in more detail, the plot segments can be selected, where the selected segment is highlighted. Then, the animation time is set to the selected time step and a contour rendering is activated on the 2D map and the 3D surface to uncover the chosen scalar field.

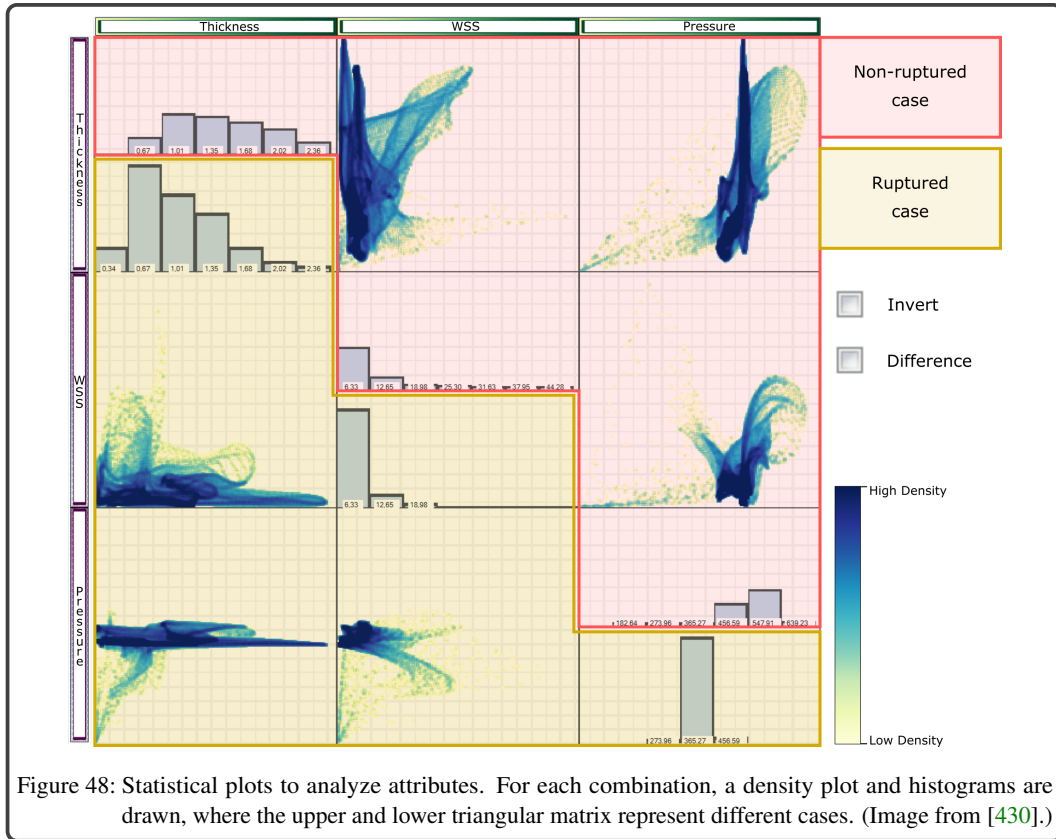




### 6.2.5 Multi-Field Correlation Analysis using Statistical Plots

The second view shows a matrix-based visualization that enables a comparison of data sets (Req. 3). Each entry of the matrix represents a combination of two scalar fields, see Figure 48. Statistical plots are shown that give an overview of the distribution of scalar quantities. Thereby, the upper triangle matrix represents the first case, e.g., a non-ruptured case. In the lower triangle matrix, another case can be loaded, e.g., a ruptured aneurysm. In the remaining views, only the first case is visualized to reduce the visual complexity.

The non-diagonal entries of the matrix present scatterplots for each scalar field combination. The diagonal entries are used for a histogram that shows occurring values of the corresponding scalar field. To show the histograms for both data sets, the diagonal entries are split and display on top the histograms of the first case and below the values of the second case. By default, we used five equally-sized bins for the histogram, where the user can change the number of bins. Besides the distribution, each plot shows the density of an attribute combination using a yellow-to-blue color scale. For this, a counter for each plot pixel is increased when the corresponding combination occurs. Blueish regions indicate often occurring values, whereas yellow areas represent values that occur only in few regions. To ensure comparability between the two data sets, statistical plots showing the same combination between the upper and lower matrix, e.g., the top right entry and bottom left entry, are depicted within the same attribute range. The attribute range depends on the minimum and maximum values of the respective scalar fields of both data sets. During the animation, the plots are updated to show the temporal development of the scalar distributions.



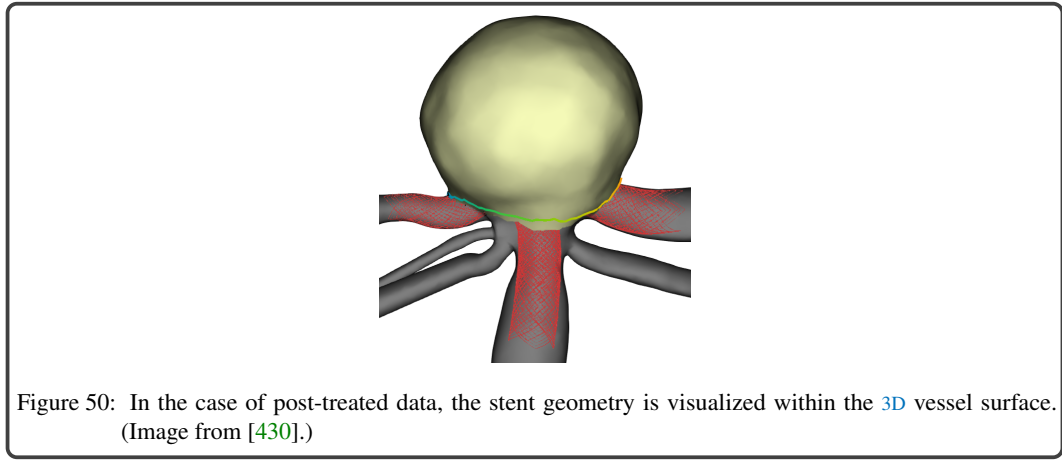
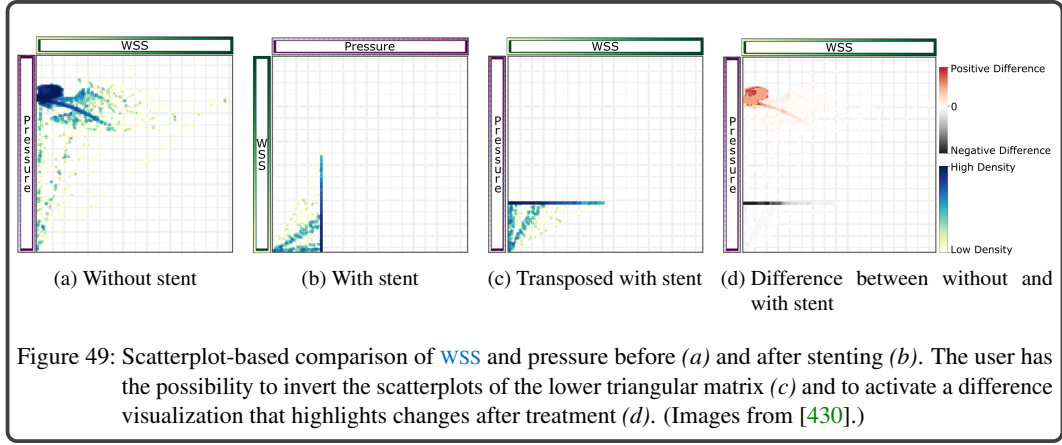
Moreover, the user can switch between a global and a local scatterplot. The global plot shows the scalar distribution independent from the view direction. The local plot shows only the visible data of the current 3D scene. This allows a local examination of specific surface regions such as blebs.

**Comparative scatterplots.** Comparing two cases requires to mentally rotate the plots in the lower triangular matrix around  $90^\circ$ . To further facilitate such comparisons, the plots in the non-diagonal entries of the lower matrix can be transposed. Figure 49 shows this for the combination of WSS and pressure for an aneurysm before (upper matrix) and after treatment (lower matrix). The first image represents the second entry of the first row in the matrix and the second image represents the bottom left matrix entry. Activating the transposed view flips the scatterplot orientation of the bottom left matrix entry, where the axis labels at the matrix sides stay the same. Then, the scatterplots before and after treatment have the same orientation, which facilitates their comparison. Moreover, a difference visualization can be activated showing changes between the cases using a gray-to-red color scale, see Figure 49d. For this purpose, the lower matrix entries are used. High attribute values represented by red areas do not longer exist after stenting since there is a positive difference. Only smaller values represented by white-to-gray areas exist after stenting. With this, the expert can immediately see if attribute values could be reduced by using a specific stent configuration. Deactivating this rendering reloads the original scatterplots of the second case. In case that more stents were simulated, the user can select which scenario should be presented in the upper and lower matrix to compare the results.

#### 6.2.6 Multi-Field Analysis on the Aneurysm Surface

The 3D and 2D aneurysm visualizations provide a detailed exploration of high-risk wall regions over time. To create a spatial correlation between both views, the ostium contour is highlighted. In case of post-treated data, we provide a depiction of existing stent configurations, see Figure 50. In the following, we explain several techniques to analyze two scalar attributes simultaneously on the 2D map as well as on the 3D surface to investigate possible rupture-prone correlations.



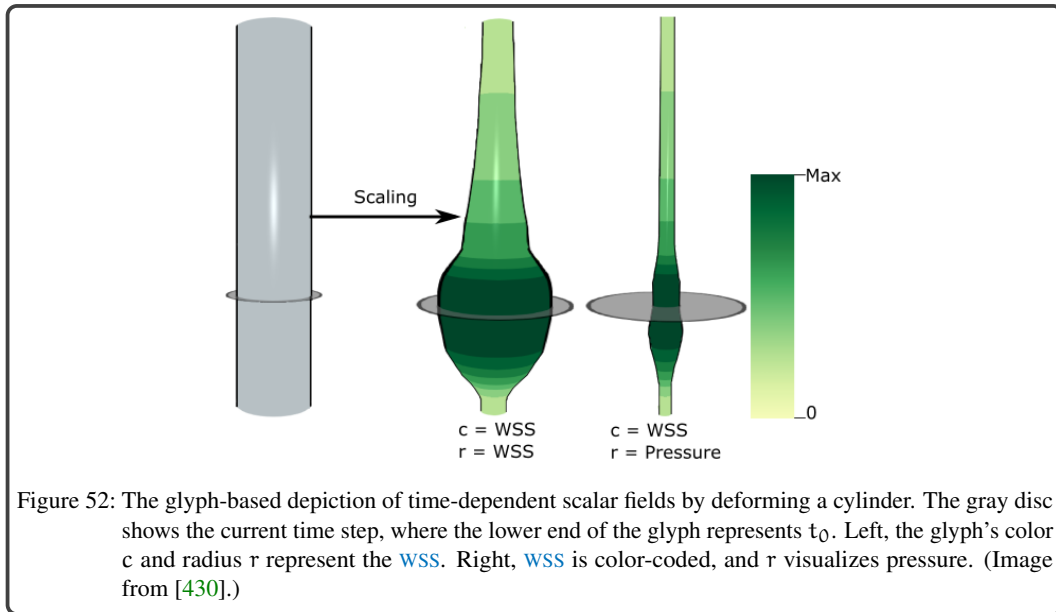
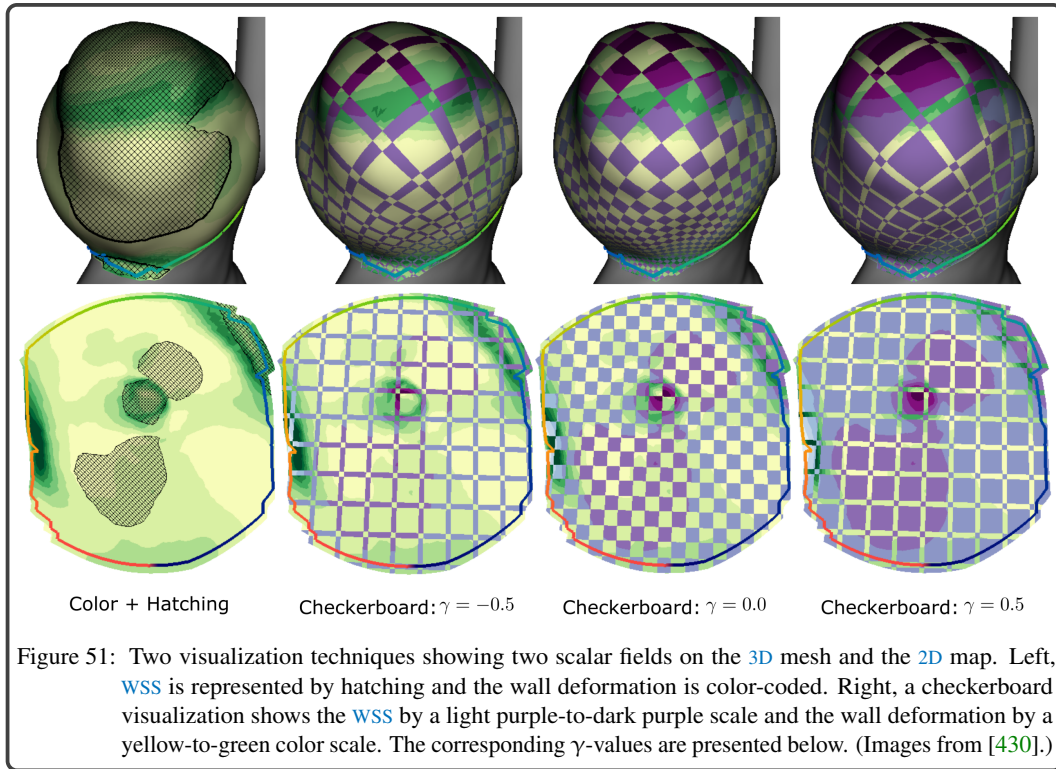


#### Attribute Visualization using a Checkerboard Visualization

The hatching approach, described in Section 6.1.4, discretizes the data range into four patterns, which restricts the quantitative analysis of the scalar field. To avoid this, we developed a checkerboard visualization that allows a simultaneous exploration of two attributes by generating a linear transition between them, see Figure 51. For this, we divided the **2D** map into a grid of size  $\text{num}_x \times \text{num}_y$ , where  $\text{num}_x, \text{num}_y$  yield the number of cells in x- and y-direction, respectively. As a default, we set  $\text{num}_x = \text{num}_y = 20$ , but the user can adjust these values. Additionally, we provide a slider ranging from  $\gamma \in [-1, 1]$ , emphasizing the first or the second field, see Figure 51. Setting  $\gamma = -1$  shows the first scalar field only, if we set  $\gamma = 1$  only the second quantity is displayed. The continuous value  $\gamma$  provides a smooth transition between both states, where  $\gamma = 0.0$  results in an equal distribution of both fields. Algorithm 1 presents the pseudo-code for the checkerboard depiction.

#### Attribute Visualization using Glyphs

As we deal with time-dependent data, the attributes on the aneurysm change during the cardiac cycle. Using the bar charts, recall Section 6.1.3, a third scalar field could be explored over time. However, they do not allow to perceive the temporal behavior of two attributes at a glance. The user has to watch an animation over the cardiac cycle. To improve this, we employ **3D** violin surfaces to show the temporal behavior of up to two attributes, which are inspired by the pencil glyphs [367]. We create a cylinder with a fixed number of points for the radius and the height, see Figure 52. The first attribute is depicted using a yellow-to-green color scale. For visualizing the second attribute, every point of the cylinder is shifted along the normal such that the radius corresponds to the specific scalar value. A disc indicates the current time at the corresponding glyph height. Figure 52 (left) shows an



example, where the [WSS](#) is encoded by color and radius, where the right glyph encodes [WSS](#) by color and pressure by the radius. The glyphs are placed on the 2D map at regular grid points using [OpenGL instance rendering](#). For the sampling rate, we use 10 % of the map's extent in x- and y-direction. Additionally, the user can add glyphs at specific regions by clicking on the map to analyze quantities at different points.

**Algorithm 1** Pseudo-code for the checkerboard. Input parameters are  $\gamma$ ,  $\text{pos.xy}$  the position of the fragments,  $x_{\max}$  the maximal x value in the map (analogous y and min), and  $\text{num}_x, \text{num}_y$ .

```

x:=(pos.x-x_min)/(x_max-x_min)*num_x;
y:=(pos.y-y_min)/(y_max-y_min)*num_y;

f_x:=floor(x); rem_x:=x-floor(x);
f_y:=floor(y); rem_y:=y-floor(y);

if( $\gamma \leq 0.0$  && mod(f_x, 2.0)==0.0)
    if(rem_x>1.0+ $\gamma/2$  || rem_x<- $\gamma/2$ )
        f_x=1.0;
if( $\gamma \leq 0.0$  && mod(f_y, 2.0)==0.0)
    if(rem_y>1.0+ $\gamma/2$  || rem_y<- $\gamma/2$ )
        f_y=1.0;

if( $\gamma > 0.0$  && mod(f_x, 2.0)==1.0)
    if(rem_x>1.0- $\gamma/2$  || rem_x< $\gamma/2$ )
        f_x=0.0;
if( $\gamma > 0.0$  && mod(f_y, 2.0)==0.0)
    if(rem_y>1.0- $\gamma/2$  || rem_y< $\gamma/2$ )
        f_y=1.0;

if ((mod(f_x, 2.0)==0.0 && mod(f_y, 2.0)==0.0) ||
    (mod(f_x, 2.0)==1.0 && mod(f_y, 2.0)==1.0))
    show(Scalarfield1);
else
    show(Scalarfield2);

```

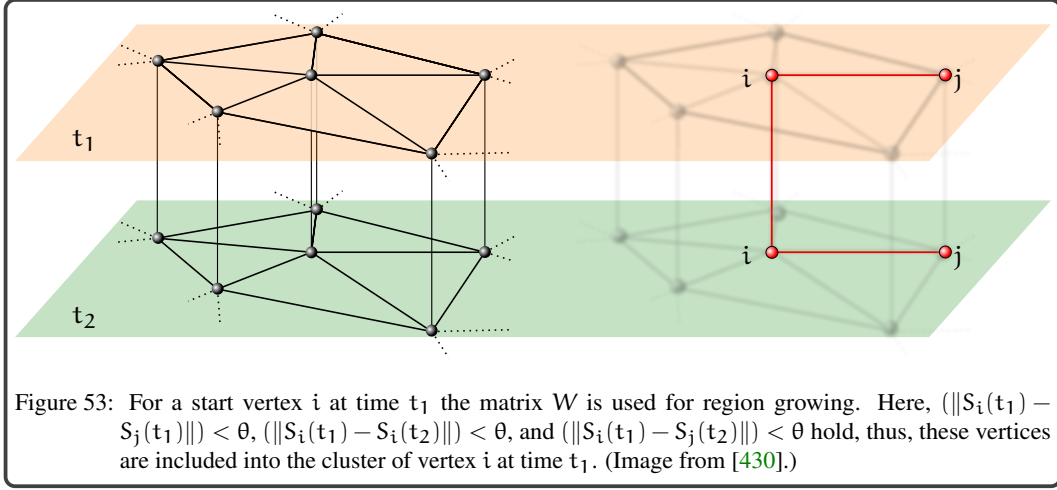
### Attribute-Based Clustering

To more easily detect regions of interesting attribute combinations, we provide a clustering scheme that results in surface regions with similar scalar values. In contrast to Glaßer et al. [132], who defined a fixed combination of **WSS** and wall thickness for a single time step, different combinations over time are possible. In our module, we list the given  $n$  attributes, noted here with  $s_1, s_2, \dots, s_n$ . To support the process of combining attributes for clustering, we assist the experts with different facilities. First, the expert can set individual weights  $w_1, w_2, \dots, w_n$  for each attribute. Initially, we use  $w_i = \frac{1}{n}$ . Based on the selected weights, an overall scalar vector  $S$  is determined for every vertex  $i$ :

$$S_i = (\sqrt{w_1}s_1(i) \quad \sqrt{w_2}s_2(i) \quad \dots \quad \sqrt{w_n}s_n(i))^T. \quad (11)$$

Furthermore, attributes can be normalized to the range  $[0, 1]$ , which is activated as a default value. Moreover, some quantities might be more interesting if low values occur instead of high values, e.g., wall thickness. The expert may rather be interested in a cluster that exhibits high **WSS** and low wall thickness, cf. [132]. For this purpose, an attribute  $s_i$  can be inverted, where  $s_i$  is changed to  $s'_i = (\max_x s_i(x)) - s_i$ .

To identify surface regions with similar scalar values during the cardiac cycle, we incorporate the temporal component of attributes into the clustering. Based on the surface mesh, composed of vertices, we use a graph structure with edge costs. We follow an approach that resembles region growing-based segmentation where a seed point is used to initiate a growing process. While in image segmentation one structure is segmented by accumulating neighboring pixels that fulfill a condition, we apply this method to different parts of the data, effectively partitioning it like a clustering. As input, a weighted adjacency matrix is used. Besides region growing, more advanced clustering techniques such as hierarchical methods [103] or spectral clustering [344] could be used. However, these approaches need a full matrix, containing the pairwise similarity values for all vertices. On average, the aneurysm



surface part in our cases consists of 5000 vertices and up to 93 simulated time steps. The resulting similarity matrix would have been the size of  $n \cdot T \times n \cdot T$ , with  $n$  the number of vertices and  $T$  the number of time steps. This would take more than 800 GB of memory. Using the region growing, a sparse matrix can be calculated, comprising 11-13 MB. First, we explain how to apply the clustering on the surface within a fixed point in time  $t$ . The adjacency matrix  $A$  is constructed by:

$$A_{ij} = \begin{cases} 1 & \text{if } (i, j) \in E \\ 0 & \text{otherwise.} \end{cases} \quad (12)$$

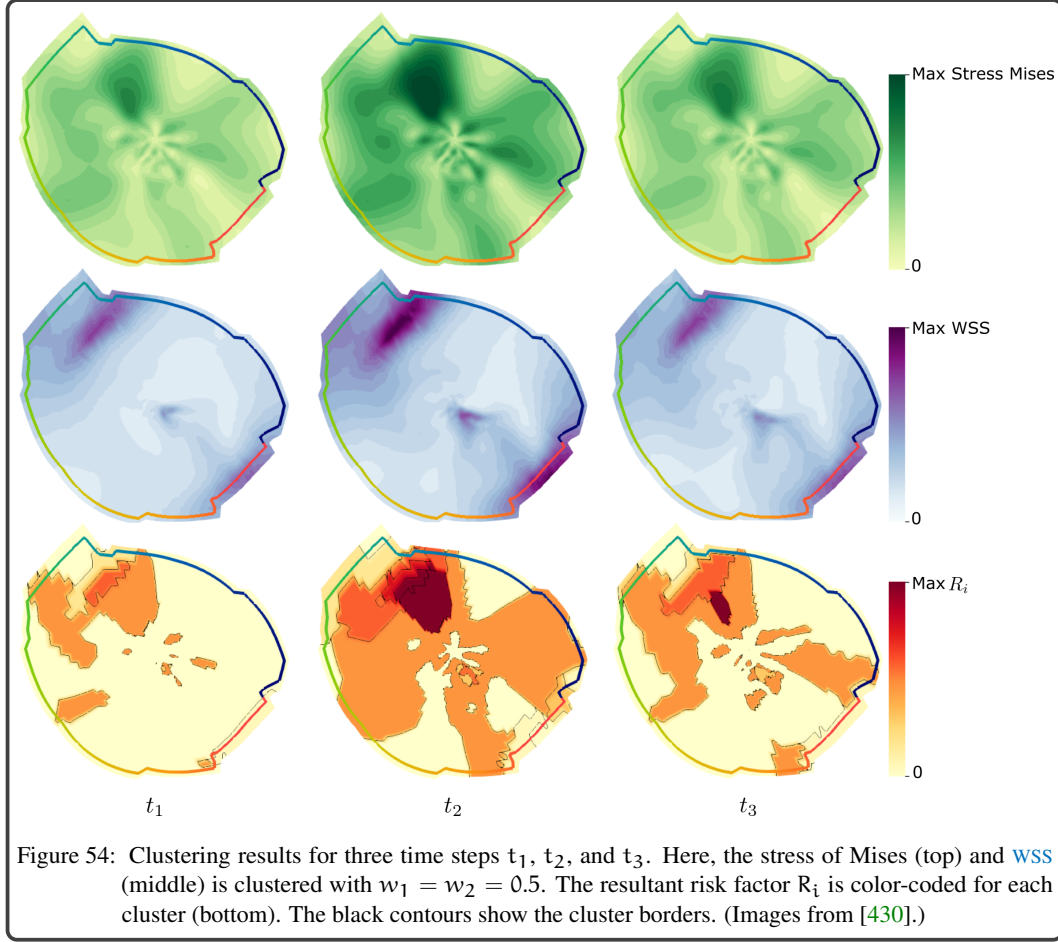
Here,  $E$  denotes the edges; thus,  $A$  is one for adjacent vertices  $i, j$ . Using  $A$  and a seed point, region growing is applied. For start point selection, we sort the vertices according to  $\|S_i(t)\|$ , where  $S_i$  is the overall scalar vector, cf. Equation 11. The vertex  $i$  with the lowest  $\|S_i\|$  is used as a seed point. Then, all vertices  $j$  that are adjacent to  $i$  are determined using  $A$ . If  $(\|S_i(t) - S_j(t)\|) < \theta$  holds, the vertex  $j$  is incorporated into the current cluster, where  $\theta$  is a pre-defined threshold. This is repeated until no more adjacent point exists that is below  $\theta$ . Then, the next point from the sorted list that was not yet visited is used as a new seed point. For  $\theta$ , we use the average of  $\|S_i(t) - S_j(t)\|$  for all point pairs on the surface. Significantly higher values result in tiny clusters, where much lower values result in quite large clusters with a broad distribution of scalar values within a cluster. However, the user can adjust  $\theta$ .

To extend the method to time-varying data, we construct a temporal adjacency matrix  $W$ . The matrix  $W$  is of size  $n \cdot T \times n \cdot T$ . Then,  $W$  is of the form:

$$W = \begin{pmatrix} A & Id & & \\ Id & A & Id & \\ & \ddots & \ddots & \ddots \\ & & Id & A \end{pmatrix} \quad (13)$$

with repetitive matrices  $A$  along the diagonal blocks ( $T$  times) given in Equation 12 and the identity matrix  $Id$  ( $n \times n$ ) on the off-diagonal blocks. By constructing  $W$ , for a fixed point in time it is simply the adjacency matrix, but changing the time from  $t_i$  to  $t_{i+1}$  only identical vertices are connected for the underlying graph, see Figure 53. With this, the sparse matrix can be generated. Then, if  $(\|S_i(t_k) - S_i(t_{k+1})\|) < \theta$  holds, the vertex  $i$  at time  $t_{k+1}$  is incorporated into the current cluster. The clustering yields non-overlapping regions, where each surface point is assigned to a cluster. It takes between 3.5 and 15 s, depending on the number of vertices and time steps. Figure 54 shows exemplary results for three time steps  $t_1$ ,  $t_2$ , and  $t_3$ , where the stress of Mises and  $wss$  is clustered using  $w_1 = w_2 = 0.5$ . To assess the homogeneity of regions, for each cluster  $c_i$  a risk factor  $R_i = \frac{1}{\#c_i} \sum_{j \in c_i} \|S_j\|$  is determined, where  $\#c_i$  is the size of the cluster. Then,  $R_i$  is color-coded

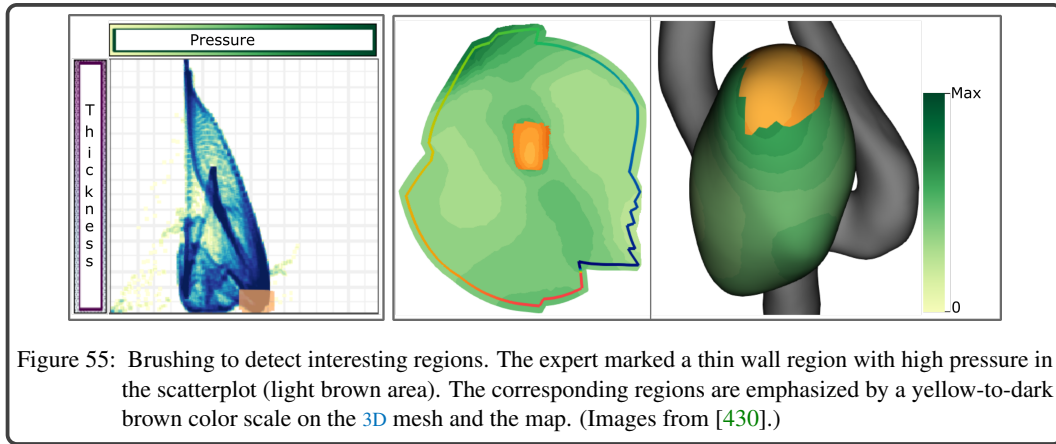
using a light yellow-to-red color scale. Inhomogeneous regions show a larger number of clusters with strongly varying risk values, whereas homogeneous regions exhibit fewer clusters with similar risk values. For clustering, we averaged the edge weights of every cluster and used this value to color-code the cluster results. Note that we also weighted the edge weights with their length, but we could not see any difference.



### 6.2.7 Brushing and Linking

The analysis of scalar quantities requires brushing and linking facilities that allow the user to explore the aneurysm morphology in interesting regions. In case the scatterplot shows interesting combinations, the expert may analyze the morphological attributes in 3D or on the 2D map. Therefore, the user can brush regions in the scatterplot, which are highlighted immediately on the 3D surface and 2D map, see Figure 55. The brush radius can be controlled with the mouse wheel. The user can also mark regions on the 3D surface or the 2D map and the corresponding regions in the other views are highlighted. Thus, linking between the scatterplot, the 2D map, and the surface mesh is simplified.

For more quantitative evaluation, statistical diagrams can be activated, see Figure 56. A diagram is rendered for each attribute and shows the minimum, maximum as well as mean value of the brushed points over time. Moreover, the areas of the 25 % and 75 % quantile are highlighted. For scalar values, the overall mean value per attribute and variance is shown. This quantitative region analysis can also either be activated for a user-selected cluster, where the clustered attributes are depicted, or a selected region in 2D or 3D based on the discretized color scale.



### 6.2.8 Evaluation and Results

The evaluation comprises three parts, where eight experts participated forming three *expert groups* (EG). EG<sub>1</sub> comprises four doctors P1 to P4 (10, 13, 18, 25 years experience in radiology). Two CFD engineers, P5 and P6, who deal with flow simulations of IA (five and eight years of experience) form EG<sub>2</sub>. EG<sub>3</sub> consists of two experts for medical visualizations P7, P8 (four and six years of experience). First, we presented the interactions and explained definable user values, e.g., the slider and number of grids using an exemplary data set. Based on this, a case study was carried out with EG<sub>1</sub> for different cases. Then, we asked all EG's to fill out a questionnaire to assess the suitability of our visualizations. For this, different exemplary data sets are presented to EG<sub>2</sub> and EG<sub>3</sub>, since they did not participate in the case study. EG<sub>2</sub> was also asked whether the distribution of attributes regarding physical plausibility can be perceived, as this is an important task of CFD experts, recall Section 5.1. Finally, we compared our visualizations to related methods dealing with the simultaneous exploration of multiple attributes.

#### Case Study

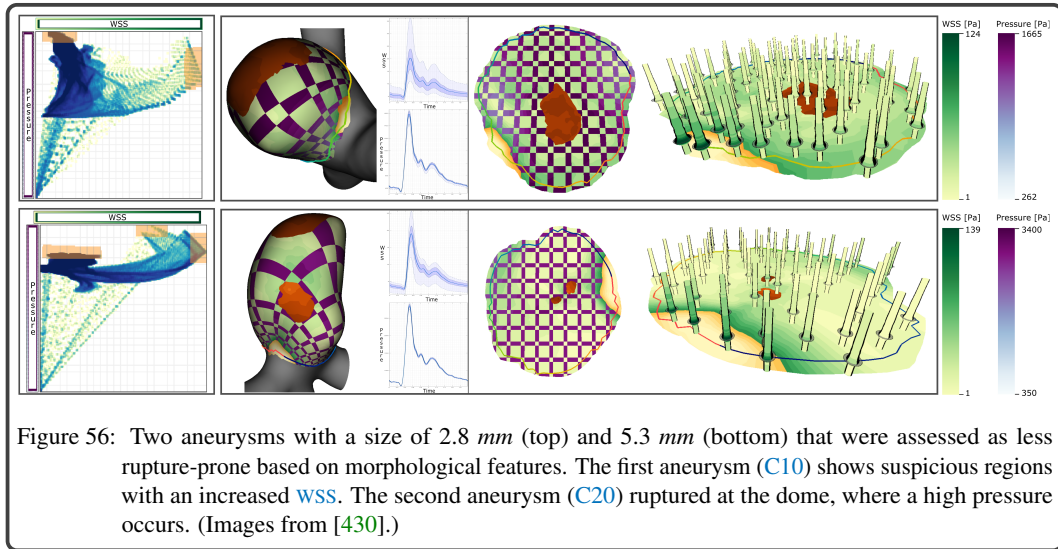
Our main goal is to improve risk assessment and treatment decision. To evaluate if the MuScaVis module fulfills this, a case study was performed focused on saccular aneurysms, see Table 1. Fusiform aneurysms are usually treated surgically due to occurring symptoms. So, in the past, the assessment of flow data played a minor role. More recently, medical studies investigated endovascular treatment options for fusiform aneurysms [252, 258], which could be an alternative to surgical interventions. However, also more complications occurred, as current stent designs seem not to be optimal for fusiform aneurysms. Thus, improving treatment is an active research area. Since we have no treated data of these aneurysms, we asked for the usefulness to be able to handle fusiform aneurysms. The experts appreciated this since soon simulations of treated cases will be available, where the 2D map would simplify data analysis.

First, we asked EG<sub>1</sub> to assess the rupture risk and treatment necessity based on morphological features for 13 data sets (C9 - C13 and C19 - C26). They were not aware of the condition (ruptured or not). Low risk was estimated for two smaller (diameter  $\leq 7$  mm), morphologically inconspicuous, non-ruptured aneurysms (C9, C10), see Figure 56 (top row). For C11, the doctors were unsure. Only considering the diameter (8 mm), they advised to treat, but no blebs were existing, so it could also be observed first. The remaining five non-ruptured cases (C12, C13, C23 - C25) are considerably larger (about 10 mm), where three of them have blebs, so the doctors advised to treat them. They predicted an increased risk for the ruptured cases C21, C22 and C26 due to blebs. For two cases, they were again uncertain, as C19 has a similar size and less risky appearing morphology to C11. C20 is even smaller (5.3 mm), see Figure 56 (bottom row), but its morphology seems a bit more conspicuous than, e.g., C10. But the doctors stated that such cases could also be observed for a while.



Then, the **MuScaVis** module was used for exploration, where we observed two workflows, one for risk analysis and one for treatment assessment. Risk analysis was explained as highly important for low-risk appearing aneurysms, having a small size or at least no blebs such as **C9** - **C11** or **C19** - **C20**. The goal is to find high-risk attribute correlations on the more harmless appearing surface. For this purpose, the circle plot was used first to identify time steps that show interesting characteristics. The plot was also described as useful to decide which attributes would be meaningful for the clustering. Then, the scatterplots and histograms are used to explore scalar distributions, since colored regions in the plot could represent singular outliers. Moreover, they brushed regions on the map, where the glyphs show increased **WSS** and pressure values. Then, they activated the statistical diagrams to analyze the brushed regions more quantitatively. Also, the checkerboards are used to analyze attributes. We observed that the experts set  $\gamma = 0$  and set the number of cells  $\text{num}_x = \text{num}_y = 25$ . Here, the spoken comment of P4 was that he first searches for abnormalities of two quantities. Then, setting  $\gamma = 1$  and  $\gamma = -1$  helps to get an impression of the regional behavior of the attribute. With this, increased pressure values are detected in the dome region, which was the rupture site of **C20**, see Figure 56 (bottom row). So a risk analysis based on morphological criteria was not appropriate. However, **C10** has similar **WSS** at the ostium region, which could also be a rupture-prone area. Similar areas were found for **C11** and **C19**, so the experts get more certain that these cases are more risky, where they were able to detect the rupture site of **C19**. For **C9** no similar regions were found, so the experts maintained their opinion of a smaller risk.

For risky appearing aneurysms, the treatment workflow follows. Here, the experts focused their analysis on regions, where they already assume a higher risk. These regions are brushed on the surface, and then the circle plot was used to analyze correlations. They selected regions within the plot and used the matrix view to investigate attribute distributions before and after treatment. They assessed how the scalar distributions are changing depending on the selected stent. If there is no clear changing of, e.g., the pressure, the selected stent or its location is probably not appropriate to prevent aneurysm inflow. For **C26**, four different stent configurations were simulated, where the experts decide for the fourth scenario to be the best, which is explained in the last paragraph of this section.



### Expert Feedback

After the case study, the experts were asked to fill out a questionnaire about the visualizations and their medical relevance. Besides questions about remarks and desired features, there were questions that could be ranked using a five-point Likert scale (—, —, —, +, ++). Meanwhile, we noted their spoken comments, which are summarized in the following. The questionnaire comprises the following aspects.



**Medical relevance.** The first aspect considers the subject's opinion about the importance of analyzing different attributes on the aneurysm wall to assess its state. Then, we inquired if changes of specific attributes before and after stenting influence the stent position. Moreover, we asked if the analysis of attributes between ruptured and non-ruptured cases is important to better understand the rupture risk.

**Circle aneurysm plot.** Here, we asked if the initial division of an aneurysm into regions is appropriate to get an overview of the data. Then, we inquired if the interactive updating of the plot based on user-selected thresholds supports a fast identification of interesting attribute correlations. In addition, the participants were questioned if the brushing of own regions allows a focused investigation of morphologically conspicuous wall regions.

**Checkerboard visualization.** Here, we inquired the suitability of the checkerboard visualization to analyze two attributes simultaneously. Moreover, we asked whether the slider and the subsequent change of the chessboard size is understandable.

**Glyph-based visualization.** Due to the importance of the time-dependent data exploration, we asked if the cylindrical glyphs are appropriate to depict the temporal behavior of two selected attributes. Next, we asked whether the manual adding of glyphs supports the analysis at specific regions.

**Brushing facilities.** We inquired if the brushing on the map helps to establish a spatial correlation between the 2D and 3D view and to detect suspicious regions in 3D. Besides, we asked whether the brushing on the scatterplots allows identification of rupture-prone regions on the 3D surface.

**Statistical visualizations.** Concerning the statistical visualizations, we asked if the scatterplots support the exploration of parameter correlations. Then, we inquired if the depiction of the scatterplots between different data sets helps to assess treatment success and rupture risk. Moreover, we asked whether the histograms provide an overview of the distribution of attributes.

**Attribute-based clustering.** Finally, we inquired the suitability of the attribute clustering. Here, we asked if the clustering supports the exploration of different attributes. Next, we asked whether the color-coding of the cluster results allows a visual perception of high-risk regions and if it allows a visual differentiation between regions with low and increased risk. Besides, we inquired if the clustering allows detecting homogeneous and inhomogeneous regions.

**RESULTS.** The user study was performed on a standard desktop computer with an Intel Core i5 with 2.8 GHz, 16 GB RAM, and an NVidia GeForce GTX 1080 Ti. For all data sets, we achieve a real-time performance of approximately 40 FPS, except for the initial calculation of the 2D map. The attribute clustering takes between 1.5 and 12 s, depending on the number of triangles and time steps, recall Section 5.2. For the interpretation of our pre-defined Likert score categories, we provide the number  $S(\cdot)$  of experts who chose the individual classes. The overall result of the empirical evaluation is shown in Figure 57.

**Medical relevance.** All domain experts, especially the radiologists emphasized the importance of analyzing different scalar fields on the aneurysm wall to assess the aneurysm's state ( $S(++) = 5$ ;  $S(+) = 3$ ). Moreover, they stated that changes of specific attributes such as the WSS before and after stenting would influence the stent position ( $S(++) = 4$ ;  $S(+) = 4$ ). Besides, they described the analysis of attributes between ruptured and non-ruptured data sets as important to better understand the patient-specific rupture risk ( $S(++) = 7$ ;  $S(+) = 1$ ).

**Circle aneurysm plot.** All participants confirmed that the initial division of an aneurysm into regions provides a fast overview of the data ( $S(++) = 3$ ;  $S(+) = 5$ ). In addition, the interactive updating of the plot based on user-selected thresholds enables a fast identification of possible attribute correlations ( $S(++) = 5$ ;  $S(+) = 3$ ). Furthermore, all experts commented that the brushing of own regions allows a focused investigation of morphologically conspicuous wall regions ( $S(++) = 6$ ;  $S(+) = 2$ ).

**Checkerboard visualization.** The suitability of the checkerboard to analyze two attributes simultaneously was rated more controversially ( $S(++) = 1$ ;  $S(+) = 4$ ;  $S(\circ) = 3$ ). Similar to that, the understandability of the slider and the subsequent change of the chessboard size was rated with  $S(++) = 4$ ,  $S(+) = 2$ ,  $S(\circ) = 2$ . P2 and P4 argued that the hatching scheme more directly indicates possible attribute correlations, whereas the experts needed more time to get used to the checkerboard.

However, they mentioned that it allows a more quantitative comparison of two attributes, which is less possible with the hatching. The medical experts could also imagine using two juxtaposed maps, where each shows one attribute, as doctors are used to combining two views mentally. However, the other experts described the identification of scalar correlations as difficult using two maps.

**Glyph-based visualization.** The cylindrical glyphs were perceived as very appropriate to depict the temporal behavior of two selected scalar fields ( $S(++) = 5$ ;  $S(+) = 3$ ). Moreover, the possibility to manually add glyphs on the map supports the analysis at specific regions ( $S(++) = 5$ ;  $S(+) = 3$ ). P8 suggested providing possibilities to filter glyphs according to specific attribute ranges, which would help to focus on high-risk regions.

**Brushing facilities.** All participants confirmed that brushing on the map helps to establish a spatial correlation between the 2D and 3D view ( $S(++) = 6$ ;  $S(+) = 2$ ) and it helps to detect suspicious regions in 3D ( $S(++) = 4$ ;  $S(+) = 4$ ). Similar to that, the brushing on the scatterplots allows an identification of rupture-prone regions on the 3D surface ( $S(++) = 7$ ;  $S(+) = 1$ ).

**Statistical visualizations.** Regarding the statistical depictions, the experts stated that the scatterplots support the exploration of attribute correlations ( $S(++) = 7$ ;  $S(+) = 1$ ). Furthermore, all experts commented that the depiction of the scatterplots before and after treatment or between ruptured and non-ruptured data sets helps to assess treatment success and rupture risk ( $S(++) = 5$ ;  $S(+) = 3$ ). Moreover, the histograms provide an overview about the distribution of scalar attributes ( $S(++) = 5$ ;  $S(+) = 2$ ;  $S(\circ) = 1$ ).

**Attribute-based clustering.** The clustering during the cardiac cycle was described as helpful for the exploration of different attributes ( $S(++) = 2$ ;  $S(+) = 4$ ;  $S(\circ) = 2$ ). P5 and P8 mentioned that a stronger user integration by providing a selection of interesting attribute ranges would strengthen the clustering. The color-coding of the cluster results allows a visual perception of high-risk regions ( $S(++) = 4$ ;  $S(+) = 4$ ) and a visual differentiation between regions with a low and increased risk ( $S(++) = 5$ ;  $S(+) = 3$ ). Finally, the experts confirmed that the clustering allows to detect homogeneous and inhomogeneous regions ( $S(++) = 1$ ;  $S(+) = 7$ ).

#### *Comparison with Related Approaches*

First, we compared the cylinder glyphs to our bar charts that also show two time-dependent attributes, recall Section 6.1.3. Then, we compared our circular plot to the pencil glyphs by Tominski et al. [367], which are designed to show multiple attributes over time. Finally, we compared the MuScaVis module to the system of van Pelt et al. [439], where flower-shaped glyphs are used to compare the influence of multiple stent configurations. Informal expert interviews are carried out to investigate if our methods are more suitable to analyze multiple attributes.

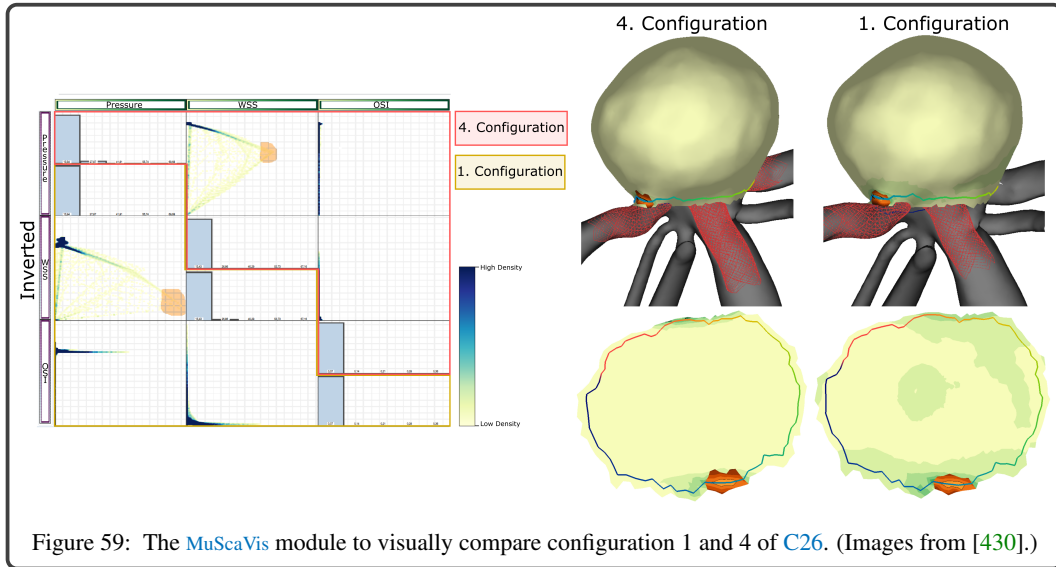
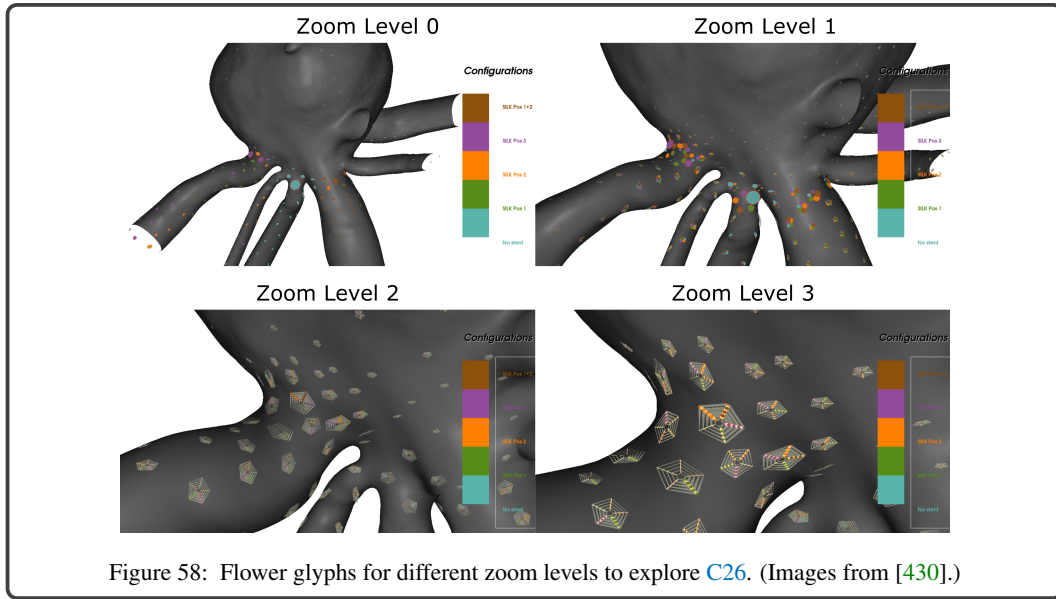
We presented different settings of two attributes to all EGs. They preferred the cylinder glyphs because the bar charts do not allow to perceive the temporal behavior of the attributes at a glance. Instead, the animation must always be viewed over the entire cycle to find hotspots. Moreover, it is difficult to locate the corresponding anatomical position on the aneurysm, since the bar charts are displayed over the 2D map. The cylinder glyphs can be easily located since they are directly placed on the map. Furthermore, the experts preferred our circular plot compared to the pencil glyphs [367]. The main criticism of the pencil glyphs was that a lot of manual rotation was required to explore attributes. It is difficult to find an appropriate camera perspective for more than three attributes, which complicates the exploration of correlations.

The system comparison was performed for C26, which was also used by van Pelt et al. [439]. It was virtually stented with four stent configurations. Since the MuScaVis module is focused on the analysis of scalar attributes on the wall, we disabled the exploration of internal flow structures in the other system. In their evaluation, two CFD experts were asked to *identify the stent leading to lowest WSS at interesting locations such as the ostium and the additional bleb*. We also asked our experts to perform this task, where we noted their spoken comments. For this purpose, we split them into two groups, comprising two clinicians as well as one CFD and one visualization expert, respectively. The first group started with the tool by van Pelt et al. [439] and proceeded with our module. For the second group, this was performed vice versa.

	<div> <div>++</div> <div>+</div> <div>0</div> <div>-</div> <div>--</div> </div>							
	Clinicians				CFD Experts		Visualization Experts	
	P1	P2	P3	P4	P5	P6	P7	P8
<b>Medical Relevance</b>								
Analyzing different scalar fields on the aneurysm wall is important to assess the aneurysm's state.	+	+	++	++	++	++	++	+
Changes of specific attributes such as the WSS before and after stenting influence the stent position.	+	+	++	+	++	++	++	+
The analysis of attributes between ruptured and non-ruptured cases is important to better understand the rupture risk.	++	++	++	++	++	++	++	+
<b>Circle Aneurysm Plot</b>								
The initial division of the aneurysm into regions is appropriate in order to get an overview of the data.	++	++	+	+	+	+	++	+
The interactive updating of the plot based on user-selected thresholds supports a fast identification of interesting attribute correlations.	++	++	++	+	+	++	++	+
Brushing own regions allows a focused investigation of morphologically conspicuous wall regions.	++	++	++	++	+	++	+	++
<b>Checkerboard Visualization</b>								
The checkerboard is suitable to analyze two attributes simultaneously.	+	+	0	0	0	+	+	++
The slider and the subsequent change of the chessboard size is understandable.	+	0	+	0	++	++	++	++
<b>Glyph-Based Visualization</b>								
The cylindrical glyphs are appropriate to depict the temporal behavior of two selected scalar fields.	++	+	++	++	+	++	+	++
The possibility to manually add glyphs on the map supports the analysis at specific regions.	+	+	+	++	++	++	++	++
<b>Brushing Facilities</b>								
The brushing on the map helps to establish a spatial correlation between the 2D and 3D aneurysm visualization.	+	+	++	++	++	++	++	++
The brushing on the map helps to detect suspicious regions in 3D.	+	+	++	++	++	++	+	+
The brushing on the scatterplots allows an identification of rupture-prone regions on the 3D surface.	++	+	++	++	++	++	++	++
<b>Statistical Visualizations</b>								
The scatterplots support the exploration of attribute correlations.	++	+	++	++	++	++	++	++
The depiction of the scatterplots between different data sets helps to assess treatment success and rupture risk.	+	+	+	++	++	++	++	++
The histograms provide an overview about the distribution of attributes.	+	0	++	++	++	+	++	++
<b>Attribute-Based Clustering</b>								
The clustering supports the exploration of different attributes.	+	+	+	+	0	++	+	0
The color-coding of the cluster allows a visual perception of high-risk regions.	++	+	+	+	++	++	++	+
The color-coding of the cluster allows a visual differentiation between regions with a low and increased risk.	+	+	++	+	++	++	++	++
The clustering allows to detect homogeneous and inhomogeneous regions.	+	+	+	+	+	+	++	+

Figure 57: The results of the evaluation of the **MuScaVis** module with color-encoded Likert scores. Each box represents the answer of one expert: the four left-most boxes depict the physicians, the middle two boxes show the **CFD** experts, and the two right-most boxes represent the medical visualization experts. (Image from [430].)

The feedback of both groups was quite similar. Figure 58 shows exemplary results using the flower glyphs. All experts criticized the high rotation and zooming effort necessary for the flower glyphs to detect critical regions. Comparing stents at different surface locations is quite challenging since the varying radii of the disks only provide indirectly quantitative information. Besides, the clinicians and **CFD** experts criticized the restriction to five presented time steps as well as that only one attribute can be explored. With this, hot spots of fluid-wall interaction can be missed. Due to these limitations, the experts were unsure about the optimal stent, since configuration 1 and 4 seems to lead to similar **WSS** distributions. Figure 59 shows exemplary results using the **MuScaVis** module for comparing configuration 1 and 4, where the scatterplots in the lower matrix were inverted. Using our module, the experts described the decision-making process as much easier, as methods are provided to explore interesting regions efficiently. The experts brushed the ostium and bleb region and analyzed the corresponding areas within the comparative scatterplots for different stents. Due to the more quantitative data representation, the experts were able to observe that configuration 4 more strongly reduces **WSS** than configuration 1, which was also described as the best option by van Pelt et al.



#### 6.2.9 Discussion and Limitations

The evaluation indicates that the MuScaVis module improves risk assessment and decision-making. All experts stated that they were able to use our module without significant problems and that they would employ it for simultaneous evaluation of morphological and hemodynamic aneurysm attributes. After a short explanation of the exploration and navigation features, the participants were able to find suspicious regions on the surface. The combination of the circle plot together with statistical plots as well as 2D and 3D views allows efficient exploration of attributes. The physicians were able to perform a more in-depth analysis leading to different or more certain assessments of rupture risk and treatment options. Moreover, our methods outperform the pencil glyphs [367] as well as the flower glyphs [439] to explore scalar data. Furthermore, compared to existing techniques [425, 432], our circle plot can depict more than one attribute. Since the checkerboard was discussed more controversially, physicians could imagine using two juxtaposed maps, where each shows one attribute, as doctors are used to combining two views mentally. However, the other experts described the detection of scalar correlations as difficult using two maps.

**Limitations.** According to the matrix view, the display size determines the number of attributes that can be visualized. We used a display with a resolution of  $2560 \times 1440$  pixels. With this, up to five attributes can be depicted so that all four views exhibit an appropriate size. Similar to this is the number of displayed attributes within a cell of the circular plot. By default, a maximum of six regions are distinguished, which can be well perceived. Theoretically, the user can brush more than six regions on the surface, which are displayed within the plot. Then, reading becomes probably more difficult. In most cases, however, experts are only interested in a few interesting regions, such as blebs, e.g., to assess whether a specific stent configuration can reduce flow attributes in these areas. Furthermore, the regular grid of the checkerboard draws the user's attention more to the regular pattern than to the data itself, which was discussed by Laidlaw et al. [201] for 2D vector field visualizations. They suggest to slightly perturbate the regular grid, called jittering. In our case, this would result in deformed grid representation. In order to check whether this draws attention more to the data, a perception-based user study would need to be conducted.

**Improvements.** The experts asked for visual hints that encode distortions between the 2D map and the 3D depiction, i.e., showing a grid in both views. For placing glyphs, the experts suggested a feature-driven sampling such that glyphs appear where the minimum and maximum values occur [354]. Moreover, P8 suggested filtering glyphs by attribute ranges, which would help to focus on high-risk regions. It may also be helpful to explore aneurysm data after other treatment options, such as coiling. This would require visualization of the used coils. According to the clustering, one expert asked for an overview that shows the progress of the cluster over time. This would allow exploring the extent to which clusters change over time. Moreover, two experts asked for a stronger user integration by providing interesting attribute ranges.

#### 6.2.10 Conclusion and Future Work

We introduced the *MuScaVis* module to explore aneurysms regarding the rupture risk and treatment planning. For this, we came up with a list of requirements that should be fulfilled. Regarding our evaluation, the module was considered successful concerning the requirements. Decision-making is supported by linked views to analyze attribute correlations over the cardiac cycle.

It is assumed that rupture is caused by the combination of different attributes, although little is known about the exact influence of individual quantities. Through the targeted exploration of suspicious surface areas, our module supports experts in generating hypotheses on the causes of rupture. This is especially important for smaller aneurysms, which seem to be morphologically less dangerous. Besides the time-dependent analysis of attributes, our module allows to compare the results of treatment options and supports physicians in their decision-making process.

For future work, the physicians proposed a workflow using the clustering for a larger aneurysm study. They want to explore attribute combinations at known rupture sites. Our clustering could be used to investigate the currently poorly understood influence of attributes on rupture by systematically changing their weights. If the clusters remain constant, the changed attribute has probably a lesser impact. The next steps are to brush regions of rupture and to analyze the data distribution.



### 6.3 COTENVIS - COMPARATIVE TENSOR VISUALIZATION MODULE

Besides morphological and hemodynamic factors, CFD simulations coupled with FSI can calculate structural stresses in the vessel walls that influence the aneurysm evolution and rupture risk. However, the obtained data are very complex. At each vertex on the aneurysm wall, a tensor is calculated, represented as a  $3 \times 3$  positive-definite symmetric matrix, that describes stresses within the aneurysm wall. Moreover, the wall is divided into an inner and outer layer, where for each vertex on both walls a tensor is available.

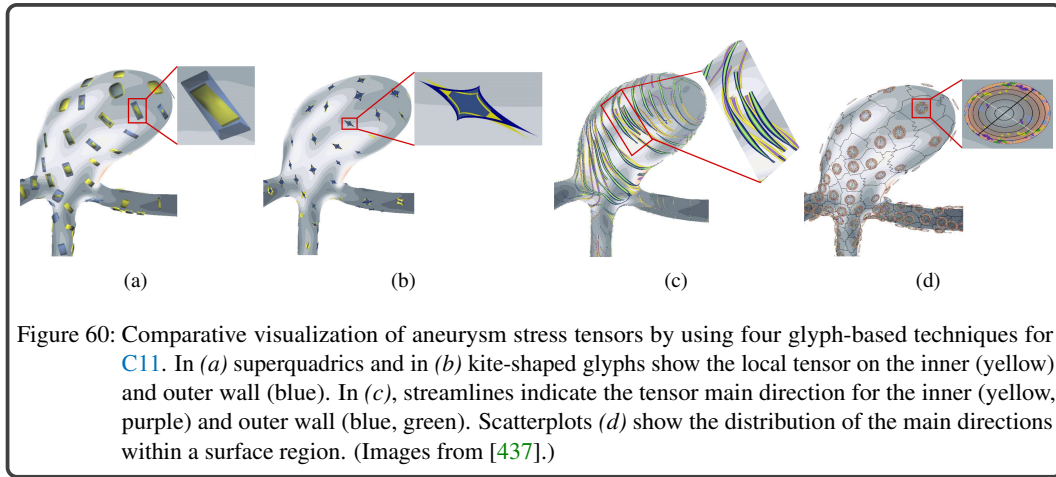
Visualizing stress tensors is strongly related to the depiction of DTI data since diffusion tensors are also represented as a  $3 \times 3$  positive-definite symmetric matrix. Ellipsoids are a common technique to visualize such tensors, where the eigenvalues and eigenvectors of a tensor are mapped to its shape and orientation [299]. Sigfridsson et al. [347] presented an approach for visualizing tensor data by combining DVR of a scalar field and glyphs. While DVR serves as a visual overview, they used ellipsoids and line-based glyphs to get detailed insights into the data. Westin et al. [404] proposed a glyph combining a sphere, a disk, and a rod to show the linear, planar, and spherical components directly. However, ellipsoids cause problems of ambiguity. Thus, Kindlmann [185] introduced *superquadric* (SQ) glyphs. SQs improve visual perception as confirmed by Jankun-Kelly et al. [168]. Schultz and Kindlmann [338] extended the SQs for general symmetric tensors. Hlawitschka et al. [157] used a GPU ray-casting technique to render a large number of SQs in interactive frame rates.

To facilitate the analysis of stress tensors on both wall layers, comparative visualizations should be used. Gleicher et al. [133] proposed a taxonomy with three major comparative designs: *juxtaposition*, *superposition*, and *explicit encoding*. *Juxtaposition* shows objects side-by-side. It is useful if the comparison is performed within an eye span. Kolesár et al. [195] introduced a more general approach to generate comparative visualizations. *Superposition* is an overlay of different objects, whereas *explicit encoding* displays relationships between objects. Both techniques are more appealing for the complex aneurysm data. Similar to our work, Zhang et al. [421] used different SQs to visualize local differences between two diffusion tensors by combining *juxtaposition* and *explicit encoding*. However, their approach is based on normalized tensor data, which is not possible for our data.

In the previous sections, methods are presented that allow a simultaneous depiction of scalar fields on the aneurysm wall, including wall thickness, wall deformation, and vectorial blood flow. However, the analysis of structural stresses without a reduction of the tensor data to a scalar field was not possible so far. Therefore, we developed the CoTenVis module that visualizes stress tensors as well as scalar and vectorial parameters describing the aneurysm morphology and hemodynamics. For the tensor depiction, we evaluated four glyph-based techniques, see Figure 60. These methods enable a comparative visualization of tensor data between the inner and outer vessel wall, which is essential to localize rupture-prone regions. Moreover, the suitability of the glyphs to perform specific tasks was evaluated in a user study with 60 participants, see Section 6.3.3. The glyph visualization is based on a details-on-demand strategy, facilitating the analysis of local stress configurations. The interactive and simultaneous exploration of these different information takes place on a 3D aneurysm depiction.

#### 6.3.1 Requirement Analysis

The typical workflow for analyzing FSI data is to reduce the tensor data to a scalar field that can be examined on the vessel surface. However, the CFD experts consider the exploration of scalar stress values as not sufficient since rupture-relevant tensor data are neglected. Thus, a visualization of local stress tensors using the common stress theory of von Mises (see [374]) is needed. This is a challenging task, as it comprises three directions with corresponding stress values that should be depicted. Moreover, the stress tensors are calculated on the inner and outer vessel wall, and the experts would prefer a simultaneous depiction of both tensors to compare their components. It would be possible to calculate differences between the walls for each component, resulting in each three scalar fields for the stress values and directions, respectively. Each scalar field could be color-coded on the surface. To correlate differences, the depictions could be juxtaposed. Then, the user would have to combine multiple views, which is quite challenging mentally. Furthermore, the experts are interested



in exploring changes in the tensor directions over time and along the aneurysm geometry. Besides, a combined visualization of all quantities would allow localizing foci of dangerous activity (e.g., where is the stress field homogeneous across the wall thickness and where not). This includes the analysis of the tensor components within a conspicuous region. Regions with a homogeneous stress field exhibit only slight changes in the tensor components. Our CFD experts assumed that thin wall regions with a homogeneous tensor field are less rupture-prone than thin wall areas with inhomogeneous tensor data. Finally, the manual effort for the time-dependent data exploration should be reduced, since this can be a time-consuming and tedious process depending on the morphological complexity. In addition to the seven more general requirements in Section 5.1 and others in Section 6.1.1 as well as in Section 6.2.1, we summarize further requirements for a comparative tensor visualization on the aneurysm surface:

**Req. 13 VISUALIZATION OF MAIN DIRECTIONS.** Display the main directions of the stress tensors during the animation.

**Req. 14 VISUALIZATION OF MAIN STRESS VALUES.** The corresponding stress values along the main directions should be depicted.

**Req. 15 STRESS TENSOR VISUALIZATION FOR BOTH WALL LAYERS.** A comparative depiction of local stress tensors on the inner and outer vessel wall is needed.

**Req. 16 VISUALIZATION OF DIRECTION DISTRIBUTION.** A visualization is needed that shows the distribution of the stress tensor directions within a surface region.

### 6.3.2 Glyph-Based Tensor Visualization

This section comprises four glyph designs to depict stress tensors that fulfill the previously defined requirements. Furthermore, we give detailed explanations about the vessel and the blood flow visualization that can be combined with the glyph depictions (Req. 5).

#### Glyph Placement

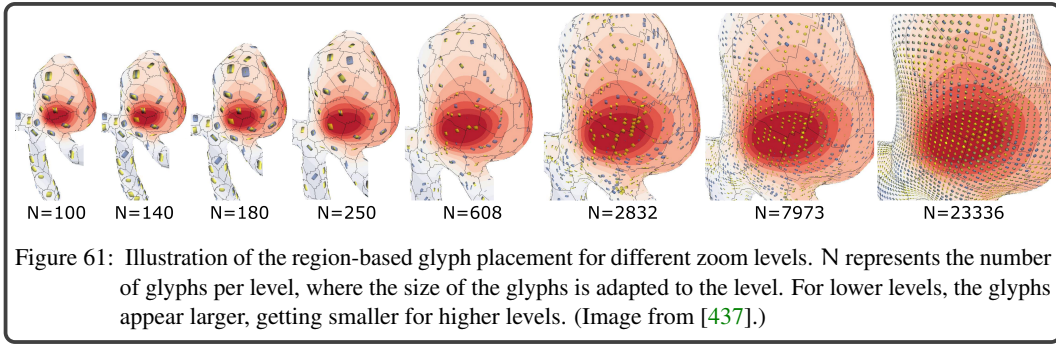
We use the surface vertices as candidates for the glyph placements. The illustration of well-sized glyphs on all vertex points simultaneously, independent from the zoom level of the camera, would lead to visual clutter. Thus, we ensure that neighbored glyphs have a minimal distance. During the interaction with the surface model, the distance may vary depending on the zoom level. This leads to a details-on-demand approach, such that glyphs are only drawn at certain regions, and whenever the user zooms into a region, more glyphs appear.



For this, a hierarchy of regions on the surface is generated. First, we start with an initial vertex  $i_1$  and determine the geodesic distance following the method by Crane et al. [78]. The heat flow is integrated by solving the heat equation  $\dot{u} = \Delta u$  at  $i_1$  for a fixed point in time  $t$  using an implicit Euler integration. Then, the normalized gradient of the heat flow  $u$  is determined:  $X = -\nabla u / |\nabla u|$ . Last, the instance of the Poisson equation  $\Delta \varphi_1 = \nabla \cdot X$  is solved, which yields the geodesic distance from  $i_1$ . Thus, the first level of the hierarchy consists of the vertex  $i_1$  and this vertex is assigned to all the other vertices, which together form a region (in the first level the whole mesh). Afterward, we search for the vertex  $i_2$  with  $i_2 = \operatorname{argmax}_{i \in V} \varphi_1(i)$ , where  $V$  encompasses all vertices of the mesh. Then, we determine the geodesic distances  $\varphi_2$  starting from vertex  $i_2$ . A vertex  $j$  is assigned to the vertex  $i_2$ , if  $\varphi_2(j) < \varphi_1(j)$ , thus the regions of both vertices are defined by means of the Voronoi area. We repeat this algorithm until the last level of the hierarchy consists of all vertices of the mesh. Note that in step  $k$  the following vertex  $i_k$  is added:

$$i_k = \operatorname{argmax}_{i \in V} \min(\varphi_1(i), \varphi_2(i), \dots, \varphi_{k-1}(i)).$$

The user can set the number of vertices  $N$  where a glyph appears. As a presetting, we used 100, 120, 140, 160, 180, 200, 250 vertices for different zoom levels. Moreover, we append six levels including the 250 representatives and each 60th, 40th, 20th, 10th, 3rd and each vertex, respectively. Figure 61 presents the glyph placement for different zoom levels  $L$  including the corresponding surface regions. The glyphs' size is adapted to the current zoom level as in [439].



### Glyph Mapping

This section presents different techniques to illustrate a stress tensor. For the remainder of this section, we use the following notation: A stress tensor  $T$  is a real-valued symmetric  $3 \times 3$  matrix:  $T \in \operatorname{Sym}(3)$ . The eigenvectors  $\mathbf{v}_1, \mathbf{v}_2, \mathbf{v}_3$  are ordered such that for the corresponding eigenvalues the property  $\lambda_1 \geq \lambda_2 \geq \lambda_3$  holds. Then, the eigenvectors express the *principal stress directions* (PSDs) of  $T$  and the eigenvalues the corresponding stress values. Note as  $T$  is symmetric, the eigenvalues are real-valued. Furthermore, the eigenvectors are mutually perpendicular. Besides,  $\lambda_3$  points in the direction of the surface normal, recall Section 3.5.6. In the following, we describe how we visualize the eigenvectors and the eigenvalues.

**3D SUPERQUADRIC VISUALIZATION** The conventional method to depict tensors is SQs [185]. Therefore, the eigenvalues are transformed into the Westin's measure [404]:

$$c_l = \frac{\lambda_1 - \lambda_2}{\lambda_1 + \lambda_2 + \lambda_3}, c_p = \frac{2 \cdot (\lambda_2 - \lambda_3)}{\lambda_1 + \lambda_2 + \lambda_3}, c_s = \frac{3\lambda_3}{\lambda_1 + \lambda_2 + \lambda_3}. \quad (14)$$

Afterward, the glyphs are defined by:

$$\mathbf{q}_z(\theta, \phi) = \begin{pmatrix} \cos^\alpha(\theta) \sin^\beta(\phi) \\ \sin^\alpha(\theta) \sin^\beta(\phi) \\ \cos^\beta(\phi) \end{pmatrix}, \quad \mathbf{q}_x(\theta, \phi) = \begin{pmatrix} \cos^\beta(\phi) \\ -\sin^\alpha(\theta) \sin^\beta(\phi) \\ \cos^\alpha(\theta) \sin^\beta(\phi) \end{pmatrix}, \quad (15)$$

with  $0 \leq \theta \leq 2\pi$ ,  $0 \leq \phi \leq \pi$ , and  $x^\alpha := \text{sgn}(x)|x|^\alpha$ .

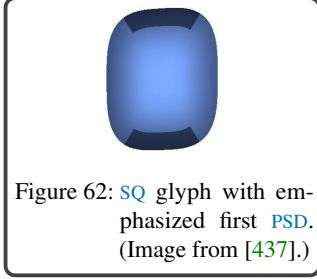


Figure 62: SQ glyph with emphasized first PSD. (Image from [437].)

If  $c_l \geq c_p$  then  $\alpha = (1 - c_p)^\gamma$ ,  $\beta = (1 - c_l)^\gamma$  and  $\mathbf{q}_x$  is used. Otherwise,  $\alpha = (1 - c_l)^\gamma$ ,  $\beta = (1 - c_p)^\gamma$  and  $\mathbf{q}_z$  is used. We use  $\gamma = 3$ . Then, the glyph is oriented such that it directs along  $\mathbf{v}_1$ , where  $\mathbf{v}_1$  and  $\mathbf{v}_2$  are scaled with  $\lambda_1$  and  $\lambda_2$ , respectively. To show tensor differences between the vessel walls, we visualized the glyphs of both walls transparent, see Figure 65. Tensors of the inner wall are depicted in yellow, whereas bluish glyphs show outer wall tensors. To visualize the PSDs even if the  $\lambda_1$  values are similar, we colored the ends in dark blue/dark yellow for the outer/inner wall respectively, see Figure 62.

**Implementation.** For rendering the SQs, we generated a plane geometry on the CPU. The plane consists of vertex indices  $\mathcal{V}$  and triangles  $\mathcal{F}$ , where  $\triangle \in \mathcal{F}$  is written as  $\triangle = (i, j, k)$  if an edge mutually connects each of the vertices  $i, j, k$ . The 3D position of the vertex  $i$  is denoted as  $\mathbf{p}_i = (x_i, y_i, z_i) \in \mathbf{R}^3$ . Each dimension  $(x_i, y_i, z_i)$  of  $\mathbf{p}_i$  is determined by:

$$x_i = 2 \cdot \pi \cdot \frac{\lfloor d/v \rfloor}{u-1}, \quad y_i = \pi \cdot \frac{\text{mod}(d, v)}{v-1}, \quad z_i = 0, \quad (16)$$

where  $\text{mod}(x, y)$  denotes the remainder of the Euclidean division of  $x$  divided by  $y$ , and  $\lfloor x \rfloor$  describes a downwards rounded operator, and let  $d \in \{0, \dots, u \cdot v - 1\}$ . Note that  $x_i \in [0, 2 \cdot \pi]$  and  $y_i \in [0, \pi]$ , which conforms with Equation 15 and the parameters  $\theta, \phi$ . For our screenshots, we used  $u = 20$  and  $v = 10$  as this yields smooth results for the glyphs. Then, we constructed the triangles  $\triangle$  with:

$$\triangle = (k, k+1, k+v), \quad (17)$$

$$\triangle = (k+v, k+1, k+v+1), \quad (18)$$

with  $k = \text{mod}(d, v-1) + d$  and  $d \in \{0, \dots, u \cdot v - 1\}$ . We transport the plane geometry to the representative positions by using *Vertex Buffer Objects* to determine the SQs according to Equation 15. For rendering them, we use the *OpenGL instance rendering*, because this effectively generates the glyphs by reducing the amount of *OpenGL* draw calls. Using *instance rendering* allows allocating memory for one plane instance that is reused to generate the following glyphs.

**2D KITE VISUALIZATION.** Inspired by Schultz et al. [338], we use kite-shaped 2D glyphs to represent  $\mathbf{v}_1$  and  $\mathbf{v}_2$  and their corresponding eigenvalues. At every vertex where a glyph should be placed, cf. Section 6.3.2, we generate a view-aligned quad oriented with the surface normal. This quad is equipped with a coordinate system  $x, y \in [-1, 1]$ , whereas the  $x$ -axis aligns with the direction of  $\mathbf{v}_1$ . Note that we scaled the axes with their stress values. Then, two glyphs are drawn on the quad, see Figure 60b. The first glyph shows the direction and the stress quantities of the inner vessel wall. Thus, for the first tensor we draw:

$$\text{Col}_{\text{Inner}} = \begin{cases} (0.94, 0.92, 0.35) & \text{if } 0 \leq x^\gamma + y^\gamma \leq 0.9 \\ (0.8, 0.79, 0.07) & \text{if } 0.9 < x^\gamma + y^\gamma \leq 1 \\ \text{discard} & \text{otherwise.} \end{cases} \quad (19)$$

We set  $\gamma = 0.6$ . The first condition describes the filled color and the second one the boundary. For the outer tensor, we use Equation 19, but with the filled color  $(0.2, 0.3, 0.5)$  and the boundary color  $(0, 0, 0.5)$ . Note that the second glyph is painted over the first tensor. However, to avoid occlusion,

the boundary of the first tensor is always drawn. Moreover, to show the PSDs even if the zoom level is quite low, we design a glyph that transforms an arrow glyph to a kite glyph based on the distance to the glyph itself. For this, we define  $z \in [0, 1]$  as the zoom level. Based on the coordinate axes  $x, y \in [-1, 1]$  of the view-aligned quad, we define an allowed  $y$ -range:

$$y_{\text{allow}} = \begin{cases} \frac{1}{4} & \text{if } |x| \leq x_0 \\ \left(1 - \left(\frac{x-x_0}{x_1-x_0}\right)^\gamma\right)^{1/\gamma} & \text{if } x_0 \leq |x| \leq x_1 \\ 0 & \text{otherwise.} \end{cases} \quad (20)$$

$$x_0 = \frac{1}{2} \cdot (1 - z), \quad x_1 = 0.9.$$

For every fragment, we test if  $|y| \leq y_{\text{allow}}$  holds. If this is the case the fragment is drawn, otherwise, it is discarded. Additionally, we draw a border around the glyph and fill the arrow with the color of the border if  $|x| \geq \max(\frac{1}{2} \cdot (1 - z), 0.3)$ . Figure 63 shows the transition of the arrow to the kite depending on the zoom level.

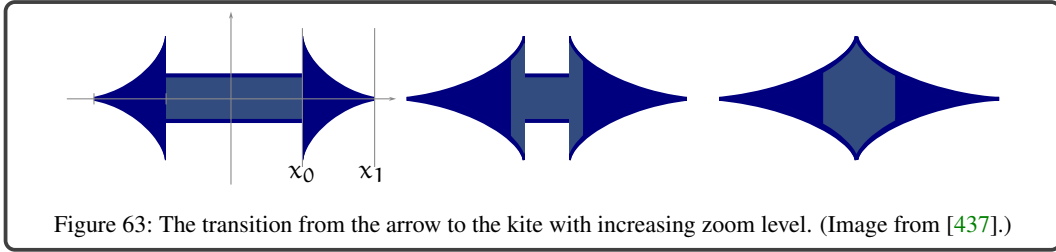


Figure 63: The transition from the arrow to the kite with increasing zoom level. (Image from [437].)

**Implementation.** Similar to the SQs, we use the generated plane to construct the glyphs. In contrast to the superquadrics, we do not transform the plane. First, we align the plane to the normal vector such that it lies in the tangent space. Then, we use the PSDs as a coordinate system on the plane. This yields texture coordinates which can be used in the fragment shader to apply Equation 19.

**2D STREAMLINE-BASED GLYPH VISUALIZATION.** Another approach to visualize the tensor is to determine *streamline* (SL) glyphs on the surface along the first PSD, see Figure 64.

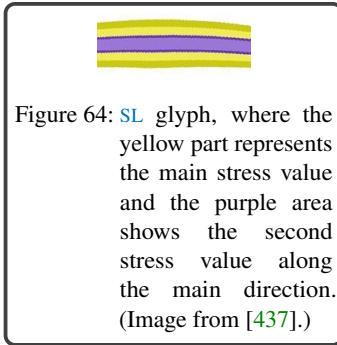


Figure 64: SL glyph, where the yellow part represents the main stress value and the purple area shows the second stress value along the main direction. (Image from [437].)

We follow the idea by Lawonn et al. [218], who generated quads along the streamlines to illustrate information. The streamline generation is based on the *ConFIS* method [219], but instead of using the principal curvature directions, we use  $\mathbf{v}_1$ . For every generated quad, we assign coordinates which represent its width (orthogonal to the first PSD) in the range  $[-1, 1]$ . The quad is then visualized with a violin plot. The radius of the outer violin plot represents  $\lambda_1$  and the radius of the inner violin is determined with  $\lambda_2$ . We enable the possibility to depict streamlines for the inner and outer vessel wall simultaneously, see Figure 60c. Thereby, yellow and purple are used to depict the eigenvalues on the inner wall and blue and green show  $\lambda_1$  and  $\lambda_2$  on the outer wall.

**Implementation.** The streamlines are computed on the GPU. For every triangle  $\triangle$  a seed point is generated at the midpoint  $\mathbf{p}_\triangle$ . At  $\mathbf{p}_\triangle$ , we use the average of the PSDs of the vertices belonging to this triangle to determine the mean PSD  $\bar{\mathbf{v}}_1$ . Afterward, the point is traced along the mean direction by:

$$\mathbf{p}_{\text{new}} = \mathbf{p}_{\text{old}} + h\mathbf{v}(\mathbf{p}_{\text{old}}), \quad (21)$$

with a step size  $h$  of half of the mean of all edge lengths on the surface. This yields the Euler integration, where at the first iteration step  $\mathbf{p}_{\text{old}} = \mathbf{p}_\triangle$  and  $\mathbf{v}(\mathbf{p})$  denotes the barycentric interpolation of  $\mathbf{v}_1$  at the triangle vertices at position  $\mathbf{p}$ . After every step, we check if the point leaves the triangle. If

this is the case, we update the current triangle to determine the subsequent iteration steps. Additionally to the position of the streamline points, we store the triangle ID. This enables to determine the current triangle normal, which is necessary for the generation of the quads on the surface [218]. Moreover, texture coordinates can be used to employ the violin plot in the fragment shader.

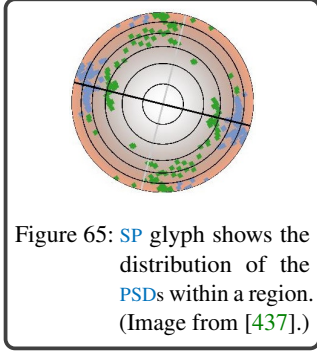


Figure 65: SP glyph shows the distribution of the PSDs within a region. (Image from [437].)

**2D SCATTERPLOT GLYPH VISUALIZATION.** We propose different glyphs to encode the PSDs. However, the presented methods indicate the local stress values, but lack of showing the direction distributions over a region (Req. 16). Thus, we developed a scatterplot-based glyph to display the PSDs at the representative  $r_i$ , see Figure 65. This gives an overview of the stress direction distribution according to the vertices in that region  $\mathbb{R}_i$ . The *scatterplot* (SP) glyph is calculated as follows: first, the representative spans the tangential space, which is given by the normal vector  $\mathbf{n}_{r_i}$  at this vertex  $r_i$ . Second, the first two PSDs yield an orthogonal coordinate system on the tangent space. Finally, the PSDs of the other vertices  $j \in \mathbb{R}_i$ , which correspond to the region  $\mathbb{R}_i$  are determined and mapped to

the tangent space of  $r_i$ . Based on the discussion with the domain experts, we used a simple projection of the PSDs onto the tangent space. For this, we define the length-preserving projection operator as:

$$P_{\mathbf{n}}(\mathbf{v}) = (\text{Id} - \mathbf{n} \cdot \mathbf{n}^T) \frac{\mathbf{v}}{\|(\text{Id} - \mathbf{n} \cdot \mathbf{n}^T)\mathbf{v}\|} \cdot \|\mathbf{v}\|, \quad (22)$$

where  $\text{Id}$  denotes the identity matrix and  $\|\cdot\|$  the Euclidean length.  $P_{\mathbf{n}_{r_i}}(\mathbf{v})$  projects the vector  $\mathbf{v}$  to the tangent space of the representative  $r_i$ . This mapping does not preserve perpendicularity of the two PSDs, but the result is more intuitive for our domain experts as it supports the idea to look from above onto the region  $\mathbb{R}_i$  and observe the directions. After the projection, we transformed the coordinates  $(x', y', z') \mapsto (x, y)$  to the coordinate system of the representative tangent space. Then, we draw small circles on the tangent space at the coordinates  $(x, y)$  and  $(-x, -y)$  as the sign is not uniquely determined. This could be done for PSDs on the inner and outer vessel wall, see Figure 64. Additionally, we draw the coordinate axes, which correspond to the PSDs of the representative vertex, where black is used for the first PSD. Then, equidistant circles are drawn for a better estimation of the stress values. The background color changes linearly from fully transparent to orange. This yields the possibility that the user gains insight into the color-coded scalar field on the surface at the current representative vertex. In the following, we explain the implementation.

**Implementation.** The SP glyph is constructed as a view-aligned quad. To show the PSDs of the vertices at the region  $\mathbb{R}_i$ , we use the OpenGL extension `SHADER_IMAGE_LOAD_STORE`. As we use maximal 250 regions, we constructed an image of size  $(25 \cdot \text{res}) \times (10 \cdot \text{res})$ . Thus, we divide the image in 250 regions with a size of  $\text{res} \times \text{res}$ . We used  $\text{res} = 200$ . Every vertex  $j$  inherits its PSDs  $\mathbf{v}_1^j, \mathbf{v}_2^j$ , their assigned region  $\mathbb{R}_i$ , and the representation's information like its PSDs and the normal. Every vertex determines first the region in the image by computing:

$$u = \text{mod}(i, 25), v = \left\lfloor \frac{i}{10} \right\rfloor.$$

Afterward, the projection operator  $P_{\mathbf{n}_{r_i}}(\mathbf{v})$  is applied to  $\mathbf{v}_1^j, \mathbf{v}_2^j$ , which yields the projected PSDs. A coordinate transformation leads to the coordinates  $(x, y)$  and  $(-x, -y)$  for one eigenvector (so four coordinates are determined for both PSDs). Finally, the OpenGL function `imagestore()` is applied to draw the directions at the corresponding image position. To display the result, the view-aligned quad of the representative  $r_i$  loads the fragment's color at the corresponding image position, which is given by the region  $\mathbb{R}_i$ .

### 6.3.3 Evaluation and Results

To assess the quality of the tensor glyphs, we conducted two evaluations. The first one was an informal evaluation with four domain experts, one physician P1 with an experience of 16 years, two CFD experts P2, and P3 with five and eight years of experience, respectively, and one visualization expert P4 with a strong focus on cerebral aneurysms, with six years of experience. The evaluation was performed on a standard desktop computer with an Intel Core i5 with 2.8 GHz, 16 GB RAM, and an NVidia GeForce GTX 1080 Ti. For all the presented methods, we achieved a real-time performance of approximately 35 FPS. The second evaluation was conducted with 60 probands (23 female, 37 male). Their age ranged from 20 to 48 years. Among them were 44 students from computer science and medical engineering, 12 researchers with a background in medical visualization, and the four domain experts. They had to answer a questionnaire that assesses how well certain quantities concerning the glyph tensors can be estimated. Section 6.3.3 covers the expert evaluation, and Section 6.3.3 deals with the user study.

#### Informal Expert Evaluation

The evaluation was conducted in two steps:

1. Introduction to the glyph-based visualizations of the stress tensors.
2. A questionnaire to inquire the importance of aneurysm stress tensors, and the glyph designs.

The first step is necessary for the experts to familiarize themselves with the visualization techniques. Afterward, the experts answered the questionnaire. All questions were divided into different categories, which were answered using a five-point Likert scale (—, —, ○, +, ++). For the analysis of the Likert score, we provide the number  $S(\cdot)$  of experts who chose the individual scale. The overall result of the empirical evaluation is shown in Figure 66.

**Medical relevance.** In this category, we inquired about the importance to estimate the stress tensor, the combination of stress tensors with scalar and vectorial data, and the visualization of stress tensors during the cardiac cycle. The first two questions were rated with  $S(++) = 2$  and  $S(+) = 2$ . P1 stated “[...] the estimation is quite important for the analysis of the potential rupture risk.” Only question three was rated as highly important by all users ( $S(++) = 4$ ). P2 and P3 stated that vessel regions, where strong local changes of the PSDs occur during the cardiac cycle could be rupture-prone areas.

**Evaluation of the tensor glyphs.** This category investigates the tensor glyphs. We asked for all glyphs (superquadrics = SQs, kites, streamlines = SLs, scatterplots = SPs), which can be used to:

- a) estimate the PSDs of the outer wall,
- b) estimate the main stress values of the outer wall,
- c) estimate the PSDs simultaneously of the outer and inner wall,
- d) estimate the main stress values simultaneously of both walls.

For **question a)**, the participants valued the SQs with  $S(+) = 4$  and the kites with  $S(++) = 2$ ,  $S(+) = 2$  as most suitable to estimate the PSDs. P3 argued that “[...] the kites give me a clear insight to the data.” The SLs ( $S(++) = 3$ ;  $S(\circ) = 1$ ) and the SPs ( $S(+) = 2$ ;  $S(\circ) = 1$ ;  $S(-) = 1$ ) are valued more divergent. For **question b)**, the kites were rated as the best glyphs with  $S(++) = 2$  and  $S(+) = 2$ . Also the SQs are suitable to determine the PSDs ( $S(++) = 2$ ;  $S(+) = 1$ ;  $S(\circ) = 1$ ). Similar to question a), the SL ( $S(+) = 2$ ;  $S(\circ) = 2$ ) and the SPs ( $S(+) = 3$ ;  $S(\circ) = 1$ ) are evaluated more different. For **question c)**, the kites and the SLs were the favorable choice that were valued in the same way with  $S(++) = 2$ ,  $S(+) = 1$  and  $S(\circ) = 1$ . The SQs were also perceived as very appropriate to assess the PSDs ( $S(+) = 3$ ;  $S(\circ) = 1$ ), whereas the SPs were least suitable for this task ( $S(+) = 1$ ;  $S(\circ) = 2$ ;  $S(-) = 1$ ). For **question d)**, all experts confirmed that the kites are very appropriate to assess the local main stress values ( $S(++) = 1$ ;  $S(+) = 3$ ). Also the SQs are suitable to determine the local main stress values ( $S(++) = 1$ ;  $S(+) = 2$ ;  $S(\circ) = 1$ ). In contrast, the SLs were perceived as least suitable ( $S(\circ) = 4$ ), whereas the SPs were rated with  $S(+) = 2$  and  $S(\circ) = 2$ .

	--	-	o	+	++
	Clinician	CFD Experts		Visualization Expert	
	P1	P2	P3	P4	
<b>Medical Relevance</b>					
Estimating stress tensors on the vessel walls is important to assess the aneurysm's state.	++	+	++	+	
The analysis of stress tensors in combination with scalar and vectorial data is important to assess the aneurysm's state.	++	+	++	+	
The visualization of stress tensors during the cardiac cycle is important to assess the aneurysm's state.	++	++	++	++	
<b>Estimate the PSDs of the outer wall by using:</b>					
Superquadrics	+	+	+	+	
Kites	+	+	++	++	
Streamlines	++	++	++	o	
Scatterplots	-	o	+	+	
<b>Estimate the main stress values of the outer wall by using:</b>					
Superquadrics	+	++	o	++	
Kites	+	++	+	++	
Streamlines	+	o	+	o	
Scatterplots	+	+	o	+	
<b>Estimate the PSDs simultaneously of the outer and inner wall by using:</b>					
Superquadrics	o	+	+	+	
Kites	+	++	o	++	
Streamlines	++	++	+	o	
Scatterplots	-	+	o	o	
<b>Estimate the main stress values simultaneously of both walls by using:</b>					
Superquadrics	+	o	++	+	
Kites	+	+	++	+	
Streamlines	o	o	o	o	
Scatterplots	+	o	o	+	

Figure 66: The results of the expert evaluation of the CoTenVis module with color-encoded Likert scores. Each box represents the answer of one subject: the left-most box depicts the physician, the middle two boxes show the CFD experts, and the right-most box represents the medical visualization expert.

#### Evaluation of the Estimation of the Glyph Tensors

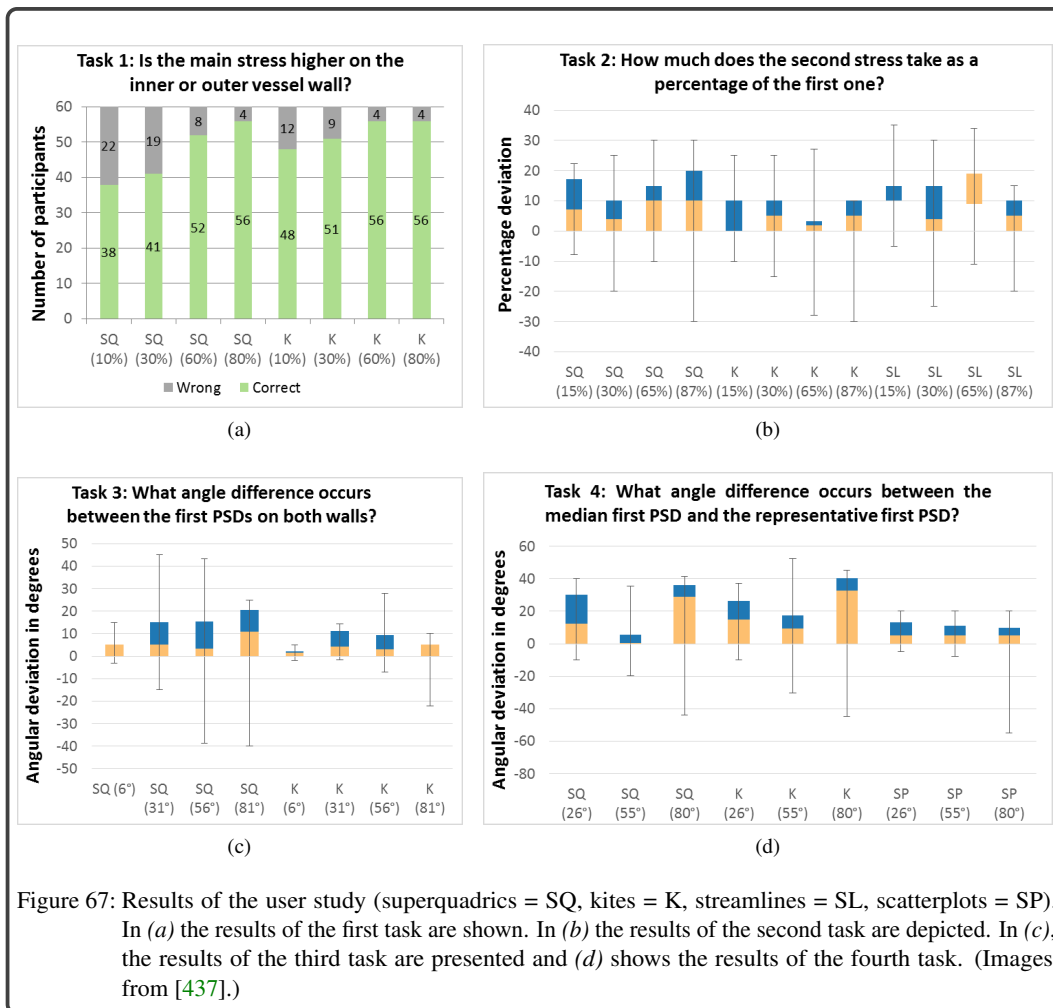
The second evaluation analyzed how well the tensor glyphs served to estimate certain quantities. We prepared an additional questionnaire with screenshots where no framework was involved. The 60 participants were shown different scenes with different glyph types. First, we showed them randomly ordered scenes where we asked whether the stress value is higher for the outer or for the inner vessel wall. Then, we analyzed the results to get a first impression which glyph might be better for the visualization of this task. We did this with four tasks, where the probands should assess:

1. whether the stress is higher for the inner or the outer vessel wall,
2. how much the second stress value takes as a percentage of the first one,
3. what angle difference occurs between the PSDs on both walls,
4. what angle difference occurs between the median main direction and the main direction of the region representative.

The results of these tasks can be found in Figure 67. For the **first task**, we compared the SQs with the kites, where we pretended different levels of difficulty with 10 %, 30 %, 60 % and 80 % difference



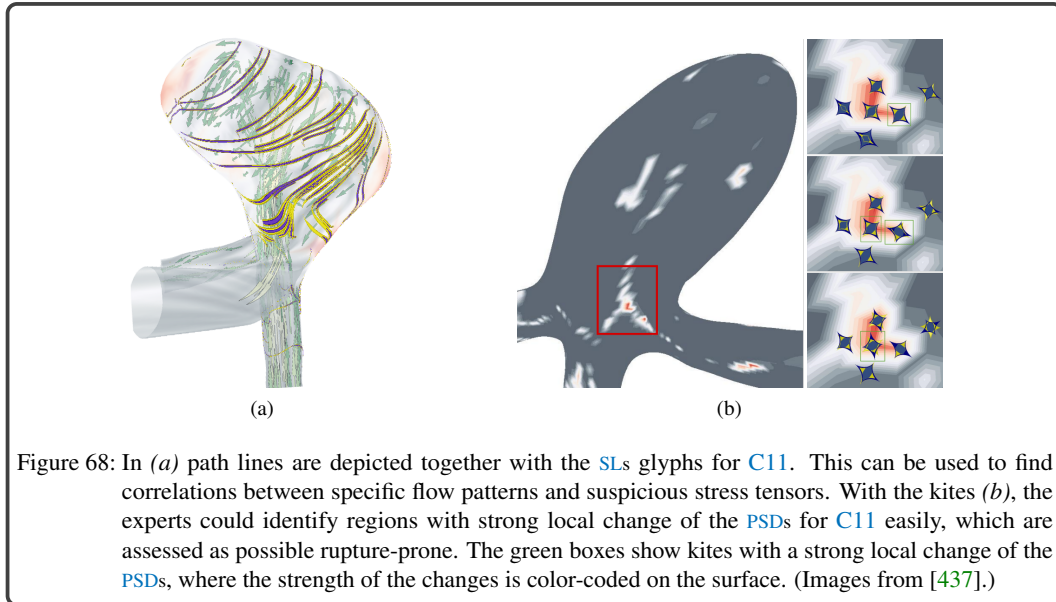
between the inner  $\lambda_1$  and outer  $\lambda_1$  value, see Figure 67a. Here, we excluded the SLs, because of possible occlusions between lines for the inner and outer wall. For more similar glyphs on both walls (10 %, 30 %, 60 % size difference), the kites were more suitable to localize the higher stress value. Compared to the SQs, twice as many answers were correct for the kites. For huge differences in size (80 %), the results were equally well. The results of the **second task** are depicted in Figure 67b by using box plots. These display the deviations of the users' given values to the correct value. Therefore, we subtracted the users' values by the ground truth. The first and third quartiles are depicted in orange and blue as well as the minimum and maximum. Here, the probands should approximate the relationship between  $\lambda_1$  and  $\lambda_2$  for the SQs, the kites and the SLs on the inner wall based on four levels of difficulty. Again the SQs and kites lead to similar good results. If the second value is comparatively small, (15 %, 30 %) the kites have a slightly lower third quartile in both cases. For 65 %, the kites dominated clearly over the SQs and the SLs in both quartiles. For 87 %, the kites and the SLs give similar results but were more suitable as the SQs. The **third task** analyzes the angle difference between the PSDs of the inner and outer wall, see Figure 67c. Here, the SQs and kites were compared, whereas the SLs cannot be used similarly to the first task. The kites dominated clearly over the SQs in all cases. In the **fourth task**, the SQs and kites are evaluated against the SPs to determine the angle difference of the median main direction to the main direction of the representative within a given surface region. Therefore, in all shown pictures a coordinate system within a surface region was given, where the x-axis represents the main direction of the representative. Here, the SPs were more suitable compared to the SQs and the kites. The distribution of the angle values is smaller than for the SQs, and the kites and the third quartile values are close to the exact value, see Figure 67d.



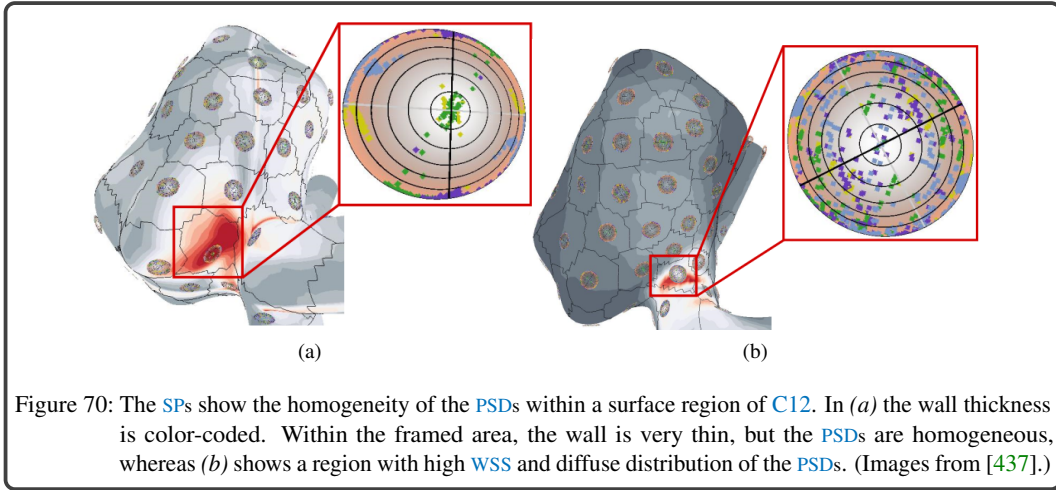
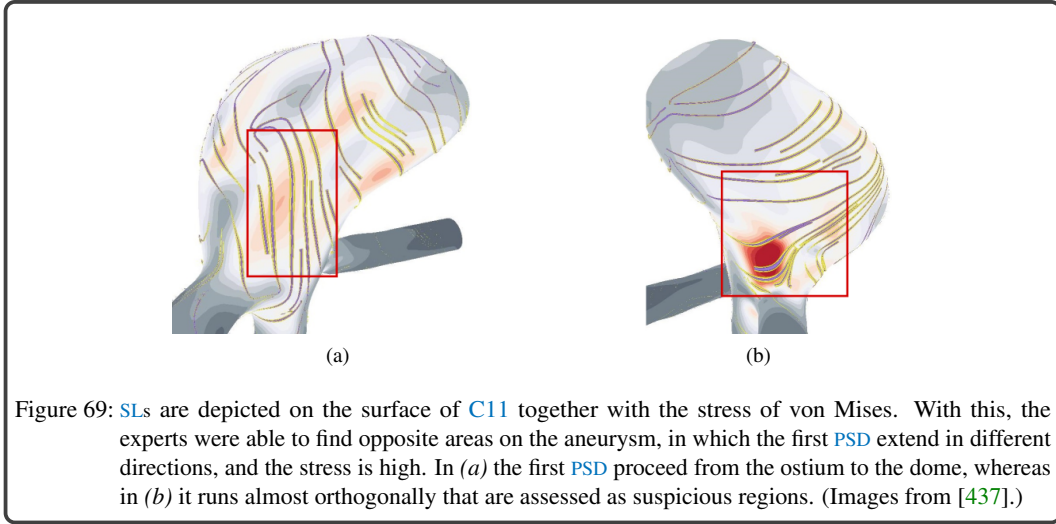


#### 6.3.4 Discussion and Limitations

We evaluated four glyph-based techniques to analyze cerebral stress tensor data comparatively. During the evaluation, it turned out that the glyphs are differently suitable depending on the task. This was further confirmed in the user study. To get a first overview of the PSDs on both walls, SLs are very appropriate. The experts were interested in exploring the internal flow together with SLs, see Figure 68a. They stated that this depiction could be used to find correlations between rupture-relevant flow patterns such as vortices and suspicious tensor configurations. Moreover, the SLs can be used to uncover opposite regions on the aneurysm with very different behavior of the PSDs that should be further explored, see Figure 69. For a more detailed exploration, other techniques such as SQs and kites are more suitable, because of attending occlusion problems between streamlines for both walls. We presented the kites in a previous interview to our experts. However, they described the determination of the PSD as very difficult, if the camera has a greater distance to the surface. We improved this by including the transition from the arrow glyph to the kite and repeat our expert evaluation, which leads to the Likert assessments, presented in Section 6.3.3. By using the kites, the experts were able to detect regions with a strong local change of the PSD immediately as possible rupture-prone areas, see Figure 68b. For the rotating kites, they used the metaphor of a compass, which was described as very intuitive to perceive strong directional changes. The suitability of the kites to represent percentage and angular differences was also confirmed in the user study.



For the estimation of the stress values, the kites are most suitable, because their shape communicates the stress magnitudes immediately. In contrast, the experts described this task based on the line width as more difficult. This was also confirmed in the user study, where the kites, followed by the SQs, led to the best results. The SPs are also less appropriate for a local approximation of the PSDs. However, they are most suitable to analyze the tensor data quantitatively within a surface region, whereas the other techniques allow a qualitative analysis. The SPs allow a quantification of the homogeneity of the PSDs. Strong inhomogeneous regions paired with suspicious scalar values such as a high WSS could be a rupture-prone criterion, see Figure 70. In this context, P1 and P2 asked for the possibility to add landmarks with notes that would facilitate the collaboration between domain experts. Moreover, P3 wished for a drawing feature that annotates various regions with different color and text.



### 6.3.5 Conclusion and Future Work

We presented the CoTenVis module to analyze IA for a potential rupture risk assessment. For the first time, we integrated stress tensors in combination with wall thickness and blood flow data for the analysis. So far, no accepted factor describes the likelihood of a rupture and the wall structure is not very much discussed clinically. CoTenVis aims to introduce the concept of wall stress into clinical discussions by providing novel glyph visualizations of the complex tensor data. To avoid open-ended exploration, we conferred with clinical experts and carried out an extensive evaluation to find out which requirements had to be met and which visualizations could be used to support the data analysis.

Besides, we identified several aspects that might be improved. First, for the kites and SPs, we would like to incorporate the *decal-maps* [317]. Moreover, we want to provide a more detailed analysis of aneurysm wall layers. Besides the inner and outer wall, there are intermediate layers in the FSI model with corresponding flow data. To analyze these layers and their characteristics, we want to integrate interactive cutting planes through the aneurysm geometry. Furthermore, we want to incorporate an automatic report generation that summarizes all interesting findings such as presented in Figure 68 - Figure 70. This would reduce the manual exploration effort and would facilitate the collaborative data analysis. Our long-term goal is to contribute to a comprehensive risk assessment that also includes inflammatory factors and real measured wall thickness values. Basic research indicates that these affect the rupture risk, however, in clinical practice, such information cannot be acquired so far.

## 6.4 ANIMATIONS FOR ANEURYSM DATA

Besides an adequate visualization of scalar parameters, a capable camera control including a proper viewpoint selection is crucial for an efficient analysis of the complex data. There are several methods to determine good views for polygonal [274, 383], volume data [39] and vector fields [221, 234, 363]. They are mainly based on *entropy* [383], which is a measure to assess the quality of a view with the aim of maximizing its information content. For polygonal meshes, Vázquez et al. used a viewpoint entropy [383] to measure the relation between visible polygons and visible area and applied it to image-based rendering [384]. Neugebauer et al. [274] used surface parameters such as the curvedness to identify ROIs for seeding NWF. For volume data, voxel-based entropy functions were optimized [39], and for vector fields, the visibility, as well as flow parameters of streamlines, are used [221, 363]. Ma et al. [234] focused on the selection of appropriate viewpoints for an automatic guide to explore flow features of time-independent vector fields. Moreover, Drucker [90] presented an assortment of camera primitives that enable an intelligent control of virtual cameras in computer graphics. The suitability of a view also depends on application-specific characteristics, e.g., familiar and preferred views in surgery. Mühler et al. [260] integrated geometric aspects to select appropriate viewpoints to support intervention planning tasks based on medical surface depictions.

Related to the approach by Neugebauer et al. [274], we also derive viewpoints from surface parameters. We developed two approaches to determine appropriate viewpoints, an interactive planning method, and an automatic viewpoint calculation. The first approach is based on user-selected thresholds of surface parameters, which determine the selection of the views. For the second approach, the user selects the scalar fields that should be considered for the viewpoint calculation. Based on this, views are calculated automatically that show surface regions of suspicious combinations of the selected scalar fields. The result of both techniques is a set of appropriate viewpoints on the aneurysm surface. From this set, an animation is built to support the exploration of aneurysm data. During the cardiac cycle, the most interesting surface regions are presented to the user.

### 6.4.1 Interactive Planning of Animations

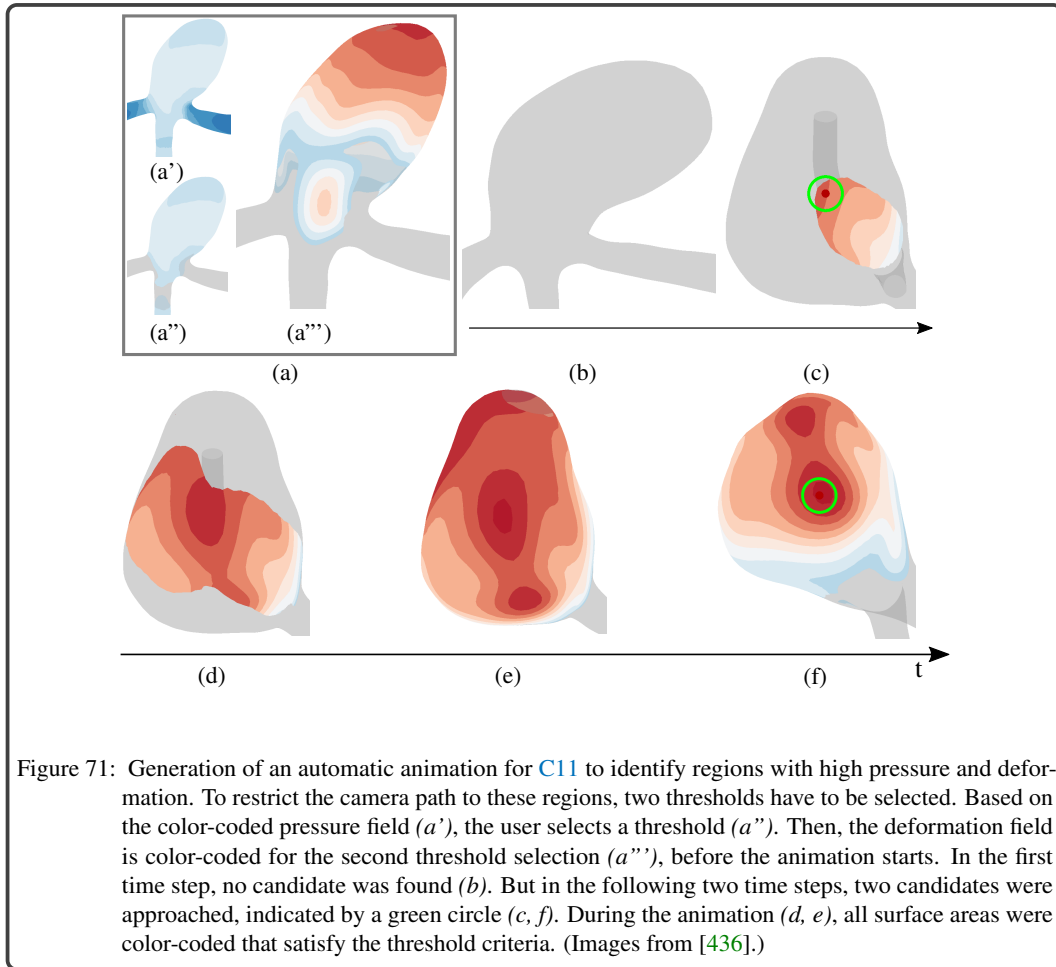
We implemented interactive planning of animations that present the most interesting regions based on the input data of the user. Our experts preferred smooth animations over keyframes because they found them easier to comprehend. For this purpose, the user is asked to set various thresholds for different scalar fields. Here, the user selects scalar fields  $s_1, s_2, \dots, s_n$  that he/she is interested in. Then, for every scalar field a threshold  $t_i$  is set. The selection of the scalar fields with the thresholds leads to a constrained region on the mesh that fulfills every criterion:

$$P = \bigcap_{i=1}^n \{p \mid s_i(p) \geq t_i\} \quad (23)$$

Note that we wrote  $s_i(p) \geq t_i$ , but for scalar fields such as the wall thickness or NWF less equal. The obtained points restrict the camera path. The thresholds can be set independently from each other, where the surface regions that fulfill all selected threshold conditions were presented using the cool-to-warm color scheme. Regions that do not comply with the thresholds are depicted in gray. Figure 71a shows an example of the threshold selection. The user starts by choosing the pressure scalar field during systole, which is color-coded on the surface 71a' and regions are interactively grayed according to the threshold 71a". Based on the result of the first selection, the user adjusts a threshold for the deformation, which is now color-coded on the surface 71a"". Finally, regions that satisfy both conditions are used to plan the camera path.

To determine positions for the animation, we select candidates that are highly interesting for the user to explore. Thus, the user selects a focus scalar field  $s_{\text{focus}}$ . Then, candidates are determined, which are first based on the points  $P$  (recall Equation 23) and on  $s_{\text{focus}}$ . The ordered points  $P_o$ , i.e.,  $s_{\text{focus}}(P_o^i) \geq s_{\text{focus}}(P_o^{i+1})$  serve as candidates for the camera path. For every time step, we use  $P_o^0$  as the ideal candidate. Thus, we need the position of the camera such that it shows the candidate.

For this, we use the position of the candidate and add the scaled surface normal. We used  $1/10$  of the diagonal of the bounding box of the surface mesh as the scalar. Thus, the camera has a constant distance to the vessel surface. With smaller values, the camera came too close to the surface, and with greater values, it was too far away. The movement of the camera on given paths with always similar distance to the object was originally described as *orbiting* by LaViola et al. [171], which is a suitable concept to generate smooth animations. The view direction of the camera is set such that it points in the direction of the candidate. From one point in time to the next, we move the camera to the candidate such that the animation stops before the next point in time is reached. This enables a smooth animation between the best candidates at different points in time. In case the domain expert is interested in various candidates at a specific point in time, e.g., the systole, he/she can start a local camera path. If the local path is activated, the animation is paused, and the camera moves beginning from the first candidate to the next ordered points. The candidate is in general highlighted with a circle around a point that indicates its position. Figure 71 shows an example of animation for three adjacent time steps. In the first time step, no point fulfills the selected threshold conditions, see Figure 71b. In the next time step, the camera rotates automatically to the most interesting point, which is highlighted by a green circle, see Figure 71c. Afterward, the camera rotates to the next candidate (Figure 71f), while all surface regions were color-coded that fulfill the threshold conditions (Figure 71(d,e)).



Mostly, the domain experts are interested in specific regions such as the dome. Therefore, we offer the possibility to restrict the region through an approach that determines the geodesic distance on the surface. For this, the user is asked to place a start point on the mesh. Then, we compute the geodesic distance from the start point by solving standard linear elliptic equations [78]. Afterward, the user can specify the distance that restricts the region for the camera path.

### 6.4.2 Automatic Calculation of Animations

The automatic determination of appropriate viewpoints is modeled as an optimization problem. We used a GPU-based implementation to find the desired optima. Our approach consists of three major steps. First, we have to formulate a target function that should be optimized. Second, we have to select start points for searching appropriate views. Based on these points, the optimization problem has to be solved. Finally, the resulting viewpoints have to be connected to a camera path. In the following sections, each of these steps is explained in more detail.

#### Target Function

To select viewpoints, a target function  $f : V \rightarrow \mathbb{R}$  has to be formulated that covers the criteria of an appropriate view  $\mathbf{x} \in V$ . Selected viewpoints are local maxima of the target function that consists of two parts. The first one is the size of the visible aneurysm surface area because mostly, domain experts are interested in regions on the aneurysm. The second part is the significance of a surface area according to a user-selected parameter combination. For the first criterion, we separate an aneurysm from the parent vessel using our automatic ostium detection, recall Section 5.5.1. For the second criterion, the user has to select two scalar attributes  $s_1$  and  $s_2$  that he/she wants to explore. Moreover, the user has to define if lower or higher values of the respective parameter should be weighted stronger. Based on the aneurysm surface, we implemented a GPU-based approach to determine the target function's value for a specific viewpoint. We provide the aneurysm surface as well as  $s_1$  and  $s_2$ , which are normalized in the vertex shader of the whole vessel surface by using vertex buffer objects and transform the information to the fragment shader with the help of varying variables.

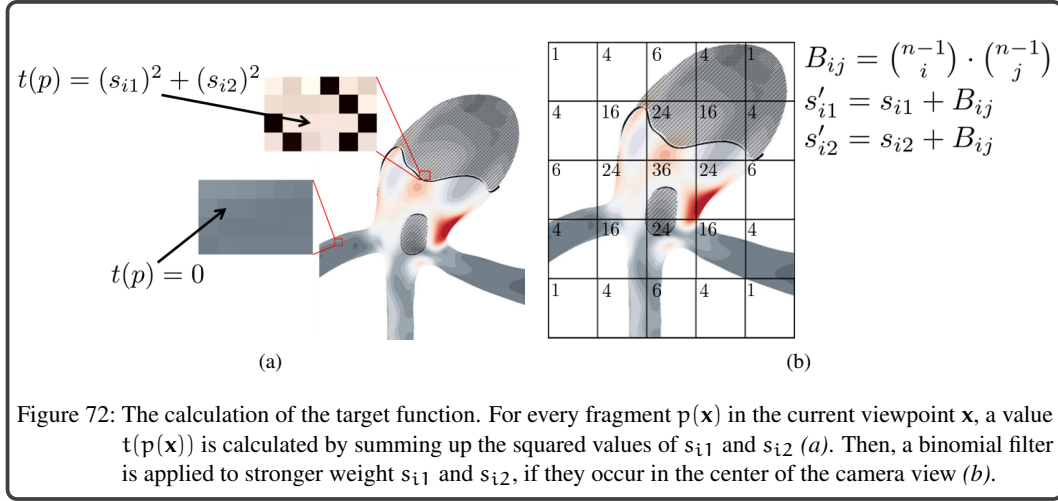
In the following, we explain how the target function  $f(\mathbf{x})$  is defined for a viewpoint  $\mathbf{x}$ . Every fragment  $p(\mathbf{x})$  in the current viewpoint  $\mathbf{x}$  is assigned a value  $t(p(\mathbf{x}))$ , see Figure 72a. The sum of the fragment's values yields the target function  $f(\mathbf{x}) = \sum_i t(p_i(\mathbf{x}))$ . If the fragment  $p$  does neither belong to the aneurysm part nor to the front faces, we assign  $t(p) = 0$ . For the fragment counting, we use the add operation of the OpenGL Atomic Counters. If  $t(p)$  is not equal to zero, the two scalar values per fragment  $s_1, s_2 \in [0, 1]$  are multiplied by 10 and truncated to the nearest integer values, yielding  $s_{i1}, s_{i2} \in \{0, \dots, 10\}$ . Moreover,  $s_{i1}$  and  $s_{i2}$  are squared to stronger weight interesting values. Additionally, we divide the framebuffer in  $n \times n$  sub images and assign a constant factor  $B_{ij} = \binom{n-1}{i} \cdot \binom{n-1}{j}$  to each sub image  $(i, j)$  in the design of a binomial filter, see Figure 72b. We used  $n = 5$ . Then,  $B_{ij}$  is added to  $s_{i1}$  and  $s_{i2}$ , depending on the sub image the current fragment belongs to, which yields the updated values  $s'_{i1}$  and  $s'_{i2}$ . This leads to a stronger weighting of  $s_{i1}$  and  $s_{i2}$ , if they occur in the center of the camera view. Lower values of  $n$  result in a too strong weighting of uninteresting surface regions, while higher values lead to an excessive weighting of small areas. We set  $t(p) = s'_{i1} + s'_{i2}$ , which represents the scalar value for a fragment  $p$ . Finally, we determine the target function  $f(\mathbf{x})$  and store the value on an image, which allows a later CPU-based access.

After we used  $f$  to find appropriate starting points. The gradient ascent method is applied to each of them. The goal is to further optimize the two camera angles and the view direction  $(x, y, z)$ , which results in five DOFs. Each DOF is changed iteratively,  $f(\mathbf{x})$  is evaluated and the gradient of  $f(\mathbf{x})$  is calculated. The new viewpoint  $\mathbf{x}_{new}$  is calculated by  $\mathbf{x}_{new} = \mathbf{x}_{old} + s \cdot \nabla f(\mathbf{x}_{old})$ , where  $\mathbf{x}_{old}$  is the current viewpoint,  $s$  is the step size and  $\nabla f(\mathbf{x}_{old})$  is the gradient of  $f(\mathbf{x}_{old})$ . The gradient ascent stops if the gradient magnitude falls below a threshold  $t$  with  $t = 0.001$ . Moreover,  $f$  is evaluated for different values of  $s$ , where the integer values range from 1 to 5.

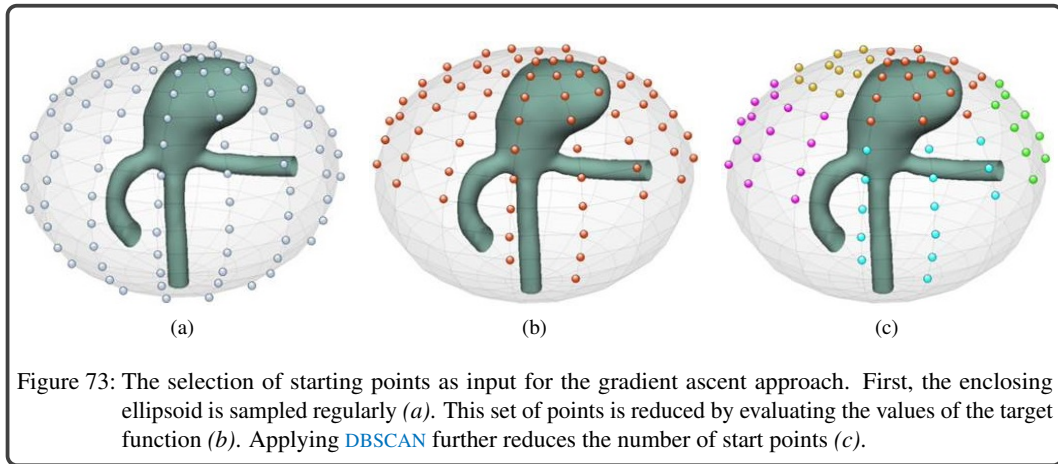
#### Starting point selection

The camera path should indicate interesting surface regions during the cardiac cycle. Within a time step, there are typically several positions where significant attributes arise. To find these local optima, we select multiple starting points per time step. It would be possible to define an arbitrary number of points at arbitrary positions around an aneurysm. However, possibly the optimization would require many iterations to find local optima. Thus, we try to select starting points close to local optima on an approximated ellipsoid around an aneurysm. The ellipsoid's axes are the eigenvectors scaled by twice





the eigenvalues of the covariance matrix of all aneurysm vertices. The ellipsoid is sampled by using polar coordinates  $\theta = 2\pi/36 \cdot i$ ,  $i \in \{0, \dots, 18\}$  and  $\phi = 2\pi/m \cdot j$ , with  $m = 2 \cdot (9 - |i - 9|) + 1$ ,  $j \in \{0, \dots, m\}$ , see Figure 73a. The scaling of the ellipsoid's eigenvalues ensures that the camera has an appropriate distance to an aneurysm, yielding the viewpoints  $\mathbf{x}_i$ . For each of these candidates, the function value  $f(\mathbf{x}_i)$  of the target function is calculated. From this scalar field, we calculate the 90 % quantile and keep the remaining viewpoints as candidates for possible starting points, see Figure 73b. To further reduce their number, we cluster the candidates by using the density-based clustering **DBSCAN** [99] that does not need a priori selection of the cluster number, because the number of appropriate views is unknown, see Figure 73c. For each cluster, the averaged position is used as a starting point. However, for **DBSCAN** two thresholds must be specified, the minimum number of objects to form a valid cluster, and a maximum allowed dissimilarity between two objects of a cluster. In our case, each cluster must contain at least one candidate, and a maximum difference of  $20^\circ$  for both angles,  $\theta$  and  $\phi$ , between a candidate and the cluster center is allowed. Smaller values lead to clusters, where the resulting starting points are very similar. With greater values, the clusters are too large so that not all belonging candidates lie within the view frustum of the averaged camera position.



### Camera path

For each time step, our approach calculates a set of appropriate viewpoints, see Figure 74. We order these viewpoints by their  $\phi$  angle within a time step and connect them to a camera path. Moreover, the viewpoints are combined between adjacent time steps to generate a global animation during the cardiac cycle. For this purpose, for each time step, the viewpoint is used first that has the smallest distance of  $\phi$  to the last viewpoint in the previous time step. We move the camera from one viewpoint in time to the next, where the camera position and view direction is interpolated from their known camera settings in each render pass. For the interpolation factor  $t$ , a cubic easing function  $f$  is used:

$$f(t) = \begin{cases} 4 \cdot t^3 & \text{if } t < .5 \\ (t - 1) \cdot (2 \cdot t - 2) \cdot (2 \cdot t - 2) + 1 & \text{otherwise.} \end{cases} \quad (24)$$

With this, the camera accelerates until halfway between two adjacent viewpoints and decelerates then. The resulting path enables a smooth animation between two adjacent viewpoints.

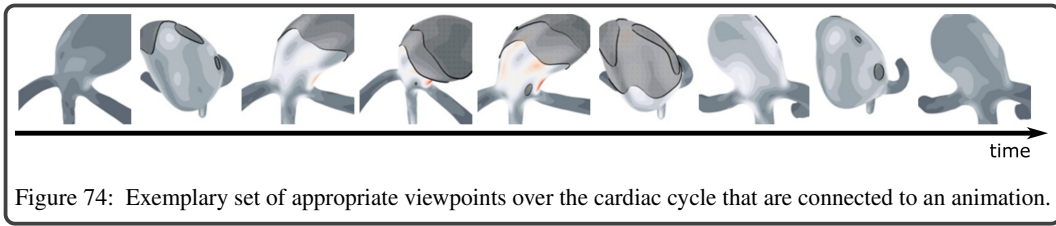


Figure 74: Exemplary set of appropriate viewpoints over the cardiac cycle that are connected to an animation.

#### 6.4.3 Evaluation and Results

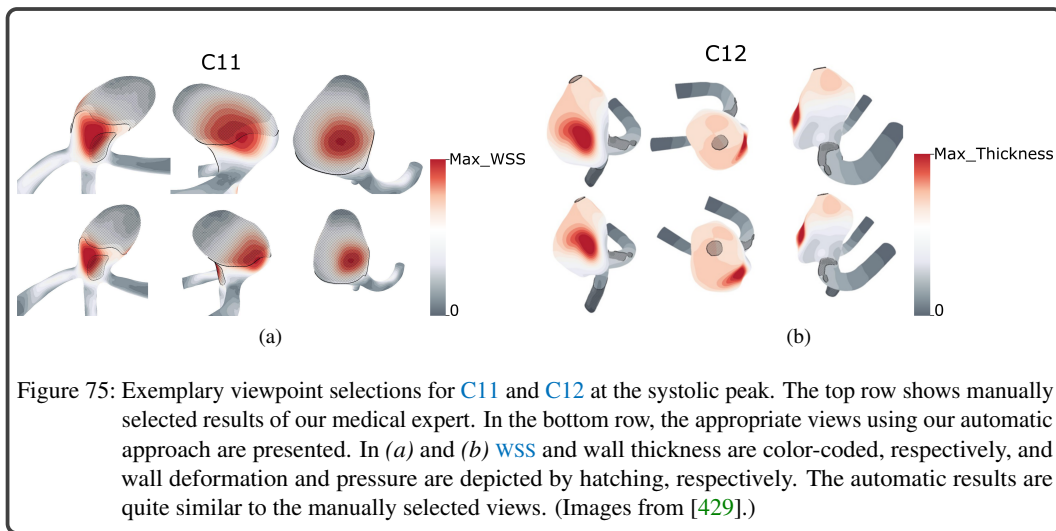
We evaluated the interactive planning of camera paths as well as the automatic calculation of animations with two domain experts by conducting informal interviews. For this purpose, five aneurysm data sets are used. According to the automatic viewpoint selection (recall Section 6.4.2) the computation time per time step is between 8 and 10 s, depending on the amount of starting points. Our testing system uses an Intel Core i5 with 2.8 GHz, 16 GB RAM, and an NVidia GeForce GTX 1080 Ti. The experts are one neuroradiologist with 16 years of work experience and one CFD engineer working on blood flow simulations for cerebral aneurysms with five years of work experience. First, they were asked to manually search for suspicious surface regions depending on the selected parameters  $s_1$  and  $s_2$ . Then, they explored the data using our animations. The experts should assess if the interactive planned as well as automatically calculated camera path support the exploration and navigation within time-dependent data. Moreover, they should state, if one of these methods is more suitable for data analysis.

Figure 75 shows the appropriate viewpoints for C11 and C12 at the systolic peak. The top row shows manually selected views of the neuroradiologist. In the bottom row, the appropriate views using our automatic approach are presented. In the two data sets the WSS and wall thickness are color-coded, respectively, and the wall deformation and pressure are depicted by hatching, respectively. Reddish, dense hatched areas indicate suspicious surface regions. The automatically selected views correlated with the manual results within that time step. However, for the manual searching, a series of rotations was necessary. Furthermore, the time-dependent behavior of the data increases the manual exploration effort, because it is difficult to find critical regions during animation.

The experts described the automatic computation as well as the interactive planning of animations as very helpful for the exploration of the time-dependent data. The interactive planning allows a stronger integration of expert knowledge by selecting multiple attributes that should be considered for generating the animation. According to the necessary candidate selection, both experts preferred the threshold-based selection to the ROI selection. The automatic camera path gives a temporal overview of two selected scalar fields that indicate possible rupture-prone areas. In this context, they liked that no further specification of thresholds is necessary for the calculation of the camera path, which



would be a challenging task if the user has no initial impression of the data distribution. Moreover, the appropriate viewpoints could be used for documentation, since occlusion problems arising from the parent vessel geometry are resolved. In contrast, interactive planning should be used for more focused data exploration. Here, they emphasized the fast computation of the camera path (8 s on average for all time steps, depending on the number of vertices) compared to a few minutes for the automatic path calculation. This allows fast analysis of possible correlations between scalar attributes. However, the CFD expert wished to have a key interaction for the temporal forward and backward exploration of the candidate points instead of a time bar. Besides, they described that both techniques are helpful for the navigation in 3D. However, it depends on which part of an aneurysm the users want to navigate their way around. If the users only want to navigate in a small region such as a bleb, a manual rotation was preferred. For the time-dependent navigation over the whole aneurysm surface, an automatic rotation is more suitable.

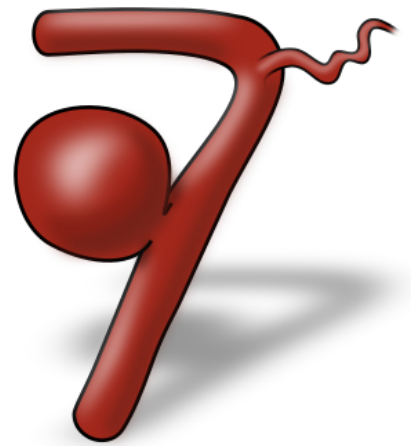


#### 6.4.4 Conclusion and Future Work

We present different methods to generate animations for aneurysm data over the cardiac cycle. Our domain experts confirmed the importance of camera paths to support the data exploration because they enable the detection of suspicious regions without a time-consuming manual search. A possible application of our methods is to get a quick overview of the aneurysm data, where rupture-prone areas are presented. Furthermore, they could support the clinical report generation and serve as a summary of a patient's rupture risk.

In the future, the camera path should be calculated in real time. Besides, a stabilization of the camera movement could be integrated to avoid larger changes in the camera orientation between two viewpoints. This could be done by defining a maximum allowed change of the camera's up vector. Moreover, we want to integrate information about specific blood flow patterns such as vortices into the target function of the automatically calculated path. Then, it would be possible to select views that present the time-dependent vortex behavior. A possible criterion in this context could be the optimization of the vortex core line visibility. Furthermore, the calculation of optimal viewpoints should be extended to post-treated data, where the visibility of treatment options such as different stents should be considered in the target function. Finally, the color-coding could be adjusted in areas where color and hatching overlap so that hatching does not affect the perception of color.

# ViFlEx - Visual Flow Exploration Module



This chapter is partly based on:

Monique Meuschke, Samuel Voß, Bernhard Preim and Kai Lawonn,  
Exploration of Blood Flow Patterns in Cerebral Aneurysms during the Cardiac Cycle;  
Computer & Graphics, 72, pp. 12-25, 2018.

Monique Meuschke, Steffen Oeltze-Jafra, Oliver Beuing, Bernhard Preim  
and Kai Lawonn,  
Classification of Blood Flow Patterns in Cerebral Aneurysms;  
IEEE Transactions on Visualization and Computer Graphics, 2018.



Besides, morphological conditions and wall-related attributes, the aneurysm progression and rupture also seem to depend on qualitative flow characteristics, e.g., specific flow patterns, such as vortices. Moreover, flow patterns are assumed to be related to the success of treatment, and their distance to the vessel wall seems to be an important factor for the assessment of the aneurysm's state [18].

To assess the influence of flow patterns on the risk of rupture, medical studies were conducted with homogeneous patient groups of ruptured and non-ruptured aneurysms [60, 267]. Therefore, blood flow data are used that were obtained by CFD simulations. Flow patterns are extracted from simulation results and manually classified according to their *complexity* and *temporal stability*. The results were compared between ruptured and non-ruptured cases to identify characteristics associated with rupture. The more complex and unstable types correlated with an increased rupture rate. Such an analysis is a time-consuming process with high inter-observer variability, where flow patterns more distant to the wall are easily overlooked due to visual clutter and occlusion. However, to uncover correlations between flow patterns and the aneurysm state, the classification results of different data sets should be comparable. This requires an objective classification according to clearly defined criteria.

To improve the analysis of flow patterns on the aneurysm state, we developed the ViFLEX module, which consists of two major components. First, blood flow-representing path lines have to be grouped to characterize individual flow patterns. For this purpose, we developed an automatic clustering of blood flow patterns over the cardiac cycle, presented in Section 7.1. Based on the clustering results, the flow patterns are classified to assess their temporal stability and complexity. For this purpose, we developed the *cerebral aneurysm vortex classification* (CAVOCLA), an automatic method to classify flow patterns according to pre-defined types, presented in Section 7.2. Thus, the time-consuming and error-prone manual process to investigate flow patterns can be replaced by a time-saving and robust automatic process that leads to reproducible results.

### 7.1 AUTOMATIC CLUSTERING OF FLOW PATTERNS

To classify flow patterns, first, the flow has to be decomposed into areas of common structure. For this purpose, partitioning techniques can be used that are mainly based on integral curves, since in contrast to local vectorial flow data, they represent continuous flow patterns. The partitioning is performed in a user-guided [42, 120, 189] or automatic fashion [98, 226, 245, 282, 433]. Less frequently, local flow vectors [380] or aneurysm wall properties [115, 274] are employed. Moreover, graphical representatives of flow regions can be computed to generate a visual summary or a subsequent visualization can be restricted to regions with specific properties, e.g., vortices.

User-guided techniques partition integral curves based on *line predicates* [331], which are Boolean functions that decide if integral curves fulfill properties of interest, c.f. Section 4.2.3. Gasteiger et al. [120] applied line predicates to CFD data of cerebral aneurysms to extract flow features, e.g., the *inflow jet* and the *impingement zone*, recall Section 3.5.5. Born et al. [42] utilized line predicates to identify relevant flow features such as jets and vortices in measured cardiac data. Köhler et al. [189] used different local vortex criteria as line predicates to filter path lines that represent aortic vortices.

Automatic techniques employ a data-driven approach and utilize clustering methods to group integral curves based on a similarity measure. McLoughlin et al. [245] introduced a streamline similarity measure by computing geometrical features based on the underlying vector field and used an AHC with average link for partitioning. Their method was applied to time-dependent data by extracting the geometrical features from the vector field of the corresponding time step. However, the temporal component was not directly considered. Two geometrically similar path lines occurring in non-overlapping time intervals would have a high similarity. Oeltze et al. [282] compared multiple streamline clustering techniques in the context of aneurysm hemodynamics. Streamline similarities

were computed based on line geometry [76]. Liu et al. [226] measured path line similarities using an octree. The space is divided into cubes either by equidistant length or by adaptive length that depends on the features of the underlying vector field. A sequence is assigned to the path lines that incorporates the passed cubes, where the similarity is based on the longest common sequence. In a previous work [433], we compared multiple clustering methods of path lines representing aortic vortex flow. Path line similarities were computed based on the spatio-temporal coordinates of line endpoints and the line's average distance to the vessel centerline. AHC with average link performed best in separating vortices.

To cluster the intra-aneurysmal blood flow, we extended an established similarity measure [76] for streamlines to path lines. In contrast to the streamline similarity measure by McLoughlin et al. [245], our method directly incorporates the temporal component. If a flow pattern occurs, decays and reoccurs during the cardiac cycle, our method results in several clusters. This is required since the stability of flow patterns is an important criterion in medical studies to predict the rupture risk [60]. Existing methods are not able to represent instable flow patterns by different clusters. Moreover, compared to existing time-dependent clustering approaches such as the approach by Liu et al. [226] or our previous method [433], we are not dependent on the centerline or the underlying partitioning of the space. To explore the behavior of individual flow patterns, we extended the 2D map and 3D depiction of an aneurysm by a visualization of the internal blood flow. The 2D map enables an occlusion-free visualization of flow patterns, including their distance to the vessel wall. The 3D visualization represents the focus upon which the exploration of morphological aneurysm characteristics together with the blood flow information over the cardiac cycle takes place.

#### 7.1.1 Requirement Analysis

The manual extraction and classification of flow patterns are affected by visual clutter due to the flow complexity, which makes the classification error-prone. To facilitate the classification of flow patterns, a computer-based detection is needed. This requires a reliable path line clustering that does not need a priori selection of the (unknown) cluster number. Therefore, a similarity measure is needed that is able to group spatio-temporally adjacent patterns. However, due to the large anatomic diversity, the automatically calculated results will not always be appropriate. Thus, the experts should be able to explore different cluster numbers if the automatically calculated number is not optimal.

To verify and interpret the clustering results, our domain experts wanted an adequate visualization of flow patterns. A more abstract depiction of the complex flow and vessel morphology would help the neuroradiologist comparing ruptured and non-ruptured cases. According to the CFD experts, a more simplified depiction would support the assessment of the most prominent flow patterns to validate the simulation results. In addition to the seven more general requirements in Section 5.1 and others in Chapter 6, we summarize further requirements for the exploration of intra-aneurysmal flow patterns:

**Req. 16** NO PRE-DEFINED CLUSTER NUMBER. The clustering should separate spatio-temporal flow patterns without a pre-defined cluster number.

**Req. 17** INTEGRATION OF EXPERT KNOWLEDGE. The experts should be able to correct the automatically calculated clustering results.

#### 7.1.2 Path Line Similarity

In the following, we give a detailed explanation of our path line similarity measure. We proceed with a description of the used clustering method that does not need a priori selection of the cluster number (Req. 16). In the remainder of this section, we use the following notation. A path line  $pl$  consists of vertices  $V = \{1, \dots, n\}$ , edges  $E = \{(i, i+1) \mid i \in \{1, \dots, n-1\}\}$ , and a time set  $T = \{t_1, \dots, t_n \mid t_i < t_{i+1}\} \in \mathbb{R}^n$ . The corresponding 3D coordinates of the vertices are denoted with  $\mathbf{p}_i \in \mathbb{R}^3$ ,  $i \in V$ . We use  $pl(t_i) = \mathbf{p}_i$  with  $i \in V$ ,  $t_i \in T$  to denote the 3D coordinates of the path line points as a function of time.

### 7.1.2.1 Calculation of the Similarity Matrix

Our path line clustering builds upon the *mean of closest point distances* (MCPD) [76] measure that was successfully used for streamline clustering [282]:

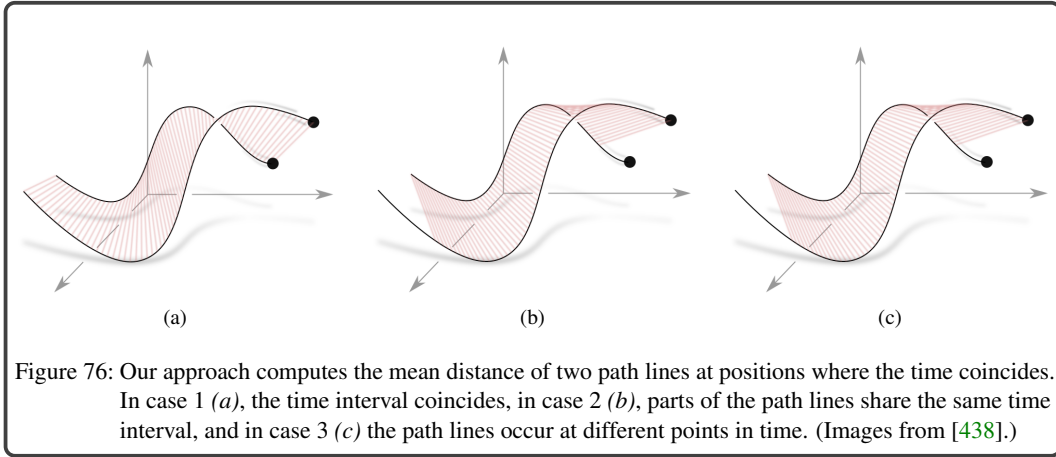
$$\begin{aligned} d_M(s_i, s_j) &= \text{mean}(d_m(s_i, s_j), d_m(s_j, s_i)) \text{ with} \\ d_m(s_i, s_j) &= \text{mean} \min_{p_l \in s_i, p_k \in s_j} \|p_k - p_l\|. \end{aligned} \quad (25)$$

This measure determines for every point on the streamline the minimum distance to another streamline and averages it. However, the temporal component is not encoded. Inspired by the MCPD, our distance measure incorporates the mean distances of path lines by considering their time component.

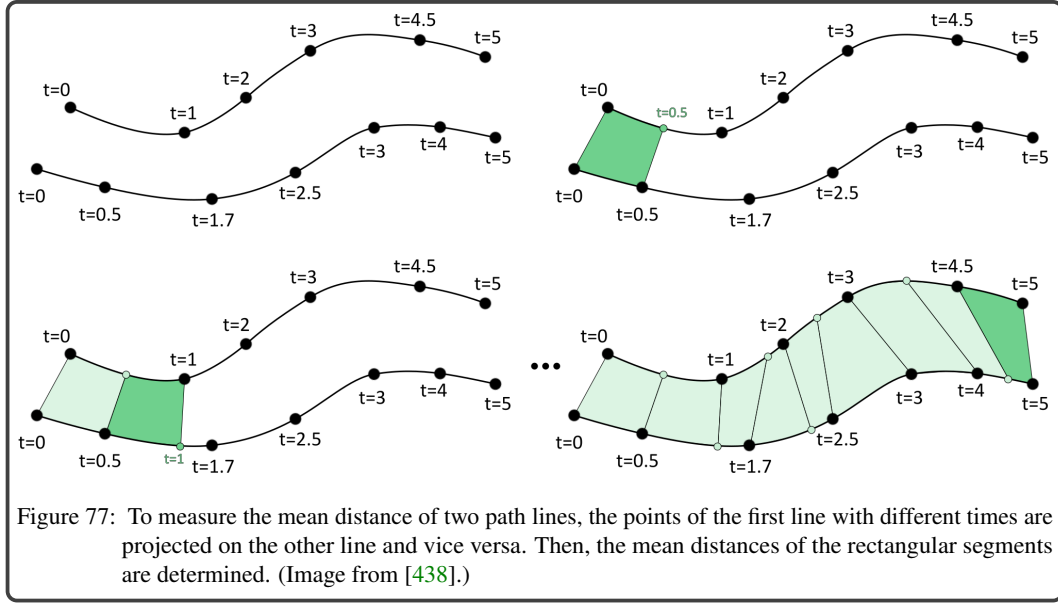
Note, that a path line usually does not exist during the whole cardiac cycle due to the high velocities (up to 1.51 m/s) and the small spatial domain size (5-11 mm in the x,y,z-direction) [31, 164]. This further means, that the temporal components of two path lines would not have been synchronized for integration with a uniform temporal step length instead of the used adaptive step length (recall Section 5.2.1). Thus, we have to determine corresponding path line points depending on their temporal component, which is explained in the following.

Given are two path lines  $p_k, p_l$  with time components  $t_1^k, \dots, t_n^k$  and  $t_1^l, \dots, t_m^l$  for which we like to calculate the mean distances. For this, we distinguish three cases, see also Figure 76:

1.  $[t_1^k, t_n^k] = [t_1^l, t_m^l]$  means both path lines occur in the same time interval, see Figure 76a.
2.  $[t_1^k, t_n^k] \neq [t_1^l, t_m^l]$  and  $[t_1^k, t_n^k] \cap [t_1^l, t_m^l] \neq \emptyset$  means the path lines share a time interval, see Figure 76b.
3.  $[t_1^k, t_n^k] \cap [t_1^l, t_m^l] = \emptyset$  means the path lines occur in different time intervals, see Figure 76c.



**Case 1:** In this case, the time components of both path lines coincide:  $[t_1^k, t_n^k] = [t_1^l, t_m^l]$ . To determine the mean distance, we need points on both path lines such that their timings coincide. In general, the time components of the points on the first path line vary compared to the points on the second line, see Figure 77 (top). Therefore, we place new points on both lines such that the time components coincide, see Figure 77 (bottom). For this, we linearize the time along an edge and determine the position such that the time at this position corresponds to the desired time component. This yields two path lines with the same number of points  $p_1^k, \dots, p_M^k, p_1^l, \dots, p_M^l$  and the same time components  $t_1^k, \dots, t_M^k, t_1^l, \dots, t_M^l$ . Note, that  $t_1^k = t_1^l, t_2^k = t_2^l, \dots, t_M^k = t_M^l$  holds by a construction of the points; thus we will omit the superscript.



Finally, we compute the  $M - 1$  mean distances between the path line parts given by the curves:

$$\begin{aligned} c_k(t) &= \mathbf{p}_i^k + t(\mathbf{p}_{i+1}^k - \mathbf{p}_i^k), \\ c_l(t) &= \mathbf{p}_i^l + t(\mathbf{p}_{i+1}^l - \mathbf{p}_i^l), \\ t &\in [0, 1], \quad i \in \{1, \dots, M - 1\}. \end{aligned} \quad (26)$$

A sample-based calculation could determine the mean distance of two path lines in the time interval  $[t_i, t_{i+1}]$ . However, the resulting mean distance would depend on the number of samples, see Figure 78. Here, both pairs would have the same mean distance, although their behavior is different. Generating enough samples would converge to the correct mean distance, but would increase the computation effort. To avoid such inaccuracies, the mean distance of two path lines in the time interval  $[t_i, t_{i+1}]$  is determined by:

$$\begin{aligned} \overline{D}^{kl}(t_i, t_{i+1}) &= \lim_{N \rightarrow \infty} \sum_{i=0}^N \frac{1}{N+1} \underbrace{\|c_k(i/N) - c_l(i/N)\|}_{d(i/N)} \\ &= \lim_{N \rightarrow \infty} \sum_{i=0}^N \left( \underbrace{\frac{i+1}{N+1} - \frac{i}{N+1}}_{t_{i+1}} \right) \cdot d(i/N) \\ &= \lim_{N \rightarrow \infty} \sum_{i=0}^N (t_{i+1} - t_i) \cdot d(t_i) \\ &= \int_0^1 d(t) dt. \end{aligned}$$

with  $d(t) = \|c_k(t) - c_l(t)\|$ . Thus, the mean distance of two moving particles is determined by a novel approach using the integral of the distances. The integral of the mean distance of two curves given in Equation 26 is of the form:

$$\overline{D}^{kl}(t_i, t_{i+1}) = \int_0^1 d(t) dt = \int_0^1 \sqrt{a + 2bt + ct^2} dt, \quad (27)$$



where

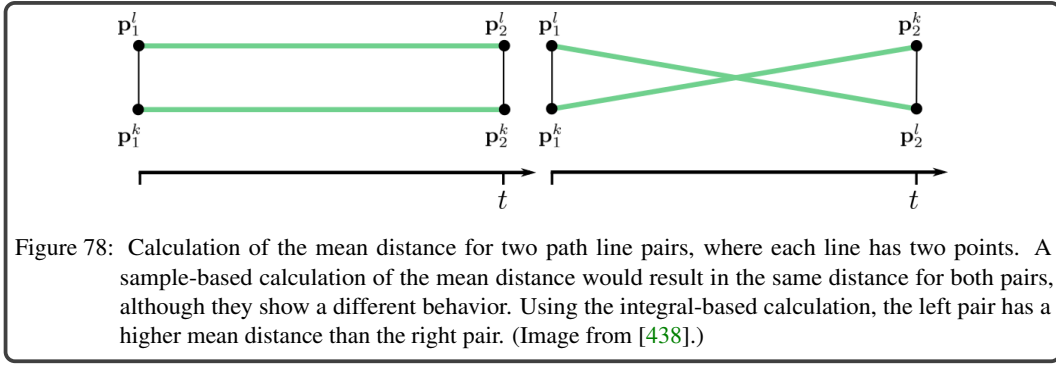
$$\begin{aligned} a &= \langle \mathbf{p}_i^k - \mathbf{p}_i^l, \mathbf{p}_i^k - \mathbf{p}_i^l \rangle, \\ b &= \langle \mathbf{p}_i^k - \mathbf{p}_i^l, \mathbf{p} - \mathbf{p}_i^k - \mathbf{p}_{i+1}^l + \mathbf{p}_i^l \rangle, \text{ and} \\ c &= \langle \mathbf{p}_{i+1}^k - \mathbf{p}_i^k - \mathbf{p}_{i+1}^l + \mathbf{p}_i^l, \mathbf{p} - \mathbf{p}_i^k - \mathbf{p}_{i+1}^l + \mathbf{p}_i^l \rangle. \end{aligned} \quad (28)$$

This integral can be solved analytically. For this purpose, we determine the  $M - 1$  mean distances between the path line parts by:

$$\bar{D}^{kl}(t_1, t_2), \bar{D}^{kl}(t_2, t_3), \dots, \bar{D}^{kl}(t_{M-1}, t_M), \quad (29)$$

which yields the overall mean distance:

$$\bar{D}_{kl} = \frac{1}{t_M - t_1} \sum_{i=1}^{M-1} (t_{i+1} - t_i) \cdot \bar{D}^{kl}(t_i, t_{i+1}). \quad (30)$$



**Case 2:** For case 2, we determine the distance of the overlapping temporal part with Equation 30. Thus, there exist two disjoint sets that partitioned the time set of the path lines such that:

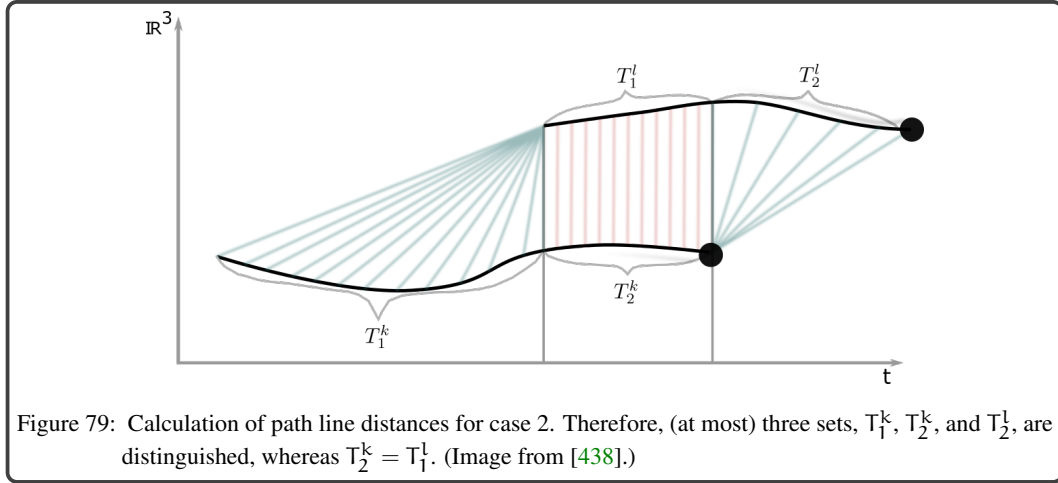
$$\begin{aligned} T_1^k \cup T_2^k &= [t_1^k, t_n^k], \\ T_1^l \cup T_2^l &= [t_1^l, t_n^l]. \end{aligned} \quad (31)$$

Without loss of generality, we assume  $T_2^k = T_1^l$ , see Figure 79. Then, the distance of the set  $T_2^k$  is determined based on Equation 30. To consider the missing parts  $T_1^k$  and  $T_2^l$ , we calculate the mean distance with Equation 30, but change the curves given in Equation 26. For  $T_1^k$ , we alter  $c_l$  to  $c_l = \mathbf{p}_{l_1}(t_1^l) = \mathbf{p}_1^l$  (and for  $T_1^k$ , we set  $c_k = \mathbf{p}_n^k$ ).

**Case 3:** In case 3, the time intervals do not overlap. Without loss of generality, we assume  $t_n^k < t_1^l$ . Again, we determine the mean distance with Equation 30, but change the curves given in Equation 26. First, we set  $c_k = \mathbf{p}_n^k$  and determine  $\bar{D}^{kl}$  (to all line segments on  $\mathbf{p}_{l_1}$ ). Then, we set  $c_l = \mathbf{p}_1^l$ , determine  $\bar{D}^{kl}$  (to all line segments on  $\mathbf{p}_{l_k}$ ), and add this to the result.

**Jaccard Matrix:** So far, we determined the mean distances of two path lines as a basis for the similarity calculation. Besides this, we want to ensure that two path lines of case 1 are more similar than path lines of case 3. For this, we compute a Jaccard matrix  $J$ , which uses a Jaccard metric. For two path lines  $\mathbf{p}_{l_k}, \mathbf{p}_{l_l}$  with time components  $T_k = \{t_1^k, \dots, t_n^k\}$  and  $T_l = \{t_1^l, \dots, t_m^l\}$ , the Jaccard matrix is given by:

$$(J)_{kl} = 1 - \frac{\max(T_k \cap T_l) - \min(T_k \cap T_l)}{\max(T_k \cup T_l) - \min(T_k \cup T_l)}. \quad (32)$$



In case  $T_k \cap T_l = \emptyset$ , we set  $\max(T_k \cap T_l) = \min(T_k \cap T_l) = 0$ . Thus, if  $(J)_{kl} = 0$ , both path lines exist in the same time interval (case 1). If  $(J)_{kl} = 1$ , both lines occur at different points in time (case 3). Otherwise, they share a time interval (case 2).

**Distance Matrix:** Based on the cases 1, 2, and 3 we construct the distance matrix  $\mathbf{D}$  with  $(D)_{ij} = \overline{D}_{ij} + J_{ij} \cdot \max_{ij} \overline{D}_{ij}$ . Note, with the construction of the Jaccard matrix we ensure that  $D(\text{case 1}) \leq D(\text{case 3})$ . For case 2, we have to split the distance calculation into (at most) three parts, one or two parts of time intervals that do not overlap. In case 3, we have two components, which are used to determine the similarity.

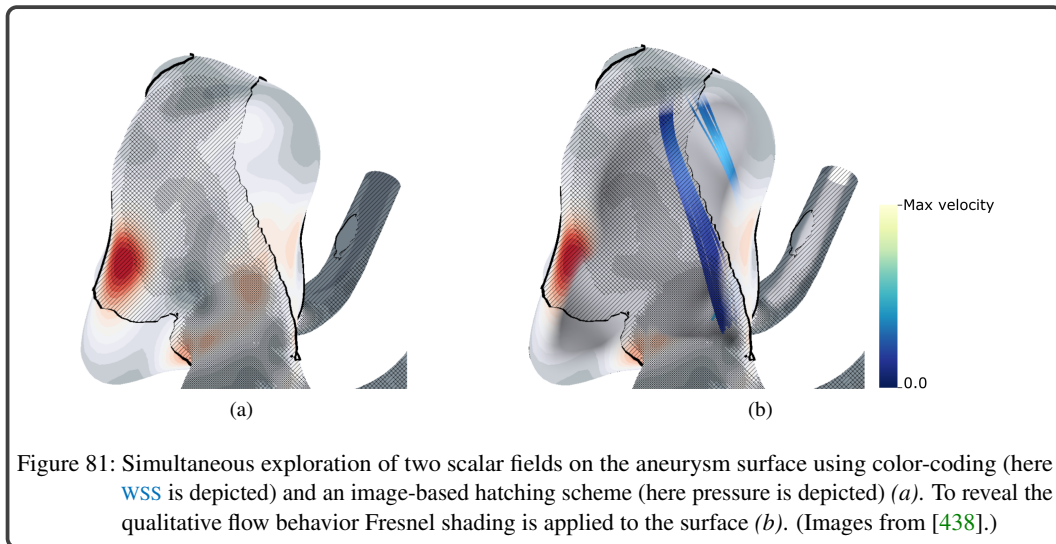
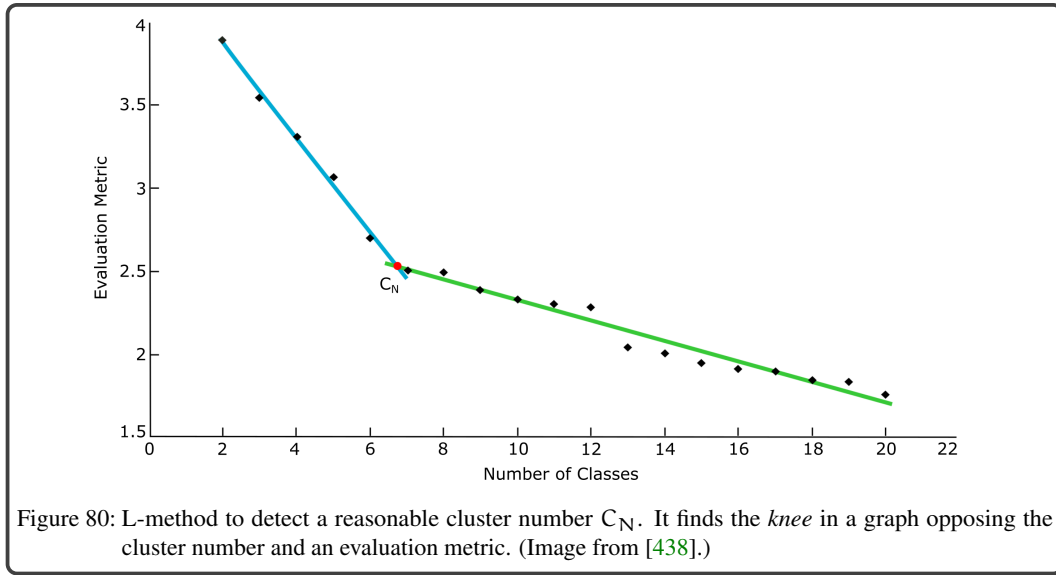
### 7.1.3 Path Line Clustering

The distance matrix is used as input for the path line clustering. Each path line is assigned to exactly one cluster. Oeltze et al. [282] recommend using [AHC](#) or [SC](#) to group streamlines in cerebral aneurysms. We extended their similarity measure for applying it on path lines and used [AHC](#). We also tested [SC](#), which leads to similar results, see Section 7.1.5. Density-based approaches such as [DBSCAN](#) are also used to cluster integral lines [98, 433]. However, we reject [DBSCAN](#), since two thresholds have to be defined, which essentially determine the cluster structure and an appropriate threshold selection can be tedious [433]. Moreover, using [AHC](#) allows comparing our similarity measure to existing techniques [282, 433] that used [AHC](#) to cluster blood flow-representing lines.

To reduce the effort for selecting an appropriate cluster number, we aim to make a "good guess" using the *L-method* [328]. It is based on finding a *knee* in a graph that opposes the cluster number and an evaluation metric, see Figure 80. The evaluation metric uses the values from  $\mathbf{D}$  leading to a fusion of two clusters. The position of the *knee* represents the appropriate cluster number but depends on the number of clusters involved in creating the graph. Therefore, a complete graph is recommended, ranging from two clusters to the number of lines. For our data sets, the maximum detected cluster number is 20. If the automatically calculated number is not appropriate, the expert can incorporate his expert knowledge by chaining the cluster number ([Req. 17](#)).

### 7.1.4 Visualization of Blood Flow Clusters

The path line clusters are visualized in two juxtaposed render contexts that are linked to each other. The first one shows the clusters within the 3D aneurysm, whereas the second provides a more abstract depiction. Here, the clusters are visualized as 2D structures. In the following, we comment on the design decisions for the different views and their interplay.



### 3D Cluster Visualization

The 3D aneurysm view enables a detailed exploration of possible correlations between individual flow patterns that are associated with an increased risk of rupture and high-risk wall regions. Therefore, the aneurysm surface is depicted following our previous approach [436]. This enables the simultaneous exploration of two user-selected scalar fields, see Figure 81a. The first is depicted using a gray-to-red color scale and the second one is visualized using an image-based hatching scheme. The blood flow is represented by lines, and color-coded according to a user-selected property, e.g., the velocity. To analyze scalar data and the internal flow simultaneously, we applied *Fresnel shading* as suggested by Gasteiger et al. [122] to the vessel surface, see Figure 81b.

The simultaneous depiction of all path lines would lead to visual clutter. Therefore, we determined a representative for each cluster that summarizes the blood flow and enables the perception of inner flow structures. Similar to Oeltze et al. [282], we used *density-based representatives* [280] to approximate the shape of the clusters. The method is based on generating a Cartesian grid around the cluster using its axis-aligned bounding box. The grid resolution corresponds to the resolution of the image data that was used to reconstruct the aneurysm morphology. For each voxel of the grid, a density value is determined by counting the number of passing lines. Finally, the densities per line are integrated,

and the line with the highest value is used as representative. The representatives are shaded as tubes to improve their perception from a more distant point of view. The user can select a specific representative by clicking into the scene, which activates the rendering of the corresponding path lines of that cluster. This allows a targeted exploration of suspicious flow patterns.

### 2D Cluster Visualization

A very irregularly deformed aneurysm surface complicates the simultaneous exploration of internal flow patterns and scalar wall properties. Manual rotations are necessary to perceive the flow behavior and to detect critical wall regions. The time-dependent behavior of the data further complicates the exploration. To facilitate the flow pattern analysis, we provide more abstract visualizations where the aneurysm surface and the clusters are depicted as 2D structures in two ways.

**MAP-BASED CLUSTER VISUALIZATION.** Similar to the **MuScaVis** module, we provide the 2D aneurysm map in an additional view to avoid visual clutter. The map ensures an occlusion-free exploration of a chosen scalar quantity and shows the flow behavior of individual clusters. Therefore, the path line points of a user-selected cluster are projected onto the map and are visualized as circles by applying depth-dependent halos [100]. Again, the ostium contour is color-coded in the 2D and 3D view to establish a spatial correlation between both views, see Figure 82.

The path lines are projected on the generated 2D map. Thus, for each path line point  $\mathbf{p}_i$  the nearest surface point of the aneurysm part  $\mathbf{p}_j$  is determined based on the Euclidean distance, see Figure 83a. For this,  $\mathbf{p}_i$  is orthogonally projected into the triangle's plane defined by its normal. We check if the projected point lies inside the triangle by computing the barycentric coordinates. If the point lies inside the triangle, we determine the distance of  $\mathbf{p}_i$  and the projection and store the previously determined barycentric coordinates of the triangle. In case the projected point lies not inside the triangle, we compute the nearest point on the triangle's boundary. For this, the distance of  $\mathbf{p}_i$  and the three edges is determined. Again, we store the minimum distance and the barycentric coordinates of the closest point with the triangle. This procedure is repeated with all triangles on the aneurysm part such that we obtain the minimum distance, the barycentric coordinates of the closest point, and the associated triangle. Then, all path line points  $\mathbf{p}_i$  are projected on the map yielding  $\mathbf{p}'_i$ .

To ensure a smooth animation of the points, we generate quads on the GPU for the successive path line points  $\mathbf{p}'_i$  and  $\mathbf{p}'_{i+1}$ , see Figure 83b. The quads are equipped with a coordinate system that reflects the extent of the quad. In y-direction we have  $[-\sqrt{r}, \sqrt{r}]$  and in x-direction we have  $[-\sqrt{r}, \|\mathbf{p}_{i+1} - \mathbf{p}_i\| + \sqrt{r}]$ . Here,  $r$  is used for the radius of the drawn circle that represents the animated path line point. A circle is drawn on the quad if the animation time  $t$  is in  $[t_i, t_{i+1}]$  (the time interval of the current period), see Figure 83c.

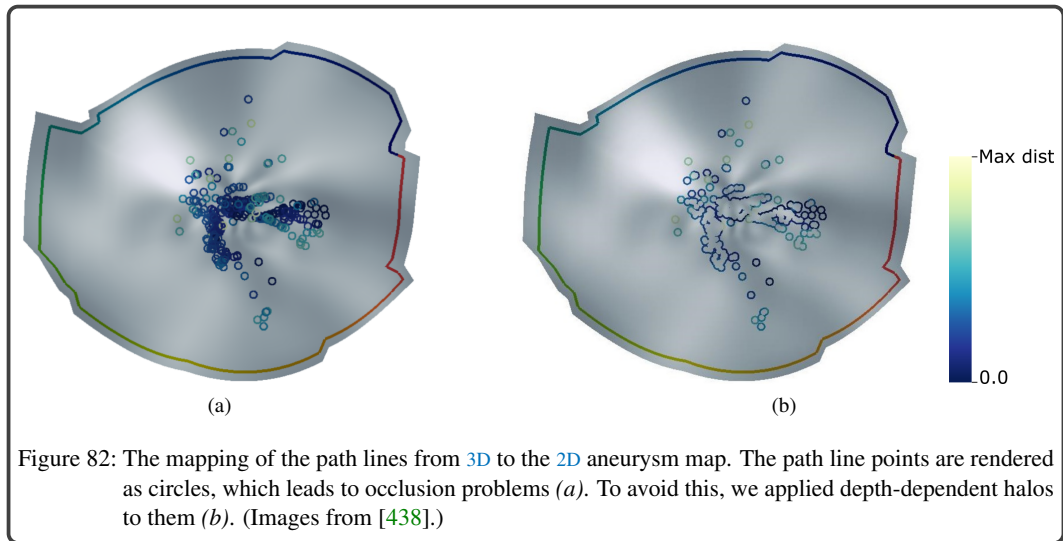
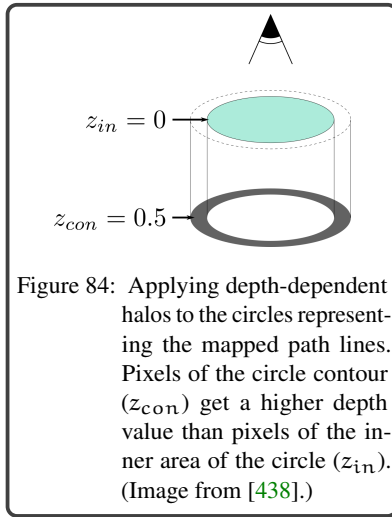
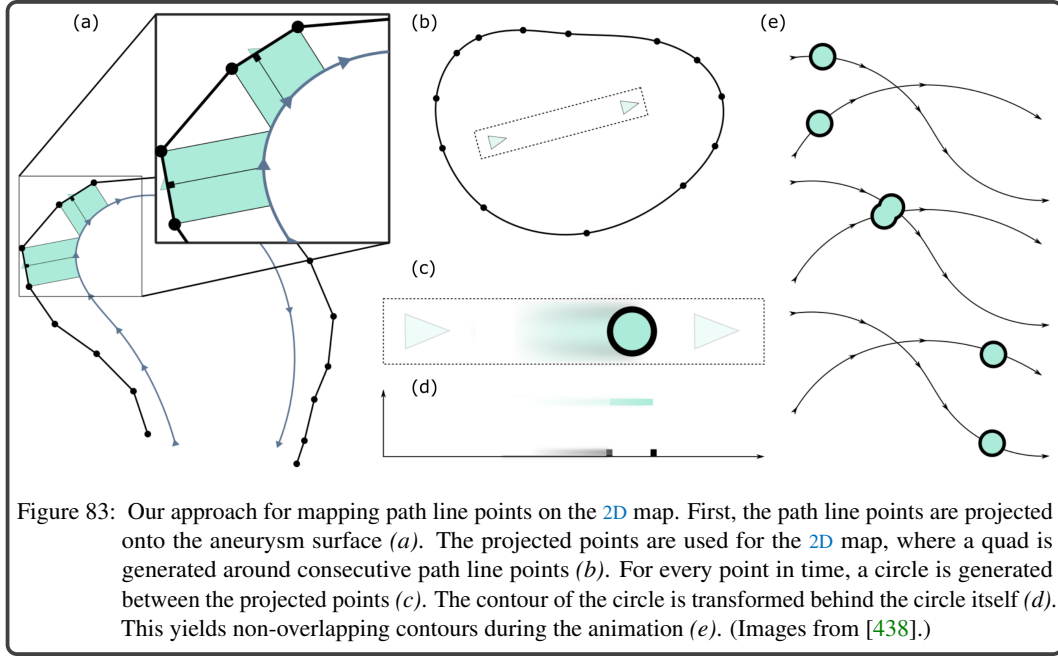


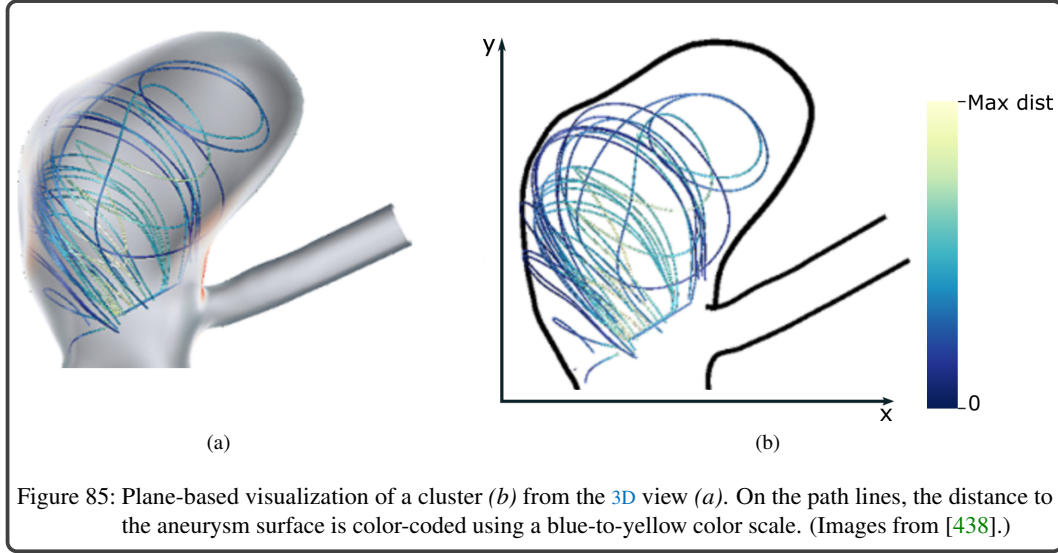
Figure 82: The mapping of the path lines from 3D to the 2D aneurysm map. The path line points are rendered as circles, which leads to occlusion problems (a). To avoid this, we applied depth-dependent halos to them (b). (Images from [438].)



Then, we define  $X(t) = \frac{t-t_i}{t_{i+1}-t_i} \cdot \|\mathbf{p}_{i+1} - \mathbf{p}_i\|$  and draw a white filled circle if  $(x - X(t))^2 + y^2 \leq r^2$ , again  $x, y$  are the coordinates of the quad, see Figure 83d. In case that  $(x - X(t))^2 + y^2 \geq r^2$  and  $(x - X(t))^2 + y^2 \leq (r + c)^2$  holds, where  $c$  denotes the thickness of the contour, we use a colored outline and set the depth of these fragments higher than the (white filled) circle, see Figure 84. This avoids overdraw between overlapping circles, see Figure 83e. However, the user can switch between the depth-dependent halos and the more cluttered image, see Figure 82. The circle contours can be color-coded according to a user-selected scalar field, e.g., the distance of the flow to the aneurysm wall, using a blue-to-yellow color map. Applying the depth-dependent halos also avoids occlusions between the circles and the color-coded scalar field on the 2D map, see Figure 82b. This enables simultaneous exploration of scalar flow and wall properties to detect probably rupture-prone wall regions (Req. 4).

**PLANE-BASED CLUSTER VISUALIZATION.** To further facilitate the perception of flow patterns, a second 2D visualization is provided. This shows the contour of the vessel surface and path lines of a user-selected cluster projected on a plane, see Figure 85. Hand-drawn sketches of aneurysms by medical experts show the aneurysm sac as the most important feature pointing upwards. To fulfill this, the aneurysm has to be oriented along the  $y$ -axis of the underlying coordinate system, see Figure 85b. Moreover, an appropriate view should show the maximum extent of a cluster. To construct a projection plane that fulfills both conditions, we perform a *principal component analysis* (PCA) of the ostium positions and determine the eigenvectors  $\mathbf{e}_{oi}$  with  $i \in 1, 2, 3$ . By using the ostium positions instead of all aneurysm vertices, the viewpoint selection is more independent from the aneurysm shape. We take the eigenvector of the ostium  $\mathbf{e}_{o3}$  with the smallest magnitude, which runs similar to the  $y$ -axis. Moreover, we perform a PCA of the spatial path line point positions of the cluster and determine the corresponding eigenvectors  $\mathbf{e}_{ci}$  with  $i \in 1, 2, 3$ . Afterward, we calculate the scalar product between the  $\mathbf{e}_{ci}$  and  $\mathbf{e}_{o3}$ . The eigenvector, which is most likely to be parallel to  $\mathbf{e}_{o3}$  is used

as the first plane vector. If this vector runs in the opposite direction of  $\mathbf{e}_{o3}$ , we invert its direction. From the remaining two  $\mathbf{e}_{ci}$ , we choose the one with the largest eigenvalue as the second plane vector. If the eigenvalues of both vectors are the same, we take the first one. The remaining  $\mathbf{e}_{ci}$  defines the view direction of the virtual camera. Finally, we project  $\mathbf{e}_{o3}$  into the constructed plane and rotate the plane that  $\mathbf{e}_{o3}$  runs along the y-axis. This guarantees a view, where an aneurysm points upwards. To calculate the surface contour, we used the approach by Lawonn et al. [213]. The contour results from the positions at which the surface normal and the view direction are mutually orthogonal.



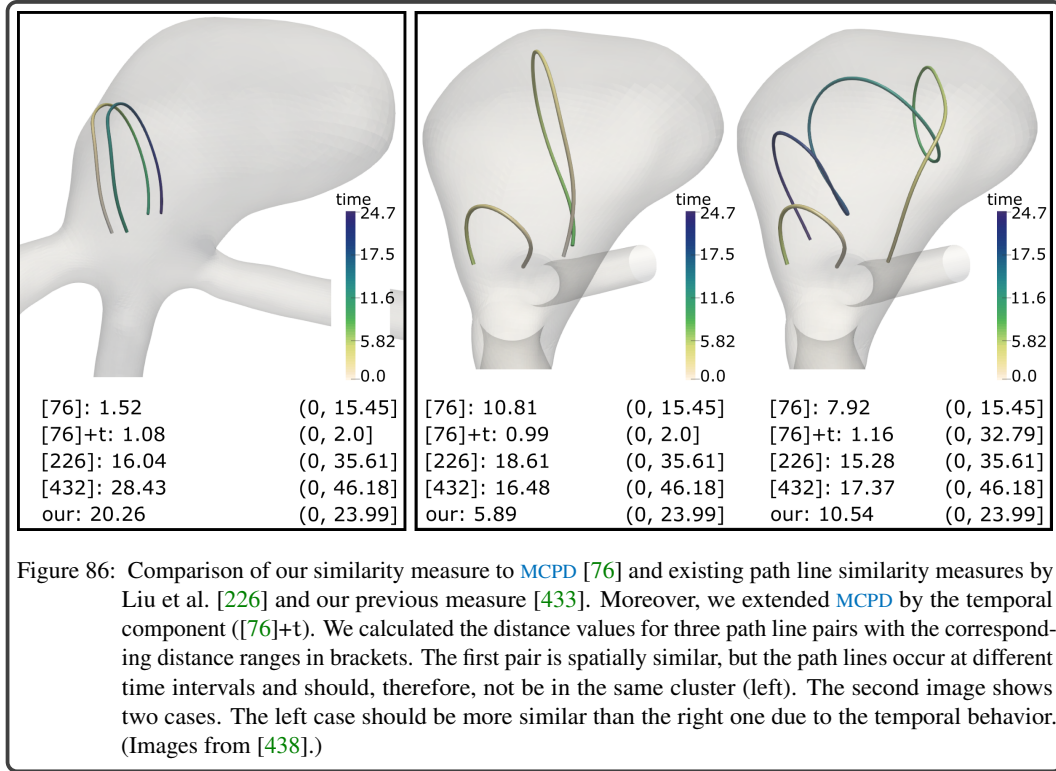
#### 7.1.5 Evaluation and Results

To assess the quality of our similarity measure, we compared it with other similarity measures. Moreover, we conducted a qualitative evaluation, where participants ranked different path lines according to their similarity. We compared the rankings to our calculated similarities to assess the suitability of our method. Furthermore, we questioned experts to assess the suitability of the visualizations and their bidirectional connection.

##### Comparison with other Similarity Measures

We compared our similarity measure with MCPD [76], which is used to calculate streamline similarities and the approaches by Liu et al. [226] and our previous method [433] to calculate similarities between path lines. Moreover, we extended the MCPD measure by the temporal component ([76]+t). For this purpose, we calculated two distance fields  $d1$  and  $d2$ , where  $d1$  represents the MCPD measure based on the 3D spatial components (x,y,z) of a path line point, and  $d2$  represents the MCPD measure based on the points' temporal component  $t$ . To be independent of spatial/temporal units of the underlying domain,  $d1$  and  $d2$  are normalized to the range  $[0, 1]$ , resulting in  $d1'$  and  $d2'$ . The final distance value between two path lines is computed by adding their corresponding  $d1'$  and  $d2'$  value. With this, we evaluated if such a simple integration of the temporal component leads to plausible results. Figure 86 shows three pairs of path lines, where the temporal component is color-coded. Below, the corresponding distances and ranges are listed. The higher the distance value, the less similar the lines are. The path lines in the left image are geometrically quite similar but do not occur in the same time interval. Therefore, they should receive a high distance. However, using MCPD the path lines have a low distance since only geometrical properties are considered. With our approach, the highest distance can be reached, ensuring that these path lines would be grouped into the same cluster only for a very low and inappropriate cluster number using AHC. For the remaining three approaches, the distances are quite similar because of the stronger influence of geometrical properties compared to





the temporal distances. The right image shows two pairs of path lines that are geometrically less similar to each other. Considering the temporal component, the left case should be more similar than the right case, which could be reached with our method. In contrast, MCPD results in a lower distance for the right case. Integrating the temporal component for MCPD ([76]+t) also results into a lower distance for the left case. However, the distance for the left case is quite similar to the first case in the left picture, which is not desired due to their different temporal behavior. Based on our previous approach [433], the distances are quite similar for both cases, since only the lines' start- and endpoints are considered for calculation. The distance of the right case using the method by [226] is also lower than for the left case, which shows the dependence of the underlying spatial partition into cubes. In contrast to the left pair, the right one shared some cubes.

To further evaluate our similarity measure, we compared our clusters with the results of existing similarity measures, see Figure 87. The first row shows a cluster that enters and leaves an aneurysm more distant to the wall, where the temporal component is color-coded on the lines. Using MCPD, lines with different temporal behavior are clustered together, see Figure 87a. Integrating the temporal component leads to a cluster where path lines with a laminar and vortical behavior are grouped, see Figure 87b. A similar result is generated with our previous method [433] (Figure 87d) since the geometrical behavior of path line points, which are no start- or endpoints is less considered. Our method leads to a cluster that exhibits only laminar behavior without integrating path lines that occur at different times, see Figure 87e. A similar result could be generated with the method by [226], see Figure 87c. However, this cluster contains path lines with different spatial behavior, and the results were sensitive to the used cube size. Small changes of the cube size led to quite different results. The second row shows a vortical flow pattern that becomes more and more tight over the cardiac cycle. Our method results in a cluster that shows a strong vortex at the end of the cycle, see Figure 87e. Using the other similarity measures, it is not possible to depict the decay of the vortex by individual clusters. Path lines, occurring more early occlude the inner vortex structure. However, to cluster instable flow patterns is important, since such patterns are correlated with rupture [60].



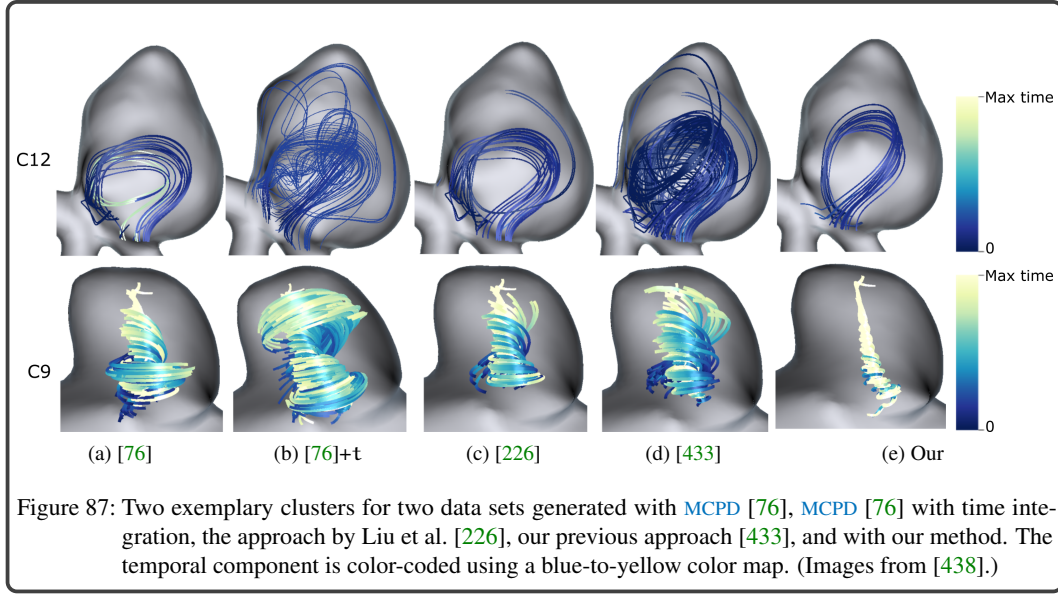


Figure 87: Two exemplary clusters for two data sets generated with MCPD [76], MCPD [76] with time integration, the approach by Liu et al. [226], our previous approach [433], and with our method. The temporal component is color-coded using a blue-to-yellow color map. (Images from [438].)

In addition, we artificially generated a vortex using:

$$C_i(u) = \begin{pmatrix} r_i \cdot \sin(u) \\ r_i \cdot \cos(u) \\ u \\ (i-1) + u \end{pmatrix}, \quad i \in \{1, \dots, 100\}, u \in [0, 10\pi], \quad (33)$$

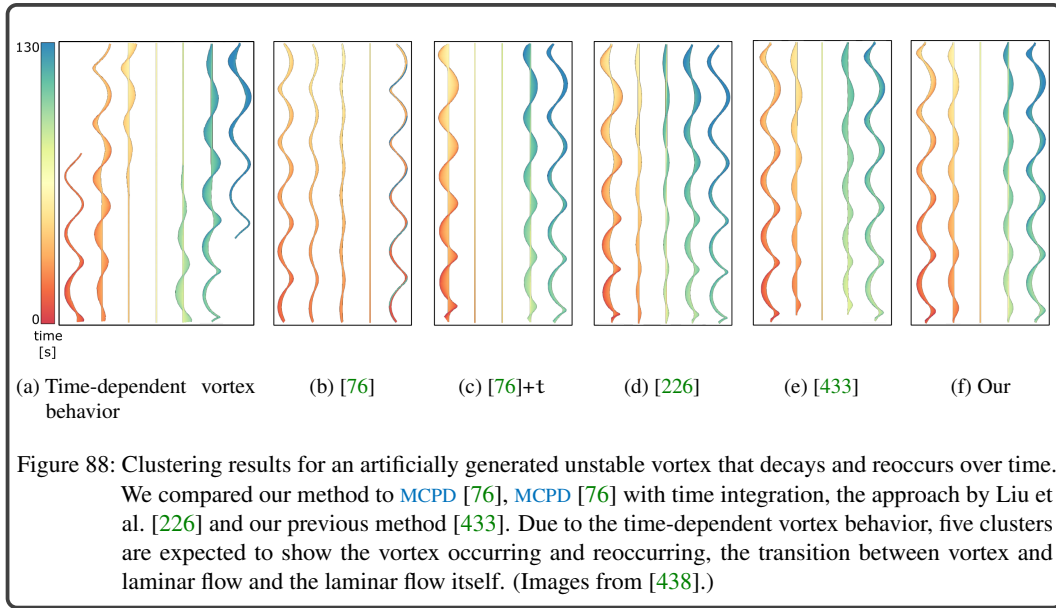
where  $r_i = \frac{1}{2} \cos(\frac{2\pi i}{100}) \cdot (1 + \text{sgn}(\cos(\frac{2\pi i}{100})))$  and

$$\text{sgn}(x) = \begin{cases} 1 & \text{if } x \geq 0 \\ -1 & \text{if } x < 0. \end{cases} \quad (34)$$

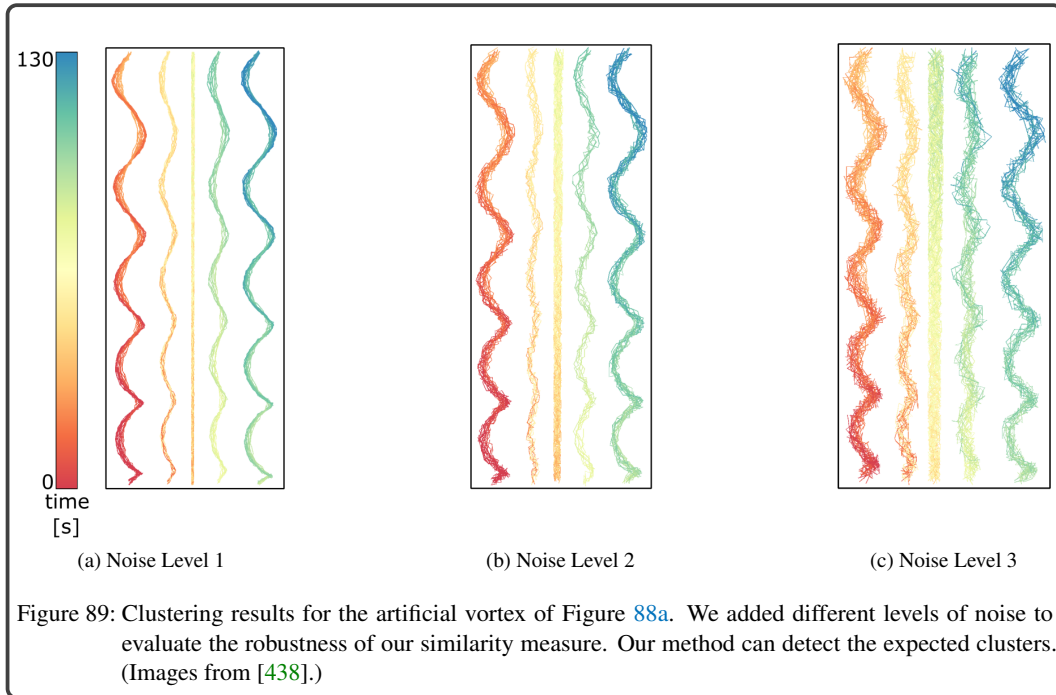
The vortex occurs, decays to a line and reoccurs over time, see Figure 88a. Due to its time-dependent behavior, five clusters are expected to show the vortex occurring and reoccurring, the transition to laminar flow, and vice versa, as well as the laminar flow itself. MCPD (Figure 88b) and MCPD with time (Figure 88c) are not able to separate these stages. Similar problems would arise with the method by McLoughlin et al. [245] since just geometrical features are considered for calculation, which are quite similar for the phases. The approach by Liu et al. [226] was again sensitive to the cube size and was not able to separate the laminar flow, see Figure 88d. Our previous method [433] (Figure 88e), where the laminar stage was used as the centerline, and our measure (see Figure 88f) can distinguish the individual stages. However, for patterns that are not so perfectly symmetric such as the example in Figure 87 (C9), our previous measure [433] is not appropriate to cluster instable patterns. These comparisons show that existing similarity measures are less reliable than our new approach.

#### Robustness Experiments

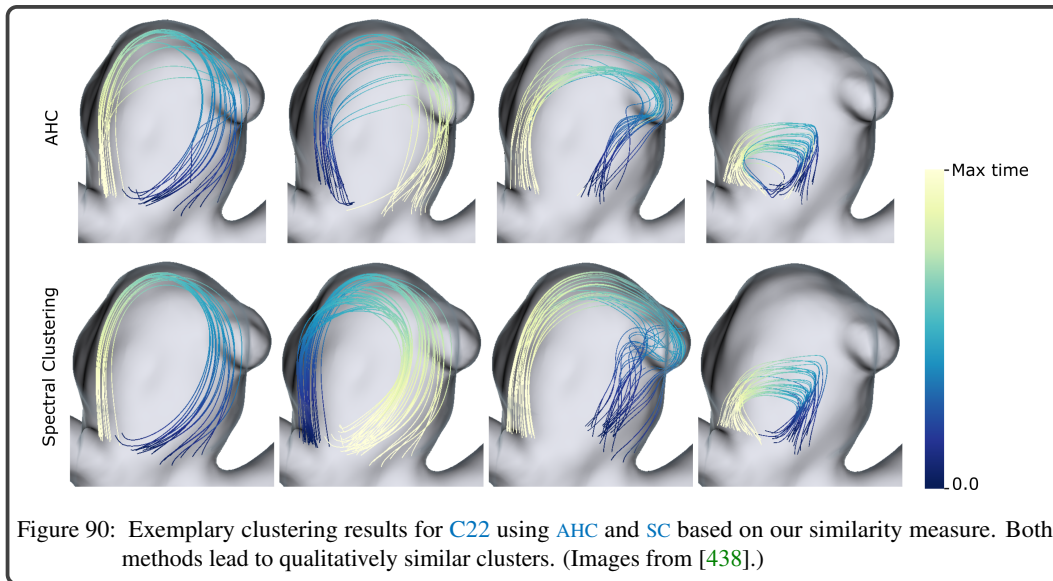
To evaluate the robustness of our similarity measure, we added different amounts of noise to the artificially generated vortex in Figure 88a. Figure 89 shows the clustering results of our measure for three noise levels. The different levels were generated by adding a random number  $rn$  to the 3D spatial components (x,y,z) of a path line point, where  $rn$  was selected in the of range of  $[0, i]$  with  $i \in [0.2, 0.6, 1.0]$ . Adding noise to the spatial position simulates possible occurring artifacts in measured or simulated data, whereas temporal noise would not occur in measured or simulated data sets due to the pre-defined time between two successive time steps. Our method can detect the five



expected clusters of the vortex representing its different stages for the different amounts of noise, which shows that our similarity measure is robust against noise.



Besides the robustness analysis of our similarity measure, we perform a qualitative comparison between AHC with average link and SC as described in Oeltze et al. [282] for the artificially generated vortex and the aneurysm data set C22. For the artificial vortex, there was no visual difference between the results of both clustering methods. SC leads to the same clusters as depicted in Figure 88f. Figure 90 shows exemplary cluster results for C22 based on AHC and SC. We yielded quite similar results for both methods, which is similar to the findings by the works of [282, 433], who state that both approaches lead to reasonable results for blood flow clustering. An in-depth comparison of these techniques based on our similarity measure would be part of future work.



### Participants' Cluster Comparison

Due to the absence of a clustering ground truth, this evaluation should show if the participants' sense of path line similarity is coherent with our similarity measure. For this, the participants ranked different path line pairs manually according to similarity for ten cases based on five data sets. Each case contains four pairs, where one path line was the same for all pairs that serves as a reference. The cases were generated in the following way: a path line was randomly chosen. Then, the other path lines were ordered according to their similarity. Afterward, the path lines were categorized in four intervals with approximately the same interval length (based on the similarity measure). For each interval, a path line was randomly chosen.

This evaluation was conducted with 12 participants with a background in flow visualization ranging from one to six years of experience. All pairs of a case were shown side-by-side within the 3D aneurysm surface. If the user rotates one scene, all pairs were rotated synchronously. The participants were asked to order the path lines according to their similarity to the reference line from the highest to the lowest value. Therefore, we color-code the time component on the lines. Besides the manual ranking, we also ranked the pairs according to our calculated similarity values. Finally, we compared our rankings with the manual user rankings, see Table 4. For this purpose, we evaluated the order of the path lines with points. If the order of our measure to the participants' order was the same, we gave one point (✓). In case the ordering of one pair was wrong, half a point (○) was given. In case two or more orderings were wrong, zero points (✗) were given. The last column of Table 4 shows the total number of points for each participant. A maximum number of ten points could be achieved in total. The higher the value, the greater the consistency between our similarity measure and the manual rankings. On average, 8.5 points were reached.

### Informal Expert Feedback

The informal evaluation was conducted with four domain experts, one neuroradiologist P1 with 16 years of experience, two CFD experts P2, and P3 with five and eight years of experience, respectively, and one expert for medical visualization P4 with six years of experience. The informal study was conducted in two steps:

1. Introduction to the ViFIEx module with the 3D and 2D visualizations of the flow patterns and the interaction techniques.
2. A questionnaire that inquires the importance of intra-aneurysmal flow analysis and the visualization of the clustering results.

Table 4: Results of the manual path line comparisons. Each column corresponds to a case. One point was given for no mistake (✓), half a point was given for one mistake (○) and zero points were given for more than one mistake (✗). The last column shows the total number of reached points for each participant.

1	2	3	4	5	6	7	8	9	10	Total
✓	✓	✓	✓	✓	○	○	✓	✓	✓	9.0
✓	○	✓	✓	✓	○	✓	✓	✓	✓	9.0
✓	✓	✓	✓	✓	✓	○	✓	✓	✓	9.5
○	○	✓	○	✓	○	✓	✓	✓	○	7.5
✓	✓	✓	✓	✓	✓	✓	✓	✓	○	9.5
✓	○	✓	○	✓	✓	✓	✓	✓	○	8.5
✓	✓	✓	✓	✓	✓	✓	○	○	✓	9.0
✓	✗	✓	✓	✓	✓	✓	✓	✓	○	8.5
✓	○	✓	✓	✓	○	✓	○	✓	○	8.0
✓	✓	○	○	✓	○	✓	○	○	✓	7.5
✓	○	✓	✓	✓	○	✗	✓	✓	✓	8.0
○	○	✓	✓	✓	✗	✓	✓	✓	✓	8.0

The first step is necessary for the experts to familiarize themselves with the module. Then, the experts answered the questionnaire using a five-point Likert scale (—, —, ○, +, ++). For the analysis of the Likert scores, we provide the number  $S(\cdot)$  of experts who chose the individual scale. The overall result of the empirical evaluation is shown in Figure 91.

**Medical relevance.** All domain experts confirmed the importance to analyze quantitative and qualitative flow properties, respectively for the patient-specific rupture risk assessment ( $S(++) = 3$ ;  $S(+) = 1$ ). The simultaneous investigation of these factors was rated as highly important ( $S(++) = 4$ ). The CFD experts stated that a combined analysis is necessary to understand the interplay between specific flow patterns and scalar data such as WSS. Furthermore, we asked about the importance to investigate the distance of flow patterns to the vessel wall that was rated with  $S(++) = 4$ . P2 stated, “[...] vortical flow patterns coming close to the wall are more associated with rupture than more distant patterns.” Finally, we ask about the importance to compare flow patterns between data sets, which is evaluated as very crucial ( $S(++) = 4$ ). All experts stated that such a comparison would allow transferring treatment decisions or rupture assessments to new cases.

**Flow pattern recognition.** The experts evaluated visualization techniques to recognize flow patterns. One possibility is to show all path lines simultaneously in an animated way. This was considered inappropriate due to occlusion problems and visual clutter ( $S(-) = 1$ ;  $S(--) = 3$ ). Coloring the path lines due to their cluster affiliation slightly improves the identification of flow patterns ( $S(○) = 1$ ;  $S(-) = 3$ ). In contrast, the selection of individual clusters based on the 3D view per mouse click was assessed as very appropriate ( $S(+) = 1$ ;  $S(++) = 3$ ).

**3D cluster visualization.** All experts confirmed that the 3D visualization of the cluster representatives allows a reasonable simplification of the complex flow behavior ( $S(++) = 4$ ). The CFD experts stated that the cluster representatives support the assessment of the most prominent flow patterns, which is one of their main tasks, recall Section 5.1. Moreover, they stated that the surface transparency reveals the qualitative flow behavior ( $S(++) = 4$ ).

**2D cluster visualization.** All participants confirmed that the path line projection on the map allows a fast detection of possible rupture-prone regions ( $S(++) = 2$ ;  $S(+) = 2$ ). Besides, the experts stated that the 2D map reduces the exploration effort ( $S(++) = 3$ ;  $S(+) = 1$ ). However, for the assessment of the most prominent flow patterns, P2 and P3 preferred the 3D cluster representatives. P1 stated that the map would support the comparison of ruptured and non-ruptured cases due to simplified visualization of scalar and vectorial data. The suitability of the plane-based visualization to support the flow analysis was rated more controversially with  $S(+) = 2$  and  $S(○) = 2$ . P1 and P3 argued that the map in combination with the 3D view is sufficient to understand individual flow patterns.

	--	-	o	+	++
	Clinician	CFD Experts		Visualization Expert	
	P1	P2	P3	P4	
<b>Medical Relevance</b>					
The analysis of quantitative and qualitative flow properties is important for the patient-specific rupture risk assessment.	++	++	++	+	
The simultaneous investigation of these factors is important to assess the aneurysm state.	++	++	++	++	
To investigate the distance of flow patterns to the vessel wall is important to assess the aneurysm risk.	++	++	++	++	
The comparison of flow patterns between data sets is important to assess the aneurysm state.	++	++	++	++	
<b>Flow Pattern Recognition</b>					
Showing all path lines simultaneously in an animated way is suited to recognize flow patterns.	--	-	--	--	
Coloring path lines due to their cluster affiliation is suited to recognize flow patterns.	-	o	-	-	
The selection of individual clusters is suited to recognize flow patterns.	++	++	++	+	
<b>3D Cluster Visualization</b>					
The 3D visualization of the cluster representatives allows a reasonable simplification of the complex flow behavior.	++	++	++	++	
The surface transparency reveals the qualitative flow behavior.	++	++	++	++	
<b>2D Cluster Visualization</b>					
The path line projection on the map allows a fast detection of possible rupture-prone wall regions.	+	++	+	++	
The 2D map reduces the exploration effort in 3D.	+	++	++	++	
The plane-based visualization supports the analysis of the flow behavior.	o	+	o	+	

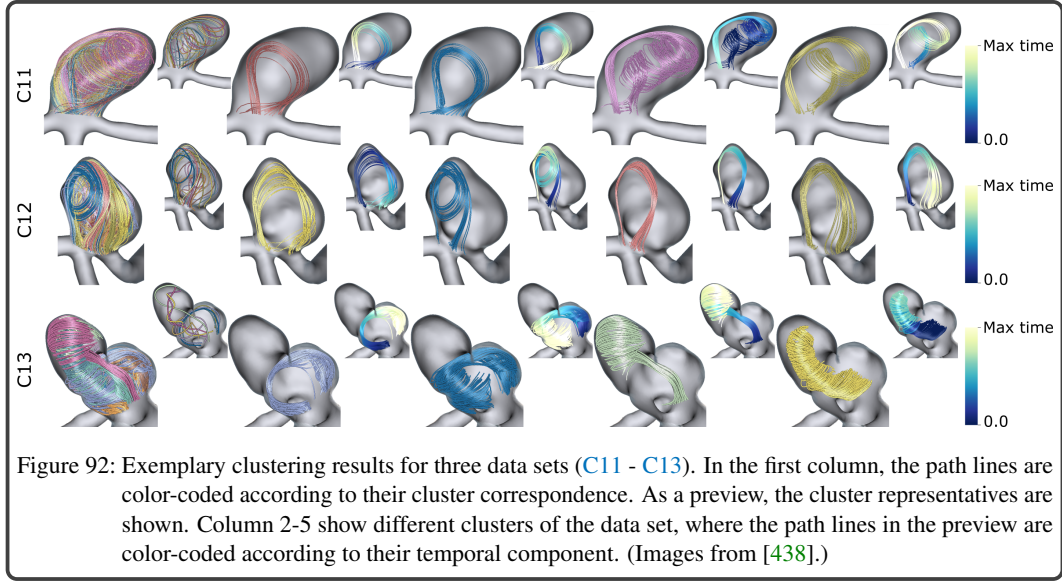
Figure 91: The results of the expert evaluation of the path line clustering with color-encoded Likert scores. Each box represents the answer of one expert: the left-most box depicts the physician, the middle two boxes show the CFD experts, and the right-most box represents the medical visualization expert (Image from [438].)

Finally, we qualitatively evaluated our clustering results with the experts. They visually inspected clusters and stated that they should be spatially compact and temporally coherent. Figure 92 shows exemplary results for three data sets C11 - C13. In the first column, the path lines are color-coded according to their cluster correspondence, and the representatives are shown as a preview. Moreover, four clusters per data set are depicted, where the temporal component is color-coded. All clusters are spatio-temporally compact. For example, the purple and blue cluster of C13 are spatially very similar but exhibit an opposite temporal behavior. Thus, they are not grouped. Reoccurring patterns over time are grouped into different clusters such as the pink and yellow cluster of C11.

### Performance

This section reports on the performance of our clustering approach. We focused on computation times since memory consumption is not critical. The time depends on the number of path lines (varying between 1435 and 7999 lines) and their average number of vertices (ranging between 117 and 209 points). While the first varies with the sampling density of the ostium, the latter depends on the line length and integration step size. We measured the computation time of AHC, where we differentiated between the computation of the distance matrix and the actual clustering including the determination of representatives. The calculation of the distance matrix represents the bottleneck (varying between 20.2 and 93.1 min), where the timings for the clustering itself are in the range of seconds (ranging between 7.1 and 53.4 s). For the visualization, we reach real-time frame rates of 60 FPS.





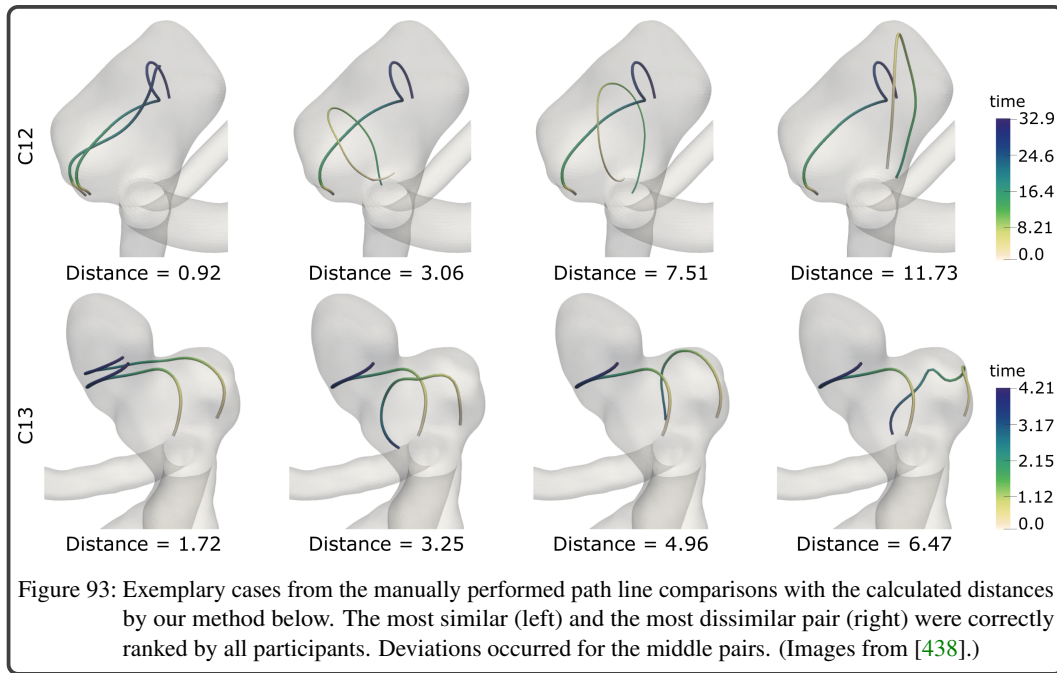
### 7.1.6 Discussion and Limitations

**Similarity validation.** Due to the absence of ground truth to validate our clustering results, we evaluated if our similarity measure leads to plausible results. For this purpose, we compared our calculated similarities with manually prepared similarity rankings. The experts stated that path lines are similar if they have a low spatial distance and occur at similar time intervals. In contrast, path lines that occur in different spatial areas or time intervals are classified as less similar. Our results were consistent with the manual orders in 8.5 points on average. Thus, in most cases, the calculated similarity values conform to the rankings of the participants. The expert's rankings of cases, showing stronger differentiation in their spatial and temporal behavior, e.g., C12, conform to our calculated ranking, see Figure 93. Deviations occurred for cases with a more complex flow behavior, such as C13, see Figure 93. They ranked the most similar and the most dissimilar pair correctly for almost all cases but interchanged the second and third rank. The reason, therefore, were problems to visually estimate the distances between corresponding points based on the temporal component. The participants stated that they are less confident with their estimations for these cases and thus, they would prefer to use our measure. Besides, generating such a ground truth is challenging. Path lines would have to be labeled manually according to pre-defined types. This would be a time-consuming and subjective process. The time-dependent behavior of the data would further complicate this task. In contrast to existing similarity measures, our method allows analysis of flow patterns that are not stable over the cardiac cycle, since instability is (besides complexity) a major predictor for rupture risk [60]. Vortices that only occur during a specific time interval may be investigated with our approach. Such patterns would probably be missed with a static clustering depending on the selected time step for seeding.

**Robustness.** We could show that our method is robust against noise. However, the measure depends on the most dissimilar path line to ensure that  $D(\text{case } 1) \leq D(\text{case } 3)$ . Thus, our measure might count the same pair of path lines either as relatively similar or as more dissimilar, depending on the presence of outliers. In our cases, this does not lead to inappropriate results. To overcome this limitation, we would have to change the calculation of  $(D)_{ij}$  to:

$$(D)_{ij} = 1 - \frac{1}{(\overline{D}_{ij} + 1)} + J_{ij} \quad \text{or}$$

$$(D)_{ij} = 1 - \exp\left(-\left(\frac{\overline{D}_{ij}^2}{\sigma}\right)\right) + J_{ij},$$



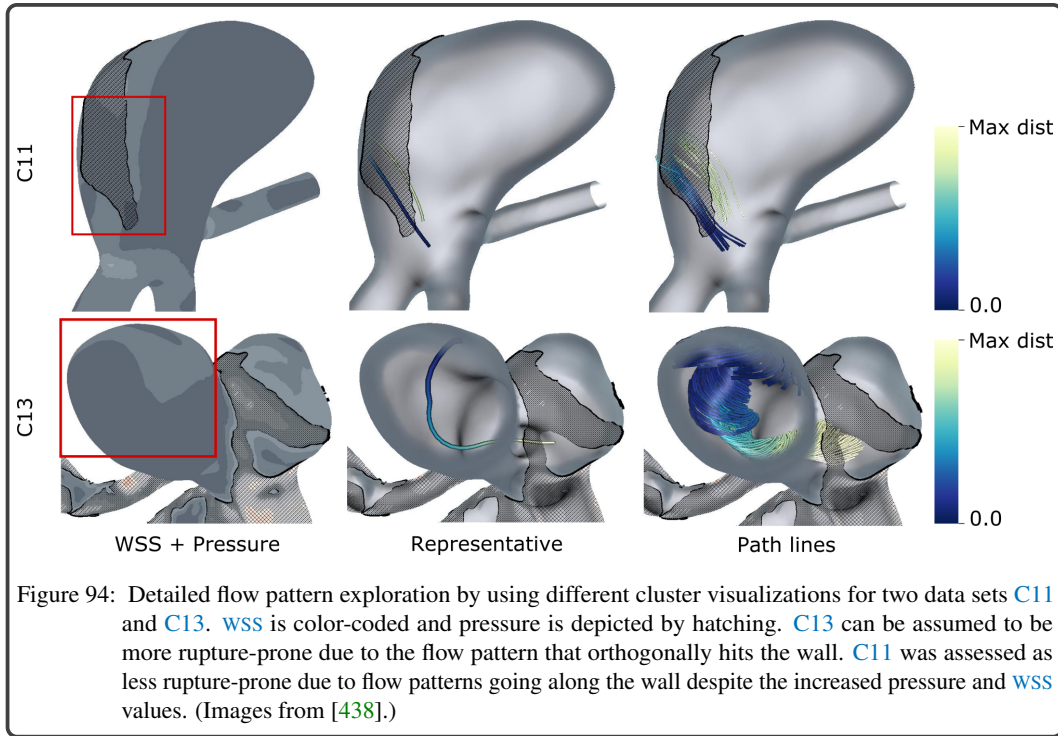
where  $\sigma$  is a user-defined variable. However, with these new calculations of  $(D)_{ij}$ , the distance values would not change linearly. This also might lead to inappropriate clustering results.

**Uncertainty.** The individual pre-processing steps, image reconstruction, segmentation, choice of inflow boundary condition, and virtual treatment are related to uncertainties [32, 333, 341, 373]. To reconstruct angiography images as input for the surface extraction, different reconstruction kernels can be used. Depending on the selected kernel, the vessel diameter and ostium area are influenced, which further leads to differences in hemodynamic values such as pressure and flow magnitude. Besides, the shape of the reconstructed surface and CFD results depend on the selected segmentation method. Finally, the chosen boundary conditions for the CFD simulation influence the resultant vector fields. Deriving flow rates from known patient-specific flow rates could lead to uncertainties in the CFD results since flow rates depend on different factors such as sex, body size and normal or pathological variants of vascular anatomy. However, patient-specific flow rates are rarely available. In summary, uncertainties arising from the individual pre-processing steps could lead to inaccuracies in the resultant flow patterns, i.e., flow patterns could be traced that are not existing. However, until now there is no clear recommendation which methods should be used for preprocessing. A more detailed analysis of possibly arising uncertainties is beyond the scope of this thesis.

**Findings.** During the evaluation, it turned out that the 3D and 2D depictions represent a meaningful combination for efficient exploration of flow patterns. The experts liked the concept of the linked and juxtaposed 3D and 2D depictions, which avoids switching between the views. The 3D view allows a detailed analysis of individual flow patterns. Thus, our experts were able to find correlations between rupture-relevant flow patterns and high-risk wall regions, see Figure 94. Here, for two data sets C11 and C13 the WSS is color-coded, and the pressure is depicted by hatching. The experts analyzed individual clusters of both cases. In C13 they detected a flow pattern that orthogonally hits the wall during the whole cardiac cycle and could lead to rupture. Conversely, the flow patterns of C11 run along the wall and have therefore been assessed as less rupture-prone despite the increased pressure and WSS values. However, in some cases, the experts were unsure if the current flow pattern is closer to the anterior or posterior wall of the vessel. Therefore, they wished to have additional clipping planes or a 2D color map, coding the distance to the respective wall side.

The 2D map gives a fast overview of possible correlations between flow patterns and scalar wall properties. By depicting the path lines as circles with depth-dependent halos, the color-coded scalar





field can be analyzed simultaneously. Existing approaches used cutaway techniques [216] or surface transparency for this purpose [274]. However, with these methods, the visibility of the displayed scalar field on the surface is severely restricted, which is avoided with our map-based visualization.

Due to the different assessment of the plane-based cluster depiction, we provide an optional activation of this view. Moreover, the experts wished to have more interaction techniques on the map that support the identification of the corresponding path lines in 3D. This could be realized by selecting a specific circle region on the map, followed by highlighting the corresponding path lines in 3D. Besides, the map-based path line rendering using circles was emphasized positively by all experts, because it provides a useful simplification of the complex 3D flow.

#### 7.1.7 Conclusion and Future Work

We presented a method for clustering path lines in cerebral aneurysms. Besides the aneurysm separation, our method performs fully automatically, which allows a faster and more objective analysis of suspicious flow patterns. Our similarity measure extends the **MCPD**, a reliable measure to determine streamline similarities. We achieved convincing results compared to manual similarity estimations of path lines. For clustering, we used **AHC**, an established method to group integral lines. This assures comparability of data sets and reproducibility of the results. In contrast, a manual analysis of flow patterns is time-consuming. A common advantage of **AHC** is the possibility to incorporate expert knowledge. The cluster number can be changed, which allows an investigation of alternative cluster configurations.

For future work, we want to perform a comparison of our current similarity measure and the suggested solution in Section 7.1.6 to overcome the global distance calculation. Another interesting point would be a perception-based user study that evaluates concepts, e.g., color or illustrative techniques, to encode scalar values on lines such as the distance of path lines to the aneurysm wall.

## 7.2 AUTOMATIC CLASSIFICATION OF FLOW PATTERNS

Several works aimed at identifying flow patterns that promote aneurysm rupture in order to build a classification scheme that can be employed in risk assessment and treatment planning [60, 114, 238, 267, 357]. These works are based on a visual inspection of integral curves displayed at peak systole in ruptured and non-ruptured aneurysms. Castro et al. [238] investigated bifurcation aneurysms according to inflow jet structure splitting into three classes. They reported associations between inflow jet structure, peak *WSS*, and aneurysm rupture. Nakayama et al. [267] manually classified systolic blood flow in side-wall aneurysms dependent on their rotational position. They distinguished two types of inflow, the side-type flow pattern, where the flow began from the side of the ostium, rotated and flowed out from the other side of the ostium. In the split type, the blood flow began from the center of the ostium, split into two directions, rotated, and flowed out from both sides. Futami et al. [114] investigated the relationship between aneurysm morphology (size ratio) and inflow jet pattern and reported four classes. Sunderland et al. [357] quantified the temporal stability of vortices in side-wall and bifurcation aneurysms during the cardiac cycle. They measured the number of vortex cores and the size of the vortices compared to a cycle-averaged vortex. No significant differences were detected between both types, probably due to the small number of data sets (10 aneurysms). Pozo et al. [304] introduced a complexity index that measures the flow complexity based on streamlines from aneurysm inlet to aneurysm outlets. The more complex the flow, the lower the ability to distinguish the outlet position by knowing the inlet position, resulting in a high complexity index. Cebal et al. [60] proposed the most extensive classification scheme. They considered each aneurysm type, the entire cardiac cycle, and the complete aneurysmal flow pattern (no restriction to parental artery flow or inflow jet). They found four classes in both small and large aneurysms, with varying flow pattern complexity and temporal stability. These classes are composed of combinations of three basic flow types: flow with an unchanging direction, flow with a changing direction and vortical flow. Moreover, their classification considers the inflow jet size and the size of the impingement zone. They reported associations between rupture and flow type two combined with flow type three, narrow jets and small impingement zones.

For cardiac blood flow, computer-based classifications were introduced. Von Spiczak et al. [392] classified aortic vortices based on the temporal evolution of vortex cores and of vorticity values in six cut planes along the aortic course. They reported the observation of differences between healthy subjects and patients. However, the approach is sensitive to noise, which reduces the resulting quality. In previous work, we proposed a scheme that classifies aortic vortices according to spatio-temporal features comprising their shape, temporal occurrence, spatial location, size, and rotation direction [432], recall Section 4.2.3. However, this method is not able to distinguish more complex cerebral flow patterns. Other works proposed vector pattern matching approaches to classify aortic flow patterns [150, 293]. However, these methods consider no morphological information, such as the distance of the flow to the vessel wall, which seems to be an important criterion in the context of cerebral aneurysms. Thus, existing techniques cannot be applied to cerebral aneurysms.

Therefore, we present *CAVOCLA* - an automatic method to classify blood flow in cerebral aneurysms during the cardiac cycle, which is integrated into the *ViFIE* module. As input, the clustered flow patterns and the corresponding representatives are used, explained in Section 7.1. In contrast to previous works, we automatically extract flow patterns for a faster, less error-prone, and reproducible classification. The classification is based on a novel mapping of the aneurysm surface to a hemisphere by calculating polar-based coordinates that circumvents restrictions of existing techniques in case of a non-convex aneurysm shape, recall Section 4.2.1. Afterward, the polar-based coordinates are assigned to the points of the cluster representatives. Using this, each representative is classified automatically according to a set of pre-defined template types based on the study by Cebal et al. [60], see Figure 95. Moreover, we refined and extended this set in collaboration with interventional neuroradiologists. The classification result for an aneurysm is a subset of template patterns, which constitutes a specific class. All classes reported by Cebal et al. can be automatically detected using our approach since they represent individual combinations of the derived template types. Moreover, we can detect further classes due to our refinements and extensions. Besides, we introduce

an interactive detail-on-demand approach to investigate the classification results. Such *level-of-detail* (LOD) visualizations are frequently used for visualizing molecular data [220, 292, 376], which generate seamless transformations between different abstraction levels for obtaining an understanding of molecular systems. Inspired by these works, we create a visual transition from the cluster representative over an enclosing surface to the associated lines to support the spatial perception of flow patterns. The respective representation of a cluster depends on the zoom level.

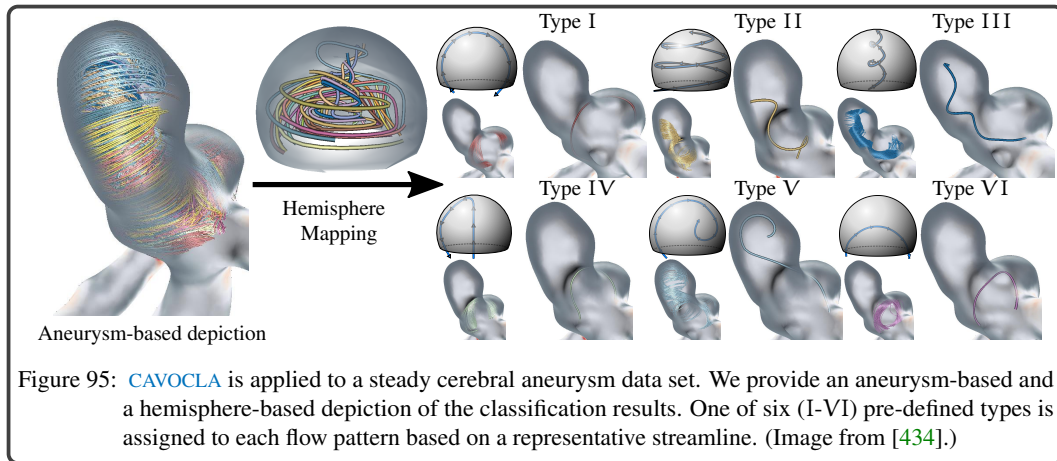


Figure 95: CAVOCLA is applied to a steady cerebral aneurysm data set. We provide an aneurysm-based and a hemisphere-based depiction of the classification results. One of six (I-VI) pre-defined types is assigned to each flow pattern based on a representative streamline. (Image from [434].)

### 7.2.1 Requirement Analysis

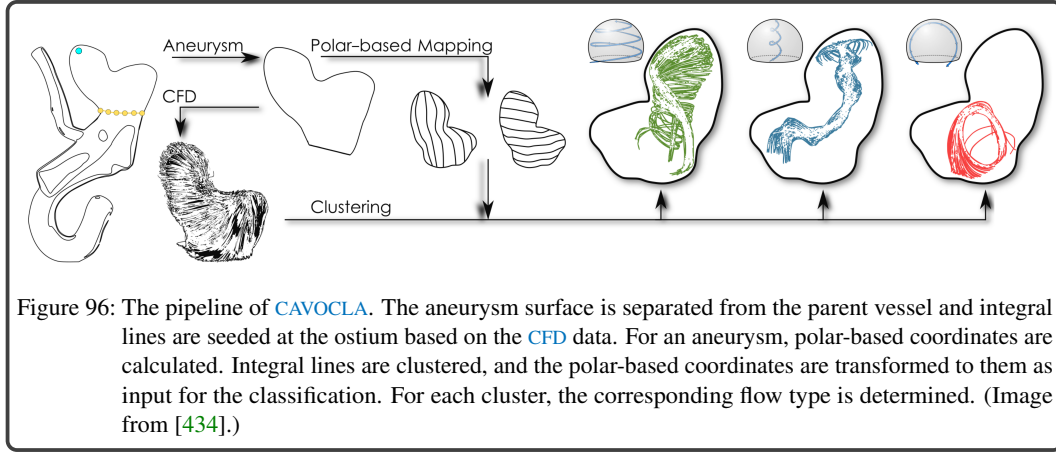
Until now, Cebal et al. [60] introduced the most detailed manual classification of flow patterns. However, the process is affected by visual clutter leading to error-prone results. Furthermore, the classification into three flow types is often not sufficient to describe the flow complexity, but a more detailed visual differentiation is challenging.

To generate comparable and reproducible classification results, a reliable clustering of steady and unsteady flow patterns without a priori determination of the cluster number is needed. Our automatic path line clustering already fulfills this, recall Section 7.1. Similar to the clustering, the classification is required to be performed automatically. However, due to the anatomic diversity, new flow types may occur that differ from the pre-defined types. Therefore, the classification should be flexible enough to include new flow types easily. Furthermore, adequate visualizations of the classified patterns are needed to verify and interpret them. A more abstract depiction of the complex flow and morphology would help to compare data sets and to assess the most prominent flow patterns. In addition to the seven more general requirements in Section 5.1 and others in Chapter 6 as well as in Section 7.1.1, we summarize further requirements for the classification of intra-aneurysmal flow patterns:

**Req. 18** AUTOMATIC CLASSIFICATION. The classification determines the most similar flow type per cluster automatically.

**Req. 19** INTEGRATION OF EXPERT KNOWLEDGE. The experts should be able to integrate new flow types.

**Req. 20** FLOW PATTERN VISUALIZATION. A more abstract visualization is needed that allows an assessment and comparison of flow patterns.



### 7.2.2 Flow Pattern Classification

In this section, we describe the details of the flow pattern classification. The method consists of the following steps, see Figure 96:

- Aneurysm separation,
- Clustering of integral lines,
- Determination of polar-based coordinates on the aneurysm,
- Assigning polar-based coordinates to integral lines,
- Definition of template types,
- Assignment of the most similar template type per cluster.

For the remainder of this section, we use the following notation. Let  $M \subset \mathbb{R}^3$  be a triangulated surface mesh, i.e., a homogeneous simplicial 2-complex.  $M$  consists of vertices  $i \in V \subset \mathbb{N}$  and their associated 3D position  $\mathbf{p}_i \in \mathbb{R}^3$ . Furthermore,  $M$  consists of (oriented) edges  $E = \{(i, j) \mid i, j \in V\}$ , where we denote  $\mathbf{e}_{ij} = \mathbf{p}_j - \mathbf{p}_i$  as the edge connecting  $\mathbf{p}_i$  to  $\mathbf{p}_j$ . Finally, we denote the triangles with  $T = \{(i, j, k) \mid (i, j), (j, k), (k, i) \in E\}$ .

#### Aneurysm Separation

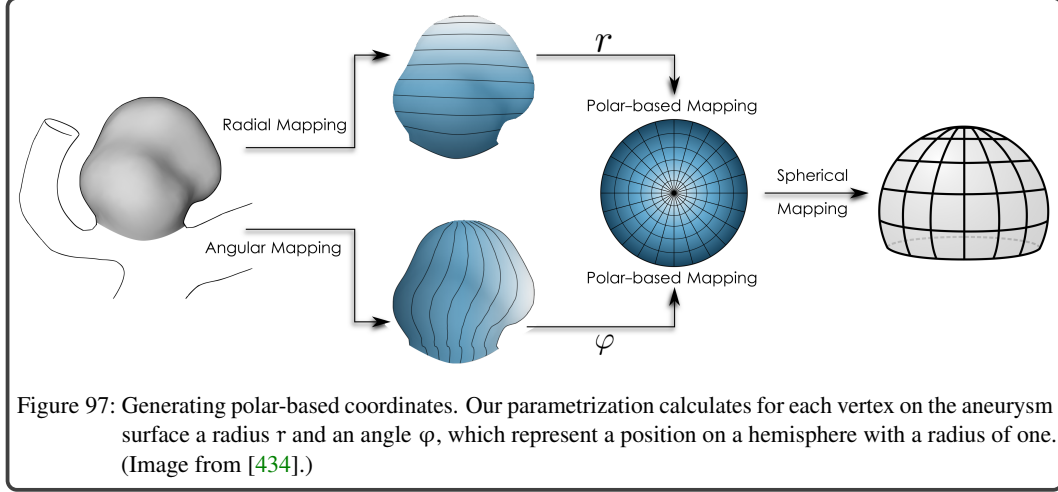
For the classification of the aneurysm flow, we have to separate it from the parent vessel, see Figure 96. For this, we use our previous approach [431], which detects the ostium automatically, recall Section 5.5.1. A closed curve represents the ostium contour, consisting of consecutive points  $c_1, \dots, c_n, c_{n+1} \in V$ , where  $c_1 = c_{n+1}$ . We cut the 3D surface mesh along the detected contour. Finally, the user clicks on a point in the aneurysm region (cyan sphere), which yields the correct part.

#### Blood Flow Clustering

The classification requires a precise definition of spatio-temporal flow entities. For this purpose, we cluster blood flow-representing lines. For steady flow, we use the approach by Oeltze et al. [282], who calculate pairwise streamline similarities based on the MCPD [76] measure. This measure determines for every streamline point the minimum distance to another streamline and averages it. Several validity measures quantitatively evaluated the suitability of the similarity measure. Since MCPD does not encode the temporal component of unsteady flow, we use our approach [438] to measure path line similarities. We use AHC with average link to cluster integral lines, recall Section 7.1.3. Finally, a representative per cluster is determined as input for the classification, recall Section 7.1.4.

### Determination of Polar-Based Coordinates

CAVOCLA aims to classify detected clusters according to pre-defined flow types. To avoid influences of the aneurysm shape, we map the separated aneurysm to a uniform structure. Since aneurysms are usually spherical structures, the aneurysm is mapped to a hemisphere with a radius of one. For each vertex, we calculate polar-based coordinates, including a radius  $r$  and an angle  $\varphi$  that represent a position on the hemisphere, see Figure 97.



A mapping from the aneurysm mesh to polar-based coordinates is a function  $f$  with  $f : V \rightarrow \mathbb{R} \times [0, 2\pi)$ . Thus, every vertex  $i$  is assigned to a radius  $r_i \in \mathbb{R}$  and an angle  $\varphi_i \in [0, 2\pi)$ . Furthermore, we demand a bijective mapping such that  $f^{-1}$  exists to enable linking and brushing between the aneurysm surface and the resulting hemisphere-based visualization. Note that the vertices  $i \in V$  and their corresponding position  $\mathbf{p}_i \in \mathbb{R}^3$  are equivalent. Thus, the inverse of  $f^{-1}$  of a region in polar-based coordinates maps to a region on the surface mesh. In the following, the mapping is split and first the mapping from  $i \mapsto r_i$  is described.

**Radial mapping.** To obtain the radial mapping, we calculate the geodesic distances between the path points  $c_i \in V$  and each vertex  $i \in V$ . For this, we follow the fast approach by Crane et al. [78]. First, the heat flow is integrated by solving the heat equation for a fixed time  $t$ :  $\dot{u} = \Delta u$  using an implicit Euler integration. Then, the vector field  $X$  is determined by  $X = -\nabla u / |\nabla u|$  describing the normalized gradient of the heat flow  $u$ . Finally, the geodesic distances  $\phi$  are calculated by solving the instance of the Poisson equation:  $\Delta \phi = \nabla \cdot X$ . We apply this method to all path points  $c_1, \dots, c_n \in V$ . This yields the geodesic distances  $\phi_c \in \mathbb{R}^{|V|}$ . Note that the geodesic distances are represented as a vector where  $\phi_c(j)$  denotes the geodesic distance from the path points  $c_1, \dots, c_n \in V$  to the vertex  $j$ , thus  $\phi_c(c_i) = 0$  for all  $i$ . The final radial mapping  $r$  is determined such that it has the greatest value at the boundary  $c_1, \dots, c_n \in V$ :

$$r_i = \frac{\max_{j \in V} (\phi_c(j)) - \phi_c(i)}{\max_{j \in V} (\phi_c(j))}. \quad (35)$$

This yields a mapping  $i \mapsto r_i \in [0, 1]$ , see Figure 98, where the (horizontal) isolines represent the radial mapping.

**Angular mapping.** To find an angular mapping:  $i \mapsto \varphi_i$ , we employ the radial mapping and calculate the angle differences per edge. For every edge  $(i, j) \in E$  we determine the change of the angle  $\varphi_{(i,j)}$  when going from vertex  $i$  to vertex  $j$ . We obtain this value by using the law of cosines:

$$\tilde{\varphi}_{(i,j)} = \cos^{-1} \left( \frac{r_i^2 + r_j^2 - |\mathbf{e}_{ij}|^2}{2r_i r_j} \right). \quad (36)$$



This gives the change of the angle, but no orientation, i.e.,  $\tilde{\varphi}_{(i,j)}$  should be different in sign than  $\tilde{\varphi}_{(j,i)}$ . Thus, we need an orientation to adapt the change of the angles. For this, we generate a consistent vector field  $G$  on the aneurysm.  $G$  is determined by the geodesic distance  $r_d$  from the dome point, i.e., the point with the highest geodesic distances from the ostium contour:  $G = \nabla r_d$ , see Botsch et al. [44] for the calculation of the gradient on meshes.  $G$  is defined for every triangle and points to the direction of highest increase. Then, we define a vector field  $\mathbf{o}_t$  in the tangent space of the triangle  $t \in T$  by applying the cross product of the normal vector  $\mathbf{n}_t$  and the vector  $G_t$ :  $\mathbf{o}_t = \mathbf{n}_t \times G_t$ . This yields the sign of the angular difference:

$$\varphi_{(i,j)} = \text{sign}(\langle \mathbf{o}_t, \mathbf{e}_{ij} \rangle) \cdot \tilde{\varphi}_{(i,j)}, \quad (37)$$

where  $(i,j) \in t$ ,  $\text{sign}(x)$  is equal 1 if  $x \geq 0$  and  $-1$  otherwise, and  $\langle \cdot, \cdot \rangle$  denotes the Euclidean dot product. Essentially, we want to find the angles of the vertices  $\varphi$  such that the energy:

$$e(\varphi) = \sum_{(i,j) \in E} w_{ij} |\varphi_{(i,j)} - (\varphi_i - \varphi_j)|^2 \quad (38)$$

is minimal, with  $w_{ij} = (\cot \beta_{ij} + \cot \beta_{ji})/2$  denoting the cotangent weights [236]. Note that  $\varphi_{(i,j)}$  is given, whereas  $\varphi_i, \varphi_j$  are unknown. Minimizing this functional would lead to erroneous results. One rotation would lead to a result where the angle of a vertex is close to  $2\pi$ , and the neighbor would be around 0. However, the difference would be small. To avoid this, we need to reformulate  $e(\varphi)$ . We transform the vertices to 2D coordinates and every vertex  $i$  is assigned  $(x_i, y_i)$ . With the condition:

$$\begin{pmatrix} x_j \\ y_j \end{pmatrix} = \underbrace{\begin{pmatrix} \cos(\varphi_{(ij)}) & -\sin(\varphi_{(ij)}) \\ \sin(\varphi_{(ij)}) & \cos(\varphi_{(ij)}) \end{pmatrix}}_{R_{ij}} \begin{pmatrix} x_i \\ y_i \end{pmatrix}, \quad (39)$$

we can reformulate the energy to:

$$e(\mathbf{x}) = \sum_{(i,j) \in E} w_{ij} |(x_j, y_j)^T - R_{ij}(x_i, y_i)^T|^2 \quad \text{s.t.} \quad \mathbf{x}^T \mathbf{M} \mathbf{x} = 1, \quad (40)$$

where  $\mathbf{M}_{2i,2i} = \mathbf{M}_{2i+1,2i+1} = \frac{1}{3} \sum_{(ijk) \in T} A_{ijk}$  denotes the mass matrix and the vector  $\mathbf{x} \in \mathbb{R}^{2|V|}$  describes the coordinates of the vertices  $\mathbf{x} = (x_0, y_0, x_1, y_1, \dots)^T$ . The condition  $\mathbf{x}^T \mathbf{M} \mathbf{x} = 1$  prevents the solution  $\mathbf{x} = \mathbf{0}$  of Equation 40. Finally, Equation 40 can be expressed as the generalized eigenvalue problem:

$$\min_{\mathbf{x} \in \mathbb{R}^{2|V|}} \mathbf{x}^T \mathbf{R} \mathbf{x} \quad \text{s.t.} \quad \mathbf{x}^T \mathbf{M} \mathbf{x} = 1, \quad (41)$$

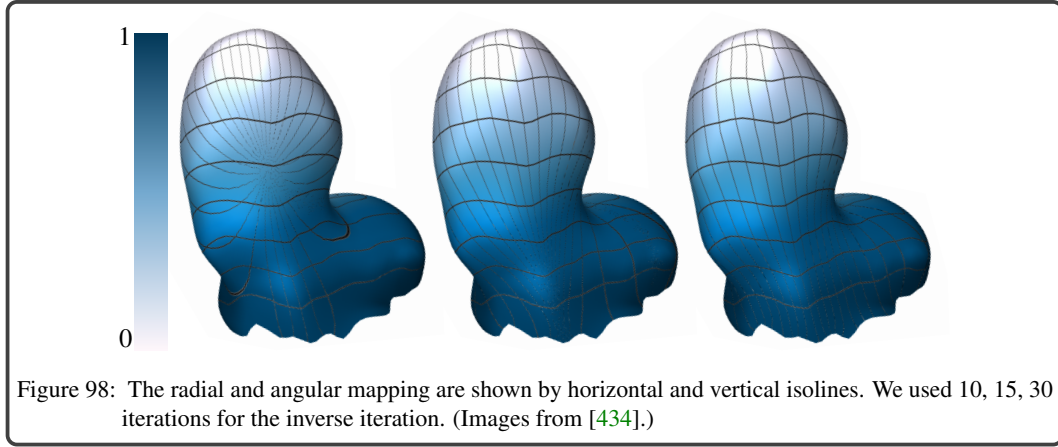
with

$$\mathbf{R}_{\begin{pmatrix} 2i, 2j & 2i, 2j+1 \\ 2i+1, 2j & 2i+1, 2j+1 \end{pmatrix}} = \begin{cases} w_{ii} \mathbf{I} & \text{if } i = j \\ 2w_{ij} R_{ji} & \text{if } i \neq j \end{cases} \quad (42)$$

where  $\mathbf{I}$  denotes the  $2 \times 2$  identity matrix and  $R_{ij}$  the rotation matrix as described in Equation 39. Note that  $\mathbf{R}_{(\cdot, \cdot)}$  is used to describe the matrix position. Equation 41 can be solved by using inverse iteration. The coordinates are then transformed with  $i \mapsto \text{atan2}(x_i, y_i)$ , which yields the angle in  $[0, 2\pi]$ . We used 30 iterations, where fewer repetitions would result in erroneous angles, see Figure 98.

#### Assigning Polar-Based Coordinates to Lines

The next step consists of assigning the polar-based coordinates at every point of an aneurysm to the integral lines. The integral line  $k$  consists of vertices  $V_P(k)$  and edges  $E_P(k)$ , and the corresponding 3D coordinates of the vertices are denoted with  $\mathbf{v}_i \in \mathbb{R}^3$ ,  $i \in V_P(k)$ . For every vertex  $i \in V_E(k)$



on the line  $k$ , the aneurysm vertex  $j \in V$  with the shortest distance is determined. To quickly find  $j$ , we build a *kd-tree* of the aneurysm surface. Then, we assign the polar-based coordinates to the line vertex  $i$ :  $i \mapsto (r_j, \varphi_j, z_j)$ ,  $z_j = |\mathbf{p}_j - \mathbf{v}_j|$ . Note that we scale the distances  $z_j$  such that for every line the distance of every point lies in  $[0, 1]$ .

#### Definition of Template Types

We generated different template flow types, whose definition is based on the work of Cebal et al. [60] as they visually classified time-dependent flow patterns. We extended their scheme concerning the proximity of flow patterns to the wall, because *NWF* may lead to further pathological vessel dilation and aneurysm growth. Our experts observed three subtypes of flow with an unchanging direction, see Figure 95 (type I, IV, VI). Type I corresponds to the unchanging flow behavior by Cebal et al. [60]. Type IV enters an aneurysm more distant to the wall, reaches its dome and flows back along the wall. Type VI enters and leaves an aneurysm close to the wall, but within an aneurysm the flow has a large distance to the wall. Type V represents flow with a changing direction, which proceeds close to the wall and then abruptly changes its direction. Vortical flow is described by type II and III, whereas we extend the definition by type III, because it has a larger distance to the wall than type II. We use these six templates, which are rotationally symmetric according to the centerline of the hemisphere, as a library for the automatic classification (Req. 18).

#### Assigning Flow Types

To determine the flow type of a cluster, we transform its representative to the hemisphere by using its polar-based coordinates. Moreover, we design for each flow type a template line based on the hemisphere, see the previews of Figure 95. Then, we calculate the similarity between the representative and each template by using the *iterative closest point (ICP)* algorithm [422]. Mapping the templates to physical space and utilize *ICP* there would not be possible, because then they would no longer be rotationally symmetric. This could lead to wrong classification results.

*ICP* results in a similarity measure where 0 means a perfect match between the representative and the tested template. The flow type with the lowest measure is assigned to the cluster. Normally, *ICP* determines the best rotation matrix that matches both input data. To avoid similarities if the flow type is rotated around the, e.g., x-axis or y-axis, we restrict the rotation around the z-axis only. Otherwise, flow types may be associated that are not entering and leaving the aneurysm, which may happen if, e.g., type I is rotated with  $90^\circ$  around the x/y-axis.

To convey how certain the classification is, we list for each cluster the three most similar flow types in a tabular view, see Figure 99. Thus, the user can follow if the most similar type dominates clearly over the others or if another type is very similar. To facilitate the interpretation of the similarity values, we calculate percentage similarities that are presented to the user. For this, all similarities are sorted in ascending order, resulting in  $s_1, s_2, \dots, s_n$ , where  $s_1$  is the smallest and  $s_n$  is the largest






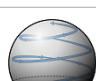
Classified Flow Patterns							
	Cluster Color	Flow Type Image	Flow Type Description	Additional Information	Cluster Visualization	Select Property	Add flow type
			Flow Type 3: similarity of: 83.33 %	Max of velocity: 1.41 m/s	Envelope	Velocity	<input type="checkbox"/>
			Flow Type 6: similarity of: 10.41 %	Min of velocity: 0.8 m/s			
			Flow Type 5: similarity of: 8.36 %	Average of velocity: 1.24 m/s			
			Flow Type 5: similarity of: 64.07 %	Max of surface distance: 2.89 mm	Streamlines	Wall distance	<input type="checkbox"/>
			Flow Type 3: similarity of: 12.48 %	Min of surface distance: 0.01 mm			
			Flow Type 6: similarity of: 4.97 %	Average of surface distance: 1.27 mm			
			Flow Type 1: similarity of: 86.57 %	Max of velocity: 1.28 m/s	Streamlines	Velocity	<input type="checkbox"/>
			Flow Type 6: similarity of: 5.49 %	Min of velocity: 0.78 m/s			
			Flow Type 4: similarity of: 1.33 %	Average of velocity: 1.09 m/s			
			Flow Type 2: similarity of: 73.31 %	Max of surface distance: 1.26 mm	Representative	Wall distance	<input type="checkbox"/>
			Flow Type 3: similarity of: 9.99 %	Min of surface distance: 0.03 mm			
			Flow Type 5: similarity of: 5.65 %	Average of surface distance: 0.65 mm			

Figure 99: A table summarizing information about classified flow patterns. For each cluster, the three most similar flow types sorted by their similarity are presented. Moreover, additional information about a user-selected scalar field is shown, and the user can switch between different cluster visualizations. If all similarities are low, the cluster can be recorded as new flow type.

similarity value with  $n$  as the number of similarities. Then, a percentage factor  $fac$  is determined by:  $fac = \sum_{i=1}^n 1/s_i$ . Based on this, for each  $s_i$  the percentage similarity value  $p_i$  is given by:  $p_i = \frac{1}{fac \cdot s_i}$ , where  $p_i = 1$  means 100 %. Note, in case of  $s_1 = 0$ , we set  $p_1 = 1$ .

Due to the anatomic diversity, a cluster could be dissimilar to all pre-defined types or two types may have similar values. Therefore, new flow types can be recorded (**Req. 19**). Existing types are stored as lines in a database. If the user wants to save a new type, a checkbox can be activated for each cluster in the table, where new types are numbered consecutively. However, to prevent the insertion of meaningless types, we are looking for the three most similar types within the database. A preview of these types and the percentage of similarities to the new type are presented to the user. Then, the user is asked if she/he wants to integrate the new type. Confirming this adds the corresponding representative to the database, which is then used for upcoming classifications.

### 7.2.3 Visualization of the Classification Results

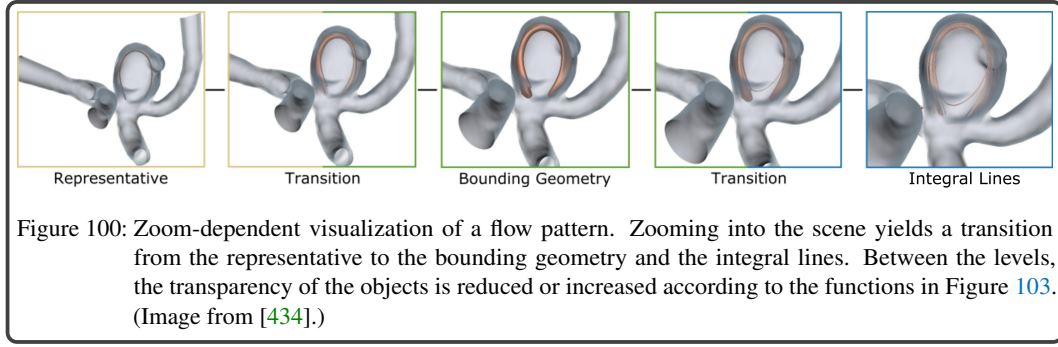
The classified flow patterns are visualized in two juxtaposed render contexts that are linked to each other, see Figure 95. The first one shows the clusters within the 3D aneurysm, whereas the second provides a more abstract depiction. Here, the representatives are visualized within a hemisphere. In the following, we comment on the design decisions for the different views and their interplay.

#### Aneurysm-Based Visualization

The aneurysm-based visualization enables a detailed exploration of correlations between high-risk wall regions and individual flow patterns. Besides the already described visualization aspects for the 3D aneurysm surface and internal flow in Section 7.1.4, we integrate an additional linked view that shows the vessel surface fully opaque. Thus, the visual perception of the mapped attributes on the surface is not negatively influenced by the applied *Fresnel shading* [122].

During the exploration, the distance to the camera may vary depending on the zoom level. The simultaneous illustration of clusters in an appropriate size, independent from the zoom level, would lead to visual clutter. Thus, we provide a details-on-demand approach, such that zooming into the scene yields a transition between different abstraction levels, progressively revealing more information about the clusters' extent and the corresponding flow type, see Figure 100.

**Zoom level 1: representative.** The first level shows the cluster representatives that summarize the complex flow and enable a perception of inner flow structures that would be occluded by displaying



thousands of path lines. Each representative should indicate the cluster's flow shape and its path. The representatives are shaded as tubes to improve their perception from a more distant point of view. For this, we construct view-aligned quads on the GPU [216]. The successive line points  $p_i$  and  $p_{i+1}$  are used to determine the normalized tangent vector:  $\mathbf{t} = \mathbf{p}_{i+1} - \mathbf{p}_i$ . With the given view direction  $\mathbf{v}$ , we calculate the extent of the representative by using the normalized cross-product  $\mathbf{e} = \mathbf{v} \times \mathbf{t}$ . For every quad, we assign a parameter  $y \in [-1, 1]$  to define its color:

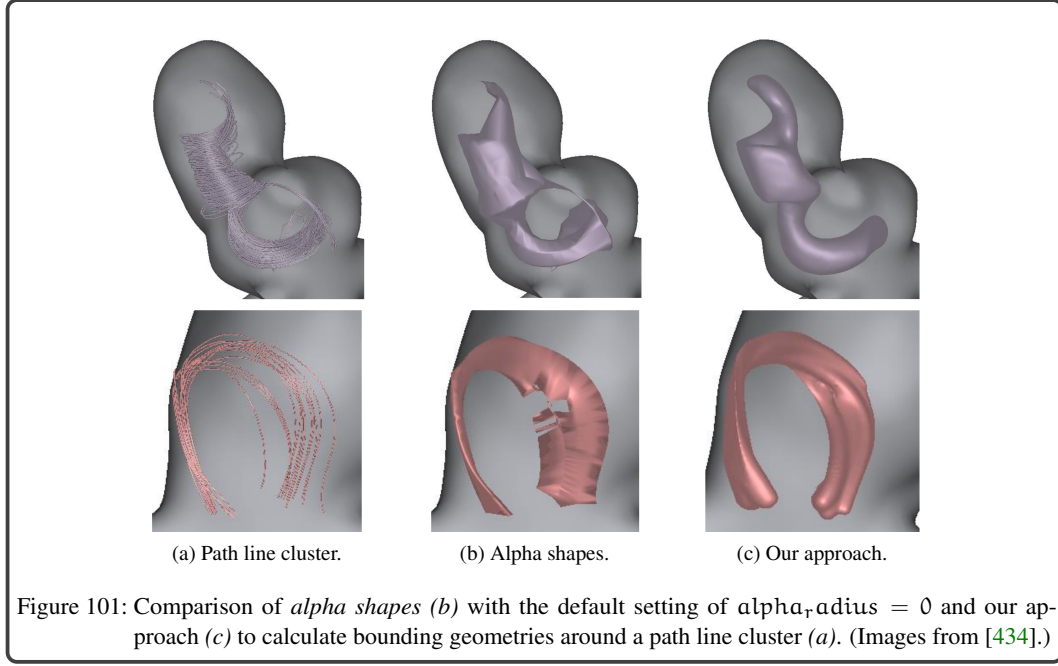
$$\text{color} = c_{\text{col}} \cdot \cos(0.5y \cdot \pi), \quad (43)$$

where  $c_{\text{col}}$  is set to a cluster-specific RGB color. We use the *ColorBrewer* website [239] to find 20 colors, which perceptually differ as much as possible since a maximum of 20 clusters is distinguished.

**Zoom level 2: bounding geometry.** Zooming into the scene initiates a transition to a bounding geometry of each cluster that supports the visual perception of color-coded parameters. For this purpose, we determine the cluster's enveloping surface, whereupon scalar values, e.g., *WSS* can be depicted using a blue-to-yellow color map. The enveloping surface should approximate the cluster extent. However, line segments showing a slightly different flow behavior should be neglected. To determine this surface, *alpha shapes* [93] could be used. Here, the user parameter  $\alpha_{\text{radius}}$  controls how tighten or loosen the fit around the points will be created. We tested different values for this parameter. However, due to the vortical flow behavior, this approach leads to geometries with a jagged boundary and holes, see Figure 101b. Other works used the cluster's centerline to calculate bounding geometries but may fail for vortical curve behavior [95, 432]. Integral surfaces are also used to calculate bounding geometries around groups of integral lines [198]. However, this is a local method where errors are accumulated during integration. In contrast, Ferstl et al. [104] computed bounding geometries of streamline clusters by transforming the lines to a PCA space where they are clustered. To avoid such a transformation and to be independent of the clustering, we developed a new calculation of the bounding geometries in the 3D space, which globally minimizes the error of the surface estimation.

First, we generate a regular 3D grid  $G$  around the lines of a cluster. For the distance between two adjacent grid points, we used  $1/100$  of the diagonal of the bounding box around an aneurysm. Greater values lead to irregular shapes, whereas lower values increase the computation time without significantly better results. Then, for each grid point  $g \in G$  two distance values  $g_{d1}$  and  $g_{d2}$  are determined. We identify for each  $g \in G$  the line vertex  $i$  with the shortest Euclidean distance to  $g$ , which yields  $g_{d1}$ . The shortest Euclidean distance between each grid point and the respective point of the cluster representative yields  $g_{d2}$ . To increase the performance, we built two *kd-trees* of the path line vertices and vertices of the representative. The distance values are stored at the grid points resulting in two distance fields  $D_1$  and  $D_2$ . Next, a third distance field  $D_3$  is generated by:  $D_3 = t \cdot D_2 + (1 - t) \cdot D_1$ , setting the interpolation factor  $t = 0.25$ . Besides linear interpolation, more advanced techniques such as progressive transformations [110] or radon transforms [369] could be used. However, the bounding geometry should only allow a more abstract cluster visualization, which could be reached by linear interpolation. Then,  $D_3$  is smoothed by applying a  $9 \times 9$  Gaussian filter to getting smooth surfaces that are extracted via Marching Cubes and an isovalue  $\text{iso} = 0.5$ , see

Figure 101c. Figure 102 exemplary shows the results for different values for  $t$  and different isovalues. With a greater isovalue, the resulting geometry is too large, whereas with smaller values many lines lie outside the surface. However, the user can interactively change the interpolation factor  $t$  to explore the cluster extent within the vessel lumen further.



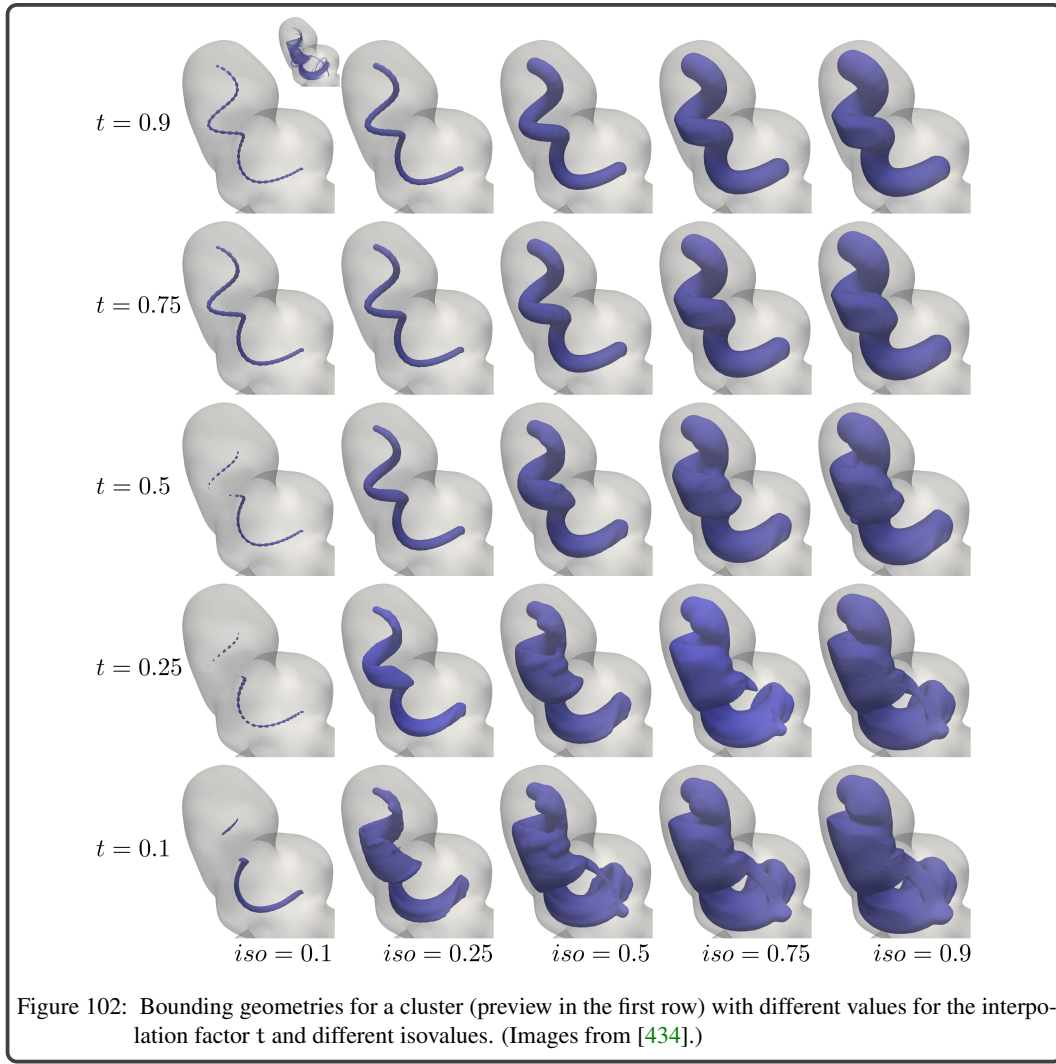
**Zoom level 3: integral lines.** Moving in even closer activates the line-based representation using illuminated streamlines [424] combined with halos [161] to improve the visual line perception. Similar to the bounding geometry, flow properties can be mapped on the lines. This depiction enables a detailed exploration of individual clusters. However, the simultaneous depiction of all clusters could lead to visual clutter. Therefore, we provide a tabular representation of all clusters including an image of their flow type, a drop-down list to select a specific property that should be color-coded and additional information such as the maximum value of the selected property, see Figure 99. The user can select one or more clusters for rendering.

**Zoom level transition.** We provide a smooth transition between the zoom levels by using transparency, see Figure 103. For this purpose, the Euclidean distance between the center of the cluster and the camera  $d_{cam}$  is calculated. Moreover, four distance values  $d_{min}$ ,  $d_{mid1}$ ,  $d_{mid2}$ , and  $d_{max}$  are defined and set to 75 %, 65 %, 35 % and 25 %, respectively of the ratio of the visible aneurysm surface to the size of the view plane. To determine the visible aneurysm size, the aneurysm's bounding sphere is calculated and the amount of visible sphere pixels is counted in the fragment shader. Using the bounding sphere avoids inaccuracies of the rendered cluster representation caused by rotating the scene. Based on  $d_{min}$ ,  $d_{mid1}$ ,  $d_{mid2}$ , and  $d_{max}$ , two further distance values  $d_1$ ,  $d_2$  are specified:

$$d_1 = \left( \frac{d_{cam} - d_{mid2}}{d_{max} - d_{mid2}} \right), \quad d_2 = \left( \frac{d_{cam} - d_{min}}{d_{mid1} - d_{min}} \right). \quad (44)$$

Then, the opacity of the three cluster representations is defined by:

$$\text{opacity} = \begin{cases} (1 - \text{clamp}(d_2))_{[0,1]} & \text{representative} \\ (1 - \text{clamp}(d_1))_{[0,1]} \cdot \text{clamp}(d_2)_{[0,1]} & \text{bounding geometry} \\ (1 - \text{clamp}(d_2))_{[0,1]} & \text{integral lines} \end{cases} \quad (45)$$



With lower or greater values for  $d_{\min}$ ,  $d_{\text{mid1}}$ ,  $d_{\text{mid2}}$ , and  $d_{\max}$ , the representations appear too early when the camera is too far away, or too late when the camera is too close. Moreover, the user can manually switch between the depictions and can select clusters by clicking into the scene.

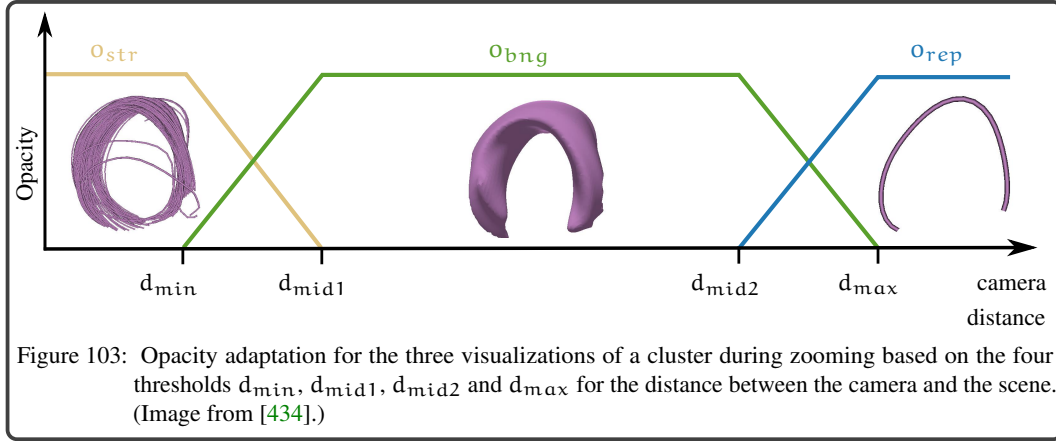
#### *Hemisphere-Based Visualization*

A very irregularly deformed aneurysm surface complicates the exploration of flow patterns including the recognition of the calculated flow types. Manual rotations of the surface are necessary to perceive the behavior of individual patterns. To facilitate the flow pattern analysis, we provide a more abstract visualization where the aneurysm surface is mapped to a hemisphere. Within the hemisphere, the cluster representatives are depicted, see Figure 95.

For the generation of the hemisphere, we employ the polar-based coordinates  $(r_i, \varphi_i)$  for each vertex  $i$  of the aneurysm surface. According to the aneurysm,  $r_i$  is in the range of  $[0, 2]$  and  $\varphi_i \in [0, 2\pi]$ , which leads to the topology of the hemisphere:

$$i_{sp} = [\sin(r_i) \cdot \cos(\varphi_i); \sin(r_i) \cdot \sin(\varphi_i); \cos(r_i)] \quad (46)$$

with  $i_{sp}$  being the vertices of the hemisphere. Moreover,  $r_j$  of the line points of the representatives are transformed to the range  $[0, 2]$ . Otherwise, they would not lie within the hemisphere.



The hemisphere is visualized by using *Fresnel shading* [122] to enable an investigation of the internal flow structure. The representatives are also visualized as tubes, where each tube is assigned the corresponding cluster color. If all representatives are depicted simultaneously, the hemisphere-based visualization provides a fast overview of existing flow patterns. Moreover, the user can select individual representatives or groups of them having the same flow type for a more detailed analysis.

To facilitate the spatial correlation between the hemisphere and the 3D depiction, the user can pick a specific point on the hemisphere, and the camera rotates automatically to the corresponding 3D position in a smooth way. Moreover, the user can define landmarks on the hemisphere that are rendered as colored small circles on the hemisphere. These landmarks are then visualized on the 3D aneurysm surface, where the user can define individual labels for each landmark. The landmarks and their labels can be stored and loaded for collaborative data exploration.

#### 7.2.4 Evaluation and Results

To assess the quality of our aneurysm mapping, we compared it with other mapping strategies and evaluate the robustness of our approach. Moreover, we conducted an informal evaluation with five domain experts to assess the quality of the classification results. Among the experts were one neuroradiologist P1 with 16 years of experience, two CFD experts P2, and P3 with five and eight years of experience, and two experts for medical visualization P4, and P5 with four and six years of experience. Firstly, the experts manually classified different patterns. Afterward, the experts were asked to assess the suitability of CAVOCLA and the corresponding visualizations.

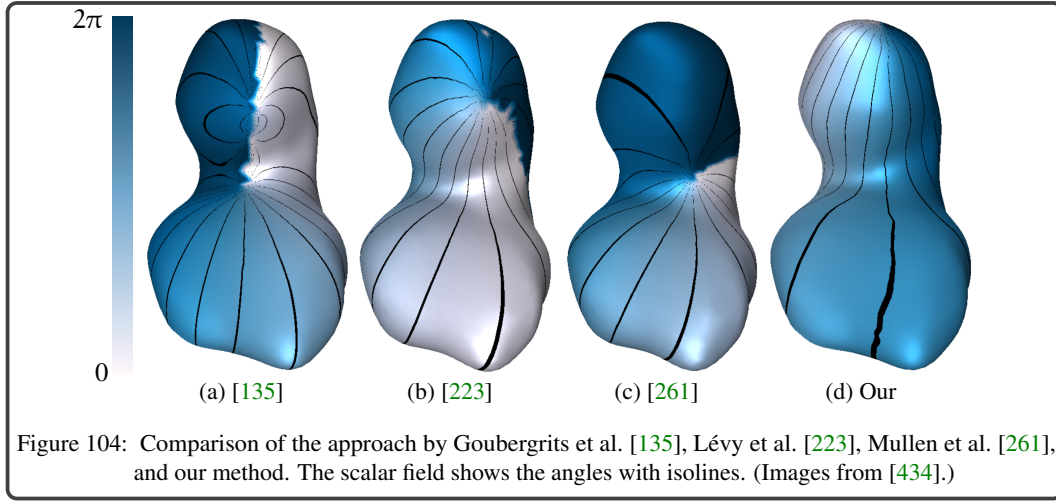
##### Parametrization of the Aneurysm Surface

Closest to our work, regarding the mapping of an aneurysm to polar-based coordinates, is the approach by Goubergrits et al. [135]. They transformed the vertices towards the mass center of an aneurysm, where they ensured that the distance to the center is equal for all vertices. This method produces reasonable results for convex structures, i.e., the mass center lies inside the surface. If the center of mass is located outside the surface, such as in Figure 96, this method gives erroneous results as presented in Figure 104a.

To calculate polar-based coordinates, we need a parametrization that preserves angles instead of areas. The LSCM technique by Lévy et al. [223] and the SCP algorithm by Mullen et al. [261] are commonly used techniques to generate a surface parametrization, which reduces angle distortions. Since our mapping also tends to reduce angular distortions, we compare it to LSCM and SCP. LSCM needs constraints as input. For this, we choose four vertices on the boundary that approximately differ in  $90^\circ$  and map them to  $(1, 0)$ ,  $(0, 1)$ ,  $(-1, 0)$ ,  $(0, -1)$ . Then, we set the vertex which is farthest away from the boundary to the coordinates  $(0, 0)$ . Setting constraints inside the mesh is not recommended, as this may lead to overlapping triangles indicated by isolines that do not converge at the top of an



aneurysm, illustrated in Figure 104b. If we omit this constraint, we obtain a result similar to SCP that parametrizes the mesh without constraints. Thus, we do not influence on the vertex representing the origin of the parametrization, see Figure 104c. With our method, the origin lies on the vertex which is farthest away from the boundary, shown in Figure 104d.

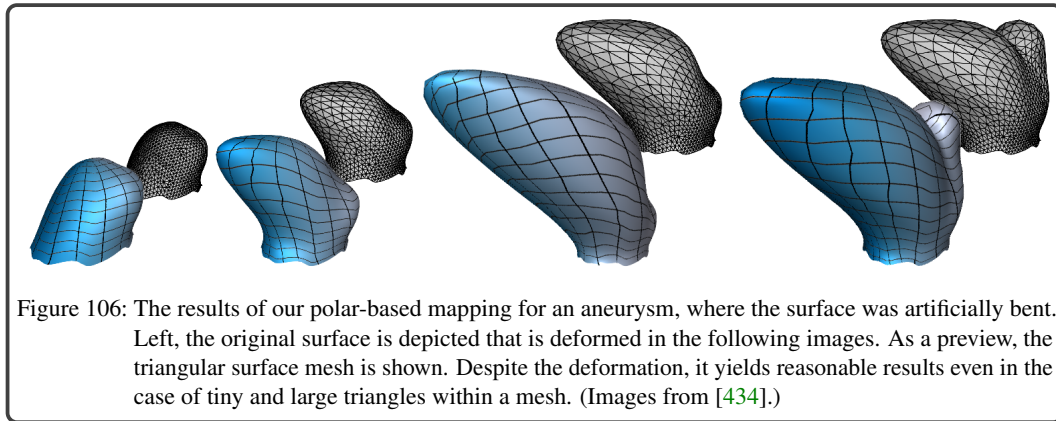
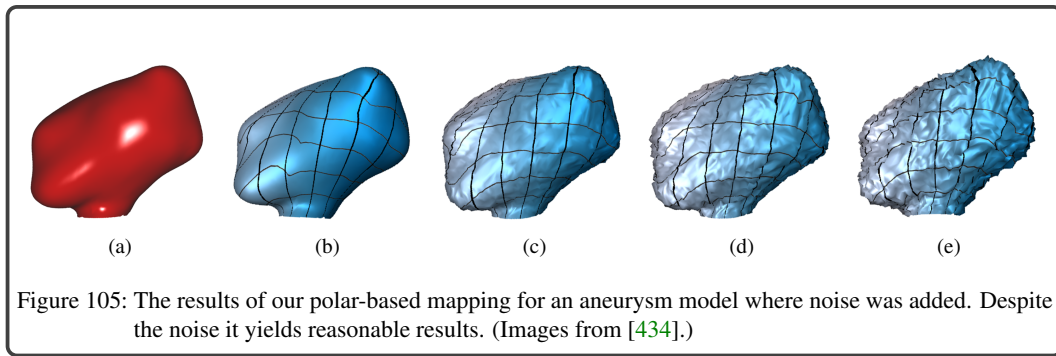


To assess the robustness of our polar-based mapping, we applied different amounts of noise to an aneurysm model. Thus, random values are generated to disturb the vertex positions. Besides this, we artificially bend the aneurysm surface. Afterward, we determine the polar-based mapping. Figure 105 and Figure 106 show the isolines of the radial as well as the angular mapping of the noisy and deformed meshes. The color map additionally shows the angular mapping. Our mapping yields reasonable results even in case of very noisy or deformed meshes.

### Manual Flow Classification

Our experts classified different flow patterns manually according to the pre-defined types based on streamline visualizations such as in Figure 101. We compared their results to the results of CAVOCLA. For each flow type, three examples from seven data sets (C11 - C13 and C19 - C22) were chosen, resulting in 15 estimations per type (5 participants  $\times$  3 examples). We selected clusters whose percentage similarity for the respective flow type is larger than 80 % to enable a unique assignment. The experts were allowed to assign only one type per cluster. After completing a task, the experts were asked to rate their confidence on a five-point Likert confidence scale where 5 means very confident and 1 very unconfident. For the analysis of the confidence score, we provide the number  $C(\cdot)$  of experts who chose the individual scale.

Flow patterns classified as III by CAVOCLA conformed with the manual classifications of all experts, see Figure 107a for example. In addition, the experts were quite confident with their assessments for these cases ( $C(5) = 3; C(4) = 2$ ). P3 classified an example of type I and type II different from CAVOCLA. The type I case was classified as type IV and the type II case as type III. However, depending on the morphological complexity these types appear quite similar within an aneurysm. This shows that a manual classification is often challenging, which was confirmed by the experts' reduced confidence ( $C(3) = 4; C(2) = 1$ ). Similar to that, clusters of type IV were classified as type I in six cases, see Figure 107b. The experts were also unconfident with their assessments for these cases ( $C(3) = 1; C(2) = 4$ ). For the remaining cases of type IV, the experts were more confident with their assessments ( $C(5) = 1; C(4) = 3; C(3) = 1$ ), see Figure 107c for an example. The experts rated the classification of type V patterns as challenging because the visual perception of the changing flow behavior needs a lot of manual rotation effort. In six cases, the patterns were classified as type V (Figure 107d), but for the remaining cases, type II or III was estimated with a confidence of  $C(2) = 3$  and  $C(1) = 2$ . With regard to type VI, results of CAVOCLA conformed with 13 manual classifications, where the experts were quite confident ( $C(5) = 4; C(4) = 1$ ), see Figure 107e. For the remaining



two examples, type IV was assigned by P2, see Figure 107f. The expert was unsure how close the cluster came to the wall and alternated between type IV and VI.

Besides the comparison of classification results, we applied **CAVOCLA** to time-dependent flow data. For this purpose, path lines instead of streamlines were integrated. Figure 108 shows exemplary classification results for path line representations. Besides the classified type, the temporal path line component is color-coded in the preview, using a blue-to-yellow color map. Our experts confirmed that **CAVOCLA** also leads to appropriate results in the case of time-dependent flow patterns.

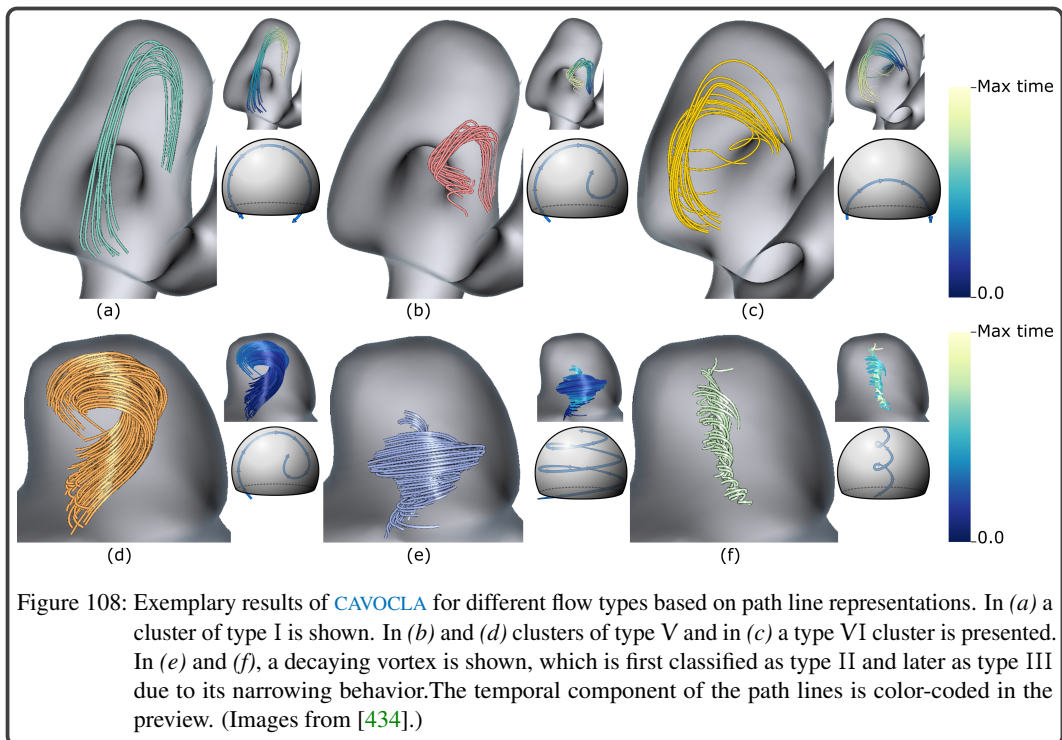
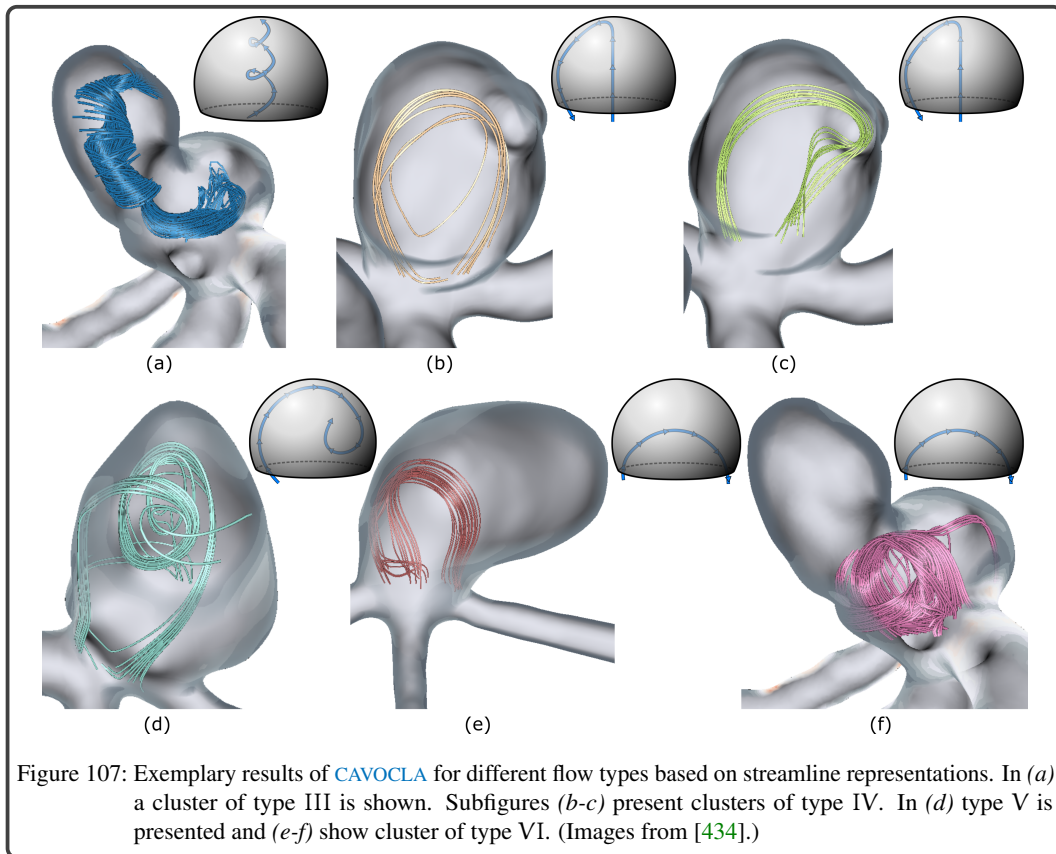
#### *Informal Expert Feedback*

The study is conducted in two steps:

1. Introducing **CAVOCLA** with the zoom-dependent visualization of flow patterns and the hemisphere-based depiction.
2. A questionnaire that inquires the suitability of the visualizations of the classification results.

First, the experts familiarize themselves with **CAVOCLA**. Then, they answered the questionnaire using a five-point Likert scale (—, —, ○, +, ++). For the analysis of the Likert score, we provide the number  $S(\cdot)$  of experts who chose the individual scale. The overall result of the empirical evaluation is shown in Figure 109.



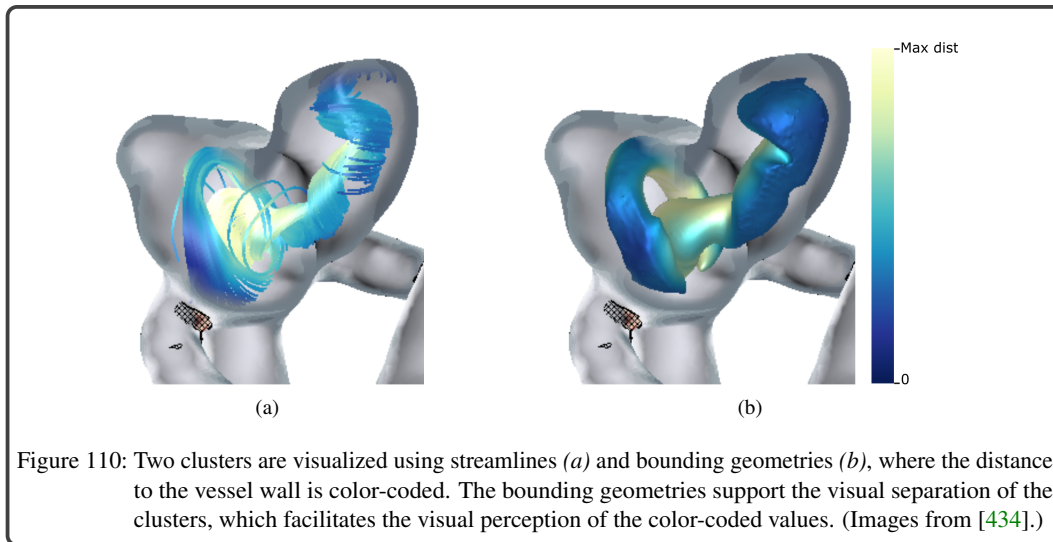


**Aneurysm-based visualization.** All experts confirmed that the combination of the main render context and additional view that shows the vessel fully opaque enables simultaneous exploration of the blood flow and scalar data on the wall ( $S(++) = 4$ ;  $S(+) = 1$ ). Moreover, the surface transparency reveals the qualitative flow behavior ( $S(++) = 5$ ). Furthermore, all experts confirmed that the details-on-demand approach allows to recognize flow types even if the camera is more distant ( $S(++) = 3$ ;  $S(+) = 2$ ). Related to this, the bounding geometry, including the possibility to color-code an attribute on it, was described as a convenient abstraction of the line representation ( $S(++) = 4$ ;  $S(+) = 1$ ). P1 stated that the bounding geometry facilitates the comparison of clusters according to color-coded properties because it supports their visual separation. Figure 110 shows two clusters, where the distance to the surface is color-coded. Using the bounding geometries, it was easier for our experts to analyze the visualized properties. Besides, we asked if the blending of the three cluster visualizations during zooming does not lead to confusion, which was confirmed by the experts ( $S(++) = 2$ ;  $S(+) = 3$ ). For the selection of specific clusters, the tabular view was assessed as very appropriate ( $S(++) = 2$ ;  $S(+) = 3$ ). Moreover, the 3D cluster selection per mouse click was rated with  $S(++) = 3$  and  $S(+) = 2$ . P3 argued: “[...] the 3D selection allows a faster cluster selection than the tabular view. However, the tabular view provides interesting cluster information such as the maximum occurring flow velocity.”

**Hemisphere-based visualization.** All participants found that the hemisphere-based visualization including the mapped scalar fields provides a reasonable simplification of the 3D aneurysm depiction ( $S(++) = 3$ ;  $S(+) = 2$ ). Moreover, they confirmed that the depiction of the representatives within the hemisphere helps to comprehend the classification results ( $S(++) = 3$ ;  $S(+) = 2$ ). P1 stated that the hemisphere-based visualization would be appropriate for documentation since it provides a compact and comparable visual summary of the patient-specific flow. However, two experts wished to have a stronger linking between the two views such as automatic detection of specific landmarks, e.g., blebs.

	--	-	0	+	++
	Clinician	CFD Experts		Visualization Experts	
	P1	P2	P3	P4	P5
<b>Aneurysm-Based Visualization</b>					
The combination of the main render context and additional view enables a simultaneous exploration of blood flow and scalar data on the wall.	++	++	+	++	++
The surface transparency reveals the qualitative flow behavior.	++	++	++	++	++
The details-on-demand approach allows to recognize flow types even if the camera is more distant.	++	++	+	++	+
The bounding geometry, including the possibility to color-code an attribute on it, is a helpful abstraction of the line representation.	++	++	+	++	++
The blending of the three cluster visualizations during zooming does not lead to confusion.	++	+	+	++	+
The tabular view is appropriate to select specific cluster.	++	++	+	++	+
The picking in 3D is appropriate to select specific cluster.	++	++	+	++	++
<b>Hemisphere-Based Visualization</b>					
The hemisphere-based visualization including the mapped scalar fields provides a reasonable simplification of the 3D aneurysm depiction.	++	++	+	++	+
The depiction of representatives within the hemisphere helps to comprehend the classification results.	++	++	+	++	+
The selection of individual clusters is suited to recognize flow patterns.	++	++	++	+	+

Figure 109: The results of the expert evaluation of CAVOCLA with color-encoded Likert scores. Each box represents the answer of one expert: the left-most box depicts the physician, the middle two boxes show the CFD experts, and the two right-most boxes represent the two medical visualization experts. (Image from [434].)

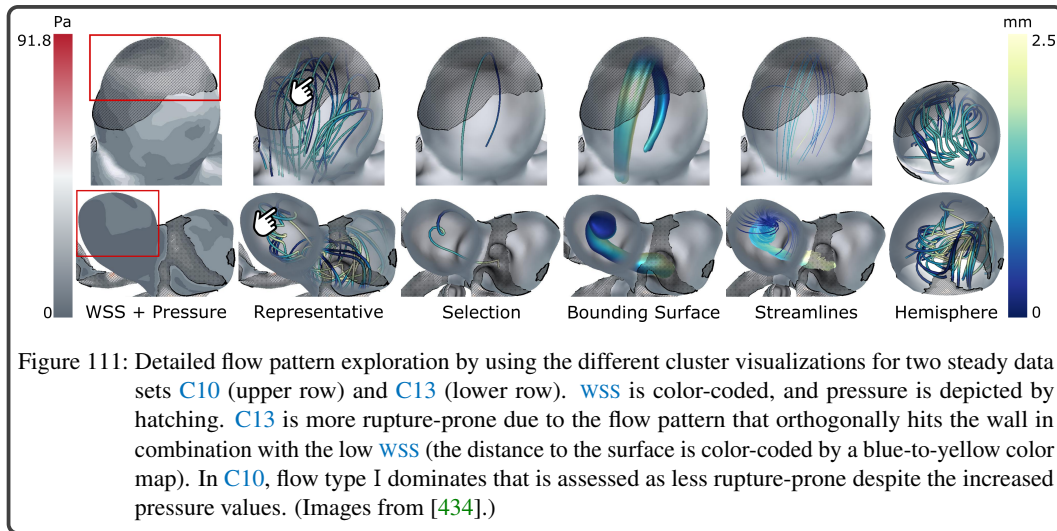


### 7.2.5 Discussion and Limitations

We compared the results of **CAVOCLA** with manual classifications of our experts and discussed occurring deviations with them. Problems to follow the flow behavior within the complex aneurysm morphology were the main reason for mismatches, which also led to reduced confidence of the experts. Moreover, the manual classifications adopted as ground truth are subjective assessments. In the future, further expert assessments have to be recorded, and comparisons with the results of **CAVOCLA** have to be made. A major advantage of **CAVOCLA** is the reproducibility of the results, which is essential for clinical use. Occurring deviations are systematic and thus a reliable assessment is ensured.

In the nine used data sets (C9 - C13, C19 - C22) a total of 80 clusters are identified, with 30 % type I, 15 % type II, 13 % type III, 8 % type IV, 6 % type V and 28 % type VI. Besides, type IV and VI had comparable similarities to type I (difference  $< 0.05$ ) in 15 % and 9 % of the cases. Type V had a comparable similarity to type II and III in 5 % and 7 % of the cases, respectively. In the future, a study with more data sets has to be carried out to be able to evaluate the results of **CAVOCLA** statistically. Moreover, the results of the used clustering and our classification approach depend on the used seeding technique. We use a standard seeding technique that was already used by Oeltze et al. [282] to analyze intra-aneurysmal blood flow. A comparison of different seeding strategies according to the clustering and classification results would be an interesting point for future work.

Similar to the majority of works about **CFD** simulations in cerebral arteries, our simulations are laminar, without turbulence modeling due to the low *Reynolds* number. But there are also isolated studies that transition/turbulence is possible and could play an important role [371]. However, turbulence probably plays only a role in large aneurysms, where high speeds occur, and a sharp segmentation kernel was used. If we would model turbulence, flow patterns may arise, which are dissimilar to the six pre-defined types. To handle such cases, the user can add new flow types. The detection of flow patterns in turbulent areas depends on the clustering method, where large uncertainties are likely to occur. Thus, probably multiple smaller clusters would be detected for lines showing chaotic behavior. **AHC** enables the expert to change the cluster number, where possible wrong clustering results can be corrected. Besides turbulent flows, in unsteady data, flow patterns are observed that decay over the cardiac cycle [60]. Such unstable patterns are also represented by multiple clusters, such as the vortex in Figure 108e,f. For each cluster, the corresponding flow type is determined. Here, a significant extension would be the integration of visual hints that support the user to perceive which clusters represent an unstable flow pattern.



Currently, **CAVOCLA** is designed for saccular shaped aneurysms, where an ostium can be defined. To handle fusiform aneurysms, which occur more frequently in cardiac arteries, another mapping geometry would have to be used that represents their cylindrical shape, e.g., an ellipsoid. This would probably also require the definition of other flow templates.

During the evaluation, it turned out that the aneurysm-based and hemisphere-based depiction represent a useful combination for efficient exploration of flow patterns. The aneurysm-based visualization, including the additional view, allows a detailed analysis of individual flow patterns. Thus, our experts were able to find correlations between rupture-relevant flow patterns and high-risk wall regions, see Figure 111. Here, for two data sets **C10** and **C13** the **WSS** is color-coded and the pressure is depicted by hatching. In **C10** (upper row), flow type I dominates, while all flow types are present in **C13** (lower row). The experts analyzed individual clusters of both cases. In **C13**, they detected a flow pattern that orthogonally hits the wall and could lead to rupture. Conversely, the flow patterns of **C10** run along the wall and have therefore been assessed as less rupture-prone despite the increased pressure values. However, in some cases, the experts were unsure if the current flow pattern is closer to the anterior or posterior wall of the vessel. Therefore, they wished to have additional clipping planes or a 2D color map coding the distance to the respective wall side. The hemisphere-based visualization gives a fast visual overview of existing flow patterns in a data set. Moreover, our experts stated that similarities between the aneurysms considering their scalar fields and flow patterns were easier to perceive on the hemisphere than on the aneurysms themselves.

However, in case of large blebs on the aneurysm, the hemisphere could create visual distortion if multiple flow patterns are mapped simultaneously. Figure 111 shows an example of this. The first aneurysm exhibits no further blebs, leading to no visual distortion of the representatives within the sphere. In contrast, for the second aneurysm, the hemisphere view shows more distortion compared with the view of the representatives (second column) due to the large bleb. This could be reduced by using another reference geometry such as an ellipsoid, determined by a **PCA** of the aneurysm surface. However, our domain experts stated that this would decrease the comparability of data sets according to rupture-prone flow information. Compared to a sphere, an ellipsoid would suggest a higher rupture risk only by its shape, although there may be more suspicious attribute correlations on the sphere. Moreover, they stated that occurring distortions do not prevent to get a quick overview of existing flow patterns, which is the main goal of this view.

### 7.2.6 Conclusion and Future Work

We presented **CAVOCLA** to classify flow patterns in cerebral aneurysms. Besides the separation of the aneurysm surface, **CAVOCLA** performs fully automatically and assigns the most similar flow type to every pattern chosen from a library of pre-defined types. The classification is based on a mathematical description of the flow types and their similarity to the flow patterns. This ensures the comparability of different data sets and reproducible results. In contrast, manual classifications are time-consuming and not standardized. An advantage of **CAVOCLA** is the possibility to incorporate expert knowledge. The cluster number can be changed and new flow types can be easily integrated into the classification process. Thus, **CAVOCLA** allows a faster and more objective analysis of suspicious flow patterns in clinical discussions by providing an automatic classification and efficient exploration techniques.

For future work, we want to integrate an automatic determination of inflow jets and impingement zones based on the approach by Gasteiger et al. [120] to enable an even better rupture risk analysis. In addition, we would like to apply our computation of the bounding geometries to other applications such as aortic flow patterns or fiber bundles extracted from **DTI** data to overcome limitations of existing methods [95, 432] for vortical curve behavior. Moreover, the aneurysm mapping to a hemisphere allows for a fast comparison between classified data sets and a new data set, where the rupture risk should be assessed and an optimal treatment must be found. Therefore, the mapped scalar fields have to be clustered. Then, a comparison of these clusters and detected flow types between existing data sets and the new case would allow to transfer treatment decisions. This could be extended by a user-driven specification of rupture-prone wall regions according to suspicious parameters or flow types. The user could brush regions on the hemisphere that are assigned to a specific parameter range, e.g., high **WSS** values. Then, similar data sets containing information about a possible rupture or treatment could be searched. Therefore, the hemisphere including scalar data and flow types has to be transformed to a **2D** image, which allows an image-based comparison of different cases.



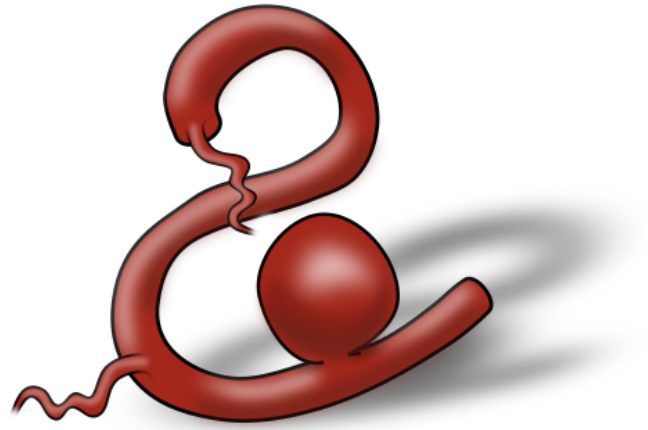
## Part IV

# CONCLUSION





# Conclusion





## CONCLUSION

This chapter summarizes the main contributions of this thesis and suggests ideas for future work.

## 8.1 SUMMARY

The interplay of vessel morphology and blood flow is the starting point for a deeper understanding of the course of [IA](#) and the development of optimized intravascular therapies. Usually, flow information is obtained from [CFD](#) simulations based on patient-specific models leading to complex, multidimensional data. To understand the correlations between the data characteristics and aneurysm evolution, visual exploration techniques are needed. In this way, qualitative relationships can be identified and confirmed as relevant or refuted in subsequent quantitative analysis. This thesis gives a comprehensive overview of [CFD](#) simulations, including necessary pre- and post-processing steps, as well as state-of-the-art in quantitative and qualitative data visualization. This provides future researchers in the field of medical blood flow visualization with a strong starting point for further progress.

Recently (November 2018), Detmer et al. [83] presented a machine learning-based approach to determine a factor that describes the likelihood of a rupture based on 1061 data sets containing 1631 aneurysms. Their model considers several morphological and hemodynamic attributes as well as patient-specific meta information comprising gender, age, aneurysm location, and smoker status. Based on this, an accuracy of ~86 % according to the rupture status was achieved. Although their approach leads to meaningful results that help clinicians to assess the risk of rupture, some limitations require visual analysis of flow data. First, they consider only a temporal snapshot of the patient-specific conditions. Accordingly, aneurysms that are still small and inconspicuous at present are assessed as low risk. Over time, however, patient-specific conditions that lead to a change in wall and flow properties can occur, resulting in aneurysm growth. Here, visual analysis techniques are needed to observe the aneurysm development. Moreover, their model does not consider the wall structure or qualitative flow characteristics, although these aspects seem to influence the aneurysm state. Possibly, there are dependencies between these characteristics and already implemented attributes. However, this would have to be evaluated extensively. Furthermore, the machine learning approach does not support treatment planning. For this purpose, interactive visualization is needed. There are several techniques for aneurysm data visualization that aim to facilitate the exploration of the complex information. However, these methods have still limitations that we want to overcome with our contributions to advance the integration of simulation results into clinical discussions.

For the visual exploration process, the knowledge of two highly specific expert domains, fluid mechanics and neuroradiology are needed. To allow an efficient, collaborative data analysis, consistent management of the aneurysm information is needed, where experts from both domains have access to the data. Since current visualization frameworks neglect this, we developed *Aneulysis* that provides guided management and exploration of aneurysm data. Based on a redundancy-free structure, the complex information comprising morphological and hemodynamic aspects are stored. With this, new data sets can be easily integrated. Moreover, *Aneulysis* provides five additional visualization modules that support the visual exploration of different data characteristics. Detected findings during exploration can be stored and loaded by different domain experts to support the collaborative data analysis further. Furthermore, optimal views on the aneurysm surface and animations summarizing the most interesting aspects of the time-dependent data support the exploration.

The first module, [MorAVis](#) enables automatic analysis of the aneurysm morphology. For this purpose, an automatic ostium extraction was developed, which is not possible with existing techniques. Based on this, different morphological descriptors are calculated to avoid errors induced by manual measurements. Occurring deviations are systematic, and thus a reliable assessment of the aneurysm morphology is ensured. Furthermore, experts can quickly correct possible wrong ostium detections.

In addition to [MorAVis](#), three modules were developed that support a surface-based data exploration. The [CoWaFloVis](#) module provides an integrated visualization of the vessel morphology as well as hemodynamic attributes and the internal blood flow. In contrast to existing techniques, it focuses on an extended visualization of morphological attributes comprising wall thickness and wall deformation. Moreover, it includes a novel [2.5D](#) aneurysm visualization that gives an occlusion-free overview of the wall- and flow-related attributes over the cardiac cycle. The [MuScaVis](#) module focuses on the visual analysis of multiple scalar attributes and time-dependent correlations between them. Here, a comparative analysis of data sets is integrated to evaluate treatment options, which is also neglected in most of the existing techniques. Furthermore, previous methods are restricted to the simultaneous depiction of two attributes. Thus, finding suspicious attribute combinations is a time-consuming process. Therefore, we developed several techniques that allow more efficient analysis of attribute correlations. Moreover, the establishment of a more general risk factor is supported by providing a novel surface-based clustering of attributes. With the [CoTenVis](#) module, a visualization of tensor-based aneurysm information becomes possible for the first time. Multiple glyph-based techniques allow a comparative analysis of stress tensors on the inner and outer vessel wall. The glyphs are suitable for different tasks, where quantitative as well as qualitative comparisons are enabled.

The last module, [ViFIEx](#) focuses on the qualitative analysis of intra-aneurysmal flow patterns. Despite some computer-aided methods to extract the inflow jet and impingement zone [120], a more extensive classification of time-dependent flow patterns was just done manually before [60]. However, this is a time-consuming and error-prone process with high inter-observer variability. To improve this, we developed an automatic classification of aneurysm flow patterns according to pre-defined flow types based on an automatic clustering of blood flow-representing path lines. Besides [3D](#) morphology-based representations, more abstract visualizations of flow patterns are integrated that facilitate the comparison of existing patterns between different data sets.

In summary, *Aneulysis* together with the five visualization modules supports the research to get a deeper understanding of aneurysm initiation and development as well as to make optimal treatment decisions. Due to the absence of simulation results after neurosurgical clipping, the integrated visualization methods aim at supporting endovascular treatments. To avoid an open-ended visual exploration, we conferred with clinical and [CFD](#) experts to determine requirements for efficient analysis. We carried out extensive evaluations to verify if our new techniques fulfill the defined requirements, which was confirmed in all our performed studies.

## 8.2 FUTURE WORK

The field of simulated blood flow data for [IA](#) provides a vast amount of potential future topics. Besides, possible improvements of the visualization modules already described in the corresponding future work sections, this section elaborates on additional recent research trends and future challenges.

**Comparative visualization.** To further improve the decision-making process, the *comparison* task should receive more attention. Methods are needed that allow a comparison of multiple instances of dynamic data, which is particularly challenging with existing techniques. The comparison of two time-dependent vector fields along with the vascular anatomy and different treatment options such as stents or coils would benefit from detection of corresponding and unique features in both data sets to focus the comparison on such features. Besides, comparative overview visualizations showing the *k-nearest neighbors* for a requested aneurysm would probably allow transferring treatment decisions of already treated aneurysms to new cases. Besides treatment planning, a fusion of simulated and measured data strongly demands dedicated comparative visualizations. This would enable validation of the former and compensation for the limited spatial and temporal resolution of the latter.

**Perception-based medical flow visualization.** The simultaneous display of complex vessel anatomies together with partially complex flow features and optional planning information, such as stenting, poses great challenges to the interpretability of the results [305]. The careful consideration of perception-based knowledge regarding the development of vessel [218] and flow visualization techniques [398] may guide the refinement of visualization techniques. Flow perception, e.g., the

importance of long continuous flow lines, depth and shape perception are particularly important. The ambient occlusion for lines (*LineAO*) [94] is a promising example of a perceptually-motivated visualization technique that may bring great benefits to medical flow visualization. Originally developed for a clear depiction of *DTI* fiber tracts, it may also be useful for streamlines and path lines that represent the medical flow.

**Uncertainty.** To quantify the uncertainty associated with blood flow simulations, first ensemble simulations were performed [294, 303]. At present, it is not clear which parameters need to be changed and how many different gradations are required for each parameter. A compromise between a careful analysis of the combined influence of different parameters and a reasonable calculation effort is necessary. Since the generation of simulated flow data is based on many not-patient-specific assumptions and parameter choices, they carry a large amount of uncertainty. Uncertainty-aware techniques for simulated data must, therefore, be developed, where the key challenge is to consider user needs carefully. Here, too, a compromise must be found between the displayed information content related to uncertainty and the load on the user. Flow visualizations techniques focused on the depiction of uncertainty, e.g., Otto et al. [287] and Ferstl et al. [104], may serve as a starting point.

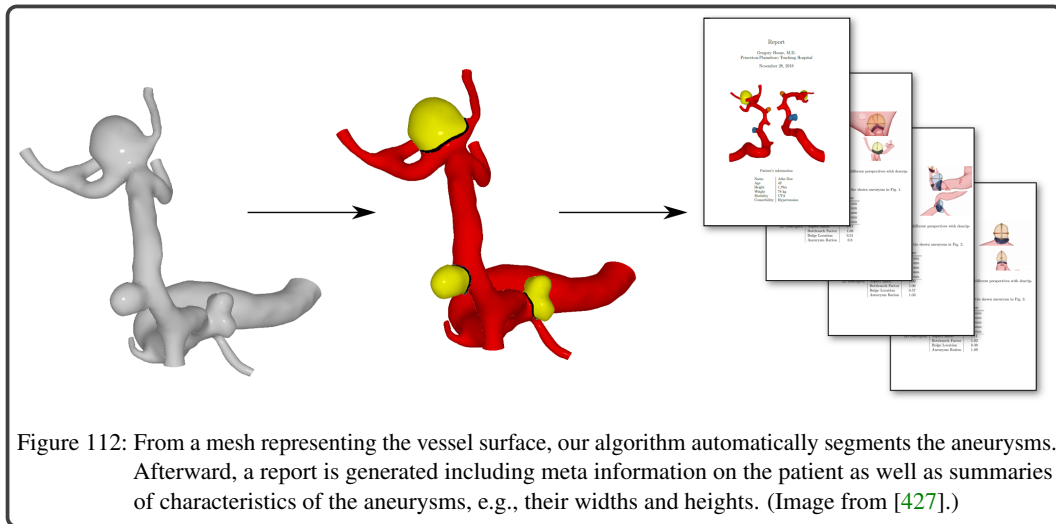
**Vector field topology.** There are many approaches to extract and visualize topological characteristics of vector fields in steady and unsteady flow fields [208, 300]. These methods have a great potential to reduce the complexity of the flow data. However, they have rarely been applied to medical data so far. The main reason for this is the difficulty in deriving a medical meaning from the extracted structures such as the topological skeleton or a *Morse* decomposition. Besides, cerebral flow can be modeled as turbulent, where Galilean-invariant approaches must be used instead of vector field topology based on critical points to extract flow features [179, 326].

**Wall behavior.** The behavior of the aneurysm wall under pulsatile conditions seems to be an important aspect for the aneurysm state evaluation. To incorporate information about the aneurysm wall into the generation of blood flow data, approaches were developed analyzing data of intravascular imaging techniques [132, 216], combining *FSI* with *CFD* simulations [393, 394], and ex-vivo measuring of wall properties based on resection results [61]. A relation between aneurysm wall thickness, inner wall stresses, and wall deformation and hemodynamics has been reported. Since these relations are crucial to assess the aneurysm state and to find an optimal treatment, more research in this direction is expected. We already present an approach for integrated visualization of wall thickness and deformation [436], which overcomes the limitations of existing techniques [132, 216]. In the future, visualization approaches that better support the analysis of ensemble simulations in this area would strengthen the understanding of wall behavior considering rupture and treatment decisions. Here, also the integration of knowledge from new *MRI* sequences such as *phase-based amplified magnetic resonance imaging* (*aMRI*) [366] showing the deformation of the brain tissue by the heartbeat could further improve the definition of simulation models. Thus, it might also be possible to quantify the influence of surrounding structures on the aneurysm over the cardiac cycle. For example, whether surrounding tissue presses on the aneurysm wall by the movement of the tissue itself.

**Report generation.** The exploration of both, measured and simulated flow data, is an interdisciplinary and collaborative process, where medical and hemodynamic experts want to get insights into the patient-specific conditions. An important aspect here is the sharing of specific findings with other researchers or physicians, where current computer-aided methods largely neglect targeted support of this point. An essential question is how the analyst can be supported to create a report with measurements, annotated screenshots and video sequences that summarize the essential features of a data set? We proposed some interactive and automatic techniques to select appropriate viewpoints of suspicious aneurysm surface regions that can be combined to video sequences as well as an annotation of essential structures [429, 436]. However, these methods are mainly focused on wall and flow attributes mapped to the vessel wall. This could be improved by a stronger consideration of the qualitative flow behavior. Transferring methods from storytelling to the analysis of complex time-resolved data [418, 419] may help to develop techniques that are standardized to some extent but also offer flexibility to reflect analysts' assessments.

**Multiple aneurysm exploration.** Multiple aneurysms occur in about one-fifth of aneurysm patients [308, 315] and require more specific analysis methods than the presence of a single aneurysm, since they may require several treatment cycles. During treatment planning, the physician has to decide which aneurysm should be treated first and how does treatment affect the remaining aneurysms? However, the visual analysis and treatment planning of multiple aneurysms is neglected in most visualization methods. Perception-based studies such as the work by Behrendt et al. [28] could serve as a starting point to design visualization frameworks for multiple aneurysms.

Besides an adequate visualization of multiple aneurysms, computer-aided methods that support their morphological and hemodynamic analysis are needed. A first step in this direction was done by our recent extension of the ostium extraction to multiple aneurysms [427], where the aneurysms were automatically detected, see Figure 112. For the aneurysm detection, an analytic characterization is used to generate a list of candidate regions on the 3D triangular vessel tree surface. Afterward, we reduced the candidate set and thus the number of false positives with an appropriate classifier. For the aneurysm classification scheme, we identified four suitable features and modeled appropriate training data. The features comprise the mean shape index of each region as well as the three *Westin's measures* [405], where we achieved an accuracy of 99 % for the aneurysm detection. Finally, morphological descriptors based on the ostium surfaces are computed, and a report including the results of the analysis and renderings of the aneurysms is generated.



For future work, qualitative flow structures should be integrated into the analysis of multiple aneurysms. The treatment of one aneurysm may affect the flow behavior, leading to different flow patterns in the other aneurysms. One could try to visualize the change such that the physician can inspect the difference and the effects of the treatment. Moreover, it would be interesting to explore the detection and segmentation of fusiform shaped aneurysms.

**Integration with visual analytics.** For a better understanding of risk factors that favor the development and progression of aneurysms, a variety of data needs to be analyzed. If flow data is collected on a larger scale, e.g., in studies with hundreds of data sets, it will be possible to analyze correlations between measurements derived from the flow and other variables, such as patient age or blood pressure. This would contribute to a better understanding of the range of normal flow rates depending on age and gender and can also support research to understand the physiology of normal and pathological flow better. As a long-term goal one may even aim for a flow atlas that represents the probability of certain flow characteristics in certain regions of the aorta or cerebral vessels. Besides the acquisition of a large number of data sets, also the observation and analysis of data sets over a longer period would be important to evaluate the stability of aneurysms. Since the aneurysm growth seems to influence the rupture probability, such long-term studies are needed to evaluate which of the initially non-ruptured aneurysms ruptured over time. This fact was not considered in recent works that aim



at calculating a rupture probability [83, 277]. Visual analytic techniques combined with concepts of multivariate and time-oriented data visualization could be a powerful option to give insights into these high dimensional data. We refer to [6, 71, 356] for an overview of these topics. The work by Girardi et al. [126] could serve as a starting point to design visual exploration frameworks, where the knowledge discovery is based on a strong consideration of expert knowledge.

**Medical evaluations.** The evaluation of medical visualizations is essential to get a better understanding of how new and existing techniques relate to each other and which use they have in practice [381, 307]. However, there is a lack of convincing empirical evaluations performed under realistic settings for many medical visualization applications including the visual analysis of blood flow data. Currently, assessments of blood flow visualizations are often based on questionnaires and informal expert feedback that relate to visual coding and the selection of specific algorithms performed in a controlled lab environment. Although these short qualitative assessments can be focused on practical tasks, more in-depth evaluations are needed that verify how flow visualizations changes or improves clinical decisions by considering the high clinical workload. Based on extensive discussions with medical experts, practical tasks and typical cases, in particular where diagnosis and treatment planning is stressful, should be prepared for empirical evaluations. Here, the automatic creation of user studies would save a lot of time. Recently, we presented a system to quickly generate perceptual task-based user studies for surface visualizations [435]. We applied our technique to liver vessel trees, but an adaption to cerebral arteries trees would be meaningful. Besides, the application of methods widely used in information visualization [36], such as eye-tracking and think-aloud, can improve the understanding of how physicians interact with visualization techniques. Another important topic is the conduct of long-term case studies to verify the suitability of interactive visualization techniques. Related to this, is the usage of collaborative visualization technologies such as the *Medical Visualization Table* [230], which is a powerful multi-touch system. It would allow a collaborative diagnosis and treatment planning of aneurysms by, e.g., discussing different treatment scenarios. Moreover, the usage of more advanced visualization systems based on a *virtual reality* (VR) setup [54, 286] should be part of future evaluations to assess how such approaches can improve aneurysm data exploration and the practice of treatments such as clipping and endovascular embolization [8, 134]. Similar to this, more quantitative visualizations should be developed and evaluated that aim to support surgical treatment planning, which is not the case with existing methods.

**Clinical adoption.** CFD simulations of hemodynamic conditions within the cerebral arteries have so far only been used in medical and biomedical research. Most clinicians are neither familiar with these simulations nor with the techniques for visualizing their results or do not trust the simulation results because of the numerous assumptions and simplifications [34]. This may change if the pipeline from patient-specific image data to simulation results is mainly automated and simulations are proven to contribute significantly to predict a reliable risk of rupture. Berg et al. [34] suggested a prototype, where clinicians were able to generate hemodynamic predictions within several minutes at low spatial resolution. For the clinical usability, the resolution has to be improved while the computation time should remain the same. Recently, Detmer et al. [83] developed a promising method for rupture status prediction using machine learning. However, the underlying pre-processing and extraction of the considered hemodynamic and morphological properties is still too complex for clinical routine. The use of CFD simulations in clinical treatment planning is somewhat more advanced. It has been shown that virtual stenting of cerebral aneurysms supports decision-making within an acceptable time frame [166]. Clinicians can test different stent types and positions and receive visual feedback including visualizations of the blood flow pattern and its changes after the virtual procedure.



Part V

APPENDIX



## BIBLIOGRAPHY

---

- [1] Proc. of the International Meshing Roundtable, <http://imr.sandia.gov/papers/mesh.html>, 1992-2017.
- [2] A. Abdelsamie, G. Fru, T. Oster, F. Dietzsch, G. Janiga, and D. Thévenin. Towards direct numerical simulations of low-Mach number turbulent reacting and two-phase flows using immersed boundaries. *Computers & Fluids*, 131:123–141, 2016.
- [3] G. Acevedo-Bolton, L.-D. Jou, B. P. Dispensa, M. T. Lawton, R. T. Higashida, A. J. Martin, W. L. Young, and D. Saloner. Estimating the hemodynamic impact of interventional treatments of aneurysms: numerical simulation with experimental validation: technical case report. *Neurosurgery*, 59(2):E429–E430, 2006.
- [4] A. K. Ai-Awami, J. Beyer, D. Haehn, N. Kasthuri, J. W. Lichtman, H. Pfister, and M. Hadwiger. Neuroblocks—visual tracking of segmentation and proofreading for large connectomics projects. *IEEE Transactions on Visualization and Computer Graphics*, 22(1):738–746, 2016.
- [5] W. Aigner, S. Miksch, W. Müller, H. Schumann, and C. Tominski. Visualizing time-oriented data - A systematic view. *Computers & Graphics*, 31(3):401–409, 2007.
- [6] W. Aigner, S. Miksch, W. Müller, H. Schumann, and C. Tominski. Visual methods for analyzing time-oriented data. *IEEE Transactions on Visualization and Computer Graphics*, 14(1):47–60, 2008.
- [7] W. Aigner, S. Miksch, H. Schumann, and C. Tominski. *Visualization of Time-Oriented Data*. Human-Computer Interaction Series. Springer, 2011.
- [8] A. Alaraj, C. J. Luciano, D. P. Bailey, A. Elsenousi, B. Z. Roitberg, A. Bernardo, P. P. Banerjee, and F. T. Charbel. Virtual reality cerebral aneurysm clipping simulation with real-time haptic feedback. *Operative Neurosurgery*, 11(1):52–58, 2015.
- [9] P. Alliez, G. Ucelli, C. Gotsman, and M. Attene. Recent advances in remeshing of surfaces. In *Shape Analysis and Structuring*, pages 53–82. Springer, 2008.
- [10] R. Amar, J. Eagan, and J. Stasko. Low-level components of analytic activity in information visualization. In *Proc. of IEEE Symposium on Information Visualization*, pages 111–117, 2005.
- [11] K. Amuluru, F. Al-Mufti, I. P. Singh, C. Prestigiacomo, and C. Gandhi. Flow diverters for treatment of intracranial aneurysms: Technical and clinical updates. *World Neurosurgery*, 85:15–19, 2016.
- [12] M. Andersson, J. Lantz, T. Ebbens, and M. Karlsson. Quantitative assessment of turbulence and flow eccentricity in an aortic coarctation: Impact of virtual interventions. *Cardiovascular Engineering and Technology*, 6(3):281–293, 2015.
- [13] P. Angelelli and H. Hauser. Straightening tubular flow for side-by-side visualization. *IEEE Transactions on Visualization and Computer Graphics*, 17(12):2063–2070, 2011.
- [14] J. A. Anson, M. T. Lawton, and R. F. Spetzler. Characteristics and surgical treatment of dolichoectatic and fusiform aneurysms. *Journal of Neurosurgery*, 84(2):185–193, 1996.
- [15] ANSYS, Inc. *ANSYS ICEM CFD User’s Manual, Release 17.2*, 2016.
- [16] L. Antiga, B. Ene-Iordache, and A. Remuzzi. Computational geometry for patient-specific reconstruction and meshing of blood vessels from MR and CT angiography. *IEEE Transactions on Bio-Medical Engineering*, 22(5):674–684, 2003.

- [17] L. Antiga, M. Piccinelli, L. Botti, B. Ene-Iordache, A. Remuzzi, and D. A. Steinman. An image-based modeling framework for patient-specific computational hemodynamics. *Medical & Biological Engineering & Computing*, 46(11):1097, 2008.
- [18] S. Appanaboyina, F. Mut, R. Löhner, C. Putman, and J. Cebal. Simulation of intracranial aneurysm stenting: Techniques and challenges. *Computer Methods in Applied Mechanics and Engineering*, 198(45):3567–3582, 2009.
- [19] N. Ashgriz and J. Mostaghimi. An introduction to computational fluid dynamics. *Fluid Flow Handbook, McGraw-Hill Professional*, pages 24–1, 2002.
- [20] O. K.-C. Au, C.-L. Tai, H.-K. Chu, D. Cohen-Or, and T.-Y. Lee. Skeleton extraction by mesh contraction. *ACM Transactions on Graphics*, 27(3):44, 2008.
- [21] L. Augsburger, P. Reymond, E. Fonck, Z. Kulcsar, M. Farhat, M. Ohta, N. Stergiopoulos, and D. Rüfenacht. Methodologies to assess blood flow in cerebral aneurysms: Current state of research and perspectives. *Journal of Neuroradiology*, 1601(5):249–306, 2009.
- [22] M. H. Babiker, B. Chong, L. F. Gonzalez, S. Cheema, and D. H. Frakes. Finite element modeling of embolic coil deployment: Multifactor characterization of treatment effects on cerebral aneurysm hemodynamics. *Journal of Biomechanics*, 46(16):2809–2816, 2013.
- [23] A. Baer, R. Gasteiger, D. W. Cunningham, and B. Preim. Perceptual evaluation of ghosted view techniques for the exploration of vascular structures and embedded flow. *Computer Graphics Forum*, 30(3):811–820, 2011.
- [24] A. Bannach, J. Bernard, Jung, J. Florian, Kohlhammer, T. May, K. Scheckenbach, and S. Weisarg. Visual analytics for radiomics: Combining medical imaging with patient data for clinical research. In *Proc. of Workshop on Visual Analytics in Healthcare*, pages 84–91, 2017.
- [25] A. V. Bartolí, R. Wegenkittl, A. König, M. E. Gröller, and E. Sorantin. Virtual colon flattening. In *Proceedings of the Joint Eurographics and IEEE TCVG Symposium on Visualization*, pages 127–136, 2001.
- [26] A. J. Bates, D. J. Doorly, R. Cetto, H. Calmet, A. Gambaruto, N. Tolley, G. Houzeaux, and R. Schroter. Dynamics of airflow in a short inhalation. *Journal of the Royal Society Interface*, 12(102):20140880, 2015.
- [27] B. Behrendt, P. Berg, O. Beuing, B. Preim, and S. Saalfeld. Explorative blood flow visualization using dynamic line filtering based on surface features. *Computer Graphics Forum*, 37(3):183–194, 2018.
- [28] B. Behrendt, P. Berg, B. Preim, and S. Saalfeld. Combining pseudo chroma depth enhancement and parameter mapping for vascular surface models. In *Proc. of Eurographics Workshop on Visual Computing for Biology and Medicine*, pages 159–168, 2017.
- [29] B. Behrendt, B. Köhler, U. Preim, and B. Preim. Enhancing visibility of blood flow in volume rendered cardiac 4D PC-MRI data. In *Proc. of Bildverarbeitung für die Medizin*, pages 188–193, 2016.
- [30] P. Berg, L. Daróczy, and G. Janiga. Virtual stenting for intracranial aneurysms: A risk-free, patient-specific treatment planning support for neuroradiologists and neurosurgeons. In *Computing and Visualization for Intravascular Imaging and Computer-Assisted Stenting*, pages 371–411. Elsevier, 2017.
- [31] P. Berg, C. Roloff, O. Beuing, S. Voss, S.-I. Sugiyama, N. Aristokleous, A. S. Anayiotos, N. Ashton, et al. The computational fluid dynamics rupture challenge 2013 – phase II: Variability of hemodynamic simulations in two intracranial aneurysms. *Journal of Biomechanical Engineering*, 137(12):121008/1–121008/13, 2015.

- [32] P. Berg, S. Saalfeld, S. Voss, T. Redel, B. Preim, G. Janiga, and O. Beuing. Does the DSA reconstruction kernel affect hemodynamic predictions in intracranial aneurysms? An analysis of geometry and blood flow variations. *Journal of Neurointerventional Surgery*, page 012996, 2017.
- [33] P. Berg, D. Stucht, G. Janiga, O. Beuing, O. Speck, and D. Thévenin. Cerebral blood flow in a healthy Circle of Willis and two intracranial aneurysms: Computational fluid dynamics versus four-dimensional phase-contrast magnetic resonance imaging. *Journal of Biomechanical Engineering*, 136(4):041003, 2014.
- [34] P. Berg, S. Voß, M. Becker, S. Serowy, T. Redel, G. Janiga, M. Skalej, and O. Beuing. Bringing hemodynamic simulations closer to the clinics: A CFD prototype study for intracranial aneurysms. In *Proc. of Engineering in Medicine and Biology Society*, pages 3302–3305, 2016.
- [35] R. Blankena, R. Kleinloog, B. Verweij, P. van Ooij, B. Ten Haken, Luijten, and et al. Thinner regions of intracranial aneurysm wall correlate with regions of higher wall shear stress: A 7T MRI study. *American Journal of Neuroradiology*, 2016.
- [36] T. Blascheck, K. Kurzhals, M. Raschke, M. Burch, D. Weiskopf, and T. Ertl. State-of-the-art of visualization for eye tracking data. *Computer Graphics Forum*, 2014, 2014.
- [37] J. Bols, L. Taelman, G. De Santis, J. Degroote, B. Verhegghe, P. Segers, and J. Vierendeels. Unstructured hexahedral mesh generation of complex vascular trees using a multi-block grid-based approach. *Computer Methods in Biomechanics and Biomedical Engineering*, 19(6):663–672, 2016.
- [38] G.-P. Bonneau, H.-C. Hege, C. R. Johnson, M. M. Oliveira, K. Potter, P. Rheingans, and T. Schultz. *Overview and State-of-the-Art of Uncertainty Visualization*, pages 3–27. Springer, 2014.
- [39] U. D. Bordoloi and H.-W. Shen. View selection for volume rendering. In *Proc. of IEEE Visualization Conference*, pages 487–494, 2005.
- [40] R. Borgo, J. Kehler, D. H. Chung, E. Maguire, and et al. Glyph-based visualization: Foundations, design guidelines, techniques and applications. *Eurographics*, pages 39–63, 2013.
- [41] S. Born, M. Markl, M. Gutberlet, and G. Scheuermann. Illustrative visualization of cardiac and aortic blood flow from 4D MRI data. In *Proc. of IEEE Pacific Visualization Symposium*, pages 129–136, 2013.
- [42] S. Born, M. Pfeifle, M. Markl, M. Gutberlet, and G. Scheuermann. Visual analysis of cardiac 4D MRI blood flow using line predicates. *IEEE Transactions on Visualization and Computer Graphics*, 19(6):900–912, 2013.
- [43] A. Botella, B. Lévy, and G. Caumon. Indirect unstructured hex-dominant mesh generation using tetrahedra recombination. *Computational Geosciences*, 20(3):437–451, 2016.
- [44] M. Botsch, L. Kobbelt, M. Pauly, P. Alliez, and B. Lévy. *Polygon Mesh Processing*. AK Peters/CRC Press, 2010.
- [45] C. V. Bourantas, F. A. Jaffer, F. J. Gijssen, G. van Soest, S. P. Madden, B. K. Courtney, A. M. Fard, E. Tenekecioglu, Y. Zeng, A. F. van der Steen, S. Emelianov, J. Muller, P. H. Stone, L. Marcu, G. J. Tearney, and P. W. Serruys. Hybrid intravascular imaging: Recent advances, technical considerations, and current applications in the study of plaque pathophysiology. *European Heart Journal*, 38(6):400–412, 2017.
- [46] L. Boussel, V. Rayz, A. Martin, G. Acevedo-Bolton, M. T. Lawton, R. Higashida, W. S. Smith, W. L. Young, and D. Saloner. Phase-contrast magnetic resonance imaging measurements in intracranial aneurysms in vivo of flow patterns, velocity fields, and wall shear stress:



- Comparison with computational fluid dynamics. *Magnetic Resonance in Medicine*, 61(2):409–417, 2009.
- [47] J. L. Brisman, J. K. Song, and D. W. Newell. Cerebral aneurysms. *New England Journal of Medicine*, 355(9):928–939, 2006.
  - [48] K. Brodlie, R. A. Osorio, and A. Lopes. A review of uncertainty in data visualization. In *Expanding the Frontiers of Visual Analytics and Visualization*, pages 81–109. Springer, 2012.
  - [49] A. J. Broos, N. H. de Hoon, P. J. de Koning, R. J. Geest, A. Vilanova, and A. C. Jalba. A framework for fast initial exploration of PC-MRI cardiac flow. In *Proc. of Eurographics Workshop on Visual Computing for Biology and Medicine*, pages 69–78, 2016.
  - [50] M. H. Buonocore. Visualizing blood flow patterns using streamlines, arrows, and particle paths. *Magnetic Resonance in Medicine*, 40(2):210–226, 1998.
  - [51] G. Byrne and J. R. Cebral. Vortex dynamics in cerebral aneurysms. *ArXiv e-prints*, 2013.
  - [52] G. Byrne, F. Mut, and J. R. Cebral. Quantifying the large-scale hemodynamics of intracranial aneurysms. *American Journal of Neuroradiology*, 35(2):333–338, 2014.
  - [53] B. Cabral and L. C. Leedom. Imaging vector fields using line integral convolution. In *Proc. of Computer Graphics and Interactive Techniques*, pages 263–270, 1993.
  - [54] I. Cabrilo, P. Bijlenga, and K. Schaller. Augmented reality in the surgery of cerebral aneurysms: A technical report. *Operative Neurosurgery*, 10(2):252–261, 2014.
  - [55] R. Cárdenes, I. Larrabide, L. San Román, and A. F. Frangi. Performance assessment of isolation methods for geometrical cerebral aneurysm analysis. *Medical & Biological Engineering & Computing*, 51(3):343–352, 2013.
  - [56] R. Cárdenes, J. M. Pozo, H. Bogunovic, I. Larrabide, and A. F. Frangi. Automatic aneurysm neck detection using surface Voronoi diagrams. *IEEE Transactions on Bio-Medical Engineering*, 30(10):1863–1876, 2011.
  - [57] J. Cebral, F. Mut, B. Chung, L. Spelle, J. Moret, F. van Nijnatten, and D. Ruijters. Understanding angiography-based aneurysm flow fields through comparison with computational fluid dynamics. *American Journal of Neuroradiology*, 38(6):1180–1186, 2017.
  - [58] J. Cebral, F. Mut, M. Raschi, E. Scrivano, R. Ceratto, P. Lylyk, and C. Putman. Aneurysm rupture following treatment with flow-diverting stents: Computational hemodynamics analysis of treatment. *American Journal of Neuroradiology*, 32(1):27–33, 2011.
  - [59] J. R. Cebral, M. A. Castro, S. Appanaboyina, C. M. Putmann, D. Millan, and A. F. Frangi. Efficient pipeline for image-based patient-specific analysis of cerebral aneurysm hemodynamics: Technique and sensitivity. *IEEE Transactions on Bio-Medical Engineering*, pages 457–467, 2005.
  - [60] J. R. Cebral, M. A. Castro, J. E. Burgess, R. S. Pergolizzi, M. J. Sheridan, and C. M. Putman. Characterization of cerebral aneurysms for assessing risk of rupture by using patient-specific computational hemodynamics models. *American Journal of Neuroradiology*, 26(10):2550–2559, 2005.
  - [61] J. R. Cebral, X. Duan, P. S. Gade, B. J. Chung, F. Mut, K. Aziz, and A. M. Robertson. Regional mapping of flow and wall characteristics of intracranial aneurysms. *Annals of Biomedical Engineering*, 44(12):3553–3567, 2016.
  - [62] J. R. Cebral, M. Hernandez, A. Frangi, C. Putman, R. Pergolizzi, and J. Burgess. Subject-specific modeling of intracranial aneurysms. In *Proc. of Medical Imaging: Physiology, Function, and Structure from Medical Images*, volume 5369, pages 319–328, 2004.

- [63] J. R. Cebral and R. Lohner. From medical images to CFD meshes. In *Proc. of International Meshing Roundtable*, pages 321–331, 1999.
- [64] J. R. Cebral and R. Lohner. Efficient simulation of blood flow past complex endovascular devices using an adaptive embedding technique. *IEEE Transactions on Medical Imaging*, 24(4):468–476, 2005.
- [65] J. R. Cebral, F. Mut, J. Weir, and C. M. Putman. Association of hemodynamic characteristics and cerebral aneurysm rupture. *American Journal of Neuroradiology*, 32(2):264–270, 2011.
- [66] J. R. Cebral, F. Mut, J. Weir, and C. M. Putman. Quantitative characterization of the hemodynamic environment in ruptured and unruptured brain aneurysms. *American Journal of Neuroradiology*, 32(1):145–151, 2011.
- [67] J. R. Cebral, C. M. Putman, M. T. Alley, T. Hope, R. Bammer, and F. Calamante. Hemodynamics in normal cerebral arteries: Qualitative comparison of 4D phase-contrast magnetic resonance and image-based computational fluid dynamics. *Journal of Engineering Mathematics*, 64(4):367, 2009.
- [68] J. R. Cebral, M. Sheridan, and C. M. Putman. Hemodynamics and bleb formation in intracranial aneurysms. *American Journal of Neuroradiology*, 31(2):304–310, 2010.
- [69] J. R. Cebral, M. Vazquez, D. M. Sforza, G. Houzeaux, and et al. Analysis of hemodynamics and wall mechanics at sites of cerebral aneurysm rupture. *Journal of Neurointerventional Surgery*, 7(7):530–536, 2015.
- [70] V. Challa and H.-C. Han. Spatial variations in wall thickness, material stiffness and initial shape affect wall stress and shape of intracranial aneurysms. *Neurological Research*, 29(6):569–577, 2007.
- [71] W. W.-Y. Chan. A survey on multivariate data visualization. *Department of Computer Science and Engineering. Hong Kong University of Science and Technology*, 8(6):1–29, 2006.
- [72] A. Chandra and S. Mondal. Amalgamation of iterative double automated thresholding and morphological filtering: A new proposition in the early detection of cerebral aneurysm. *Multimedia Tools and Applications*, 76(22):23957–23979, 2016.
- [73] T. Chung. *Computational Fluid Dynamics*. Cambridge University Press, 2010.
- [74] E. S. Connolly, A. A. Rabinstein, J. R. Carhuapoma, C. P. Derdeyn, J. Dion, R. T. Higashida, B. L. Hoh, C. J. Kirkness, A. M. Naidech, C. S. Ogilvy, et al. Guidelines for the management of aneurysmal subarachnoid hemorrhage: A guideline for healthcare professionals from the American Heart Association/American Stroke Association. *Stroke*, 43(6):1711–1737, 2012.
- [75] P. Coppin, J. Harvey, K. Valen-Sendstad, D. Steinman, and D. Steinman. Illustration-inspired visualization of blood flow dynamics. In *Proc. of International Conference on Information Visualisation*, pages 333–335, 2014.
- [76] I. Corouge, S. Gouttard, and G. Gerig. Towards a shape model of white matter fiber bundles using diffusion tensor MRI. In *Proc. of IEEE International Symposium on Biomedical Imaging*, pages 344–347, 2004.
- [77] V. Costalat, M. Sanchez, D. Ambard, L. Thines, N. Lonjon, F. Nicoud, H. Brunel, J. Lejeune, et al. Biomechanical wall properties of human intracranial aneurysms resected following surgical clipping. *Journal of Biomechanics*, 44(15):2685–2691, 2011.
- [78] K. Crane, C. Weischedel, and M. Wardetzky. Geodesics in heat: A new approach to computing distance based on heat flow. *ACM Transactions on Graphics*, 32(5):152, 2013.

- [79] N. de Hoon, R. van Pelt, A. Jalba, and A. Vilanova. 4D MRI flow coupled to physics-based fluid simulation for blood-flow visualization. *Computer Graphics Forum*, 33(3):121–130, 2014.
- [80] D. DeCarlo, A. Finkelstein, S. Rusinkiewicz, and A. Santella. Suggestive contours for conveying shape. *ACM Transactions on Graphics*, 22(3):848–855, 2003.
- [81] J. Dequidt, C. Duriez, S. Cotin, and E. Kerrien. Towards interactive planning of coil embolization in brain aneurysms. In *Proc. of International Conference on Medical Image Computing and Computer-Assisted Intervention*, pages 377–385, 2009.
- [82] J. Dequidt, M. Marchal, C. Duriez, E. Kerrien, and S. Cotin. Interactive simulation of embolization coils: Modeling and experimental validation. In *Proc. of International Conference on Medical Image Computing and Computer-Assisted Intervention*, pages 695–702, 2008.
- [83] F. J. Detmer, B. J. Chung, F. Mut, M. Slawski, F. Hamzei-Sichani, C. Putman, C. Jiménez, and J. R. Cebal. Development and internal validation of an aneurysm rupture probability model based on patient characteristics and aneurysm location, morphology, and hemodynamics. *International Journal of Computer Assisted Radiology and Surgery*, 13(11):1767–1779, 2018.
- [84] S. Dhar, M. Tremmel, J. Mocco, M. Kim, J. Yamamoto, A. H. Siddiqui, L. N. Hopkins, and H. Meng. Morphology parameters for intracranial aneurysm rupture risk assessment. *Journal of Neurosurgery*, 63(2):185–197, 2008.
- [85] C. Díaz and L. A. Robles. Fast noncontinuous path phase-unwrapping algorithm based on gradients and mask. In *Proc. of Iberoamerican Congress on Pattern Recognition*, pages 116–123, 2004.
- [86] H. Doleisch, M. Gasser, and H. Hauser. Interactive feature specification for focus+context visualization of complex simulation data. In *Proc. of the Symposium on Data Visualisation*, pages 239–248, 2003.
- [87] H. Doleisch, M. Mayer, M. Gasser, R. Wanker, and H. Hauser. Case study: Visual analysis of complex, time-dependent simulation results of a diesel exhaust system. In *Proc. of the Symposium on Data Visualisation*, pages 91–96, 2004.
- [88] D. J. Doorly, D. J. Taylor, A. M. Gambaruto, R. C. Schroter, and N. Tolley. Nasal architecture: form and flow. *Philosophical Transactions of the Royal Society A: Mathematical, Physical and Engineering Sciences*, 366:3225–3246, 2008.
- [89] C. G. Drake, A. H. Friedman, and S. J. Peerless. Failed aneurysm surgery: Reoperation in 115 cases. *Journal of Neurosurgery*, 61(5):848–856, 1984.
- [90] S. M. Drucker. *Intelligent Camera Control for Graphical Environments*. PhD thesis, Massachusetts Institute of Technology, 1994.
- [91] P. Dyverfeldt, M. Bissell, A. J. Barker, A. F. Bolger, and et al. 4D flow cardiovascular magnetic resonance consensus statement. *Journal of Cardiovascular Magnetic Resonance*, 17(1):72, 2015.
- [92] H. Edelsbrunner. *Geometry and topology for mesh generation*, volume 7. Cambridge University Press, 2001.
- [93] H. Edelsbrunner and E. P. Mücke. Three-dimensional alpha shapes. *ACM Transactions on Graphics*, 13(1):43–72, 1994.
- [94] S. Eichelbaum, M. Hlawitschka, and G. Scheuermann. LineAO - Improved three-dimensional line rendering. *IEEE Transactions on Visualization and Computer Graphics*, 19(3):433–445, 2013.

- [95] F. Enders, N. Sauber, D. Merhof, P. Hastreiter, C. Nimsy, and M. Stamminger. Visualization of white matter tracts with wrapped streamlines. In *Proc. of IEEE Visualization Conference*, pages 51–58, 2005.
- [96] W. Engelke and I. Hotz. Evolutionary lines for flow visualization. In *Proc. of EuroVis - Short Papers*, 2018.
- [97] W. Engelke, K. Lawonn, B. Preim, and I. Hotz. Autonomous particles for interactive flow visualization. *Computer Graphics Forum*, 2018.
- [98] R. Englund, T. Ropinski, and I. Hotz. Coherence maps for blood flow exploration. In *Proc. of Eurographics Workshop on Visual Computing for Biology and Medicine*, pages 79–88, 2016.
- [99] M. Ester, H.-P. Kriegel, J. Sander, and X. Xu. A density-based algorithm for discovering clusters in large spatial databases with noise. In *Proc. of Knowledge Discovery and Data Mining*, pages 226–231, 1996.
- [100] M. H. Everts, H. Bekker, J. B. Roerdink, and T. Isenberg. Depth-dependent halos: Illustrative rendering of dense line data. *IEEE Transactions on Visualization and Computer Graphics*, 15(6), 2009.
- [101] M. H. Everts, H. Bekker, J. B. T. M. Roerdink, and T. Isenberg. Illustrative line styles for flow visualization. In *Proc. of the Pacific Conference on Computer Graphics and Applications*, pages 105–110, 2011.
- [102] G. Feliciani, W. V. Potters, P. van Ooij, J. J. Schneiders, A. J. Nederveen, E. van Bavel, C. B. Majoie, and H. A. Marquering. Multiscale 3D+ t intracranial aneurysmal flow vortex detection. *IEEE Transactions on Bio-Medical Engineering*, 62(5):1355–1362, 2015.
- [103] L. Ferreira and D. B. Hitchcock. A comparison of hierarchical methods for clustering functional data. *Communications in Statistics: Simulation and computation*, 38(9):1925–1949, 2009.
- [104] F. Ferstl, K. Bürger, and R. Westermann. Streamline variability plots for characterizing the uncertainty in vector field ensembles. *IEEE Transactions on Visualization and Computer Graphics*, 22(1):767–776, 2016.
- [105] R. W. Fleming and H. H. Bühlhoff. Low-level image cues in the perception of translucent materials. *ACM Transactions on Applied Perception*, 2(3):346–382, 2005.
- [106] M. S. Floater and K. Hormann. Surface parameterization: a tutorial and survey. In *Advances in Multiresolution for Geometric Modelling*, pages 157–186. Springer, 2005.
- [107] M. Ford, Y. Hoi, M. Piccinelli, L. Antiga, and D. Steinman. An objective approach to digital removal of saccular aneurysms: Technique and applications. *British Journal of Radiology*, 82(Special Issue 1):55–61, 2009.
- [108] M. D. Ford, H. N. Nikolov, J. S. Milner, S. P. Lownie, E. M. DeMont, W. Kalata, F. Loth, D. W. Holdsworth, and D. A. Steinman. PIV-measured versus CFD-predicted flow dynamics in anatomically realistic cerebral aneurysm models. *Journal of Biomechanical Engineering*, 130(2):021015, 2008.
- [109] M. D. Ford, G. R. Stuhne, H. N. Nikolov, D. F. Habets, S. P. Lownie, D. W. Holdsworth, and D. A. Steinman. Virtual angiography for visualization and validation of computational models of aneurysm hemodynamics. *IEEE Transactions on Medical Imaging*, 24(12):1586–1592, 2005.
- [110] S. Frey and T. Ertl. Progressive direct volume-to-volume transformation. *IEEE Transactions on Visualization and Computer Graphics*, 23(1):921–930, 2017.

- [111] O. Friman, A. Hennemuth, A. Harloff, J. Bock, M. Markl, and H.-O. Peitgen. Probabilistic 4D blood flow mapping. In *Proc. of International Conference on Medical Image Computing and Computer-Assisted Intervention*, pages 416–423, 2010.
- [112] J. Frösen, A. Piippo, A. Paetau, M. Kangasniemi, M. Niemelä, J. Hernesniemi, and J. Jaäskeläinen. Remodeling of saccular cerebral artery aneurysm wall is associated with rupture: histological analysis of 24 unruptured and 42 ruptured cases. *Stroke*, 35(10):2287–2293, 2004.
- [113] J. Frösen, R. Tulamo, A. Paetau, E. Laaksamo, M. Korja, A. Laakso, M. Niemelä, and J. Hernesniemi. Saccular intracranial aneurysm: Pathology and mechanisms. *Acta neuropathologica*, 123(6):773–786, 2012.
- [114] K. Futami, I. Nambu, T. Kitabayashi, H. Sano, and et al. Inflow hemodynamics evaluated by using four-dimensional flow magnetic resonance imaging and the size ratio of unruptured cerebral aneurysms. *Journal of Neuroradiology*, pages 1–8, 2017.
- [115] A. Gambaruto and A. João. Flow structures in cerebral aneurysms. *Computers & Fluids*, 65:56–65, 2012.
- [116] X. Gao, W. Jakob, M. Tarini, and D. Panozzo. Robust hex-dominant mesh generation using field-guided polyhedral agglomeration. *ACM Transactions on Graphics*, 36(4):114, 2017.
- [117] G. J. M. Garcia, N. Bailie, D. A. Martins, and J. S. Kimbell. Atrophic rhinitis: A CFD study of air conditioning in the nasal cavity. *Journal of Applied Physiology*, 103:1082–1092, 2007.
- [118] R. Gasteiger. *Visual Exploration of Cardiovascular Hemodynamics*. PhD thesis, University of Magdeburg, 2014.
- [119] R. Gasteiger, G. Janiga, D. Stucht, A. Hennemuth, O. Friman, O. Speck, M. Markl, and B. Preim. Vergleich zwischen 7 Tesla 4D PC-MRI-Flussmessung und CFD-Simulation. In *Proc. of Bildverarbeitung für die Medizin*, pages 304–308. Springer, 2011.
- [120] R. Gasteiger, D. J. Lehmann, R. van Pelt, G. Janiga, O. Beuing, A. Vilanova, H. Theisel, and B. Preim. Automatic detection and visualization of qualitative hemodynamic characteristics in cerebral aneurysms. *IEEE Transactions on Visualization and Computer Graphics*, 18(12):2178–2187, 2012.
- [121] R. Gasteiger, M. Neugebauer, O. Beuing, and B. Preim. The FLOWLENS: A focus-and-context visualization approach for exploration of blood flow in cerebral aneurysms. *IEEE Transactions on Visualization and Computer Graphics*, 17(12):2183–2192, 2011.
- [122] R. Gasteiger, M. Neugebauer, C. Kubisch, and B. Preim. Adapted surface visualization of cerebral aneurysms with embedded blood flow information. In *Proc. of Eurographics Workshop on Visual Computing for Biology and Medicine*, pages 25–32, 2010.
- [123] P. L. George. *Automatic mesh generation: Applications to finite element methods*. John Wiley & Sons, Inc., 1991.
- [124] W. Gerbino, C. I. Stultiens, J. M. Troost, and C. M. de Weert. Transparent layer constancy. *Journal of Experimental Psychology: Human Perception and Performance*, 16(1):3, 1990.
- [125] F. J. Gijssen, F. N. van de Vosse, and J. Janssen. The influence of the non-Newtonian properties of blood on the flow in large arteries: Steady flow in a carotid bifurcation model. *Journal of Biomechanics*, 32(6):601–608, 1999.
- [126] D. Girardi, J. Küng, R. Kleiser, M. Sonnberger, D. Csillag, J. Trenkler, and A. Holzinger. Interactive knowledge discovery with the doctor-in-the-loop: A practical example of cerebral aneurysms research. *Brain Informatics*, 3(3):133, 2016.

- [127] S. Glaßer, P. Berg, S. Voß, S. Serowy, G. Janiga, B. Preim, and O. Beuing. From imaging to hemodynamics - how reconstruction kernels influence the blood flow predictions in intracranial aneurysms. *Current Directions in Biomedical Engineering*, 2(1):679–683, 2016.
- [128] S. Glaßer, P. Berg, M. Neugebauer, and B. Preim. Reconstruction of 3D surface meshes for blood flow simulations of intracranial aneurysms. In *Proc. of Deutschen Gesellschaft für Computer- und Roboterassistierte Chirurgie*, pages 163–168, 2015.
- [129] S. Glaßer, J. Hirsch, P. Berg, P. Saalfeld, O. Beuing, G. Janiga, and B. Preim. Evaluation of time-dependent wall shear stress visualizations for cerebral aneurysms. In *Proc. of Bildverarbeitung für die Medizin*, pages 236–241, 2016.
- [130] S. Glaßer, T. Hoffmann, A. Boese, S. Voß, T. Kalinski, M. Skalej, and B. Preim. Virtual inflation of the cerebral artery wall for the integrated exploration of OCT and histology data. *Computer Graphics Forum*, 36(8):57–68, 2017.
- [131] S. Glaßer, T. Hoffmann, S. Voß, F. Klink, and B. Preim. Extraction of patient-specific 3D cerebral artery and wall thickness models from 2D OCT and structured-light 3D scanner data. In *CURAC*, pages 197–202, 2016.
- [132] S. Glaßer, K. Lawonn, T. Hoffmann, M. Skalej, and B. Preim. Combined visualization of wall thickness and wall shear stress for the evaluation of aneurysms. *IEEE Transactions on Visualization and Computer Graphics*, pages 2506–2515, 2014.
- [133] M. Gleicher, D. Albers, R. Walker, I. Jusufi, C. D. Hansen, and J. C. Roberts. Visual comparison for information visualization. *Information Visualization*, 10(4):289–309, 2011.
- [134] M. Gmeiner, J. Dirnberger, W. Fenz, M. Gollwitzer, G. Wurm, J. Trenkler, and A. Gruber. Virtual cerebral aneurysm clipping with real-time haptic force feedback in neurosurgical education. *World neurosurgery*, 112:e313–e323, 2018.
- [135] L. Goubergrits, J. Schaller, U. Kertzscher, N. van den Bruck, K. Poethkow, C. Petz, H. C. Hege, and A. Spuler. Statistical wall shear stress maps of ruptured and unruptured middle cerebral artery aneurysms. *Journal of the Royal Society Interface*, 9(69):677–688, 2012.
- [136] L. Goubergrits, B. Thamsen, A. Berthe, J. Poethke, U. Kertzscher, K. Affeld, C. Petz, H.-C. Hege, H. Hoch, and A. Spuler. In vitro study of near-wall flow in a cerebral aneurysm model with and without coils. *American Journal of Neuroradiology*, 31(8):1521–1528, 2010.
- [137] M. R. Goyal. *Biofluid Dynamics of Human Body Systems*. Taylor Francis, 2013.
- [138] N. E. Green, S.-Y. J. Chen, J. C. Messenger, B. M. Groves, and J. D. Carroll. Three-dimensional vascular angiography. *Current Problems in Cardiology*, 29(3):104–142, 2004.
- [139] D. L. Gresh, B. E. Rogowitz, R. L. Winslow, D. F. Scollan, and C. K. Yung. WEAVE: a system for visually linking 3D and statistical visualizations applied to cardiac simulation and measurement data. In *Proc. of IEEE Visualization Conference*, pages 489–492, 2000.
- [140] H. Grotjans and F. R. Menter. Wall functions for industrial applications. *Computational Fluid Dynamics*, 1(2):1112–1117, 1998.
- [141] T. Günther, C. Rössl, and H. Theisel. Opacity optimization for 3D line fields. *ACM Transactions on Graphics*, 32(4):120, 2013.
- [142] K. C. Gurijala, R. Shi, W. Zeng, X. Gu, and A. Kaufman. Colon flattening using heat diffusion Riemannian metric. *IEEE Transactions on Visualization and Computer Graphics*, 19(12):2848–2857, 2013.

- [143] G. Hademenos, T. Massoud, F. Turjman, and J. Sayre. Anatomical and morphological factors correlating with rupture of intracranial aneurysms in patients referred for endovascular treatment. *Neuroradiology*, 40(11):755–760, 1998.
- [144] S. Haker, S. Angenent, A. Tannenbaur, and R. Kikinis. Nondistorting flattening maps and the 3D visualization of colon CT images. *IEEE Transactions on Visualization and Computer Graphics*, 19(7):665–670, 2000.
- [145] T. Hashimoto, H. Meng, and W. L. Young. Intracranial aneurysms: Links among inflammation, hemodynamics and vascular remodeling. *Neurological Research*, 28(4):372–380, 2006.
- [146] S. Hassan, F. Hétry, F. Faure, and O. Palombi. Automatic localization and quantification of intracranial aneurysms. In *Proc. of Computer Analysis of Images and Patterns*, pages 554–562, 2011.
- [147] P. Hastreiter, C. Rezk-Salama, B. Tomandl, K. Eberhardt, and T. Ertl. Fast analysis of intracranial aneurysms based on interactive direct volume rendering and CTA. In *Proc. of International Conference on Medical Image Computing and Computer-Assisted Intervention*, pages 660–669. Springer, 1998.
- [148] H. Hauser, R. S. Laramée, and H. Doleisch. State-of-the-art report 2002 in flow visualization, 2002.
- [149] J. Heer and B. Shneiderman. Interactive dynamics for visual analysis. *Queue*, 10(2):30, 2012.
- [150] E. Heiberg, T. Ebbens, L. Wigström, and M. Karlsson. Three-dimensional flow characterization using vector pattern matching. *IEEE Transactions on Visualization and Computer Graphics*, 9(3):313–319, 2003.
- [151] A. Hennemuth, O. Friman, C. Schumann, J. Bock, J. Drexler, M. Markl, and H.-O. Peitgen. Fast interactive exploration of 4D MRI flow data. In *Proc. of SPIE Medical Imaging*, volume 7964, page 79640E, 2011.
- [152] C. M. Hentschke. *Computer-aided Detection of Cerebral Aneurysms in Angiographies*. PhD thesis, Otto-von-Guericke University, Magdeburg, Germany, 2013.
- [153] C. M. Hentschke, O. Beuing, H. Paukisch, C. Scherlach, M. Skalej, and K. D. Tönnies. A system to detect cerebral aneurysms in multimodality angiographic data sets. *Medical Physics*, 41(9), 2014.
- [154] C. M. Hentschke, K. D. Tönnies, O. Beuing, and R. Nickl. A new feature for automatic aneurysm detection. In *Proc. of IEEE International Symposium on Biomedical Imaging*, pages 800–803, 2012.
- [155] F. V. Higuera, N. Sauber, B. Tomandl, C. Nimsy, G. Greiner, and P. Hastreiter. Enhanced 3D-visualization of intracranial aneurysms involving the skull base. In *Proc. of International Conference on Medical Image Computing and Computer-Assisted Intervention*, pages 256–263. Springer, 2003.
- [156] F. V. Higuera, N. Sauber, B. Tomandl, C. Nimsy, G. Greiner, and P. Hastreiter. Automatic adjustment of bidimensional transfer functions for direct volume visualization of intracranial aneurysms. In *Proc. of SPIE Medical Imaging*, pages 275–284, 2004.
- [157] M. Hlawitschka, S. Eichelbaum, and G. Scheuermann. Fast and memory efficient GPU-based rendering of tensor data. *Computer Graphics and Visualization*, 2008:28–30, 2008.
- [158] T. Hoffmann, S. Glaßer, A. Boese, K. Brandstädter, T. Kalinski, O. Beuing, and M. Skalej. Experimental investigation of intravascular OCT for imaging of intracranial aneurysms. *International Journal of Computer Assisted Radiology and Surgery*, 11(2):231–241, 2016.



- [159] B. L. Hoh, C. L. Siström, C. S. Firment, G. L. Fautheree, G. J. Velat, J. H. Whiting, J. F. Reavey-Cantwell, and S. B. Lewis. Bottleneck factor and height-width ratio: Association with ruptured aneurysms in patients with multiple cerebral aneurysms. *Journal of Neurosurgery*, 61(4):716–723, 2007.
- [160] T. Ingall, K. Asplund, M. Mähönen, and R. Bonita. A multinational comparison of subarachnoid hemorrhage epidemiology in the WHO MONICA stroke study. *Stroke*, 31(5):1054–1061, 2000.
- [161] V. Interrante and C. Grosch. Strategies for effectively visualizing 3D flow with volume LIC. In *Proc. of IEEE Visualization Conference*, pages 421–424, 1997.
- [162] H. Isoda, Y. Ohkura, T. Kosugi, M. Hirano, M. T. Alley, R. Bammer, N. J. Pelc, H. Namba, and H. Sakahara. Comparison of hemodynamics of intracranial aneurysms between MR fluid dynamics using 3D cine phase-contrast MRI and MR-based computational fluid dynamics. *Neuroradiology*, 52(10):913–920, 2010.
- [163] G. Janiga, P. Berg, O. Beuing, M. Neugebauer, R. Gasteiger, B. Preim, G. Rose, M. Skalej, and D. Thévenin. Recommendations for accurate numerical blood flow simulations of stented intracranial aneurysms. *Biomedical Engineering*, 58(3):303–314, 2013.
- [164] G. Janiga, P. Berg, S. Sugiyama, K. Kono, and D. Steinman. The computational fluid dynamics rupture challenge 2013—phase I: Prediction of rupture status in intracranial aneurysms. *American Journal of Neuroradiology*, 2015.
- [165] G. Janiga, L. Daróczy, P. Berg, D. Thévenin, M. Skalej, and O. Beuing. An automatic CFD-based flow diverter optimization principle for patient-specific intracranial aneurysms. *Journal of Biomechanics*, 48(14):3846–3852, 2015.
- [166] G. Janiga, C. Rössl, M. Skalej, and D. Thévenin. Realistic virtual intracranial stenting and computational fluid dynamics for treatment analysis. *Journal of Biomechanics*, 46(1):7–12, 2013.
- [167] J. Jankowai, R. Englund, T. Ropinski, and I. Hotz. Interactive 4D MRI blood flow exploration and analysis using line predicates. In *Proc. of SIGRAD*, volume 127, pages 35–42, 2016.
- [168] T. Jankun-Kelly, Y. Lanka, and J. Swan. An evaluation of glyph perception for real symmetric traceless tensor properties. *Computer Graphics Forum*, 29(3):1133–1142, 2010.
- [169] T. Jerman, F. Pernuš, B. Likar, and Ž. Špiclin. Computer-aided detection and quantification of intracranial aneurysms. In *Proc. of International Conference on Medical Image Computing and Computer-Assisted Intervention*, pages 3–10. Springer, 2015.
- [170] A. Joshi, X. Qian, D. P. Dione, K. R. Bulsara, C. K. Breuer, A. J. Sinusas, and X. Papademetris. Effective visualization of complex vascular structures using a non-parametric vessel detection method. *IEEE Transactions on Visualization and Computer Graphics*, 14(6):1603–1610, 2008.
- [171] L. Jr, E. Kruijff, R. McMahan, D. Bowman, and I. P. Poupyrev. *3D User Interfaces, Theory and Practice*. Addison-Wesley, 2nd edition edition, 2017.
- [172] S. Juvela. Prevalence of and risk factors for intracranial aneurysms. *The Lancet Neurology*, 10(7):595–597, 2011.
- [173] S. Juvela, M. Porras, and O. Heiskanen. Natural history of unruptured intracranial aneurysms: A long-term follow-up study. *Journal of Neurosurgery*, 79(2):174–182, 1993.
- [174] L. M. Kadasi, W. C. Dent, and A. M. Malek. Cerebral aneurysm wall thickness analysis using intraoperative microscopy: Effect of size and gender on thin translucent regions. *Journal of Neurointerventional Surgery*, 5(3):201–206, 2013.

- [175] M. Kanzler, F. Ferstl, and R. Westermann. Line density control in screen-space via balanced line hierarchies. *Computers and Graphics*, 61:29–39, 2016.
- [176] M. Kanzler and R. Westermann. Interactive visual exploration of line clusters. *Proc. of Vision, Modelling und Visualization*, 2018.
- [177] S. Karim, C. Fegeler, D. Boeckler, L. H. Schwartz, H.-U. Kauczor, and H. von Tengg-Kobligh. Development, implementation, and evaluation of a structured reporting web tool for abdominal aortic aneurysms. *Journal of Medical Internet Research, Research Protocols*, 2(2), 2013.
- [178] C. Karmonik, A. Arat, G. Benndorf, S. Akpek, R. Klucznik, M. E. Mawad, and C. M. Strother. A technique for improved quantitative characterization of intracranial aneurysms. *American Journal of Neuroradiology*, 25(7):1158–1161, 2004.
- [179] J. Kasten, J. Reininghaus, I. Hotz, H.-C. Hege, B. R. Noack, G. Daviller, and M. Morzynski. Acceleration feature points of unsteady shear flows. *arXiv preprint arXiv:1401.2462*, 2014.
- [180] J. Kehrler, P. Muigg, H. Doleisch, and H. Hauser. Interactive visual analysis of heterogeneous scientific data across an interface. *IEEE Transactions on Visualization and Computer Graphics*, 17(7):934–946, 2011.
- [181] M. Kersten-Oertel, S. J.-S. Chen, and D. L. Collins. An evaluation of depth enhancing perceptual cues for vascular volume visualization in neurosurgery. *IEEE Transactions on Visualization and Computer Graphics*, 20(3):391–403, 2014.
- [182] R. K. Khanna, G. M. Malik, and N. Qureshi. Predicting outcome following surgical treatment of unruptured intracranial aneurysms: A proposed grading system. *Journal of Neurosurgery*, 84(1):49–54, 1996.
- [183] J. Kiefer. Sequential minimax search for a maximum. In *Proc. of the American Mathematical Society*, volume 4, pages 502–506, 1953.
- [184] M. Kim, D. B. Taulbee, M. Tremmel, and H. Meng. Comparison of two stents in modifying cerebral aneurysm hemodynamics. *Annals of Biomedical Engineering*, 36(5):726–741, 2008.
- [185] G. Kindlmann. Superquadric tensor glyphs. In *Proc. of the Joint Eurographics-IEEE TCVG Conference on Visualization*, pages 147–154, 2004.
- [186] R. Kleinloog, N. de Mul, B. H. Verweij, J. A. Post, G. J. Rinkel, and Y. M. Ruigrok. Risk factors for intracranial aneurysm rupture: A systematic review. *Neurosurgery*, 82(4):431–440, 2017.
- [187] C. Kleinstreuer. *Biofluid dynamics: Principles and selected applications*. CRC Press, 2006.
- [188] B. Köhler, S. Born, R. F. P. V. Pelt, A. Hennemuth, U. Preim, and B. Preim. A survey of cardiac 4D PC-MRI data processing. *Computer Graphics Forum*, 36(6):5–35, 2017.
- [189] B. Köhler, R. Gasteiger, U. Preim, H. Theisel, M. Gutberlet, and B. Preim. Semi-automatic vortex extraction in 4D PC-MRI cardiac blood flow data using line predicates. *IEEE Transactions on Visualization and Computer Graphics*, 19(12):2773–2782, 2013.
- [190] B. Köhler, M. Grothoff, M. Gutberlet, and B. Preim. Visualization of cardiac blood flow using anisotropic ambient occlusion for lines. In *Proc. of Vision, Modelling und Visualization*, 2017.
- [191] B. Köhler, M. Grothoff, M. Gutberlet, and B. Preim. Pressure-based vortex extraction in cardiac 4D PC-MRI blood flow data. In *Proc. of EuroVis - Short Papers*, 2018.
- [192] B. Köhler, M. Grothoff, M. Gutberlet, and B. Preim. Visual and quantitative analysis of great arteries’ blood flow jets in cardiac 4D PC-MRI data. *Computer Graphics Forum*, 37(3):195–204, 2018.

- [193] B. Köhler, U. Preim, M. Grothoff, M. Gutberlet, K. Fischbach, and B. Preim. Robust cardiac function assessment in 4D PC-MRI data of the aorta and pulmonary artery. *Computer Graphics Forum*, 35(1):32–43, 2016.
- [194] B. Köhler, U. Preim, M. Grothoff, M. Gutberlet, and B. Preim. Adaptive animations of vortex flow extracted from cardiac 4D PC-MRI data. In *Proc. of Bildverarbeitung für die Medizin*, pages 194–199, 2016.
- [195] I. Kolesár, S. Bruckner, I. Viola, and H. Hauser. A fractional cartesian composition model for semi-spatial comparative visualization design. *IEEE Transactions on Visualization and Computer Graphics*, 2017.
- [196] C. Kouskouras, A. Charitanti, C. Giavroglou, N. Foroglou, P. Selviaridis, V. Kontopoulos, and A. S. Dimitriadis. Intracranial aneurysms: evaluation using CTA and MRA. Correlation with DSA and intraoperative findings. *Neuroradiology*, 46(10):842–850, 2004.
- [197] D. Krex, H. Schackert, and G. Schackert. Genesis of cerebral aneurysms—an update. *Acta neurochirurgica*, 143(5):429–449, 2001.
- [198] H. Krishnan, C. Garth, J. Guhring, M. A. Gulsun, A. Greiser, and K. I. Joy. Analysis of time-dependent flow-sensitive PC-MRI data. *IEEE Transactions on Visualization and Computer Graphics*, 18(6):966–977, 2012.
- [199] A. Kuhn, D. J. Lehmann, R. Gasteiger, M. Neugebauer, B. Preim, and H. Theisel. A clustering-based visualization technique to emphasize meaningful regions of vector fields. In *Proc. of Vision, Modelling und Visualization*, pages 191–198, 2011.
- [200] O. Kwon, J. Lee, B. Kim, J. Shin, and Y.-G. Shin. Efficient blood flow visualization using flowline extraction and opacity modulation based on vascular structure analysis. *Computers in Biology and Medicine*, 82:87–99, 2017.
- [201] D. H. Laidlaw, J. S. Davidson, T. S. Miller, M. da Silva, R. Kirby, W. H. Warren, and M. Tarr. Quantitative comparative evaluation of 2D vector field visualization methods. In *Proc. of IEEE Visualization Conference*, pages 143–150, 2001.
- [202] R. Lall, C. Eddleman, B. Bendok, and H. Batjer. Unruptured intracranial aneurysms and the assessment of rupture risk based on anatomical and morphological factors: Sifting through the sands of data. *Neurosurgical Focus*, 26(5):E2, 2009.
- [203] H. Lamecker, T. Mansi, J. Relan, F. Billet, M. Sermesant, N. Ayache, and H. Delingette. Adaptive tetrahedral meshing for personalized cardiac simulations. In *MICCAI Workshop on Cardiovascular Interventional Imaging and Biophysical Modelling*, pages 149–158, 2009.
- [204] J.-W. Lankhaar, M. B. Hofman, J. T. Marcus, J. J. Zwanenburg, T. J. Faes, and A. Vonk-Noordegraaf. Correction of phase offset errors in main pulmonary artery flow quantification. *Journal of Magnetic Resonance Imaging*, 22(1):73–79, 2005.
- [205] J. Lantz. *On Aortic Blood Flow Simulations - Scale-Resolved Image-based CFD*. PhD thesis, Linköping University, 2013.
- [206] J. Lantz and M. Karlsson. Large eddy simulation of LDL surface concentration in a subject specific human aorta. *Journal of Biomechanics*, 45(3):537–542, 2012.
- [207] R. S. Laramée, H. Hauser, H. Doleisch, B. Vrolijk, F. H. Post, and D. Weiskopf. The state of the art in flow visualization: Dense and texture-based techniques. *Computer Graphics Forum*, 23(2):203–221, 2004.
- [208] R. S. Laramée, H. Hauser, L. Zhao, and F. H. Post. Topology-based flow visualization, the state of the art. In *Topology-based methods in visualization*, pages 1–19. Springer, 2007.

- [209] I. Larrabide, M. Kim, L. Augsburger, M. C. Villa-Uriol, D. Rüfenacht, and A. F. Frangi. Fast virtual deployment of self-expandable stents: Method and in vitro evaluation for intracranial aneurysmal stenting. *Medical Image Analysis*, 16(3):721–730, 2012.
- [210] I. Larrabide, M. C. Villa-Uriol, R. Cárdenes, J. M. Pozo, J. Macho, L. S. Roman, and et al. Three-dimensional morphological analysis of intracranial aneurysms: A fully automated method for aneurysm sac isolation and quantification. *Medical Physics*, 38(5):2439–2449, 2011.
- [211] A. Lauric, M. I. Baharoglu, and A. M. Malek. Ruptured status discrimination performance of aspect ratio, height/width, and bottleneck factor is highly dependent on aneurysm sizing methodology. *Neurosurgery*, 71(1):38–46, 2012.
- [212] A. Lauric, E. Miller, S. Frisken, and A. M. Malek. Automated detection of intracranial aneurysms based on parent vessel 3D analysis. *Medical Image Analysis*, 14(2):149–159, 2010.
- [213] K. Lawonn, R. Gasteiger, and B. Preim. Adaptive surface visualization of vessels with embedded blood flow based on the suggestive contour measure. In *Proc. of Vision, Modelling und Visualization*, pages 113–120, 2013.
- [214] K. Lawonn, R. Gasteiger, and B. Preim. Qualitative evaluation of feature lines on anatomical surfaces. In *Proc. of Bildverarbeitung für die Medizin*, pages 187–192, 2013.
- [215] K. Lawonn, R. Gasteiger, and B. Preim. Adaptive surface visualization of vessels with animated blood flow. *Computer Graphics Forum*, 33(8):16–27, 2014.
- [216] K. Lawonn, S. Glaßer, A. Vilanova, B. Preim, and T. Isenberg. Occlusion-free blood flow animation with wall thickness visualization. *IEEE Transactions on Visualization and Computer Graphics*, 22(1):728–737, 2015.
- [217] K. Lawonn, T. Günther, and B. Preim. Coherent view-dependent streamlines for understanding blood flow. In *Proc. of EuroVis - Short Papers*, 2014.
- [218] K. Lawonn, M. Luz, B. Preim, and C. Hansen. Illustrative visualization of vascular models for static 2D representations. In *Proc. of International Conference on Medical Image Computing and Computer-Assisted Intervention*, pages 399–406, 2015.
- [219] K. Lawonn, T. Mönch, and B. Preim. Streamlines for illustrative real-time rendering. *Computer Graphics Forum*, 33(3):321–330, 2013.
- [220] M. Le Muzic, J. Parulek, A.-K. Stavrum, and I. Viola. Illustrative visualization of molecular reactions using omniscient intelligence and passive agents. *Computer Graphics Forum*, 33(3):141–150, 2014.
- [221] T.-Y. Lee, O. Mishchenko, H.-W. Shen, and R. Crawfis. View point evaluation and streamline filtering for flow visualization. In *Proc. of IEEE Pacific Visualization Symposium*, pages 83–90, 2011.
- [222] D. Lesage, E. D. Angelini, I. Bloch, and G. Funka-Lea. A review of 3D vessel lumen segmentation techniques: Models, features and extraction schemes. *Medical Image Analysis*, 13(6):819–845, 2009.
- [223] B. Lévy, S. Petitjean, N. Ray, and J. Maillot. Least squares conformal maps for automatic texture atlas generation. *ACM Transactions on Graphics*, 21(3):362–371, 2002.
- [224] M.-H. Li, B.-L. Gao, C. Fang, Y.-S. Cheng, Y.-D. Li, J. Wang, and G.-P. Xu. Prevention and management of intraprocedural rupture of intracranial aneurysm with detachable coils during embolization. *Neuroradiology*, 48(12):907–915, 2006.
- [225] V. D. Liseikin. *Grid generation methods*. Springer, 2017.

- [226] R. Liu, H. Guo, J. Zhang, and X. Yuan. Comparative visualization of vector field ensembles based on longest common subsequence. In *Proc. of IEEE Pacific Visualization Symposium*, pages 96–103, 2016.
- [227] S. Lo. Automatic mesh generation over intersecting surfaces. *International Journal for Numerical Methods in Engineering*, 38(6):943–954, 1995.
- [228] W. Longstreth, L. M. Nelson, T. D. Koepsell, and G. Van Belle. Clinical course of spontaneous subarachnoid hemorrhage: A population-based study in King County, Washington. *Neurology*, 43(4):712–712, 1993.
- [229] W. E. Lorensen and H. E. Cline. Marching cubes: A high resolution 3D surface construction algorithm. In *Proc. of the Conference on Computer Graphics and Interactive Techniques*, volume 21, pages 163–169, 1987.
- [230] C. Lundstrom, T. Rydell, C. Forsell, A. Persson, and A. Ynnerman. Multi-touch table system for medical visualization: Application to orthopedic surgery planning. *IEEE Transactions on Visualization and Computer Graphics*, 17(12):1775–1784, 2011.
- [231] B. Ma, R. E. Harbaugh, and M. L. Raghavan. Three-dimensional geometrical characterization of cerebral aneurysms. *Annals of Biomedical Engineering*, 32(2):264–273, 2004.
- [232] D. Ma, G. F. Dargush, S. K. Natarajan, E. I. Levy, A. H. Siddiqui, and H. Meng. Computer modeling of deployment and mechanical expansion of neurovascular flow diverter in patient-specific intracranial aneurysms. *Journal of Biomechanics*, 45(13):2256–2263, 2012.
- [233] D. Ma, T. M. Dumont, H. Kosukegawa, M. Ohta, X. Yang, A. H. Siddiqui, and H. Meng. High fidelity virtual stenting (HiFiVS) for intracranial aneurysm flow diversion: In vitro and in silico. *Annals of Biomedical Engineering*, 41(10):2143–2156, 2013.
- [234] J. Ma, J. W. Walker, C. Wang, S. A. Kuhl, and C. Shene. Flowtour: An automatic guide for exploring internal flow features. In *Proc. of IEEE Pacific Visualization Symposium*, pages 25–32, 2014.
- [235] D. J. MacDonald, H. M. Finlay, and P. B. Canham. Directional wall strength in saccular brain aneurysms from polarized light microscopy. *Annals of Biomedical Engineering*, 28(5):533–542, 2000.
- [236] R. MacNeal. *The Solution of Partial Differential Equations by Means of Electrical Networks*. California I. of Technology, 1949.
- [237] A. R. Mantha, G. Benndorf, A. Hernandez, and R. W. Metcalfe. Stability of pulsatile blood flow at the ostium of cerebral aneurysms. *Journal of Biomechanics*, 42(8):1081–1087, 2009.
- [238] Marcelo Castro and Christopher Putman and Alessandro Radaelli and Alejandro Frangi and Juan Cebal. Hemodynamics and rupture of terminal cerebral aneurysms. *Academic Radiology*, 16(10):1201–1207, 2009.
- [239] Mark Harrower and The Pennsylvania State University. ColorBrewer. Website, 2014. Called Mar 30, 2017 from:<http://colorbrewer2.org>.
- [240] M. Markl, S. Bredecke, J. Simon, A. Frydrychowicz, and A. Harloff. Coregistration of wall shear stress and plaque distribution within the thoracic aorta of acute stroke patients. In *Proc. of the International Society for Magnetic Resonance in Medicine*, volume 18, page 63, 2010.
- [241] M. Markl, A. Frydrychowicz, S. Kozerke, M. Hope, and O. Wieben. 4D flow MRI. *Journal of Magnetic Resonance Imaging*, 36(5):1015–1036, 2012.
- [242] S. Martinez-Muñoz, D. Ruiz-Fernandez, and J. J. Galiana-Merino. Automatic abdominal aortic aneurysm segmentation in MR images. *Expert Systems with Applications*, 54:78–87, 2016.

- [243] M. S. Mathews, J. Su, E. Heidari, E. I. Levy, M. E. Linskey, and Z. Chen. Neuroendovascular optical coherence tomography imaging and histological analysis. *Neurosurgery*, 69(2):430–439, 2011.
- [244] A. McKinney, C. Palmer, C. Truwit, A. Karagulle, and M. Teksam. Detection of aneurysms by 64-section multidetector CT angiography in patients acutely suspected of having an intracranial aneurysm and comparison with digital subtraction and 3D rotational angiography. *American Journal of Neuroradiology*, 29(3):594–602, 2008.
- [245] T. McLoughlin, M. W. Jones, R. S. Laramée, R. Malki, I. Masters, and C. D. Hansen. Similarity measures for enhancing interactive streamline seeding. *IEEE Transactions on Visualization and Computer Graphics*, 19(8):1342–1353, 2013.
- [246] T. McLoughlin, R. S. Laramée, R. Peikert, F. H. Post, and M. Chen. Over two decades of integration-based, geometric flow visualization. *Computer Graphics Forum*, 29(6):1807–1829, 2010.
- [247] M. Mehra, G. Spilberg, M. J. Gounis, and A. K. Wakhloo. Intracranial aneurysms: Clinical assessment and treatment options. In *Biomechanics and Mechanobiology of Aneurysms*, pages 331–372. Springer, 2011.
- [248] S. Mendis, P. Puska, and B. Norrving. *Global atlas on cardiovascular disease prevention and control*. World Health Organization in collaboration with the World Heart Federation and the World Stroke Organization Geneva, 2011.
- [249] H. Meng, V. Tutino, J. Xiang, and A. Siddiqui. High WSS or low WSS? complex interactions of hemodynamics with intracranial aneurysm initiation, growth, and rupture: Toward a unifying hypothesis. *American Journal of Neuroradiology*, 35(7):1254–1262, 2014.
- [250] F. R. Menter. Two-equation eddy-viscosity turbulence models for engineering applications. *Journal of American Institute of Aeronautics and Astronautics*, 32(8):269–289, 1994.
- [251] F. Metelli, O. Da Pos, and A. Cavedon. Balanced and unbalanced, complete and partial transparency. *Perception & Psychophysics*, 38(4):354–366, 1985.
- [252] P. B. Metzger, E. R. Novero, F. H. Rossi, S. M. Moreira, H. A. Barbato, N. M. Izukawa, V. L. A. d. Marco, M. N. Cano, and A. M. Kambara. Endovascular treatment of abdominal aortic aneurysms with complex anatomy: preliminary results of the second generation stent graft with a dual-ring design. *Revista Brasileira de Cardiologia Invasiva*, 20(1):69–76, 2012.
- [253] J. Meyer-Spradow, L. Stegger, C. Döring, T. Ropinski, and K. Hinrichs. Glyph-based SPECT visualization for the diagnosis of coronary artery disease. *IEEE Transactions on Visualization and Computer Graphics*, 14(6):1499–1506, 2008.
- [254] A. P. Mitsos, N. M. Kakalis, Y. P. Ventikos, and J. V. Byrne. Haemodynamic simulation of aneurysm coiling in an anatomically accurate computational fluid dynamics model. *Neuroradiology*, 50(4):341–347, 2008.
- [255] A. Mohamed, E. Sgouritsa, H. Morsi, H. Shaltoni, M. E. Mawad, and I. A. Kakadiaris. Computer-aided planning for endovascular treatment of intracranial aneurysms (CAPETA). In *Proc. of SPIE Medical Imaging*, volume 7625, 2010.
- [256] A. Molyneux, R. Kerr, I. S. A. T. I. C. Group, et al. International Subarachnoid Aneurysm Trial (ISAT) of neurosurgical clipping versus endovascular coiling in 2143 patients with ruptured intracranial aneurysms: A randomized trial. *Journal of Stroke and Cerebrovascular Diseases*, 11(6):304–314, 2002.
- [257] T. Mönch, M. Neugebauer, and B. Preim. Optimization of vascular surface models for computational fluid dynamics and rapid prototyping. In *Proc. of International Workshop on Digital Engineering*, pages 16–23, 2011.

- [258] S. J. Monteith, A. Tsimpas, A. S. Dumont, S. Tjoumakaris, L. F. Gonzalez, R. H. Rosenwasser, and P. Jabbour. Endovascular treatment of fusiform cerebral aneurysms with the Pipeline Embolization Device. *Journal of Neurosurgery*, 120(4):945–954, 2014.
- [259] H. G. Morales, I. Larrabide, A. J. Geers, L. San Roman, J. Blasco, J. M. Macho, and A. F. Frangi. A virtual coiling technique for image-based aneurysm models by dynamic path planning. *IEEE Transactions on Bio-Medical Engineering*, 32(1):119–129, 2013.
- [260] K. Mühler, M. Neugebauer, C. Tietjen, and B. Preim. Viewpoint selection for intervention planning. In *Proc. of the Joint Eurographics / IEEE VGTC conference on Visualization*, pages 267–274, 2007.
- [261] P. Mullen, Y. Tong, P. Alliez, and M. Desbrun. Spectral conformal parameterization. In *Proc. of the Symposium on Geometry Processing*, pages 1487–1494, 2008.
- [262] W. Müller and H. Schumann. Visualization for modeling and simulation: visualization methods for time-dependent data - an overview. In *Proceedings of the Simulation Conference*, pages 737–745, 2003.
- [263] C. E. Munding, E. Chérin, I. Jourard, J. J. Weyers, D. E. Goertz, B. K. Courtney, and F. S. Foster. Development of a 3 French Dual-Frequency intravascular ultrasound catheter. *Ultrasound in Medicine & Biology*, 44(1):251–266, 2018.
- [264] F. Mut and J. Cebal. Effects of flow-diverting device oversizing on hemodynamics alteration in cerebral aneurysms. *American Journal of Neuroradiology*, 2012.
- [265] K. Nael, J. Villablanca, R. Saleh, W. Pope, A. Nael, G. Laub, and J. Finn. Contrast-enhanced MR angiography at 3T in the evaluation of intracranial aneurysms: A comparison with time-of-flight MR angiography. *American Journal of Neuroradiology*, 27(10):2118–2121, 2006.
- [266] H. Nakatomi, H. Segawa, A. Kurata, Y. Shiokawa, K. Nagata, H. Kamiyama, K. Ueki, and T. Kirino. Clinicopathological study of intracranial fusiform and dolichoectatic aneurysms: Insight on the mechanism of growth. *Stroke*, 31(4):896–900, 2000.
- [267] T. Nakayama, S.-i. Sugiyama, and M. Ohta. Classification of blood flow in cerebral aneurysm considering the parent artery curves. In *Proc. of International Mechanical Engineering Congress and Exposition*, pages V03AT03A033–V03AT03A033, 2013.
- [268] M. Neugebauer. *Computergestützte Exploration von Blutfluss in zerebralen Aneurysmen - geometrische Verarbeitung und interaktive Visualisierung*. PhD thesis, Department of Simulation and Graphics, University of Magdeburg, Germany, 2014.
- [269] M. Neugebauer, V. Diehl, M. Skalej, and B. Preim. Geometric reconstruction of the ostium of cerebral aneurysms. In *Proc. of Vision, Modelling and Visualization*, pages 307–314, 2010.
- [270] M. Neugebauer, R. Gasteiger, O. Beuing, V. Diehl, M. Skalej, and B. Preim. Map displays for the analysis of scalar data on cerebral aneurysm surfaces. *Computer Graphics Forum*, 28(3):895–902, 2009.
- [271] M. Neugebauer, R. Gasteiger, V. Diehl, O. Beuing, and B. Preim. Automatic generation of context visualizations for cerebral aneurysms from MRA datasets. *International Journal of Computer Assisted Radiology and Surgery*, 4(Supplement 1):112–113, 2009.
- [272] M. Neugebauer, M. Glöckler, L. Goubergrits, M. Kelm, T. Kuehne, and A. Hennemuth. Interactive virtual stent planning for the treatment of coarctation of the aorta. *International Journal of Computer Assisted Radiology and Surgery*, 11(1):133–144, 2016.
- [273] M. Neugebauer, G. Janiga, O. Beuing, M. Skalej, and B. Preim. Anatomy-guided multi-level exploration of blood flow in cerebral aneurysms. *Computer Graphics Forum*, 30(3):1041–1050, 2011.



- [274] M. Neugebauer, K. Lawonn, O. Beuing, P. Berg, G. Janiga, and B. Preim. AmniVis - a system for qualitative exploration of near-wall hemodynamics in cerebral aneurysms. *Computer Graphics Forum*, 33(3):251–260, 2013.
- [275] M. Neugebauer, K. Lawonn, O. Beuing, and B. Preim. Automatic generation of anatomic characteristics from cerebral aneurysm surface models. *International Journal of Computer Assisted Radiology and Surgery*, 8:279–289, 2013.
- [276] M. Neugebauer and B. Preim. Generation of a smooth ostium surface for aneurysm surface models. In *Proc. of Bildverarbeitung für die Medizin*, pages 399–403, 2011.
- [277] U. Niemann, P. Berg, A. Niemann, O. Beuing, B. Preim, M. Spiliopoulou, and S. Saalfeld. Rupture status classification of intracranial aneurysms using morphological parameters. In *Proc. of the IEEE International Symposium on Computer-Based Medical Systems*, pages 48–53, 2018.
- [278] D. J. Nieuwkamp, L. E. Setz, A. Algra, F. H. Linn, N. K. de Rooij, and G. J. Rinkel. Changes in case fatality of aneurysmal subarachnoid haemorrhage over time, according to age, sex, and region: A meta-analysis. *The Lancet Neurology*, 8(7):635–642, 2009.
- [279] J. Novitzke. The basics of brain aneurysms: A guide for patients. *Journal of Vascular and Interventional Neurology*, 1(3):89, 2008.
- [280] L. J. O'Donnell, C.-F. Westin, and A. J. Golby. Tract-based morphometry for white matter group analysis. *Neuroimage*, 45(3):832–844, 2009.
- [281] S. Oeltze, A. Hennemuth, S. Glaßer, C. Kühnel, and B. Preim. Glyph-based visualization of myocardial perfusion data and enhancement with contractility and viability information. In *Proc. of Eurographics Workshop on Visual Computing for Biology and Medicine*, pages 11–20, 2008.
- [282] S. Oeltze, D. J. Lehmann, A. Kuhn, G. Janiga, H. Theisel, and B. Preim. Blood flow clustering and applications in virtual stenting of intracranial aneurysms. *IEEE Transactions on Visualization and Computer Graphics*, 20(5):686–701, 2014.
- [283] S. Oeltze-Jafra, J. R. Cebal, G. Janiga, and B. Preim. Cluster analysis of vortical flow in simulations of cerebral aneurysm hemodynamics. *IEEE Transactions on Visualization and Computer Graphics*, 22(1):757–766, 2016.
- [284] I. S. of Unruptured Intracranial Aneurysms Investigators. Unruptured intracranial aneurysms-risk of rupture and risks of surgical intervention. *New England Journal of Medicine*, 339(24):1725–1733, 1998.
- [285] A. H. A. W. G. on Myocardial Segmentation, R. for Cardiac Imaging:, M. D. Cerqueira, N. J. Weissman, V. Dilsizian, A. K. Jacobs, S. Kaul, W. K. Laskey, D. J. Pennell, J. A. Rumberger, T. Ryan, et al. Standardized myocardial segmentation and nomenclature for tomographic imaging of the heart: A statement for healthcare professionals from the Cardiac Imaging Committee of the Council on Clinical Cardiology of the American Heart Association. *Circulation*, 105(4):539–542, 2002.
- [286] C. S. Ong, G. Deib, P. Yesantharao, Y. Qiao, J. Pakpoor, N. Hibino, F. Hui, and J. R. Garcia. Virtual reality in neurointervention. *Journal of Vascular and Interventional Neurology*, 10(1):17–22, 2018.
- [287] M. Otto, T. Germer, and H. Theisel. Uncertain topology of 3D vector fields. In *Proc. of IEEE Pacific Visualization Symposium*, pages 67–74, 2011.
- [288] E. Oubel, M. De Craene, C. M. Putman, J. R. Cebal, and A. F. Frangi. Analysis of intracranial aneurysm wall motion and its effects on hemodynamic patterns. In *Proc. of SPIE Medical Imaging*, volume 6511, pages 65112A–65112A–8, 2007.

- [289] S. J. Owen. A survey of unstructured mesh generation technology. In *Proc. of International Meshing Roundtable*, pages 239–267, 1998.
- [290] N. Paliwal, H. Yu, J. Xu, J. Xiang, A. H. Siddiqui, X. Yang, H. Li, and H. Meng. Virtual stenting workflow with vessel-specific initialization and adaptive expansion for neurovascular stents and flow diverters. *Computer Methods in Biomechanics and Biomedical Engineering*, 19(13):1423–1431, 2016.
- [291] T. Pankau, G. Wichmann, T. Neumuth, B. Preim, A. Dietz, P. Stumpp, and A. Boehm. 3D model-based documentation with the Tumor Therapy Manager (TTM) improves TNM staging of head and neck tumor patients. *International Journal of Computer Assisted Radiology and Surgery*, 10(10):1617–1624, 2015.
- [292] J. Parulek, D. Jönsson, T. Ropinski, S. Bruckner, A. Ynnerman, and I. Viola. Continuous levels-of-detail and visual abstraction for seamless molecular visualization. *Computer Graphics Forum*, 33(6):276–287, 2014.
- [293] R. v. Pelt, A. Fuster, G. Claassen, and A. Vilanova. Characterization of blood-flow patterns from phase-Contrast MRI velocity fields. In *Proc. of EuroVis - Short Papers*, volume 14, 2014.
- [294] C. Petz, K. Pöthkow, and H.-C. Hege. Probabilistic local features in uncertain vector fields with spatial correlation. *Computer Graphics Forum*, 31(3):1045–1054, 2012.
- [295] L. Phan, K. Courchaine, A. Azarbal, D. Vorp, C. Grimm, and S. Rugonyi. A geodesics-based surface parameterization to assess aneurysm progression. *Journal of Biomechanical Engineering*, 138(5):0545031–0545037, 2016.
- [296] M. Piccinelli, D. A. Steinman, Y. Hoi, F. Tong, A. Veneziani, and L. Antiga. Automatic neck plane detection and 3D geometric characterization of aneurysmal sacs. *Annals of Biomedical Engineering*, 40(10):2188–211, 2012.
- [297] L. Pierot, J. Klisch, C. Cognard, I. Szikora, B. Mine, K. Kadziolka, V. Sychra, I. Gubucz, A.-C. Januel, and B. Lubicz. Endovascular WEB flow disruption in middle cerebral artery aneurysms: preliminary feasibility, clinical, and anatomical results in a multicenter study. *Neurosurgery*, 73(1):27–35, 2013.
- [298] L. Pierot, L. Spelle, X. Leclerc, C. Cognard, A. Bonafé, and J. Moret. Endovascular treatment of unruptured intracranial aneurysms: Comparison of safety of remodeling technique and standard treatment with coils. *Radiology*, 251(3):846–855, 2009.
- [299] C. Pierpaoli and P. J. Basser. Toward a quantitative assessment of diffusion anisotropy. *Magnetic Resonance in Medicine*, 36(6):893–906, 1996.
- [300] A. Pobitzer, R. Peikert, R. Fuchs, B. Schindler, A. Kuhn, H. Theisel, K. Matković, and H. Hauser. The state of the art in topology-based visualization of unsteady flow. *Computer Graphics Forum*, 30(6):1789–1811, 2011.
- [301] S. B. Pope. *Turbulent flows*. Cambridge university press, 2000.
- [302] F. H. Post, B. Vrolijk, H. Hauser, R. S. Laramée, and H. Doleisch. The state of the art in flow visualisation: Feature extraction and tracking. *Computer Graphics Forum*, 22(4):775–792, 2003.
- [303] K. Pöthkow and H.-C. Hege. Nonparametric models for uncertainty visualization. *Computer Graphics Forum*, 32(3):131–140, 2013.
- [304] J. M. Pozo, A. J. Geers, and A. F. Frangi. Information theoretic measurement of blood flow complexity in vessels and aneurysms: Interlacing complexity index. In *Proc. of International Conference on Medical Image Computing and Computer-Assisted Intervention*, pages 233–241, 2017.

- [305] B. Preim, A. Baer, D. Cunningham, T. Isenberg, and T. Ropinski. A survey of perceptually motivated 3D visualization of medical image data. *Computer Graphics Forum*, 35(3):501–525, 2016.
- [306] B. Preim and C. Botha. *Visual Computing for Medicine*. Morgan Kaufmann, 2013.
- [307] B. Preim, T. Ropinski, and P. Isenberg. A critical analysis of the evaluation practice in medical visualization. In *Proc. of Eurographics Workshop on Visual Computing for Biology and Medicine*, 2018.
- [308] A. I. Qureshi, J. I. Suarez, P. D. Parekh, G. Sung, R. Geocadin, A. Bhardwaj, R. J. Tamargo, and J. A. Ulatowski. Risk factors for multiple intracranial aneurysms. *Neurosurgery*, 43(1):22–26, 1998.
- [309] M. Raffel, C. E. Willert, F. Scarano, C. J. Kähler, S. T. Wereley, and J. Kompenhans. *Particle image velocimetry: A practical guide*. Springer, 2018.
- [310] M. L. Raghavan, B. Ma, and R. E. Harbaugh. Quantified aneurysm shape and rupture risk. *Journal of Neurosurgery*, 102(2):355–362, 2005.
- [311] M. Raschi, F. Mut, G. Byrne, C. M. Putman, S. Tateshima, F. Viñuela, T. Tanoue, K. Tanishita, and J. R. Cebral. CFD and PIV analysis of hemodynamics in a growing intracranial aneurysm. *International Journal for Numerical Methods in Biomedical Engineering*, 28(2):214–228, 2012.
- [312] A. Rassineux. Generation and optimization of tetrahedral meshes by advancing front technique. *International Journal for Numerical Methods in Engineering*, 41(4):651–674, 1998.
- [313] K. S. Rathod, S. M. Hamshire, D. A. Jones, and A. Mathur. Intravascular ultrasound versus optical coherence tomography for coronary artery imaging—apples and oranges? *Interventional Cardiology Review*, 10(1):8, 2015.
- [314] G. J. Rinkel, M. Djibuti, A. Algra, and J. V. Gijn. Prevalence and risk of rupture of intracranial aneurysms: A systematic review. *Stroke*, 29(1):251–256, 1998.
- [315] J. Rinne, J. Hernesniemi, M. Puranen, and T. Saari. Multiple intracranial aneurysms in a defined population: prospective angiographic and clinical study. *Neurosurgery*, 35(5):803–808, 1994.
- [316] P. J. Roache. *Fundamentals of computational fluid dynamics*, volume 2. Hermosa Publishers Albuquerque, NM, 1998.
- [317] A. Rocha, U. Alim, J. Silva, and M. Sousa. Decal-maps: Real-time layering of decals on surfaces for multivariate visualization. *IEEE Transactions on Visualization and Computer Graphics*, 23(1):821–830, 2017.
- [318] A. C. A. Rocha, J. D. Silva, U. R. Alim, S. Carpendale, and M. C. Sousa. Decal-lenses: Interactive lenses on surfaces for multivariate visualization. *IEEE Transactions on Visualization and Computer Graphics*, 2018.
- [319] C. Roloff, P. Berg, C. Bendicks, K. Zähringer, G. Janiga, and D. Thévenin. Flow investigation inside a cerebral giant aneurysm. In *Proc. of the International Symposium on Applications of Laser Techniques to Fluid Mechanics Lisbon*, volume 330, pages 331–330, 2014.
- [320] C. Roloff, R. Bordás, R. Nickl, Z. Mátrai, N. Szaszák, S. Szilárd, and D. Thévenin. Investigation of the velocity field in a full-scale model of a cerebral aneurysm. *International Journal of Heat and Fluid Flow*, 43:212–219, 2013.
- [321] T. Ropinski, S. Oeltze, and B. Preim. Survey of glyph-based visualization techniques for spatial multivariate medical data. *Computers & Graphics*, 35(2):392–401, 2011.

- [322] S. Rusinkiewicz. Estimating curvatures and their derivatives on triangle meshes. In *Proc. of Symposium on 3D Data Processing, Visualization, and Transmission*, pages 486–493, 2004.
- [323] P. Saalfeld, A. Baer, U. Preim, B. Preim, and K. Lawonn. Sketching 2D vessels and vascular diseases with integrated blood flow. In *Proc. of International Conference on Computer Graphics Theory and Applications*, pages 379–390, 2015.
- [324] P. Saalfeld, A. Stojnic, B. Preim, and S. Oeltze-Jafra. Semi-immersive 3D sketching of vascular structures for medical education. In *Proc. of Eurographics Workshop on Visual Computing for Biology and Medicine*, pages 123–132, 2016.
- [325] S. Saalfeld, P. Berg, A. Niemann, M. Luz, B. Preim, and O. Beuing. Semiautomatic neck curve reconstruction for intracranial aneurysm rupture risk assessment based on morphological parameters. *International Journal of Computer Assisted Radiology and Surgery*, 13(11):1781–1793, 2018.
- [326] J. Sahner, T. Weinkauff, and H.-C. Hege. Galilean invariant extraction and iconic representation of vortex core lines. In *Eurographics / IEEE VGTC Symposium on Visualization*, pages 151–160, 2005.
- [327] O. Sahni, J. Müller, K. Jansen, M. Shephard, and C. Taylor. Efficient anisotropic adaptive discretization of the cardiovascular system. *Computer Methods in Applied Mechanics and Engineering*, 195(41):5634–5655, 2006.
- [328] S. Salvador and P. Chan. Determining the number of clusters/segments in hierarchical clustering/segmentation algorithms. In *Proc. of IEEE International Conference on Tools with Artificial Intelligence*, pages 576–584, 2004.
- [329] T. Salzbrunn, C. Garth, G. Scheuermann, and J. Meyer. Pathline predicates and unsteady flow structures. *The Visual Computer*, 24(12):1039–1051, 2008.
- [330] T. Salzbrunn, H. Jänicke, T. Wischgoll, and G. Scheuermann. The state of the art in flow visualization: Partition-based techniques. In *Proc. of Simulation and Visualization*, pages 75–92, 2008.
- [331] T. Salzbrunn and G. Scheuermann. Streamline predicates. *IEEE Transactions on Visualization and Computer Graphics*, 12(6):1061–1012, 2006.
- [332] M. Sanchez, D. Ambard, V. Costalat, S. Mendez, F. Jourdan, and F. Nicoud. Biomechanical assessment of the individual risk of rupture of cerebral aneurysms: A proof of concept. *Annals of Biomedical Engineering*, 41(1):28–40, 2013.
- [333] A. Sarrami-Foroushani, T. Lassila, and A. F. Frangi. Virtual endovascular treatment of intracranial aneurysms: models and uncertainty. *Wiley Interdisciplinary Reviews: Systems Biology and Medicine*, 9(4):e1385, 2017.
- [334] W. I. Schievink. Genetics of intracranial aneurysms. *Neurosurgery*, 40(4):651–663, 1997.
- [335] J. Schneiders, H. Marquering, L. Antiga, R. Van den Berg, E. VanBavel, and C. Majoie. Intracranial aneurysm neck size overestimation with 3D rotational angiography: The impact on intra-aneurysmal hemodynamics simulated with computational fluid dynamics. *American Journal of Neuroradiology*, 34(1):121–128, 2012.
- [336] J. Schneiders, E. Vanbavel, C. Majoie, S. Ferns, and R. van den Berg. A flow-diverting stent is not a pressure-diverting stent. *American Journal of Neuroradiology*, 34(1):E1–E4, 2013.
- [337] J. Schöberl. NETGEN An advancing front 2D/3D-mesh generator based on abstract rules. *Computing and Visualization in Science*, 1(1):41–52, 1997.

- [338] T. Schultz and G. L. Kindlmann. Superquadric glyphs for symmetric second-order tensors. *IEEE Transactions on Visualization and Computer Graphics*, 16(6):1595–1604, 2010.
- [339] C. Schumann and A. Hennemuth. Three-dimensional visualization of relative pressure in vascular structures. In *Proc. of Deutschen Gesellschaft für Computer- und Roboterassistierte Chirurgie*, pages 337–342, 2015.
- [340] M. Schwenke, A. Hennemuth, B. Fischer, and O. Friman. Blood flow computation in phase-contrast MRI by minimal paths in anisotropic media. In *Proc. of International Conference on Medical Image Computing and Computer-Assisted Intervention*, pages 436–443, 2011.
- [341] Y. Sen, Y. Qian, A. Avolio, and M. Morgan. Image segmentation methods for intracranial aneurysm haemodynamic research. *Journal of Biomechanics*, 47(5):1014–1019, 2014.
- [342] D. M. Sforza, C. M. Putman, and J. R. Cebal. Hemodynamics of cerebral aneurysms. *Annual Review of Fluid Mechanics*, 41:91–107, 2009.
- [343] A. Sheffer, E. Praun, and K. Rose. Mesh parameterization methods and their applications. *Foundations and Trends in Computer Graphics and Vision*, 2(2):105–171, 2006.
- [344] J. Shi and J. Malik. Normalized cuts and image segmentation. *IEEE Transactions on Pattern Analysis and Machine Intelligence*, 22(8):888–905, 2000.
- [345] B. Shneiderman. The eyes have it: A task by data type taxonomy for information visualizations. In *Proc. of IEEE Symposium on Visual Languages*, pages 336–343, 1996.
- [346] M. Shojima, M. Oshima, K. Takagi, R. Torii, M. Hayakawa, K. Katada, A. Morita, and T. Kirino. Magnitude and role of wall shear stress on cerebral aneurysm computational fluid dynamic study of 20 middle cerebral artery aneurysms. *Stroke*, 35(11):2500–2505, 2004.
- [347] A. Sigfridsson, T. Ebbers, E. Heiberg, and L. Wigström. Tensor field visualisation using adaptive filtering of noise fields combined with glyph rendering. In *Proc. of IEEE Visualization Conference*, pages 371–378, 2002.
- [348] M. Singh and B. L. Anderson. Toward a perceptual theory of transparency. *Psychological Review*, 109(3):492, 2002.
- [349] P. K. Singh, A. Marzo, S. C. Coley, G. Berti, P. Bijlenga, P. V. Lawford, M.-C. Villa-Uriol, D. A. Rufenacht, K. M. McCormack, A. Frangi, et al. The role of computational fluid dynamics in the management of unruptured intracranial aneurysms: a clinicians’ view. *Computational Intelligence and Neuroscience*, 2009:5, 2009.
- [350] R. A. Solomon, M. E. Fink, and J. Pile-Spellman. Surgical management of unruptured intracranial aneurysms. *Journal of Neurosurgery*, 80(3):440–446, 1994.
- [351] B. Soni, D. Thompson, and R. Machiraju. Visualizing particle/flow structure interactions in the small bronchial tubes. *IEEE Transactions on Visualization and Computer Graphics*, 14(6):1412–1427, 2008.
- [352] H. Steinmetz. Unrupturierte intrakranielle Aneurysmen. *Der Nervenarzt*, 82(10):1343–1350, 2011.
- [353] C. Stoll, S. Gumhold, and H.-P. Seidel. Visualization with stylized line primitives. In *Proc. of IEEE Visualization Conference*, pages 695–702, 2005.
- [354] D. Streeb and J. Fuchs. Design considerations on glyph placement strategies. 2018.
- [355] S. Succi. *The lattice Boltzmann equation: For fluid dynamics and beyond*. Oxford University Press, 2001.

- [356] G.-D. Sun, Y.-C. Wu, R.-H. Liang, and S.-X. Liu. A survey of visual analytics techniques and applications: State-of-the-art research and future challenges. *Journal of Computer Science and Technology*, 28(5):852–867, 2013.
- [357] K. Sunderland, C. Haferman, G. Chintalapani, and J. Jiang. Vortex analysis of intra-aneurismal flow in cerebral aneurysms. *Computational and mathematical methods in medicine*, 2016, 2016.
- [358] V. Surazhsky, T. Surazhsky, D. Kirsanov, S. J. Gortler, and H. Hoppe. Fast exact and approximate geodesics on meshes. *ACM Transactions on Graphics*, 24(3):553–560, 2005.
- [359] A. Tagliasacchi. Skeletal representations and applications. *arXiv preprint arXiv:1301.6809*, 2014.
- [360] J. Tan, D. Han, J. Wang, T. Liu, T. Wang, H. Zang, Y. Li, and X. Wang. Numerical simulation of normal nasal cavity airflow in Chinese adult: A computational flow dynamics model. *European Archives of Oto-Rhino-Laryngology*, 269(3):881–889, 2012.
- [361] T. Tanoue, S. Tateshima, J. Villablanca, F. Viñuela, and K. Tanishita. Wall shear stress distribution inside growing cerebral aneurysm. *American Journal of Neuroradiology*, 32(9):1732–1737, 2011.
- [362] J. Tao, X. Huang, F. Qiu, C. Wang, J. Jiang, C.-K. Shene, Y. Zhao, and D. Yu. VesselMap: A web interface to explore multivariate vascular data. *Computers & Graphics*, 59:79–92, 2016.
- [363] J. Tao, J. Ma, C. Wang, and C. Shene. A unified approach to streamline selection and viewpoint selection for 3D flow visualization. *IEEE Transactions on Visualization and Computer Graphics*, 19:393–406, 2012.
- [364] S. Tateshima, K. Tanishita, Y. Hakata, S.-y. Tanoue, and F. Viñuela. Alteration of intra-aneurysmal hemodynamics by placement of a self-expandable stent. *Journal of Neurosurgery*, 111(1):22–27, 2009.
- [365] C. A. Taylor and D. A. Steinman. Image-based modeling of blood flow and vessel wall dynamics: Applications, methods and future directions. *Annals of Biomedical Engineering*, 38(3):1188–1203, 2010.
- [366] I. Terem, W. W. Ni, M. Goubran, M. S. Rahimi, G. Zaharchuk, K. W. Yeom, M. E. Moseley, M. Kurt, and S. J. Holdsworth. Revealing sub-voxel motions of brain tissue using phase-based amplified mri (aMRI). *Magnetic Resonance in Medicine*, 2018.
- [367] C. Tominski, P. Schulze-Wollgast, and H. Schumann. 3D information visualization for time dependent data on maps. In *Proc. of International Conference on Information Visualisation*, pages 175–181, 2005.
- [368] L. Tomycz, N. K. Bansal, C. R. Hawley, T. L. Goddard, M. J. Ayad, and R. A. Mericle. “real-world” comparison of non-invasive imaging to conventional catheter angiography in the diagnosis of cerebral aneurysms. *Surgical Neurology International*, 2(134), 2011.
- [369] M. J. Tóth and B. Csébfalvi. *Distribution Interpolation of the Radon Transforms for Shape Transformation of Gray-Scale Images and Volumes*, pages 15–28. Springer, 2015.
- [370] B. Urlick, T. M. Sanders, S. S. Hossain, Y. J. Zhang, and T. J. Hughes. Review of patient-specific vascular modeling: Template-based isogeometric framework and the case for CAD. *Archives of Computational Methods in Engineering*, pages 1–24, 2017.
- [371] K. Valen-Sendstad, K.-A. Mardal, M. Mortensen, B. A. P. Reif, and H. P. Langtangen. Direct numerical simulation of transitional flow in a patient-specific intracranial aneurysm. *Journal of Biomechanics*, 44(16):2826–2832, 2011.

- [372] K. Valen-Sendstad, K.-A. Mardal, and D. A. Steinman. High-resolution CFD detects high-frequency velocity fluctuations in bifurcation, but not sidewall, aneurysms. *Journal of Biomechanics*, 46(2):402–407, 2013.
- [373] K. Valen-Sendstad, M. Piccinelli, R. KrishnankuttyRema, and D. A. Steinman. Estimation of inlet flow rates for image-based aneurysm CFD models: Where and how to begin? *Annals of Biomedical Engineering*, 43(6):1422–1431, 2015.
- [374] A. Valencia, D. Ledermann, R. Rivera, E. Bravo, and et al. Blood flow dynamics and fluid-structure interaction in patient-specific bifurcating cerebral aneurysms. *International Journal for Numerical Methods in Fluids*, 58(10):1081–1100, 2008.
- [375] A. G. van der Kolk, J. J. Zwanenburg, M. Brundel, G.-J. Biessels, F. Visser, P. R. Luijten, and J. Hendrikse. Intracranial vessel wall imaging at 7.0-T MRI. *Stroke*, 42(9):2478–2484, 2011.
- [376] M. Van Der Zwan, W. Lueks, H. Bekker, and T. Isenberg. Illustrative molecular visualization with continuous abstraction. *Computer Graphics Forum*, 30(3):683–690, 2011.
- [377] J. Van Gijn, R. S. Kerr, and G. J. Rinkel. Subarachnoid haemorrhage. *The Lancet*, 369(9558):306–318, 2007.
- [378] R. van Pelt, J. O. Bescós, M. Breeuwer, R. Clough, M. E. Gröller, B. ter Haar Romeny, and A. Vilanova. Interactive virtual probing of 4D MRI blood-flow. *IEEE Transactions on Visualization and Computer Graphics*, 17(12):2153–2162, 2011.
- [379] R. van Pelt, J. O. Bescos, M. Breeuwer, R. E. Clough, M. E. Groller, B. ter Haar Romenij, and A. Vilanova. Exploration of 4D MRI blood flow using stylistic visualization. *IEEE Transactions on Visualization and Computer Graphics*, 16(6):1339–1347, 2010.
- [380] R. Van Pelt, S. Jacobs, B. M. ter Haar Romeny, and A. Vilanova. Visualization of 4D blood-flow fields by spatiotemporal hierarchical clustering. *Computer Graphics Forum*, 31(3pt2):1065–1074, 2012.
- [381] R. van Pelt and A. Vilanova. Understanding blood-flow dynamics: New challenges for visualization. *Computer*, 46(12):60–67, 2013.
- [382] W. van Rooij, M. Sprengers, A. de Gast, J. Peluso, and M. Sluzewski. 3D rotational angiography: The new gold standard in the detection of additional intracranial aneurysms. *American Journal of Neuroradiology*, 29(5):976–979, 2008.
- [383] P. P. Vázquez, M. Feixas, M. Sbert, and W. Heidrich. Viewpoint selection using viewpoint entropy. In *Proc. of Vision, Modelling und Visualization*, pages 273–280, 2001.
- [384] P. P. Vázquez, M. Feixas, M. Sbert, and W. Heidrich. Automatic view selection using viewpoint entropy and its application to image-based modeling. *Computer Graphics Forum*, 22(4):689–700, 2003.
- [385] S. Venkataraman. 4D visualization of cardiac flow. In *Proc. of NVIDIA GPU Technology Conference Talk*, 2010.
- [386] V. Vezhnevets and V. Konouchine. GrowCut: Interactive multi-label ND image segmentation by cellular automata. In *Proc. of Graphicon*, volume 1, pages 150–156, 2005.
- [387] A. Vilanova, B. Preim, R. van Pelt, R. Gasteiger, M. Neugebauer, and T. Wischgoll. Visual exploration of simulated and measured blood flow. In *Scientific Visualization*, pages 305–324. Springer, 2014.
- [388] M. Villa-Urriol, I. Larrabide, J. Pozo, M. Kim, M. De Craene, O. Camara, C. Zhang, A. Geers, H. Bogunović, H. Morales, et al. Cerebral aneurysms: A patient-specific and image-based management pipeline. In *Proc. of Computational Vision and Medical Image Processing*, pages 327–349, 2011.



- [389] R. Vindlacheruvu, A. Mendelow, and P. Mitchell. Risk–benefit analysis of the treatment of unruptured intracranial aneurysms. *Journal of Neurology, Neurosurgery & Psychiatry*, 76(2):234–239, 2005.
- [390] M. H. Vlak, A. Algra, R. Brandenburg, and G. J. Rinkel. Prevalence of unruptured intracranial aneurysms, with emphasis on sex, age, comorbidity, country, and time period: A systematic review and meta-analysis. *The Lancet Neurology*, 10(7):626–636, 2011.
- [391] I. Volkau, W. Zheng, R. Baimouratov, A. Aziz, and W. L. Nowinski. Geometric modeling of the human normal cerebral arterial system. *IEEE Transactions on Medical Imaging*, 24(4):529–539, 2005.
- [392] J. von Spiczak, G. Crelier, D. Giese, S. Kozerke, D. Maintz, and A. C. Bunck. Quantitative analysis of vortical blood flow in the thoracic aorta using 4D phase contrast MRI. *PLoS ONE*, 10(9):e0139025, 2015.
- [393] S. Voß, S. Glaßer, T. Hoffmann, O. Beuing, S. Weigand, K. Jachau, B. Preim, D. Thévenin, G. Janiga, and P. Berg. Fluid-structure simulations of a ruptured intracranial aneurysm: constant versus patient-specific wall thickness. *Computational and Mathematical Methods in Medicine*, 2016, 2016.
- [394] S. Voß, S. Saalfeld, T. Hoffmann, O. Beuing, G. Janiga, and P. Berg. Fluid-structure interaction in intracranial vessel walls: The role of patient-specific wall thickness. *Current Directions in Biomedical Engineering*, 4(1):587–590, 2018.
- [395] L. Wang, J. Giesen, K. T. McDonnell, P. Zolliker, and K. Mueller. Color design for illustrative visualization. *IEEE Transactions on Visualization and Computer Graphics*, 14(6):1739–1754, 2008.
- [396] Y. Wang, X. Gu, T. F. Chan, P. M. Thompson, and S.-T. Yau. Conformal slit mapping and its applications to brain surface parameterization. In *International Conference on Medical Image Computing and Computer-Assisted Intervention*, pages 585–593, 2008.
- [397] I. Wanke, A. Doerfler, B. Schoch, D. Stolke, and M. Forsting. Treatment of wide-necked intracranial aneurysms with a self-expanding stent system: initial clinical experience. *American Journal of Neuroradiology*, 24(6):1192–1199, 2003.
- [398] C. Ware. Toward a perceptual theory of flow visualization. *IEEE Computer Graphics and Applications*, 28(2), 2008.
- [399] P. N. Watton, Y. Ventikos, and G. A. Holzapfel. Modelling the growth and stabilization of cerebral aneurysms. *Mathematical Medicine and Biology*, 26(2):133–164, 2009.
- [400] Y. Wei, S. Cotin, J. Allard, L. Fang, C. Pan, and S. Ma. Interactive blood-coil simulation in real-time during aneurysm embolization. *Computers & Graphics*, 35(2):422–430, 2011.
- [401] B. Weir, C. Amidei, G. Kongable, J. M. Findlay, N. F. Kassell, J. Kelly, L. Dai, and T. G. Karrison. The aspect ratio (dome/neck) of ruptured and unruptured aneurysms. *Journal of Neurosurgery*, 99(3):447–451, 2003.
- [402] B. Weir, L. Disney, and T. Karrison. Sizes of ruptured and unruptured aneurysms in relation to their sites and the ages of patients. *Journal of Neurosurgery*, 96(1):64–70, 2002.
- [403] M. J. Wermer, I. C. van der Schaaf, A. Algra, and G. J. Rinkel. Risk of rupture of unruptured intracranial aneurysms in relation to patient and aneurysm characteristics. *Stroke*, 38(4):1404–1410, 2007.
- [404] C. F. Westin, B. Maier, S. E. and Khidhir, P. Everett, F. A. Jolesz, and R. Kikinis. Image processing for diffusion tensor magnetic resonance imaging. In *Proc. of International Conference on Medical Image Computing and Computer-Assisted Intervention*, pages 441–452, 1999.

- [405] C.-F. Westin, S. E. Maier, H. Mamata, A. Nabavi, F. A. Jolesz, and R. Kikinis. Processing and visualization for diffusion tensor MRI. *Medical Image Analysis*, 6(2):93–108, 2002.
- [406] A. Wibmer, H. A. Vargas, R. Sosa, J. Zheng, C. Moskowitz, and H. Hricak. Value of a standardized lexicon for reporting levels of diagnostic certainty in prostate MRI. *American Journal of Roentgenology*, 203(6):W651–W657, 2014.
- [407] D. O. Wiebers. Unruptured intracranial aneurysms: Natural history, clinical outcome, and risks of surgical and endovascular treatment. *The Lancet*, 362(9378):103–110, 2003.
- [408] L. Wigström, T. Ebbers, A. Fyrenius, M. Karlsson, J. Engvall, B. Wranne, and A. F. Bolger. Particle trace visualization of intracardiac flow using time-resolved 3D phase contrast MRI. *Magnetic Resonance in Medicine*, 41(4):793–799, 1999.
- [409] D. C. Wilcox. *Turbulence modelling for CFD*. DCW Industries, Inc., 1998.
- [410] L. N. Williams and R. D. Brown. Management of unruptured intracranial aneurysms. *Neurology. Clinical Practice*, 3(2):99–108, 2013.
- [411] F. Wirth, E. Laws Jr, D. Piepgras, and R. Scott. Surgical treatment of incidental intracranial aneurysms. *Neurosurgery*, 12(5):507–511, 1983.
- [412] G. K. Wong, H.-B. Tan, M. C. Kwan, R. Y. Ng, C. Simon, X.-L. Zhu, and W.-S. Poon. Evolution of intracranial aneurysm treatment: from Hunterian ligation to the flow diverter. *Surgical Practice*, 15(1):16–20, 2011.
- [413] K. K. L. Wong, R. M. Kelso, S. G. Worthley, P. Sanders, J. Mazumdar, and D. Abbott. Cardiac flow analysis applied to phase contrast magnetic resonance imaging of the heart. *Annals of Biomedical Engineering*, 37(8):1495–1515, 2009.
- [414] W. C. Wong and A. C. Chung. Augmented vessels for quantitative analysis of vascular abnormalities and endovascular treatment planning. *IEEE Transactions on Medical Imaging*, 25(6):665–684, 2006.
- [415] J. Xi, X. Si, Y. Zhou, J. Kim, and A. Berlinski. Growth of nasal-laryngeal airways in children and their implications in breathing and inhaled aerosol dynamics. *Respiratory Care*, 59(2):respcare–02568, 2014.
- [416] N. Yasui, S. Magarisawa, A. Suzuki, H. Nishimura, T. Okudera, and T. Abe. Subarachnoid hemorrhage caused by previously diagnosed, previously unruptured intracranial aneurysms: A retrospective analysis of 25 cases. *Neurosurgery*, 39(6):1096–1101, 1996.
- [417] S. Yoshimura, M. Kawasaki, K. Yamada, Y. Enomoto, Y. Egashira, A. Hattori, K. Nishigaki, S. Minatoguchi, and T. Iwama. Visualization of internal carotid artery atherosclerotic plaques in symptomatic and asymptomatic patients: a comparison of optical coherence tomography and intravascular ultrasound. *American Journal of Neuroradiology*, 33(2):308–313, 2011.
- [418] L. Yu, L. Harrison, and A. Lu. Storytelling in 3D time-varying data visualization. *Journal of Imaging Science and Technology*, 60(6):60408–1–60408–11(11), 2016.
- [419] L. Yu, A. Lu, W. Ribarsky, and W. Chen. Automatic animation for time-varying data visualization. *Computer Graphics Forum*, 29(7):2271–2280, 2010.
- [420] R. Zayer, C. Rössl, and H.-P. Seidel. Discrete tensorial quasi-harmonic maps. In *Proc. of IEEE Shape Modeling and Applications*, pages 276–285, 2005.
- [421] C. Zhang, T. Schultz, K. Lawonn, E. Eisemann, and A. Vilanova. Glyph-based comparative visualization for diffusion tensor fields. *IEEE Transactions on Visualization and Computer Graphics*, 22(1):797–806, 2016.

- [422] Z. Zhang. Iterative point matching for registration of free-form curves and surfaces. *International Journal of Computer Vision*, 13(2):119–152, 1994.
- [423] O. Zikanov. *Essential computational fluid dynamics*. John Wiley & Sons, 2010.
- [424] M. Zöckler, D. Stalling, and H.-C. Hege. Interactive visualization of 3D-vector fields using illuminated stream lines. In *Proc. of IEEE Visualization Conference*, pages 107–113, 1996.

## LIST OF PUBLICATIONS

---

- [425] B. Köhler, **M. Meuschke**, U. Preim, K. Fischbach, M. Gutberlet, and B. Preim. Two-Dimensional Plot Visualization of Aortic Vortex Flow in Cardiac 4D PC-MRI Data. In *Proc. of Bildverarbeitung für die Medizin*, pages 257–262, 2015.
- [426] J. Kreiser, **M. Meuschke**, G. Mistelbauer, B. Preim, and T. Ropinski. A survey of flattening-based medical visualization techniques. *Computer Graphics Forum*, 37(3):597–624, 2018.
- [427] K. Lawonn, **M. Meuschke**, B. Preim, and K. Hildebrandt. Automatic Detection and Segmentation of Multiple Aneurysms. *Computer Graphics Forum*, page in revision, 2019.
- [428] S. Oeltze-Jafra, **M. Meuschke**, M. Neugebauer, S. Saalfeld, K. Lawonn, G. Janiga, H.-C. Hege, S. Zachow, and B. Preim. Generation and visual exploration of medical flow data: Survey, research trends and future challenges. *Computer Graphics Forum*, 2018.
- [429] **M. Meuschke**, W. Engelke, O. Beuing, B. Preim, and K. Lawonn. Automatic Viewpoint Selection for Exploration of Time-dependent Cerebral Aneurysm Data. In *Proc. of Bildverarbeitung für die Medizin*, pages 352–357, 2017.
- [430] **M. Meuschke**, T. Günther, P. Berg, R. Wickenhöfer, B. Preim, and K. Lawonn. Visual Analysis of Aneurysm Data using Statistical Graphics. *IEEE Transactions on Visualization and Computer Graphics*, 25(1):997–1007, 2018.
- [431] **M. Meuschke**, T. Günther, R. Wickenhöfer, M. Gross, B. Preim, and K. Lawonn. Management of cerebral aneurysm descriptors based on an automatic ostium extraction. *IEEE Computer Graphics and Applications*, 38(3):58–72, 2018.
- [432] **M. Meuschke**, B. Köhler, U. Preim, B. Preim, and K. Lawonn. Semi-automatic Vortex Flow Classification in 4D PC-MRI Data of the Aorta. *Computer Graphics Forum*, 35(3):351–360, 2016.
- [433] **M. Meuschke**, K. Lawonn, B. Köhler, U. Preim, and B. Preim. Clustering of Aortic Vortex Flow in Cardiac 4D PC-MRI Data. In *Proc. of Bildverarbeitung für die Medizin*, pages 182–187, 2016.
- [434] **M. Meuschke**, S. Oeltze-Jafra, O. Beuing, B. Preim, and K. Lawonn. Classification of blood flow patterns in cerebral aneurysms. *IEEE Transactions on Visualization and Computer Graphics*, 2018.
- [435] **M. Meuschke**, N. N. Smit, N. Lichtenberg, B. Preim, and K. Lawonn. Automatic Generation of Web-Based User Studies to Evaluate Depth Perception in Vascular Surface Visualizations. In *Proc. of Eurographics Workshop on Visual Computing for Biology and Medicine*, 2018.
- [436] **M. Meuschke**, S. Voß, O. Beuing, B. Preim, and K. Lawonn. Combined Visualization of Vessel Deformation and Hemodynamics in Cerebral Aneurysms. *IEEE Transactions on Visualization and Computer Graphics*, 23(1):761–770, 2017.
- [437] **M. Meuschke**, S. Voß, O. Beuing, B. Preim, and K. Lawonn. Glyph-based Comparative Stress Tensor Visualization in Cerebral Aneurysms. *Computer Graphics Forum*, 36(3):99–108, 2017.
- [438] **M. Meuschke**, S. Voß, B. Preim, and K. Lawonn. Exploration of Blood Flow Patterns in Cerebral Aneurysms during the Cardiac Cycle. *Computers & Graphics*, 72:12–25, 2018.
- [439] R. van Pelt, R. Gasteiger, K. Lawonn, **M. Meuschke**, and B. Preim. Comparative Blood Flow Visualization for Cerebral Aneurysm Treatment Assessment. *Computer Graphics Forum*, 33(3):131–140, 2014.

## ABBREVIATIONS

---

### Symbols

<b>1D</b>	One-dimensional
<b>2D</b>	Two-dimensional
<b>2.5D</b>	Two and a half dimensional
<b>2DM</b>	Manual 2D
<b>3D</b>	Three-dimensional
<b>3DA</b>	Automatic 3D
<b>3DM</b>	Manual 3D
<b>4D</b>	Four-dimensional

### Terminology

<b>AHC</b>	Agglomerative hierarchical clustering
<b>aMRI</b>	phase-based amplified magnetic resonance imaging
<b>AO</b>	Ambient occlusion
<b>BEP</b>	Bull's eye plot
<b>CAD</b>	Computer-aided design
<b>CAVOCLA</b>	Cerebral aneurysm vortex classification
<b>CFD</b>	Computational fluid dynamics
<b>CoTenVis</b>	Comparative tensor visualization
<b>CoWaFloVis</b>	Combined wall and flow visualization
<b>CPU</b>	Central processing unit
<b>CT</b>	Computed tomography
<b>CTA</b>	Computed tomography angiography
<b>CVD</b>	Cardiovascular disease
<b>DBSCAN</b>	Density-based spatial clustering of application with noise
<b>DSA</b>	Digital subtraction angiography
<b>DTI</b>	Diffusion tensor imaging
<b>DVR</b>	Direct volume rendering
<b>DOF</b>	Degree of freedom
<b>EG</b>	Expert group
<b>FDM</b>	Finite differences method

<b>FEA</b>	Finite element analysis
<b>FEM</b>	Finite elements method
<b>FPS</b>	Frames per second
<b>FSI</b>	Fluid-structure interaction
<b>FTLE</b>	Finite-time Lyapunov Exponent
<b>FTP</b>	File transfer protocol
<b>FVM</b>	Finite volumes method
<b>FVS</b>	Fast virtual stenting
<b>GPU</b>	Graphics processing unit
<b>GUI</b>	Graphical user interface
<b>IA</b>	Intracranial aneurysm
<b>IBM</b>	Immersed boundary method
<b>ICP</b>	Iterative closest point
<b>IVUS</b>	Intravascular ultrasound
<b>LBM</b>	Lattice Boltzmann method
<b>LSCM</b>	Least squares conformal map
<b>LIC</b>	Line integral convolution
<b>LOD</b>	Level-of-detail
<b>LSCM</b>	Least squares conformal maps
<b>MCPD</b>	Mean of closest point distances
<b>MIP</b>	Maximum intensity projection
<b>MorAVis</b>	Morphological aneurysm visualization
<b>MPR</b>	Multiplanar reformation
<b>MR</b>	Magnetic resonance
<b>MRA</b>	Magnetic resonance angiography
<b>MRI</b>	Magnetic resonance imaging
<b>MuScaVis</b>	Multiple scalar field visualization
<b>NFV</b>	Net flow volume
<b>NSE</b>	Navier-Stokes equations
<b>NWF</b>	Near-wall flow
<b>OCT</b>	Optical coherence tomography
<b>OpenGL</b>	Open graphics library
<b>OpenTK</b>	Open toolkit library

<b>OSI</b>	Oscillatory shear index
<b>PACS</b>	Picture archiving and communication system
<b>PSD</b>	Principal stress direction
<b>PIV</b>	Particle image velocimetry
<b>PCA</b>	Principal component analysis
<b>PC-MRI</b>	Phase-contrast magnetic resonance imaging
<b>PDE</b>	Partial differential equation
<b>RA</b>	Rotational angiography
<b>RAM</b>	Random-access memory
<b>RaNS</b>	Reynolds-averaged Navier-Stokes
<b>ROI</b>	Region of interest
<b>RGB</b>	Red, green, blue
<b>SAH</b>	Subarachnoid hemorrhage
<b>SC</b>	Spectral clustering
<b>SCP</b>	Spectral conformal parametrization
<b>SL</b>	Streamline
<b>SP</b>	Scatterplot
<b>SQ</b>	Superquadric
<b>SST</b>	Shear-stress-transport
<b>ToF</b>	Time-of-flight
<b>tMIP</b>	Temporal maximum intensity projection
<b>ToT</b>	Turnover time
<b>ViFIEx</b>	Visual flow exploration
<b>VR</b>	Virtual reality
<b>WEB</b>	Woven EndoBridge
<b>WSS</b>	Wall shear stress





## EHRENERKLÄRUNG

---

„Ich versichere hiermit, dass ich die vorliegende Arbeit ohne unzulässige Hilfe Dritter und ohne Benutzung anderer als der angegebenen Hilfsmittel angefertigt habe; verwendete fremde und eigene Quellen sind als solche kenntlich gemacht. Insbesondere habe ich nicht die Hilfe eines kommerziellen Promotionsberaters in Anspruch genommen. Dritte haben von mir weder unmittelbar noch mittelbar geldwerte Leistungen für Arbeiten erhalten, die im Zusammenhang mit dem Inhalt der vorgelegten Dissertation stehen.

Ich habe insbesondere nicht wissentlich:

- Ergebnisse erfunden oder widersprüchliche Ergebnisse verschwiegen,
- statistische Verfahren absichtlich missbraucht, um Daten in ungerechtfertigter Weise zu interpretieren,
- fremde Ergebnisse oder Veröffentlichungen plagiiert,
- fremde Forschungsergebnisse verzerrt wiedergegeben.

Mir ist bekannt, dass Verstöße gegen das Urheberrecht Unterlassungs- und Schadensersatzansprüche des Urhebers sowie eine strafrechtliche Ahndung durch die Strafverfolgungsbehörden begründen kann. Die Arbeit wurde bisher weder im Inland noch im Ausland in gleicher oder ähnlicher Form als Dissertation eingereicht und ist als Ganzes auch noch nicht veröffentlicht.“

*Magdeburg, 21. Januar 2019*

---

Monique Meuschke



## CURRICULUM VITAE

---

### PERSONAL DETAILS

Name: **Monique Meuschke**  
Date of birth: 03.06.1988  
Place of birth: 06333 Hettstedt  
Civil Status: Unmarried, no children  
Nationality: German  
Contact: [meuschke@isg.cs.uni-magdeburg.de](mailto:meuschke@isg.cs.uni-magdeburg.de)



### EDUCATION

- since 08/2015: Otto-von-Guericke University Magdeburg, research assistant / PhD student
- Teaching: Computer-aided Diagnosis and Therapy (Bachelor courses)
  - Thesis topic: *"Visualization, Classification, and Interaction for Risk Analysis and Treatment Planning of Cerebral Aneurysms"*
  - Desired degree: **Doktoringenieur (Dr.-Ing.)**
- 04/2013 – 07/2015: Otto-von-Guericke University Magdeburg, studies of Computational Visualistics (Master):
- Thesis title: *"Computer-aided analysis of vortices in 4D PC-MRI blood flow data of the aorta"*, original title: *"Computergestützte Analyse von Verwirbelungen in 4D PC-MRI Blutflussdaten der Aorta"*, grade: 1.0
  - Degree: **Master of Science (M. Sc.)**, grade: **1.0**
- 10/2009 – 03/2013: Otto-von-Guericke University Magdeburg, studies of Computational Visualistics (Bachelor):
- Application subject: Medicine
  - Thesis title: *"Development and evaluation of a local, atlas-based adaptive fiber tracking method"*, original title: *"Entwicklung und Evaluation eines lokalen, atlasbasiert-adaptiven Fiber-Tracking-Verfahrens"*, grade: 1.0
  - Degree: **Bachelor of Science (B. Sc.)**, grade: **1.5**
- 09/2000 – 06/2009: Gymnasium am Markt Hettstedt:
- Degree: **"Abitur"**, grade: **1.7**

## WORK EXPERIENCE

- since 08/2015: Otto-von-Guericke University Magdeburg, research assistant  
 – Research Campus STIMUALTE (research group: "Tools/Hemodynamics"): *"Standardized evaluation of CFD data"*, original title: *"Standardisierte Auswertung von CFD Daten"*
- 07/2017 – 10/2017: ETH Zurich, research assistant  
 – Topic: Extraction and visualization of morphological characteristics in cerebral aneurysms
- 05/2013 – 10/2014: Otto-von-Guericke University Magdeburg, student assistant  
 – Topic: Visualization of simulated and measured blood flow data
- 05/2013 – 11/2013: Fraunhofer MeVis, Bremen, external student assistant  
 – Topic: Integration of the developed method during the Bachelor thesis as a module for MeVisLab
- 10/2012 – 03/2013: Fraunhofer MeVis, Bremen, combined internship and Bachelor thesis  
 – Topic: Local, atlas-based adaptive fiber tracking
- 04/2012 – 09/2012: Otto-von-Guericke University Magdeburg, student assistant  
 – Topic: Management of simulated and measured blood flow data
- 2010 – 2012: Magdeburg, temporary help in a riding shop

## EXPERTISE

- Programming: C#, OpenGL, GLSL, VTK, MATLAB, C/C++, Python
- Applications: Microsoft Office, MeVisLab, Visual Studio, Inkscape, Gimp, ParaView, Meshlab, Camtasia Studio, Sculptris, 3D Studio Max
- Typesetting: L<sup>A</sup>T<sub>E</sub>X, Microsoft Word

## AWARDS

- 09/2018: 1. Place Best Poster Eurographics Workshop on Visual Computing for Biology and Medicine
- 12/2017: Research Award of the Faculty of Computer Science of the Otto-von-Guericke-University Magdeburg
- 03/2017: 3. Place Best Paper Bildverarbeitung für die Medizin
- 09/2016: 3. Place Karl-Heinz Höhne Award for Medical Visualization
- 11/2015: Best Graduate of the Faculty of Computer Science of the Otto-von-Guericke-University Magdeburg